UNIMORE
UNIVERSITÀ DEGLI STUDI DI MODENA E REGGIO EMILIA

DOCTORATE SCHOOL
INDUSTRIAL INNOVATION ENGINEERING
XXXVIII CYCLE

COMPREHENSIVE MODELING AND EXPERIMENTAL ANALYSIS OF ADVANCED HEATING VENTILATION AND AIR CONDITIONING SYSTEMS

Scientific Tutors:
Prof. Ing. Diego Angeli
Prof. Ing. Paolo Emilio Santangelo

School Dean:
Prof. Ing. Franco Zambonelli

Candidate:
Roberto Sedoni

UNIVERSITY OF MODENA AND REGGIO EMILIA
ACADEMIC YEAR 2024/2025

Abstract

Decarbonization in the building sector requires substantial improvement in the efficiency of heating, cooling and ventilation systems, the energy demand of which is the most relevant in residential buildings. In nearly Zero Energy Buildings (nZEB), highly insulated and airtight envelopes may reduce the need for air conditioning, but at the same time they increase the impact of ventilation-related load. Multifunctional balanced ventilation units, also known as exhaust air heat pumps, which integrate mechanical ventilation, heat recovery and air-to-air heat pumps, represent a promising pathway to combine indoor air-quality requirements with low-energy operation. However, their performance is determined by the interactions among multiple subsystems, which require advanced modeling and validation.

In this work—carried out in collaboration with Zehnder Group Competence Center Campogalliano—a high-fidelity digital twin of a multifunctional balanced ventilation unit for residential applications was developed and subsequently validated. The proposed model combines detailed physics-based representation of all the major components involved; system control logics is also integrated into the model, thus enabling it to reproduce and predict both steady-state and transient behavior. The digital twin was calibrated and validated against an extensive experimental dataset acquired at the Kompaktgeräteprüfstand laboratory of Universität Innsbruck, Austria; the employed facility is specifically designed for the assessment of compact units and heat pumps under controlled environmental conditions.

The reliability of the digital twin in predicting system behavior was successfully proven over a broad range of operating conditions, encompassing summer and winter regime, as well as frosting events. Upon validation, the model was employed as a predictive tool to explore scenarios not tested in the experiments, such as alternative bypass strategies of the recovery exchanger, integration of an auxiliary fan in the heat pump unit and the

comparative evaluation of sensible heat and enthalpy recovery. The analysis revealed the need for pursuing a trade-off between energy efficiency and fulfillment of heating and cooling demands. The findings highlight how different design and control strategies impact the energy management of the system, also providing a new insight into its flexibility and limitations.

The study also demonstrates the potential of digital twins to support the development of the next generation of HVAC (Heating, Ventilation and Air Conditioning) systems. By bridging rigorous experimental testing with advanced modeling, digital twins stand as a robust tool for optimizing design, enhancing control strategies and facilitating the transition of the buildiing sector toward current and future energy saving and climate objectives.

Sommario

Il raggiungimento degli obiettivi di decarbonizzazione nel settore edilizio richiede un sostanziale incremento dell'efficienza nei sistemi di riscaldamento, raffrescamento e ventilazione, che tuttora implicano la maggior parte del consumo energetico in edifici residenziali. Negli edifici a consumo virtualmente nullo (nZEB, acronimo in lingua inglese), involucri altamente isolati e a tenuta riducono il fabbisogno di climatizzazione, ma allo stesso tempo aumentano l'incidenza del carico legato alla ventilazione. Le unità di ventilazione bilanciata multifunzionali, che integrano ventilazione meccanica a recupero di calore e pompe di calore aria-aria, rappresentano una soluzione promettente per conciliare i requisiti di qualità dell'aria interna con un funzionamento a basso consumo energetico. Tuttavia, le loro prestazioni sono governate da interazioni fortemente accoppiate, che richiedono modelli avanzati e una validazione sperimentale sistematica.

In questo lavoro, svolto in collaborazione con Zehnder Group Competence Center Campogalliano, è stato sviluppato e validato un gemello digitale (digital twin) ad alta fedeltà di un'unità di ventilazione bilanciata multifunzionale per applicazioni residenziali. Il modello combina rappresentazioni fisiche dettagliate di tutti i principali componenti, oltre a integrare le logiche di controllo del sistema al suo interno, risultando in grado di riprodurre con elevata accuratezza sia il comportamento in regime stazionario, sia in regime transitorio. Il digital twin è stato calibrato e validato sulla base di un'ampia campagna sperimentale svolta presso il laboratorio Kompaktgeräteprüfstand di Universität Innsbruck, Austria, una struttura appositamente progettata per la caratterizzazione di unità compatte e pompe di calore in condizioni di prova controllate.

I risultati confermano l'affidabilità predittiva del digital twin rispetto al comportamento del sistema su un ampio spettro di condizioni operative, che includono regime estivo, invernale e fenomeni di brinamento. Una volta validato, il modello è stato impiegato come strumento predittivo per esplorare scenari non coperti dalla campagna speri-

mentale, quali strategie alternative di bypass del recuperatore di calore, integrazione di un ventilatore ausiliario nella pompa di calore e confronto tra recupero di calore sensibile ed entalpico. L'analisi mette in evidenza la necessità di perseguire un compromesso tra la massimizzazione dell'efficienza energetica del sistema e il soddisfacimento del fabbisogno termico di riscaldamento e raffrescamento dell'edificio. I risultati mostrano come diverse scelte progettuali e di controllo possano supportare la gestione energetica del sistema, offrendo nuove prospettive sulla flessibilità operativa e sui limiti di queste unità.

Nel complesso, è stato dimostrato il potenziale dei digital twin come strumenti a supporto dello sviluppo della prossima generazione di sistemi di climatizzazione. Unendo sperimentazione rigorosa e modellazione avanzata, i digital twin incarnano una metodologia robusta per ottimizzare la progettazione, migliorare le strategie di controllo e facilitare la transizione degli edifici verso i nuovi obiettivi energetici e climatici.

Contents

List of symbols

Latin letters

A	area [m^2]
C	heat capacity rate [$W K^{-1}$]
c_p	specific heat at constant pressure [$J kg^{-1} K^{-1}$]
c_{wall}	wall specific heat [$J kg^{-1} K^{-1}$]
CL	cooling load [W]
D	water vapor diffusion coefficient [$m^2 s^{-1}$]
D_{AB}	binary diffusion coefficient [$m^2 s^{-1}$]
D_c	fin collar outside diameter ($OD + \delta_{fin}$) [m]
D_h	hydraulic diameter [m]
DP	dew point [°C]
Δh_{sub}	latent heat of sublimation [$J kg^{-1}$]
Δh_{vap}	latent heat of evaporation [$J kg^{-1}$]
F_p	fin pitch [m]
f	Darcy friction factor [—]
$\tilde{f}$	Fanning friction factor [—]
h	specific enthalpy [$J kg^{-1}$]
HL	heating load [W]
ID	inner tube diameter [m]
J	water vapor mass flux [$kg m^{-2} s^{-1}$]
j_{MA}	Colburn j-factor [—]

K	Chisholm parameter [−] or loss coefficient [−]
K_v	valve flow coefficient [$m^3\,h^{-1}$]
k	thermal conductivity [$W\,m^{-1}\,K^{-1}$]
L	length [m]
Le	Lewis number [m]
M	mass [kg]
M_w	molecular weight of water [$kg\,mol^{-1}$]
$\dot{m}"_t$	thickening water vapor mass flux [$kg\,m^{-2}\,s^{-1}$]
$\dot{m}"_\rho$	densification water vapor mass flux [$kg\,m^{-2}\,s^{-1}$]
$\dot{m}"_w$	total water vapor mass flux [$kg\,m^{-2}\,s^{-1}$]
$\dot{m}$	mass flow rate [$kg\,s^{-1}$]
Nu	Nusselt number [−]
NTU	Number of Transfer Units [−]
n	number [−]
OD	outer tube diameter [m]
p	pressure [Pa]
PC	power consumption [W]
P_l	longitudinal tube pitch [m]
Pr	Prandtl number [−]
P_t	transverse tube pitch [m]
$\dot{Q}$	heat flow rate [W]
$q"$	heat flux [$W\,m^{-2}$]
Re	Reynolds number [−]
R	specific gas constant [$J\,kg^{-1}\,K^{-1}$] or mass flow rate ratio [−]
R_e	equivalent fin external radius [m]
RH	relative humidity [%]
S	cross-section [m^2]
T	temperature [K]
t	time [s]
u	specific internal energy [$J\,kg^{-1}$]
U	overall heat transfer coefficient [$W\,m^{-2}\,K^{-1}$]
V	volume [m^3]

$\dot{W}$	mechanical power [W]
w	velocity [$\mathrm{m\,s^{-1}}$]
W	humidity ratio [$\mathrm{kg\,kg_{dry}^{-1}}$]
W_s	saturation humidity ratio [$\mathrm{kg\,kg_{dry}^{-1}}$]
X	generic variable
x	vapor quality [−]
x_w	specific humidity [$\mathrm{kg\,kg^{-1}}$]
z	axial length [m]
z^*	dimensionless axial length [m]
z_L	liquid volume fraction [−]

Greek letters

α	heat transfer coefficient [$\mathrm{W\,m^{-2}\,K^{-1}}$]
α_m	mass transfer coefficient [$\mathrm{m\,s^{-1}}$]
δ	thickness [m]
ε	effectiveness [−]
ε_r	relative roughness [−]
ϵ	channel aspect ratio [−] or porosity [−]
η	efficiency [−]
ν	specific volume [$\mathrm{m^3\,kg^{-1}}$]
ϕ	phase multiplier [−]
Φ	total energy [W]
ρ	density [$\mathrm{kg\,m^{-3}}$]
σ	ratio of the minimum free flow area to the frontal-area [−]
τ	time constant [s] or tortuosity factor [−]
ω	rotational speed [rpm]

Subscripts

$2P$	refrigerant
A, B, C, D	component ports
air	air
avg	average
$cond$	condensed water

$conv$	convective
$count$	counter-flow
$cross$	cross-flow
cc	cross-counter-flow
$disp$	displacement
dry	dry air
e	evaporation
EE	extract-exhaust side
eff	effective
f	frost
$film$	film
fs	frost surface
in	inlet
ise	isentropic
L	liquid
l	latent
MA	moist air
m	membrane
max	max
$meas$	measured
min	min
out	outlet
OS	outdoor-supply side
R	throat
s	sensible
seg	segments
sim	simulated
SL	saturated liquid
SV	saturated vapor
sat	saturation
sys	overall system
std	steady-state
V	vapor
vap,t	vapor transfer

w	water
wl	liquid water
x	moisture

Superscripts

ch	channel
V	volume
W	wall

Abbreviations

EAHP	Exhaust Air Heat Pump
ERV	Energy Recovery Ventilation
ETA	Extract Air
EXH	Exhaust Air
HVAC	Heating Ventilation and Air Conditioning
HP	Heat Pump
HRV	Heat Recovery Ventilation
MFRBV	Multifunctional Balanced Ventilation for residential
MPC	Model Predictive Control
MVHR	Mechanical Ventilation with Heat Recovery
ODA	Outdoor Air
OEA	Outdoor to Exhaust Air
PEXH	Post-Exhaust Air
PSUP	Post-Supply Air
SUP	Supply Air

Chapter 1

Introduction

1.1. Motivations

As global temperatures rise and urbanization intensifies, ensuring thermally comfortable and healthy indoor environments is emerging as a critical energy and environmental challenge. The combined effects of growing population density, improved living standards, and the increasing frequency of climate extremes are leading to a substantial increase in energy demand for heating, cooling, and ventilation in buildings. Without a shift toward more efficient and sustainable systems, such a demand is expected to add further strain on the energy infrastructure and significantly contribute to the increase of greenhouse gas (GHG) emissions [1, 2]. The building sector currently accounts for approximately 30-40% of final energy consumption [3] and a comparable share of carbon dioxide (CO_2) [4] emissions in developed countries, positioning it as a key area for decarbonization. Within this sector, space conditioning (heating and cooling) and domestic hot water production represent the dominant energy end uses, up to 60% in many residential buildings [5], underscoring the urgency of improving energy performance in these applications.

In the European context, this challenge is particularly pronounced: space heating continues to dominate energy use in northern and central countries, while cooling demand is rapidly growing in southern regions due to hotter and longer summers. To address these challenges, the European Union has adopted ambitious targets aligned with the Paris Agreement and established a robust regulatory framework to guide the building sector toward decarbonization. At the core of this framework lies the Energy Performance of Buildings Directive (EPBD) [6], originally introduced in 2010 and subsequently revised, most recently in 2024, which mandates the progressive improvement of building energy standards across the EU. A pivotal element of the EPBD is the requirement that all new

buildings, and those undergoing major renovation, meet the criteria for nearly Zero Energy Buildings (nZEBs) [7]. These are defined as buildings with very high energy performance, where the limited amount of required energy is covered, to a significant extent, by energy from renewable sources produced on-site or nearby.

To comply with the European Union's regulatory framework—specifically the Minimum Energy Performance Standards (MEPS) [8]—the retrofitting of the existing building stock toward Nearly Zero Energy Building (nZEB) standards requires a rigorous minimization of operational energy demand. A cornerstone of this strategy is the deep renovation of the building envelope, aimed at achieving superior thermal insulation and airtightness. However, this improvement introduces a critical trade-off: while increased airtightness drastically reduces transmission losses, it eliminates the natural infiltration traditionally relied upon for air exchange. Consequently, mechanical ventilation becomes mandatory to ensure acceptable Indoor Air Quality (IAQ) [9]. This physical reconfiguration fundamentally alters the building's energy balance; as transmission losses diminish, the energy required to condition outdoor air becomes the dominant component of the residual thermal load. In this context, maximizing and optimazing the interaction between the heating/cooling system and the mechanical ventilation system becomes the critical strategy for reducing these dominant ventilation energy losses.

To address this need for integration, advanced HVAC technologies are increasingly converging into multifunctional solutions. In particular, units that combine mechanical ventilation, heat recovery, and a heat pump within a single device offer a coherent approach to meet nZEB requirements. By simultaneously managing space conditioning and fresh air supply, these systems optimize the thermodynamic synergies between subsystems, ensuring that the rigorous energy demands of the building envelope are met with maximum efficiency.

These multifunctional units form a class of advanced HVAC technologies that align well with nZEB requirements. They contribute not only to space heating and cooling but also to the efficient treatment of outdoor air, which is essential both for maintaining proper indoor air quality and for reducing the ventilation-related energy penalty. Given this dual function, the overall performance of the system increasingly depends on the degree of integration between the heat pump and the ventilation module, since their coupling directly governs the unit's energy efficiency.

This technological evolution aligns with the International Energy Agency's (IEA) identification of HVAC efficiency as a primary driver for decarbonization [10]. In this framework, advaced HVAC systems serve as the central enabling technology, driving the electrification of thermal loads and facilitating the integration of on-site renewable sources, such as solar thermal and geothermal energy. Furthermore, the deployment of smart HVAC systems—integrated into Building Energy Management Systems (BEMS)—allows for the implementation of demand-response strategies, which are essential for balancing

grid flexibility requirements with occupant comfort [11].

Despite the benefits offered by integrated HVAC technologies efficient operation of these systems is still hampered by suboptimal control strategies and operational inefficiencies in the existing building stock; this and the continued reliance on high Global Warming Potential (GWP) refrigerants, can significantly reduce the environmental gains expected from electrification [12]. In this context, the rigorous optimization of HVAC operation becomes essential for achieving high indoor environmental quality while meeting the decarbonization targets set by current regulatory frameworks.

1.2. Background

1.2.1. Mechanical ventilation with heat recovery (MVHR)

Mechanical ventilation systems are essential for ensuring adequate indoor air quality and managing energy consumption in modern buildings. These systems are conventionally categorized into two principal typologies based on their installation and operational scope:

- **Centralized**: ventilation units that serve multiple rooms or entire buildings through a network of air ducts, typically installed in technical rooms, attics, or on the roofs. These systems can be configured as either **single-flow** or **dual-flow**. In the single-flow setup, only the extraction of stale, humid air from rooms like bathrooms and kitchens is mechanically driven, while fresh air is passively drawn in through wall or window vents. Although simpler and more cost-effective, this configuration does not include heat recovery and may lead to slight imbalances in indoor pressure distribution. It still represents a practical solution in retrofitting projects or in buildings with limited budgets. In contrast, modern centralized systems are predominantly dual-flow (balanced), meaning they actively and simultaneously manage both supply and exhaust air streams in equal volumes. This balanced operation not only maintains indoor pressure equilibrium but also allows for the integration of a recovery heat exchanger. Dual-flow centralized systems are widely used in non-residential buildings such as offices, hospitals, and schools, and are increasingly common in residential applications, especially in energy-efficient single-family homes and blocks of flats.

- **Decentralized**: ventilation units that are designed to ventilate individual rooms or small isolated zones without the need for centralized ductwork. These units are typically wall-mounted and compact, which makes them particularly suitable for renovation or retrofit projects where installing ducts would be impractical or invasive. These systems can be either **single-flow**, extracting stale air while relying on passive inlets for fresh air supply, or **dual-flow**, where both intake and exhaust are managed within the same compact device. Single-flow devices often

include alternating through-wall ventilators equipped with ceramic heat storage elements, which periodically reverse airflow to provide basic heat recovery. Dual-flow decentralized units, on the other hand, operate with continuous supply and exhaust flows through separate ducts and typically integrate compact counter-flow heat exchangers and electronically commutated fans. These systems are commonly used in settings such as hotel rooms, classrooms, or apartments where a centralized ventilation solution is not feasible due to space limitations or cost considerations.

To better illustrate the internal configuration and operating principles of a MVHR unit, Figure 1.1 depicts a typical centralized solution. The system is enclosed in a thermally

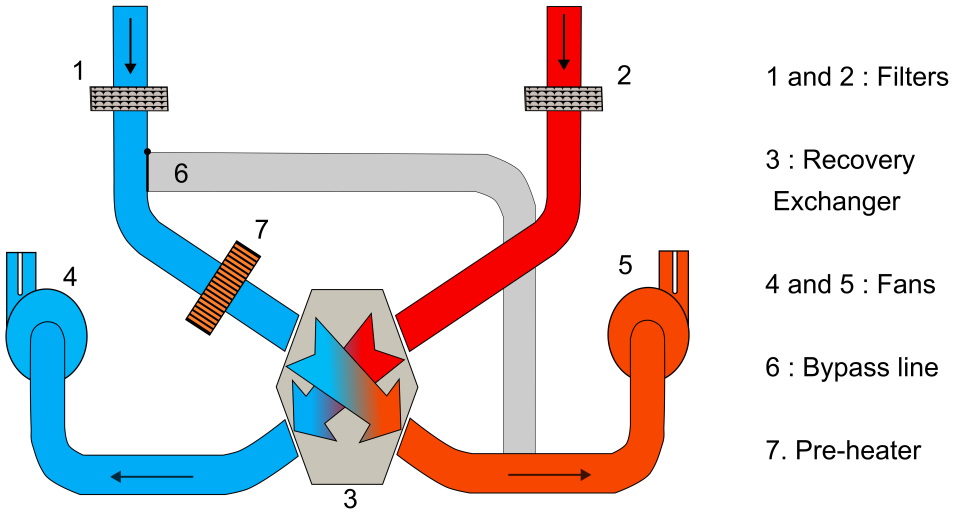

Figure 1.1: General structure of a centralized MVHR unit.

insulated metal casing and includes the following key components:

- **Filters** (1 and 2): both incoming and outgoing air streams pass through dedicated filters to remove particulates such as dust, pollen, and other airborne pollutants. This protects the health of occupants as well as the internal components of the system.

- **Recovery exchanger** (3): this component is at the core of the MVHR unit, and it is responsible for the transfer of energy from the outgoing exhaust air to the incoming fresh air. By recovering energy that would otherwise be lost, it improves the overall efficiency of Heating, Ventilation, and Air Conditioning (HVAC) systems. The recovery process depends on the adopted technology. Devices that transfer only sensible heat operate as Heat Recovery Ventilators (HRVs), while those capable of transferring both sensible heat and moisture operate as Energy Recovery Ventilators (ERVs). Beyond this functional distinction, recovery devices can also be classified

according to their construction, with two main categories commonly adopted in MVHR units: plate heat exchangers and rotary exchangers.

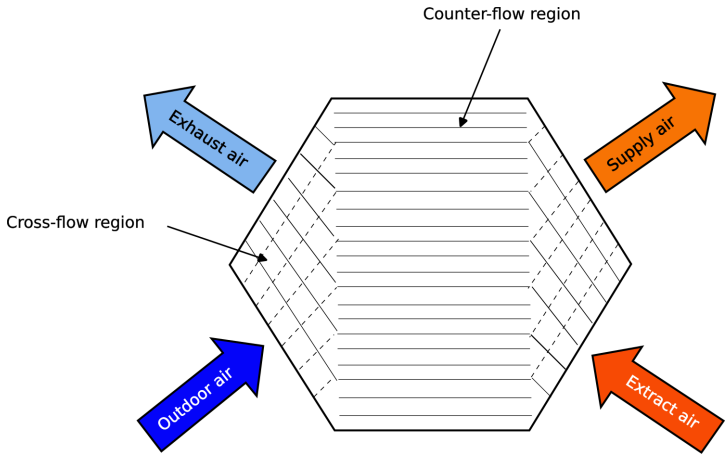

Figure 1.2: Schematic of a plate of a cross-counter-flow recovery exchanger.

Plate exchangers consist of alternating flat plates that form separate supply and exhaust channels, ensuring complete separation between the two airstreams. Their performance largely depends on the internal flow configuration. Compact models often adopt a cross-flow layout, whereas many high-efficiency designs use a cross-counter-flow configuration such as the one illustrated in Figure 1.2. In this configuration, the internal channel geometry is shaped so that a substantial portion of the flow path operates in counter-flow, preserving a strong temperature gradient and improving overall effectiveness.

The distinction between sensible and enthalpy plate exchangers is fundamentally rooted in the physicochemical properties and mechanical rigidity of the material used to manufacture the plates, which impose specific constraints on the design and directly influence the achievable core geometry of the counter-flow region. Sensible plate exchangers use vapor-impermeable solid plates that are sufficiently rigid to form a cellular core, as shown in Figure 1.3a. This cellular structure is applied specifically to sensible devices, since the thicker and stiffer plates can define narrow, stable channels that provide high surface density, good flow distribution, and high mechanical strength. Historically, these plates were often made of aluminum or coated steel. However, many modern sensible exchangers now employ very thin polymeric plates, typically below 200 μm. Indeed, despite the lower intrinsic thermal conductivity of polymers, the small thickness keeps the overall thermal resistance low. At the same time, polymers offer important practical advantages: they are easier to form into complex cellular geometries, they exhibit superior corrosion resistance in humid airflows, and their lower axial thermal conductivity helps to limit unwanted heat conduction along the plate, which preserves the temperature gradients that drive efficient counter-flow heat transfer.

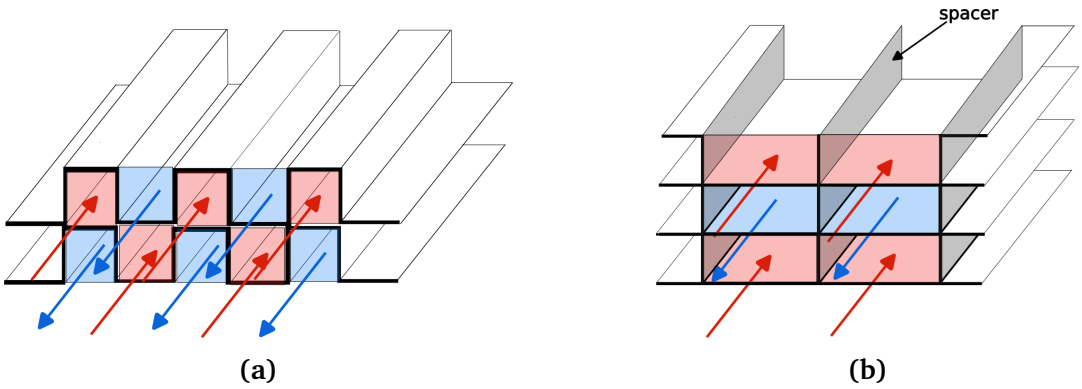

Figure 1.3: Typical structure of the counter-flow region for a sensible heat exchanger (a) and for an enthalpy heat exchanger (b).

Enthalpy plate exchangers, in contrast, employ water-vapor-permeable membranes to enable moisture transfer between the airstreams. These membranes are much thinner and more flexible than the solid plates used in sensible exchangers and therefore cannot be shaped into a self-supporting cellular core. For this reason, the channel spacing and mechanical stability in enthalpy devices are provided by spacer elements, such as plastic meshes or shaped polymer sheets, as illustrated in Figure 1.3b. This spacer-based architecture allows moisture exchange but restricts geometric compactness and limits the achievable surface density, which typically results in slightly lower sensible effectiveness compared to cellular sensible cores. Nevertheless, the ability to transfer moisture provides substantial benefits in terms of indoor humidity control and can significantly reduce the overall energy demand associated with ventilation, especially in well-insulated buildings and in climates where latent loads are relevant.

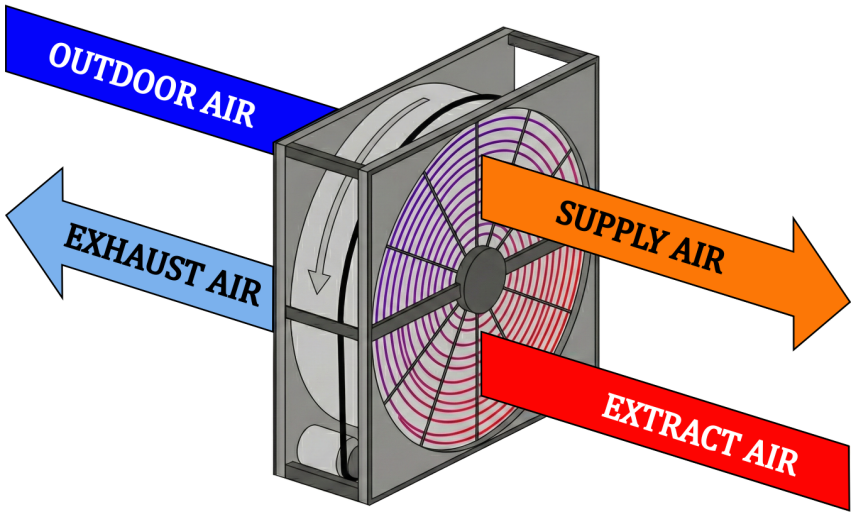

Figure 1.4: Rotary wheel.

Rotary exchangers represent the second major category and rely on a regenerative operating principle. They consist of a rotating wheel (Figure 1.4) made of a

porous matrix that is alternately exposed to the extract and outdoor airstreams. As each sector of the wheel passes through the warmer stream, the matrix absorbs heat (and moisture, in the case of enthalpy wheels), and then releases it into the colder stream during the subsequent half-rotation. In sensible rotary wheels, the matrix is typically made of aluminum or other metallic materials with high thermal mass and good thermal conductivity, which promotes rapid energy uptake and release. On the other hand, enthalpy wheels employ the same structure but incorporate hygroscopic coatings—commonly silica gel, lithium chloride, or polymeric sorbents—that enable the adsorption of water vapor in the more humid stream and its subsequent desorption into the drier one as the wheel rotates. Through this mechanism, enthalpy wheels generally achieve higher moisture-recovery effectiveness than membrane-based energy exchangers. Compared to plate exchangers, they also offer lower pressure drops and can handle larger airflow rates within more compact volumes, which makes them suitable for medium-to-large ventilation systems. However, their operation requires moving parts and motor drives, with associated maintenance needs, and they inherently allow for a small degree of carry-over between the airstreams, which may limit their applicability in scenarios where complete separation is required. In residential units with stringent hygiene constraints or where cross-contamination must be avoided, plate exchangers often remain preferable, whereas rotary wheels offer clear advantages in applications that prioritize airflow capacity, low pressure drop, and efficient moisture recovery.

- **Fans** (4 and 5): two electronically commutated (EC) fans drive the airflows through the unit. One fan (4) extracts stale indoor air and expels it outdoors, while the other (5) pulls in fresh outdoor air and delivers it indoors after pre-conditioning.

- **Bypass line** (6): during intermediate seasons or under mild climatic conditions, the ventilation unit can operate in bypass mode, allowing the outdoor air to circumvent the recovery exchanger. This mode is activated when the outdoor conditions are more favorable than the indoor ones, thereby enabling free-cooling or free-heating and enhancing comfort while avoiding unnecessary heat exchange.

- **Pre-heater** (7): an optional electric or hydronic pre-heating coil is often installed upstream of the recovery exchanger on the outdoor air intake. Its function is to prevent frost formation inside the recovery core during cold weather conditions and to ensure a minimum supply air temperature, safeguarding system efficiency and occupant comfort in winter climates.

Although mechanical ventilation systems do not operate through an active thermodynamic cycle, their performance can still be evaluated using a COP/EER metric:

$$\text{COP/EER}_{\text{MVHR}} = \frac{\dot{Q}_{\text{tot,rec}}}{PC_{\text{fans}}} \tag{1.1}$$

where $\dot{Q}_{\text{tot,rec}}$ is the total amount of energy transferred between exhaust and intake flows, and PC_{fans} is the electrical power consumed by the ventilation fans. For high-efficiency units operating under typical conditions, these ratios can range from 5 to 10 or even higher, indicating that the recovered amount of energy exceeds by far the electricity required to drive the fans.

In addition to the core components and operation principles outlined above, advanced centralized units incorporate features that further improve efficiency and control. These include pressure sensors to detect filter clogging, variable-speed EC fans for energy-efficient airflow regulation, and digital controllers for dynamic performance management. Many models also allow integration with building management systems via standard communication protocols such as Modbus [13].

1.2.2. Heat pump (HP)

Among the most thermodynamically efficient technologies for the delivery of space heating and cooling, vapor compression heat pumps stand out due to their ability to provide more thermal energy than the electrical work they consume. This is made possible by leveraging the principles of thermodynamics, particularly the second law, which allows heat to be transferred from a colder source to a warmer sink with the input of mechanical work. In contrast to conventional heating systems, such as electric resistive heaters or gas boilers, which convert energy into heat with efficiencies close to unity, heat pumps can achieve much higher performance by moving rather than generating heat. This process is realized through a reversed Rankine cycle, in which a refrigerant circulates through four main components: a compressor, a condenser, an expansion valve, and an evaporator.

The operating principles of a vapor compression heat pump are illustrated in Figure 1.5, which shows a simplified layout of the system along with the associated energy flows. In the evaporator, the refrigerant absorbs heat from an external source, such as ambient air, groundwater, or soil, and evaporates at low pressure. The resulting low-pressure vapor is then conveyed to the compressor, where mechanical work is applied to raise its pressure and enthalpy. The high-energy vapor subsequently enters the condenser, through which heat is released to the indoor environment. The condensed refrigerant then passes through the expansion valve, where its pressure and temperature drop sharply, completing the cycle.

An analysis of energy flows within the system shows that the total thermal energy delivered by the condenser ($\dot{Q}_{sink}$) consists of two distinct contributions: the heat absorbed from the external source at the evaporator ($\dot{Q}_{source}$) and the mechanical work ($\dot{W}$) performed by the compressor. In other words, energy conservation across the cycle can be

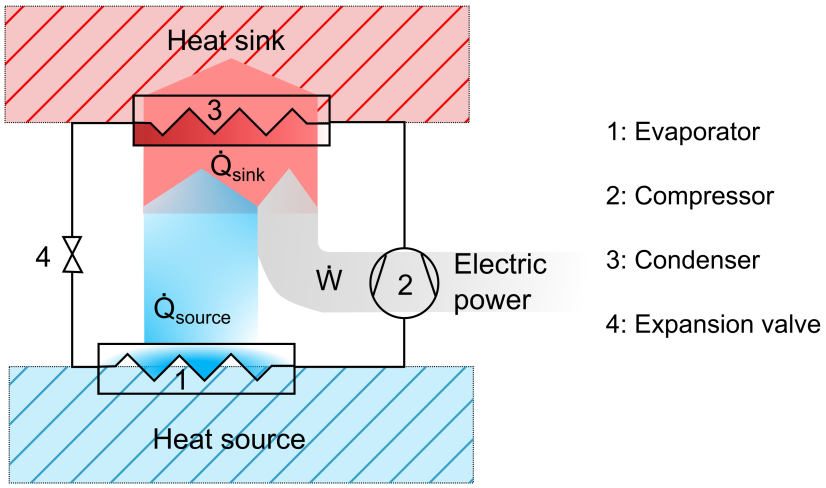

Figure 1.5: Energy flows in a simple vapor compression heat pump.

expressed as:

$$\dot{Q}_{sink} = \dot{Q}_{source} + \dot{W} \tag{1.2}$$

This highlights the fundamental operating principle of the heat pump: it does not create thermal energy but transfers it, using a relatively small amount of work to move a significantly larger quantity of heat.

From a thermodynamic standpoint, the performance of vapor compression systems is expressed through mode-specific instantaneous indices. In cooling operation, the Energy Efficiency Ratio (EER) quantifies how effectively the system removes heat from the environment relative to the electrical input (PC), and can be written as:

$$EER = \frac{\dot{Q}_{\text{source}}}{PC} \tag{1.3}$$

In heating operation, the corresponding metric is the Coefficient of Performance (COP), defined with respect to the useful heat delivered to the environment:

$$COP = \frac{\dot{Q}_{\text{sink}}}{PC} \tag{1.4}$$

In these definitions, PC denotes the total electrical power drawn from the grid and it is linked to the thermodynamic work rate performed by the compressor, through the overall electromechanical efficiency (η):

$$PC = \frac{\dot{W}}{\eta} \tag{1.5}$$

Here, $\eta = \eta_{\text{motor}}\eta_{\text{drive}}\eta_{\text{mech}}$, where η_{motor} denotes the electric-motor efficiency, η_{drive} accounts for losses in the inverter and drive electronics, and η_{mech} represents the mechanical losses associated with transmission and internal friction within the compressor.

Under typical operating conditions, for standard heat pump unit, both EER and COP take values between 2 and 5, depending on the temperature lift between the source and the sink.

The theoretical upper limit of performance is set by the Carnot cycle, which assumes ideal reversible processes between two isothermal reservoirs at absolute temperatures T_{sink} and T_{source}. In heating mode, the Carnot COP is given by:

$$COP_{Carnot} = \frac{T_{sink}}{T_{sink} - T_{source}} \tag{1.6}$$

while in cooling mode the Carnot EER is expressed as:

$$EER_{Carnot} = \frac{T_{source}}{T_{sink} - T_{source}} \tag{1.7}$$

These expressions reveal a key thermodynamic insight: the smaller the temperature lift ($T_{sink} - T_{source}$), the higher the potential maximum performance, explaining why heat pumps perform particularly well with low-temperature heating systems or stable heat sources such as ground or water reservoirs. However, in real systems, the source and sink temperatures vary along the heat exchangers (for example, the air stream feeding the condenser gradually warms up as it flows through the heat exchanger), and the finite temperature differences between the fluids and the heat-transfer surfaces (i.e., the thermal driving force required to sustain heat transfer) cause the refrigerant to evaporate and condense at internal temperatures T_{evap} and T_{cond}. For this reason, it is common to define internal Carnot limits:

$$COP_{Carnot,int} = \frac{T_{cond}}{T_{cond} - T_{evap}}, \qquad EER_{Carnot,int} = \frac{T_{evap}}{T_{cond} - T_{evap}} \tag{1.8}$$

which represent the maximum achievable performance under given internal cycle conditions in heating and cooling mode, respectively. Comparing the actual performance with these internal Carnot limits yields the second-law efficiency, which quantifies the impact of irreversibilities such as pressure drops, throttling losses, and non-ideal compression.

An additional layer of complexity arises when considering how heat pumps operate under real-world conditions. Instantaneous performance indicators such as COP and EER, although useful for characterizing the thermodynamic behavior at a specific operating point, provide only a partial view of system efficiency. Seasonal variations in outdoor temperature, fluctuating load demands, and control strategies strongly affect system performance. For this reason, seasonal performance indicators have been introduced: the

Seasonal Coefficient of Performance (SCOP) for heating and the Seasonal Energy Efficiency Ratio (SEER) for cooling. Both are defined as the ratio between the total useful thermal energy delivered (heating or cooling) and the total electrical energy consumed over a representative period, typically based on standardized climate profiles (e.g., EN 14825:2022 [14]). These seasonal metrics account for part-load operation, defrost cycles, auxiliary consumption, and other dynamic effects. As a result, SCOP and SEER are generally lower than the corresponding instantaneous indices, since they reflect the influence of average environmental and operating conditions over the entire season.

Even in their basic single-stage configuration, vapor compression heat pumps and air conditioners offer substantial energy savings and emission reductions compared to conventional heating technologies, particularly when operated with low-carbon electricity. Advanced cycle configurations, such as two-stage compression, vapor injection, or intermediate heat exchangers, can further enhance performance under extreme temperature conditions, for which maintaining high COP and EER values is more challenging.

1.2.3. Multifunctional residential balanced ventilation (MFRBV)

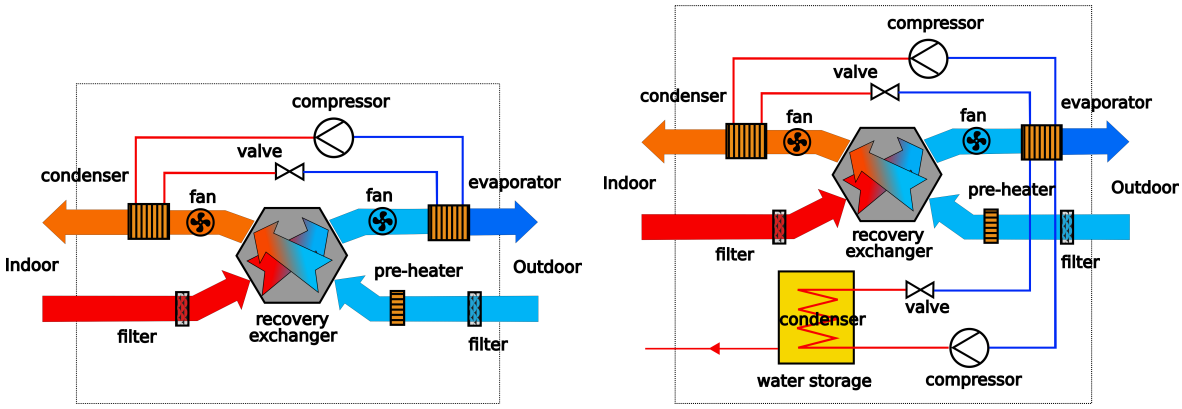

(a) Basic exhaust air heat pump **(b)** Compact unit

Figure 1.6: Example of two MFRBV configurations.

Recent technological developments have enabled heat pump technology to be integrated into mechanical ventilation systems, leading to the development of multifunctional balanced ventilation units for both residential (MFRBV) and non-residential applications (MFBV). These systems are also often referred to as exhaust-air heat pumps (EAHP) or, more broadly, as thermodynamic heat-recovery units. In all cases, they combine mechanical ventilation and heat-pump operation, which are traditionally implemented as separate subsystems, within a single compact and energy-efficient device.

Figure 1.6a schematically represents the typical configuration of a multifunctional balanced ventilation unit. At the core of these devices lies a conventional mechanical ventilation unit, often equipped with a cross-counter-flow or cross-flow heat exchanger that passively transfers heat between supply and exhaust streams. What distinguishes MFRBV

from MVHR devices is the integration of a refrigeration loop immediately downstream of the passive heat-recovery exchanger, where the exhaust air leaving the ventilation unit is available at conditions that differ markedly from the outdoor environment. In winter, this exhaust stream is still warmer and more humid than the colder and drier outdoor intake air, making it a more favorable source for the evaporator. In summer, it is generally colder and less humid than the hot, moisture-laden ambient air, providing a more favorable sink for the condenser. In both operating modes, utilizing this intermediate-temperature exhaust stream minimizes the temperature lift required for the refrigeration cycle, particularly when compared to a conventional air-to-air heat pump that operates solely with outdoor ambient air. This reduction in temperature lift directly enhances heat-pump efficiency. Moreover, the same fans used to provide mechanical ventilation also ensure the necessary airflow across the heat pump's heat exchangers (condenser and evaporator). This eliminates the need for separate, dedicated fans for the heat pump and reduces auxiliary electricity consumption. The combined effect of a more favorable heat source/sink and shared air-moving components leads to a measurable increase in overall system efficiency.

In heating mode, the performance of a MFRBV is typically expressed in terms of the overall *Coefficient of Performance* (COP_{sys}):

$$\mathrm{COP}_{sys} = \frac{\dot{Q}_{\mathrm{useful}}}{PC_{\mathrm{comp}} + PC_{\mathrm{aux}}} \tag{1.9}$$

where $\dot{Q}_{\mathrm{useful}}$ is the useful heating capacity supplied to the building (sum of the MVHR and HP heating capacities), PC_{comp} is the electrical power consumed by the compressor, and PC_{aux} accounts for auxiliary electricity use, including ventilation fans and on-board electronics. In cooling mode, the corresponding efficiency indicator is the overall *Energy Efficiency Ratio* (EER_{sys}), defined analogously as the ratio between the useful cooling capacity and the total electrical input.

Thanks to the enhanced configuration of these systems, the seasonal performance indicators are generally superior to those of conventional systems: SCOP values for heating often range from 3.0 to 4.5, compared to 2.0 to 2.5 typically observed for conventional ambient-air heat pumps under cold-climate conditions. Similarly, in cooling mode, SEER values are generally higher than those of standard air-source air conditioners, reflecting the advantage of exploiting the exhaust airstream as a more favorable heat sink.

In many cases, these integrated systems include a secondary refrigeration loop and a small water storage tank, which can be used for both domestic hot water production and space heating support. When all these functions (mechanical ventilation, air treatment, space conditioning, and water-based heat delivery) are combined within a single enclosure, the resulting configuration is commonly referred to as a compact unit (Figure 1.6b). These units are particularly well suited for low-energy or passive buildings, where

their high efficiency and space-saving design offer clear advantages.

Beyond the energy-related benefits already discussed, MFRBV also provide several additional advantages:

i. **Equipment consolidation and space savings**
Traditional MVHR and heat pump systems occupy separate spatial envelopes, on the other side MFRBV systems consolidate both functions into one compact module. This reduces installation complexity, shortens ductwork and the associated pressure losses, and preserves valuable floor or rooftop space, which is an important feature in high-density residential settings and retrofit applications.

ii. **Integrated control and load matching**
The combined unit can modulate ventilation rate in response to IAQ sensors (CO_2, VOCs, humidity) while simultaneously adjusting compressor speed or expansion-valve opening to meet variable thermal loads. Such coordinated control reduces cycling losses and enables demand-driven operation, thereby enhancing system efficiency and occupant comfort.

iii. **Simplified commissioning and maintenance**
Using a single integrated system allows for the coordinated setup of both the ventilation unit and the heat pump unit during commissioning. At the same time, maintenance tasks such as filter replacement, heat-exchanger cleaning, and refrigerant-level checks are centralized. This approach helps lower lifecycle operation and maintenance costs while reducing the risk of misconfiguration.

iv. **Flexible integration with renewable sources**
The MFRBV architecture offers inherent flexibility for integration with various renewable energy technologies, including photovoltaic (PV) arrays, battery storage systems (BESS), and district heating/cooling networks. For instance, during periods of high solar irradiance, on-site PV generation can directly supply the compressor drive motor, with any surplus electrical energy being stored thermally within hot water storage tanks or buffers. Furthermore, certain MFRBV designs facilitate cascade operational modes with external resources, such as ground-source heat exchanger loops or centralized thermal storage repositories, which effectively decouples energy supply from building demand across varying temporal scales.

Despite the many advantages of MFRBV units, their adoption presents several challenges that must be carefully addressed. A first limitation concerns the selection of low-GWP refrigerants, which is increasingly restricted by stringent safety standards and the limited market availability of components designed to operate with these fluids. Acoustic

performance is another critical aspect in residential applications, since both fans and the integrated heat pump must operate quietly to ensure acceptable noise levels. Moreover, in cold climates, maintaining reliable operation requires robust frosting-prevention and defrost-management strategies for both the heat pump and the recovery exchanger, since frost accumulation can rapidly degrade airflow, heat-transfer effectiveness, and overall system stability.

Furthermore, integrated systems that combine both space heating/cooling and ventilation often face inherent challenges in decoupling airflow from thermal requirements. The nominal ventilation flow rates needed for maintaining adequate Indoor Air Quality (IAQ) are frequently substantially lower than the volumetric flow rate required to enable the heat pump component to operate at its optimum COP/EER. This operational discrepancy creates a conflict: prioritizing thermal load regulation may lead to reduced air exchange rates when temperature set-points are met, thus compromising IAQ. Conversely, constraining the airflow to the low levels typical of ventilation requirements prevents the heat pump from operating at its design conditions, impairing both capacity and thermodynamic efficiency. Consequently, the deployment of sophisticated control algorithms is mandatory to dynamically manage and reconcile these divergent demands. Such control strategies must necessarily rely on robust IAQ sensing technologies to ensure the provision of sufficient fresh air without imposing an excessive volumetric flow rate, thus compromising thermal efficiency. Maintaining this dynamic balance is critical for achieving sustainable energy performance while simultaneously guaranteeing stable indoor thermal comfort and air quality.

1.3. Objective and scope

In modern residential buildings with highly airtight envelopes, maintaining indoor air quality requires a constant and controlled exchange of indoor and outdoor air [15, 16]. For energy efficiency reasons, this ventilationis typically achieved through a Mechanical Ventilation Heat Recovery (MVHR) system [17] capable of recovering a significant portion of sensible or total (sensible and latent) energy from the exhaust stream. While PassivHaus certified buildings can often meet comfort requirements with minimal reliance on active climatization (e.g., thermal load $\leq$10 W m^{-2}), most new or renovated dwellings still require a modest but non-negligible active thermal conditioning to maintain indoor thermo-hygrometric comfort.

Air-to-air heat pumps are frequently selected to meet this residual demand because they are cost-effective, non-invasive, and straightforward to install [18, 19]. These characteristics make them suitable both for new constructions compliant with current energy regulations and for retrofit applications, particularly in historic buildings or heritage urban areas where conservation requirements often prevent the installation of more efficient but more intrusive systems such as air-to-water or water-to-water heat pumps.

When the residual thermal load is low (e.g., typically ranging from 20 to 40 W m^{-2}) and an MVHR system is already present, integrating an air-to-air heat pump into the ventilation circuit in the configuration known as an Exhaust Air Heat Pump (EAHP) represents a technically and economically appropriate solution.

In order to keep manufacturing and installation costs low while ensuring operational reliability, the conventional EAHP layout described in the previous section is generally preferred. However, the fixed and limited airflow rate imposed by the MVHR often forces the heat pump to operate under suboptimal conditions, leading to noticeable performance degradation [20]. This sensitivity to airflow and boundary conditions is further amplified by the adopted control strategy, making the overall performance highly dependent on regulation. Despite their growing relevance in high-efficiency residential buildings, comprehensive experimental characterization of these systems is rare, as testing in dedicated climatic chambers is usually costly for manufacturers. Consequently, detailed performance data under realistic and variable operating conditions (such as partial loads) are scarce, limiting the ability to refine the design and optimize control strategies. In this context, high-fidelity simulation models become essential tools for analyzing system behavior across a wide range of operating scenarios that would be costly or impractical to replicate experimentally. Coupled with advanced control approaches such as Model Predictive Control (MPC), simulation enables the systematic optimization of operating logic to improve seasonal efficiency, enhance indoor comfort, and increase the reliability of air-to-air EAHP systems.

To address these challenges, a modeling framework capable of accurately reproducing the thermodynamic behavior of the EAHP, while remaining applicable to a broad range of operating conditions, is required. Therefore, the objective of this research work is to develop a physics-based digital twin of a commercially available EAHP, validated through an extensive experimental campaign. The physics-based approach has been chosen to reproduce the thermodynamic and heat transfer phenomena governing the system' behavior, thus endowing the model with predictive capabilities going beyond the specific conditions used for calibration. This reduces the amount of experimental data required for calibration and allows a more focused and cost-effective validation campaign. The validated model is then employed to investigate the operational behavior of these type of systems and to optimize their control logic. This study aims to address the following research questions, which reflect the key gaps identified in the literature regarding the understanding of how these systems operate, under both heating and cooling conditions.

- Does the use of an auxiliary outdoor-to-exhaust air (OEA) fan, which increases the airflow rate across the outdoor coil, improve system performance?
- Does the system perform more effectively when coupled with an enthalpy (ERV) or a heat (HRV) recovery exchanger?

- Under conditions without free-cooling or free-heating, does partial or full bypass of the recovery exchanger enhance overall system performance, and what are the consequences for indoor thermo-hygrometric comfort?

1.4. Problem statement

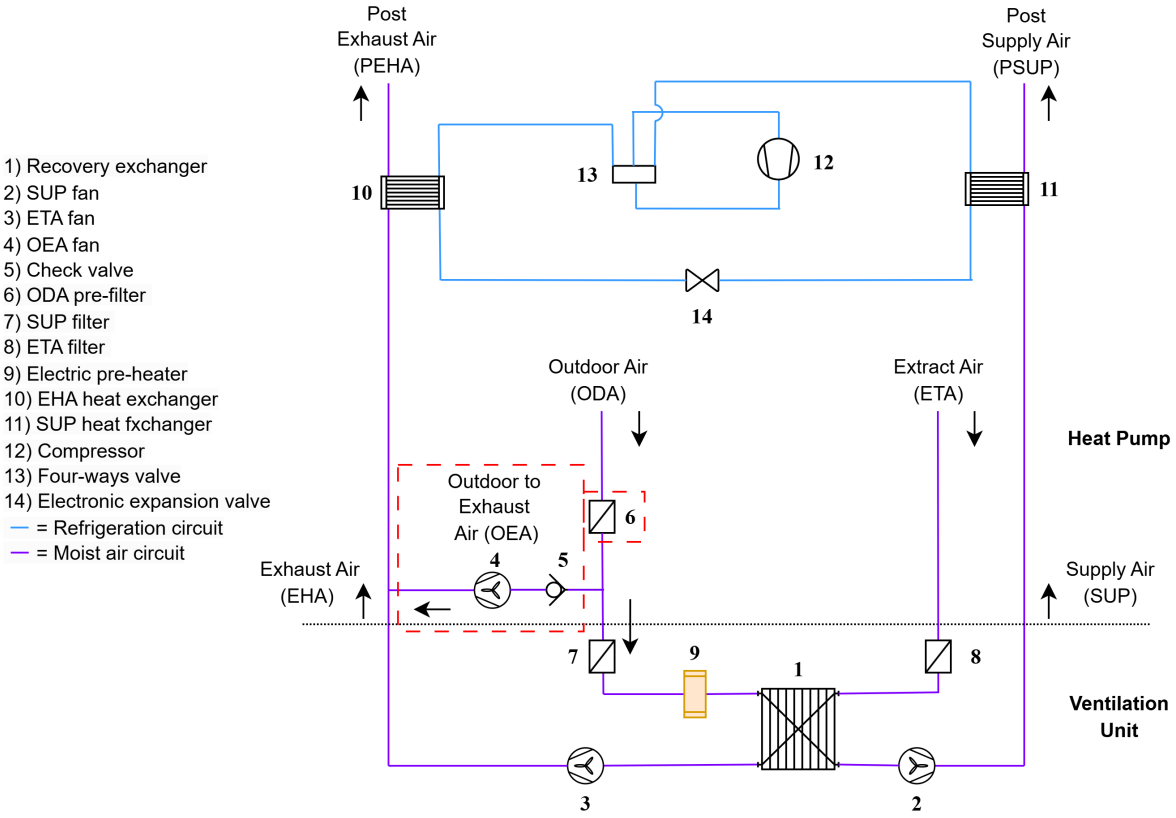

Figure 1.7: Full schematic of the HVAC unit investigated.

The two configurations of the air-to-air multifunctional ventilation unit investigated in this work are illustrated in Fig. 1.7. Both share the same base layout, consisting of a mechanical recovery ventilation unit coupled in series with a reversible air-to-air heat pump.

In its basic (standard) configuration, the unit operates with balanced mass flow rates on both the indoor and outdoor sides. It includes a supply air (SUP) and extract air (ETA) stream, each handled by dedicated fans (components 2 and 3), and an energy or heat recovery exchanger (component 1) that enables sensible or enthalpic (sensible + latent) heat transfer between the extract and outdoor air streams, depending on the specific configuration. A heat pump circuit is arranged downstream of the ventilation unit, including a compressor (component 12), a four-way reversing valve (component 13), an electronic expansion valve (component 14), and two finned-tube heat exchangers (components 10 and 11), which serve as the outdoor and indoor coils of the refrigeration cycle. An accumulator (not shown in the scheme) is included upstream of the compressor, on the

suction line, to prevent liquid refrigerant from entering the compressor and potentially damaging it. During winter operation, defrosting of the outdoor coil is carried out by reversing the refrigeration cycle through the four-way valve.

The heat pump is equipped with a dedicated control system designed to ensure both efficiency and safe operation. Three temperature sensors, factory-installed on the refrigeration circuit, are used for this purpose: one on each heat exchanger to measure the condensation and evaporation temperatures, and one at the compressor discharge to monitor the discharge temperature. These measurements are used to implement a low-level protection logic that prevents the compressor from operating outside its envelope curve. In particular, both the condensation and discharge temperatures must remain below specific thresholds derived from the compressor manufacturer's specifications to prevent oil degradation and mechanical stress. Conversely, in cooling mode, the evaporation temperature must not drop excessively to avoid frosting of the indoor coil. In addition to this, a high-level protection logic dynamically limits the maximum compressor frequency as a function of the air temperature conditions and ventilation flow rate. This additional layer of protection is specifically intended to prevent the system from frequently triggering the low-level protection logic, thereby ensuring more stable and reliable operation. The same temperature measurements are also used to regulate the electronic expansion valve, which indirectly controls refrigerant superheat and ensures proper refrigerant distribution within the evaporator.

The airflow paths within the system are as follows. On the outdoor side, the outdoor air (ODA) first passes through a coarse filter (component 6). Depending on the system configuration, a portion of this air may be redirected through the recirculation loop. The remaining air (i.e., not recirculated) continues through a finer filter (component 7) and enters first in the electric pre-heater (component 9) and then in the recovery heat exchanger (component 1), where it exchanges heat and, in case of enthalpy recovery, also moisture with the extract air stream. The pre-conditioned air is then further treated by the SUP heat exchanger (component 11), which functions as the indoor coil of the heat pump, before being delivered to the indoor environment by the supply fan (component 2). On the return side, the extract air (ETA) is drawn in by the extract fan (component 3), filtered (component 10), and directed through the recovery heat exchanger (component 1). The exhaust air stream from the ventilation unit then passes through the EHA heat exchanger (component 10), which functions as the outdoor coil of the heat pump, before being discharged outdoors.

In its alternative configuration, the unit incorporates an outdoor-air recirculation loop (OEA), highlighted in red in Figure 1.7. In this arrangement, a dedicated fan (component 4) draws an auxiliary stream of outdoor air and mixes it with the exhaust air discharged by the ventilation unit. The resulting mixture is then conveyed to the outdoor-side heat exchanger (component 10). By injecting outdoor air into the exhaust stream, the OEA

fan lowers the evaporator inlet temperature in winter and raises the condenser inlet temperature in summer. As a result, this configuraion only improves performance for what concerns the ventilation flow rate. In this configuration, a check valve (component 5) is installed in the recirculation line to prevent backflow. To limit the noise impact of the system, the OEA fan speed is subject to an upper limit, which constrains the maximum airflow rate through the recirculation loop.

The eletric pre-heater (component 9) is activated when the outdoor air temperature drops below a predefined threshold of -5°C for the enthalpy recovery configuration and 0°C for the sensible recovery configuration, in order to prevent frost formation within the recovery core.

1.5. Thesis outline

This dissertation is organised into seven chapters, each addressing a specific element of the research framework and collectively guiding the reader from the conceptual motivation to the development, validation, and application of the proposed digital twin.

- In **Chapter 1** the motivations underlying the study, the scientific and technological background, and the scope of the work are introduced.
- In **Chapter 2** the state of the art for advanced HVAC systems is reviewed, with a particular focus on coupled ventilation-heat pump technologies. Special attention is devoted to heat exchangers, as their performance critically shapes both the thermodynamic efficiency and the overall behavior of EAHPs. The chapter summarizes the most relevant experimental and modelling approaches adopted for these components and outlines the key findings from previous investigations.
- In **Chapter 3** the development of the digital twin is described. The mathematical framework is introduced first, followed by a detailed discussion of the component-level models.
- In **Chapter 4** the experimental campaign conducted to support validation activities is presented. The test rig, instrumentation, and measurement procedures are detailed, as well as the operating conditions analyzed during the summer and winter campaigns.
- In **Chapter 5** the experimental results and the model validation are reported. The performance of the digital twin is assessed for both cooling and heating modes, comparing measured and simulated quantities at system-level. The accuracy, limitations, and calibration aspects of the model are also discussed.
- In **Chapter 6** the predictive capability of the digital twin is exploited to analyze several design and control alternatives, including the use of enthalpy versus sensible

recovery ventilation, the integration of auxiliary fans, and the application of different bypass strategies of the recovery exchanger. Results of the analysis highlight the potential benefits and trade-offs associated with each configuration.

- In **Chapter 7** the conclusions of the research are presented. The key findings and their implications are summarized and discussed. Directions for future developments in modelling, control, and design optimization of multifunctional ventilation-heat pump systems are also outlined.

Overall, the thesis aims at providing a comprehensive and experimentally grounded contribution to the modelling and optimization of coupled ventilation–heat pump technologies, offering insights that may support the design of next-generation high-efficiency residential HVAC solutions.

CHAPTER 2

State of the art

In this chapter, a comprehensive survey of the scientific literature on advaced HVAC systems is proposed, with a focus that progressively moves from general system concepts to detailed aspects of modelling and experimental evaluation, encompassing both physical system optimization and advanced control strategies, to identify key research challenges addressed in the following chapters. In the first part, the main characteristics and recent evolution of HVAC systems are outlined, in the context of building decarbonization, focusing on hybrid configurations that combine ventilation and heat pump functionalities to enhance thermodynamic integration. Particular attention is given to novel system layouts and to the growing role of advanced control strategies, such as model predictive control (MPC), which enable adaptive and energy-efficient operation in response to dynamic environmental and occupancy conditions. In the second part, the focus shifts toward component, innovative design solutions and modelling approaches. Special care is devoted to heat exchangers, due to their critical role in system-level behavior. Finally, standardized testing procedures currently used to characterize multifunctional ventilation units are critically examineted.

2.1. State of art in the advanced HVAC systems

While the need to decarbonize the building sector has been widely discussed in the previous chapter, it is appropriate to question how this transition can be effectively achieved. In this regard, recent research has converged on two complementary innovation pathways: the reconfiguration and optimization of HVAC system architectures to exploit novel thermodynamic interactions, and the development of intelligent control strategies grounded in predictive modelling (MPC).

2.1.1. Layout optimization

The first pathway is addressed through a review of recent studies investigating alternative HVAC system layouts, with particular emphasis on configurations developed for heating- and cooling-dominated operation.

Heating-focused innovative configurations. Several studies have explored enhanced EAHP and hybrid configurations capable of improving winter performance, mitigating frosting, or increasing the available heating output. Siegele et al. [21] developed a speed-controlled EAHP with a double air recirculation loop and multiple heat exchangers, demonstrating COP values between 2.5 and over 4.5 across 446 laboratory-tested points and showing how passive recovery and optimal condenser sizing can further enhance performance. Xu et al. [22] proposed a composite two-stage ventilation heat recovery system that integrates a split heat pipe with a heat pump circuit. This hybrid configuration was benchmarked against parallel-loop heat pump ventilation units—which utilize dual independent cycles to approximate a Lorenz cycle—demonstrating that the passive preconditioning stage allows for winter COPs up to 7.17. Specifically, under sub-zero conditions, the composite system exhibited temperature efficiency and heating capacity up to 66.6% and 67.2% higher, respectively, than the reference parallel-loop architectures. Jia et al. [23] developed a novel parallel-loop EAHP driven by a dual-cylinder compressor and showed that adjusting the fresh-air to return-air ratio can strongly enhance winter performance, with heating capacity and COP increasing by up to 77% and 64%, respectively, under optimized recirculation conditions. Furthermore, Liang et al. [24] tackled one of the primary limitations of air-source systems in cold and humid climates by proposing a multi-evaporator layout that enables alternating coil defrosting while maintaining heating delivery, reducing heating-capacity decay during defrosting to about 20% and potentially below 10% after further optimization.

Cooling-focused innovative configurations. Other works have focused on configurations aimed at improving cooling efficiency or enabling combined sensible–latent control. Cao et al. [25] proposed an EAHP system featuring a decoupled subcooler and condenser, achieving an EER of 3.65 and a dehumidification rate of 78.2 kg/day. Liang et al. [26] investigated a direct-expansion dehumidification system coupled with a membrane-based total heat exchanger, showing that simultaneous heat and moisture recovery can significantly reduce energy use while ensuring comfort even under hot and humid climates. Li et al. [20] proposed an EAHP integrating an indirect evaporative cooler with an evaporative condenser, reporting increases in cooling capacity and EER of 53% and 135% relative to conventional systems. These works highlight the potential of advanced evaporative, hybrid, and coupled-loop approaches for boosting EER and improving latent-load handling in compact HVAC systems.

Overall, these contributions reveal a clear trend: performance gains are not only achievable by upgrading individual components, but also by rethinking the spatial, functional, and thermal coupling of the entire system layout to address the specific challenges of both heating- and cooling-dominated operation.

2.1.2. Controls optimization

Parallel to physical optimization, the second strategic pathway focuses on the development of advanced control algorithms capable of dynamically adjusting system operation based on internal and external conditions. Among them, Model Predictive Control (MPC) is particularly promising, as it uses a dynamic model of the system to forecast its future behavior, continuously optimizing control inputs while accounting for operational constraints. Guo et al. [27] implemented a two-stage event-triggered MPC scheme in an air source HP based hybrid HVAC retrofit, combining black-box modeling of the heat pump with a physics-based building model, and achieved 8.6% energy savings and 9.06% cost reduction. Tang et al. [28] extended this approach by incorporating deep learning (multilayer perceptrons and graph convolutional networks) into a physics-aware MPC structure, successfully reducing electrical consumption by 17.5% and lowering peak loads in commercial buildings. Further simulation and experimental validation reinforce MPC's practical feasibility and robustness under real-world conditions. Li et al. [29], through work on Building 101 at the Philadelphia Navy Yard, demonstrated that MPC employing reduced-order models and Kalman filtering could maintain thermal comfort while significantly reducing electricity demand associated with HVAC compressors and fans. Similarly, Si et al. [30] proposed a simplified MPC approach that uses mean radiant temperature as the feedback variable, derived from a reduced-order thermal model built in a Modelica environment. Their experimental results showed that this control variable could effectively track load variations, maintaining indoor comfort while improving energy efficiency and implementation simplicity.

Evidence from simpler but well-targeted controllers also underscores the value of tailored control design: Dermentzis et al. [31] showed that façade-integrated micro-heat pumps (μHPs) operated with PI control can achieve efficiency gains of about 15% compared to conventional on/off operation, while Anderson et al. [32] verified through hardware-in-the-loop testing that adaptive MIMO control can consistently outperform PID logic when managing the nonlinear behavior typical of HVAC systems. A similar conclusion applies to hybrid heat-pump configurations: Dongellini et al. [33] demonstrated that even in these systems, where a heat pump operates alongside an auxiliary boiler, the control rules themselves—particularly the choice of the bivalence-point temperature and the activation sequence between the two generators—play a decisive role in seasonal performance. Their results indicated that preventing premature switching to the backup heater and extending monovalent heat-pump operation can reduce primary energy con-

sumption by up to 22% in standard residential conditions. These findings highlight that, regardless of the algorithm's complexity, the precise optimization of the control strategy constitutes a fundamental prerequisite for maximizing overall system performance.

2.1.3. Model-based optimization

Despite the practical advantages of advanced control strategies such as MPC, their accuracy and robustness critically depends on the underlying models. Black-box and grey-box approaches, including Gaussian Process Regression (GPR) and machine-learning methods trained on performance maps or field data, offer computational simplicity and ease of implementation but remain fundamentally empirical. Their predictions rely solely on historical data, limiting interpretability and generalization, particularly under conditions not covered by the training data. As highlighted by Siegele et al. [21], empirical models often fail to capture key nonlinearities and transient interactions, which can lead to suboptimal or poorly justified control actions in real-world applications. In contrast, physics-based models offer superior reliability, particularly in capturing complex thermodynamic phenomena and interactions among system components. Their interpretability also supports advanced optimization concepts, specifically those involving exergy-based analyses. Indeed, studies by Sakulpipatsin et al. [34] and Sun et al. [35] have demonstrated that exergy evaluations can reveal inefficiencies not evident from energy-only assessments, especially in systems heavily dependent on electricity for functions like hot water production or heat recovery.

In addition to their relevance for control design, high-fidelity physical models provide a solid foundation for digital-twin implementations: virtual replicas that reproduce the real-time behavior of a system for monitoring, diagnostics, and predictive control. Although these applications ideally rely on physically informed models, recent studies have also explored hybrid and fully data-driven alternatives. Ispir et al. [36], for example, developed a digital twin of a 1 MW_{th} industrial heat pump using Gaussian Process Regression (GPR), a purely data-driven approach. Despite its empirical nature, the model achieved prediction errors below 7% and enabled more than 3000 MWh per year of energy savings through optimized operation. Similarly, Shirani et al. [37] proposed a hybrid framework combining a data-driven black-box model with a physics-based formulation to describe the defrost behavior of an EAHP. Their results showed that higher exhaust-air humidity can raise COP by up to 15% for a 10% increase in moisture content, and that an optimized backup-heater control strategy can reduce the electrical consumption of the heating system by up to 43%. These examples demonstrate that empirical and hybrid models, when carefully trained and validated, can successfully integrate real-time data with predictive capabilities. However, approaches that are not grounded in physical principles present inherent interpretability limits. Because they do not explicitly describe the underlying thermodynamic and transport mechanisms, they cannot reliably capture

causal relationships between variables or explain why the system behaves in a certain way. This lack of physical insight increases the risk of drawing incorrect or weakly justified conclusions, particularly when models are applied outside the range of conditions included in the training dataset or when the system exhibits behaviors not previously observed. For these reasons, the use of non-physical or predominantly data-driven models requires caution. While they can serve as valuable tools for monitoring and short-term prediction, their application to design, diagnostics, or performance assessment should be supported, and ideally complemented, by physics-based models that provide mechanistic understanding and ensure reliability beyond controlled experimental conditions.

In conclusion, the evolution of HVAC systems requires integrating novel thermodynamic layouts with high-fidelity, physics-based modeling. While data-driven methods offer operational simplicity, the complexity of hybrid architectures demands control strategies grounded in physical principles to ensure robustness and interpretability. Consequently, coupling layout optimization with model-based predictive frameworks constitutes the essential pathway for achieving sustained energy efficiency and effective decarbonization.

2.2. Experimentation and modelling of heat exchangers in MFRBV systems

This section provides an overview of the scientific literature on the main types of heat exchangers used in air-to-air MFRBV systems, with particular emphasis on sensible and enthalpy recovery exchangers and fin-and-tube coils, as they significantly affect the thermal behavior, energy consumption, and dynamic response of the overall system. In addition to a general discussion on the recent technological developments and their integration within these systems, particular emphasis is placed on the modelling strategies employed to represent these components, highlighting key research trends, challenges, and performance considerations.

2.2.1. Recovery exchanger

Within the wide range of technologies for air-to-air energy recovery, plate heat exchangers represent the most common solution in compact ventilation units. These can be designed either with vapor-tight plates, enabling only sensible heat transfer, or with semipermeable membranes, which also allow for latent heat (moisture) transfer and are therefore referred to as membrane-based enthalpy exchangers. The latter have gained particular relevance due to their ability to improve seasonal efficiency while contributing to indoor humidity control. In both cases, the compact geometry, absence of moving parts, and complete separation between supply and exhaust air streams make plate exchangers particularly suitable for multifunctional balanced ventilation systems. Rotary wheels still represent a valid alternative in larger installations thanks to their high effectiveness, but issues related to particle carry-over and increased maintenance limit their

application in residential compact units. For these reasons, research and development efforts in recent years have increasingly dealt with on plate-type recovery exchangers, with a special focus on material-level innovations and on the optimization of membrane-based enthalpy designs through simulation.

Material science and membrane development through experimentation. Recent research has increasingly focused on enhancing the performance of enthalpy exchangers through the development of advanced materials such as nanocomposites, polymer blends, and metal-organic frameworks. These materials are designed to boost heat and moisture transfer rates while ensuring long-term durability. To support effective material selection and system design, it is crucial to understand how specific membrane properties influence exchanger effectiveness. Several studies have therefore investigated the relationship between membrane characteristics and thermohygrometric performance, providing a solid foundation for innovation in this area.

Albdoor et al. [38], for example, functionalized PVDF membranes with metal-organic frameworks (ZIF-8 and HKUST-1), achieving increased surface hydrophilicity and enhanced moisture permeability. This modification improved latent effectiveness without compromising mechanical integrity. In a related study [39], the same authors developed a crosslinked sulfonated poly(ether-etherketone) (XL SPEEK) membrane that delivered heat and moisture transfer performance comparable to that of commercial Nafion membranes. Similarly, Lee et al. [40] investigated a LiCl-impregnated paper membrane and found that, although its diffusion coefficients were lower than those of typical hydrophilic polymers, its moisture permeability was comparable. These results suggest that low-cost alternatives such as XL SPEEK and LiCl-impregnated paper may be suitable for enthalpy recovery applications in temperate climates.

Other studies have explored the effect of membrane structure and morphology on performance. Baldinelli et al. [41] conducted a comparative analysis of porous membranes with different compositions and pore sizes. They identified a PVDF membrane with 0.45 μm pores as the most effective in terms of moisture diffusivity, and found its diffusion resistance to be relatively stable under varying humidity and temperature conditions. This confirms the robustness of such membranes in practical applications. Complementing this, Rahgozar Abadi et al. [42] studied asymmetric composite membranes and showed that permeability is significantly affected by membrane orientation, particularly at high vapor activities. Their findings emphasize the importance of both intrinsic material properties and configuration in real-world performance.

In parallel with these material-level investigations, researchers have also examined system-level design parameters. Al-Zubaydi et al. [43] demonstrated that exchanger geometry plays a key role in performance, showing that a dimpled quasi-counter-flow design significantly enhances cooling capacity and efficiency compared to flat-plate con-

figurations, especially under low airflow and high inlet temperature conditions. Extending the analysis from component-level performance to system-level application, Nasif et al. [44] investigated the integration of a lightweight Kraft-paper enthalpy membrane into a conventional air-conditioning cycle. They demonstrated that this configuration can yield meaningful energy savings in hot and humid climates, where managing latent loads is particularly critical. Similarly Cho et al. [45] introduced a hybrid energy-recovery unit that combines a hollow-fiber latent exchanger with a flat-plate sensible core. This configuration, when operated in season-specific modes, achieved enthalpy effectiveness ranging from 76% to 90% and reduced ventilation loads by approximately 75% during both summer and winter, exceeding local performance benchmarks.

Numerical modeling and optimization. Advanced computational fluid dynamics (CFD) and coupled heat-moisture transfer models have been developed to accurately predict exchanger performance and optimize internal geometries.

Early numerical efforts focused on the fundamental modeling of conjugate heat and mass transfer across membranes. Al-Waked et al. [46] developed a CFD model incorporating volumetric species transport for H_2O-air mixtures, showing that counter-flow configurations were particularly sensitive to mesh resolution but generally yielded higher effectiveness than cross-flow and parallel-flow arrangements. In a subsequent study, the same authors [47] introduced a variable membrane moisture resistance model, highlighting that moisture resistance decreases with increasing airflow rates and decreasing vapor mass fraction, directly affecting energy recovery and thermal effectiveness.

Engarnevis et al. [48] developed a detailed modeling approach for asymmetric composite membranes by introducing a permeability model dependent on local humidity and temperature, derived from kinetic sorption tests. Coupled with a finite-difference formulation of conjugate heat and mass transfer in a cross-flow core and validated against a commercial-scale exchanger, the model showed that assuming constant permeability can lead to deviations of up to 15% in effectiveness. They also found that outdoor air relative humidity may alter effectiveness by up to 12%, whereas the impact of outdoor air temperature was negligible. These results highlight the importance of accounting for variable membrane properties in performance prediction.

Zhang [49] introduced the use of naturally formed boundary conditions for heat and mass transfer in cross-flow membrane exchangers, moving beyond the conventional uniform temperature or flux assumptions. By solving the coupled momentum, energy, and moisture transport equations, the study provided more accurate predictions of local and mean Nusselt and Sherwood numbers. Experimental validation of outlet moisture content confirmed the improved reliability of this approach compared to traditional methods.

Several others numerical contributions also dealt with the influence of exchanger geometry and flow distribution. Pourhoseinian et al. [50] utilized CFD to evaluate the

impact of inserting internal flow dividers within the exchanger module. Their analysis compared conventional unobstructed single-channel designs against partitioned multi-channel configurations, demonstrating that while the latter can improve effectiveness at certain Reynolds numbers by extending fluid residence time, the introduced partitions often induce detrimental stagnation zones and flow maldistribution at higher volumetric flow rates. Sebai et al. [51] explored balanced and unbalanced flow in cross-flow exchangers using a control volume approach, demonstrating that unbalanced flow, while more realistic, introduces additional complexities in predicting effectiveness, particularly under varying Reynolds numbers and temperature gradients. Kang et al. [52] further examined the impact of exchanger channel shape, finding through CFD simulations and experimental validation that curved geometries provide superior thermal effectiveness in both heating and cooling modes.

Overall, these research efforts have considerably improved the understanding of local transport mechanisms and the role of geometry, material properties, and boundary conditions on exchanger performance. However, the computational cost and complexity of high-fidelity models often limit their direct applicability in system-level simulations or control-oriented models. For this reason, simplified formulations based on analytical or reduced-order approaches remain essential. Such models allow for the inclusion of recovery exchangers in dynamic simulations of complete ventilation or heat pump units, where the primary objective is to capture the dominant thermo-hygrometric interactions with sufficient accuracy while preserving numerical robustness and computational efficiency. In this context, high-fidelity CFD models serve as a necessary reference for validation and for guiding the development of reliable yet tractable simplified models. A representative example of this transition from detailed to reduced-order modeling is provided by Siegele et al. [53], who validated both a numerical model and a simplified effectiveness-NTU based formulation against full-range experimental data from commercial membrane exchangers. Although the effectiveness-NTU method showed deviations of about 5% under summer conditions, it proved sufficiently accurate and computationally efficient for system-level studies. Their results also confirmed the superior energy transfer capability of enthalpy exchangers compared to sensible-only units, despite their smaller surface area, thereby reinforcing the relevance of simplified but well-validated models in practical applications.

Collectively, these studies point to a clear direction for future development: by optimizing membrane chemistry and structural design of the recovery exchanger through simulation and experimentation, it is possible to significantly enhance both sensible and latent heat recovery in energy-recovery ventilation systems.

2.2.2. Fin and tube heat exchanger

Fin and tube heat exchangers used in air-to-air heat pumps consist of a mechanically expanded copper tube bundle embedded in a dense aluminum fin pack, designed to maximize air-side surface area while ensuring compactness and structural rigidity. The tubes are mechanically bonded to the fins through the expansion process, ensuring intimate thermal contact without the need for additional joining materials. The fin spacing is carefully selected to balance heat transfer performance with acceptable air-side pressure drop and to limit frost formation during heating mode. Fin geometry may vary from plain to wavy or louvered designs, with louvered fins often preferred in heat pumps for their ability to disrupt the boundary layer and enhance air-side heat transfer. The refrigerant circuiting within the tube bundle is often arranged in multiple parallel paths to ensure uniform refrigerant distribution and an even thermal load across the coil surface, while headers or manifolds provide robust connections between the refrigerant piping and the coil assembly. Surface treatments, such as hydrophilic or anti-corrosion coatings, are commonly applied to promote condensate drainage in cooling mode, reduce frost adhesion in heating mode, and extend the coil's service life under outdoor exposure. These construction features have direct implications for the seasonal efficiency and reliability of air-to-air heat pumps. For example, the optimization of fin spacing and geometry affects both the frost formation rate and the resulting frequency of defrost cycles required during winter operation, while the refrigerant circuit layout influences pressure drop and heat exchanger utilization. Surface treatments not only improve moisture management but also preserve long-term thermal performance by mitigating corrosion-related degradation. Since the condenser and evaporator in an air-to-air heat pump must operate efficiently under a wide range of ambient conditions, the mechanical and thermal design of the finned-and-tube heat exchangers is a critical factor determining the overall performance and durability of the unit.

Modelling approaches. From a modeling perspective, the accurate representation of these components is essential for the analysis, control, and optimization of vapor compression systems such as heat pumps and air conditioners. In scientific literature, several low-order dynamic approaches have been developed to capture the thermal behavior of finned-and-tube heat exchangers while maintaining low computational cost. These include lumped parameter models [54], moving boundary models [55, 56], and finite volume formulations [57, 58]. Lumped models offer high computational efficiency with minimal state variables, making them suitable for real-time simulations, especially when embedded in model-based control strategies or hardware-in-the-loop environments. Nonetheless, their strong assumptions, such as uniform temperature and pressure distributions within control volumes, can significantly limit their predictive capability in two-phase flow conditions, where rapid changes in temperature, pressure, and refrigerant phase

strongly influence the performance of the heat exchanger. These limitations become particularly critical when such models are used to evaluate transient behaviors, capacity modulation, or startup/shutdown cycles, where phase dynamics are dominant. For this reason, more detailed yet still computationally efficient low-order models, such as moving boundary or discretized finite volume models, are often preferred in applications where higher fidelity is required. Moving boundary models offer a compromise between lumped and finite volume models by subdividing the domain in three zones and tracking the interfaces between these regions (e.g., subcooled, two-phase, superheated), thereby providing a more realistic description of phase-change dynamics. However, their structure is tightly linked to predefined flow regimes, making them less robust under off-design or transient conditions [59, 60]. In addition, since each region is modeled as a single control volume, the local wall temperature is typically approximated in a coarse way, which limits the accuracy in evaluating wall condensation phenomena. This limitation becomes even more critical under winter conditions, when the heat exchanger model is possibly coupled with a frosting model, as an accurate prediction of local surface temperatures is essential for reliably estimating frost formation and its impact on heat exchanger performance [61, 62]. Moreover, pressure drop predictions can also be inaccurate, as they are highly sensitive to the local thermodynamic state of the refrigerant, especially during phase transitions. In contrast, finite volume models—also known as segment-by-segment models—discretize the entire domain into a fixed grid of segments, enabling the accurate reconstruction of the refrigerant thermodynamic state along the flow path. This spatial resolution allows for a precise evaluation of local heat transfer coefficients, pressure drops, and wall temperature distributions, which vary significantly across different phase regimes and are critical for predicting the heat exchanger performance. However, achieving sufficient accuracy often requires a high number of control volumes, resulting in increased computational cost [63]. This modeling approach constitutes the backbone of established commercial software such as CoilDesigner® [64] and EVAP-COND [65], which are extensively employed for detailed geometric design and steady-state performance rating of fin-and-tube heat exchangers. Yet, since these tools are inherently formulated for steady-steate conditions, they are ill-suited for capturing transient behaviors. This fundamental limitation, compounded by their closed-source architecture and prohibitive computational cost, effectively precludes the direct integration of such models into dynamic system-level simulations or real-time control environments.

Frost formation in finned heat exchangers. During heating operation, moisture carried by the outdoor airflow may desublimate onto the evaporator surface when the wall temperature drops below the freezing point. The resulting frost accumulation progressively reduces the local heat-transfer effectiveness and increases the air-side pressure drop, thereby degrading system heating capacity and potentially compromising opera-

tional stability.

Frost formation on cooled surfaces and finned heat exchangers has been extensively studied for decades. Early experimental investigations commonly relied on imaging-based techniques to observe frost evolution and infer the properties of the growing porous layer. For example, Hayashi et al. [66] employed photographic observation to classify frost morphologies across multiple temperature-dependent frosting stages, quantified frost density and effective thermal conductivity down to -25 °C, and proposed a structural model for predicting the effective thermal conductivity of the evolving porous frost layer. Consistent with the observations reported in that study and other related experimental works [67, 68], frost formation can be described as a multistage evolution (Figure 2.1):

i. **Initial crystal growth stage**, where a very thin frost film forms on the cold surface, followed by the wall-normal growth of isolated, rod-like columns that increase layer height at nearly linear rates, yielding a low-density, highly open, pillar-type structure.

ii. **Frost growth and densification stage**, where the pillars develop branches and begin interacting laterally, progressively forming bridges and a more interconnected porous matrix. During this period, mass deposition shifts from tip-dominated growth to a combination of vertical and side deposition, driving a nonlinear, approximately parabolic increase in bulk density.

iii. **Full-growth, aging and stabilization stage**, where crystal branching gradually decreases, the frost-air interface becomes smoother, and local melt-freeze cycles may start as thermal resistance rises. Melted condensate can wick into the pores and refreeze, temporarily increasing density and lowering local thermal resistance before new deposition resumes. Over time, the layer develops into a denser, tighter "aged frost" structure, with lower porosity and more stable thermal behavior.

Beyond morphological classification, extensive experimental investigations have been directed toward characterizing the physical properties of the frost layer and correlating them with specific growth conditions. Early contributions, such as those by Sanders [69] and Yonko and Sepsy [70], focused on developing empirical correlations for thermal conductivity as a function of frost density. Notably, they demonstrated that frost layers with the same thickness can exhibit different thermal conductivity depending on the growth conditions of the frost layer. Building on these property-focused studies, further research examined the sensitivity of frost development to airflow and humidity conditions. For instance, Brian et al. [71] analyzed frost growth on cryogenically cooled plates, studying the effects of Reynolds number and humidity, proposing correlations that account for internal vapor diffusion, and showing that frost densification governs the post-transient stabilization of thermal resistance. Similarly, O'Neal et al. [72] examined frost

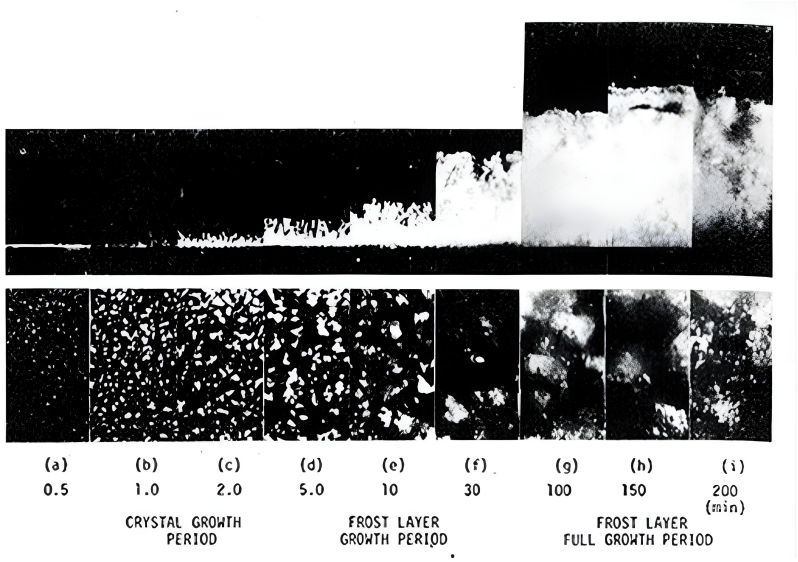

Figure 2.1: Main stages of frost growth on cooled surfaces, from Hayashi et al. [66].

evolution on flat plates under controlled surface-temperature and humidity conditions, identifying a critical Reynolds number (approximately $Re \approx 15900$) beyond which frost growth becomes largely independent of air velocity, and reporting pronounced spatial non-uniformities, including consistently denser and thicker frost layers near the leading edge of the geometry.

From a modeling perspective, simulating frost growth requires resolving the strong interdependence between phase change rates and the evolving thermophysical properties of the porous layer. Since these properties vary significantly with density and temperature, establishing accurate constitutive relations is a prerequisite for reliable dynamic predictions. In this regard, Dietenberger [73] advanced the field by deriving generalized semi-empirical correlations for frost thermal conductivity and introducing the water seepage mechanism for quasi-steady growth. Complementing this work, Kandula [74] extended the physical description of the frost layer by accounting for the airflow turbulence within the porous structure, demonstrating that the resulting eddy convection is a transport mechanism as critical as internal vapor diffusion for determining the effective thermal conductivity. Moving from constitutive parameters to the resolution of the spatial domain, Tao et al. [75] applied local volume-averaging techniques to determine the distribution of frost density and temperature, highlighting the role of internal vapor diffusion. Similarly, Le Gall et al. [76] employed the same volume-averaging method to refine a one-dimensional transient modeling approach, establishing that the effective vapor mass diffusivity must be significantly enhanced relative to molecular diffusivity to accurately predict experimental densification rates. Later studies, including the work of Padhmanabhan et al. [77], coupled transient frost formulations with segment-wise discretized heat-exchanger models and introduced airflow-redistribution algorithms to

represent frost-induced maldistribution, thereby improving the predictive capability of component-level simulations. Building on these advances, more recent contributions have demonstrated that distributed-parameter evaporator model with frosting can be embedded within a full dynamic heat-pump simulations to enable system-level assessments. For example, Qiao et al. [78] integrated a spatially resolved transient evaporator model with frosting, conceptually aligned with the segment-based approach of Padhmanabhan et al. [77], into a two-stage vapor-injection heat-pump simulation and showed its suitability for complete performance analyses. Similarly, Bai et al. [79] coupled a distributed outdoor-coil model with frosting in a dynamic heat-pump model and used the resulting tool to quantify how frosting and operating conditions affect heating capacity, power demand, and overall efficiency.

The reliability of such system-level predictions, however, still hinges on how well the model represents the onset of frosting and the strong spatial non-uniformities that develop on realistic fin-and-tube geometries, where local flow acceleration, boundary-layer separation, and surface microstructure can govern where frost first forms and how quickly the air-side resistance builds up. In this context, high-fidelity CFD models are valuable because they can resolve these local mechanisms directly and provide physics-based reference data for calibrating and validating reduced-order frost formulations used in system simulations. Following this direction, Cui et al. [80] developed a comprehensive CFD framework that integrates classical nucleation theory to resolve the initial frost deposition phase. Their simulations accurately captured the transient evolution of local frost thickness and heat transfer coefficients on complex fin-and-tube geometries, explicitly accounting for surface structural effects that are often neglected in simplified formulations. Analogously, Afrasiabian et al. [81] simulated the growth and densification processes on plate-fin evaporators using a CFD Eulerian-granular multiphase model, demonstrating that macroscopic geometric parameters, such as the distance between refrigerant tubes, play a critical role in determining the frosting time.

Overall, the field has evolved from empirical imaging-based characterization, to correlations for porous frost properties, to transient physics-based models, and finally to fully dynamic system-level simulations. Current research on multifunctional units builds on this foundation, focusing on physically predictive and numerically robust models that can resolve frost growth dynamics in simulation environments suited for control design and system-level optimization.

2.3. Overview of standardized testing methods for MFRBV units

In the European Union, a coordinated system of technical standards provides a unified framework for the evaluation of HVAC (Heating, Ventilation, and Air Conditioning) products. These European standards are designed to ensure consistent testing across manufacturers and laboratories, facilitating compliance with EU goals related to energy

efficiency, climate neutrality, and indoor environmental quality. They form the technical backbone of the Ecodesign [82] and Energy Labelling legislation [83], which imposes minimum performance requirements and transparency in energy consumption and labeling.

Standardized testing protocols constitute a prerequisite for the accurate characterization of ventilation and heat pump systems, particularly as these technologies evolve toward greater complexity and multifunctionality. The increasing integration of active thermodynamic recovery—specifically through embedded heat pump circuits—within ventilation units necessitates rigorous, transparent, and reproducible testing methodologies. Such standardized procedures are indispensable for validating performance metrics, ensuring regulatory compliance, and fostering fair market competition.

For mechanical ventilation systems in residential buildings, the primary reference standard is the **EN 13141** series, which specifies laboratory test methods for various types of ventilation units. **EN 13141-7** [84] applies to ducted supply and exhaust systems, typically found in single-family homes. These systems often include air-to-air heat recovery devices or extract-air to outdoor-air heat pumps, aimed at reducing space heating needs by recovering thermal energy from exhaust air. The standard defines how to measure key parameters such as airflow rates, pressure/flow characteristics, thermal recovery efficiency, specific electric power input, and acoustic emissions, all under controlled, repeatable conditions that enable accurate product comparison. Complementing this, **EN 13141-8** [85] focuses on non-ducted, single-room ventilation units, commonly used in renovations or in buildings where centralized systems are not practical. While the test metrics are similar to those in **EN 13141-7**, this part of the series adapts them to suit the characteristics of decentralized systems, such as through-wall or wall-mounted units. A particularly relevant standard in the context of multifunctional systems is **EN 16573:2017** [86], which is specifically dedicated to balanced ventilation units incorporating heat pump technology. Unlike standards that assess ventilation and heating/-cooling functions separately, **EN 16573:2017** introduces an integrated methodology to evaluate the combined performance of such systems. In particular, **EN 16573:2017** does not redefine ventilation testing procedures, but refers directly to **EN 13141-7** for measuring core ventilation parameters. This ensures methodological consistency and avoids duplication, while allowing **EN 16573:2017** to focus on how the ventilation and heat pump subsystems perform both individually and together.

The standard introduces procedures to characterize the unit's combined performance under typical operating conditions, while also enabling the disaggregation of results, supposing that the heat pump does not thermodynamically influence the ventilation system during testing. This means that the operation of the heat pump must not significantly alter air temperature, pressure, or flow in inlet and outlet of the ventilation unit. When this condition is met, the standard permits a separate assessment of each subsystem, result-

ing in a more complete understanding of the product's energy efficiency, heating/cooling output, and sound emissions. The testing procedure described in the **EN 16573:2017** is structured into two distinct phases: in the first phase, the unit operates solely in ventilation mode with the heat pump turned off. During this stage, key parameters such as the electrical power consumption of the ventilation system and the thermal energy recovered from exhaust air are measured, helping quantify the standalone performance of the ventilation component. In the second phase, the heat pump is activated to deliver active space heating or cooling while the ventilation continues in heat recovery mode. By comparing the results of the two phases, it is possible not only to evaluate the combined performance of the multifunctional unit but also to isolate and determine the specific contribution of the heat pump to the overall energy output and consumption. All these standards (**EN 13141-7**, **EN 13141-8**, and **EN 16573:2017**) are embedded within the EU's legal framework through Commission Regulation (EU) **No. 1253/2014** [87] for ventilation units and Regulation (EU) **No. 813/2013** [88] for space heaters and heat pumps. These European standards are widely adopted by manufacturers, testing bodies, and notified organizations to demonstrate conformity, obtain CE marking, and provide verifiable data for energy labelling, product development, and market surveillance.

Beyond the European context, these standards are also gaining traction internationally, serving as technical benchmarks in global markets that seek greater consistency and transparency in HVAC performance assessment. Their adoption reflects a broader move toward globally aligned testing practices, enabling manufacturers to design products that are not only compliant with EU requirements but also competitive on the world stage.

Recent scientific literature further builds on this standardization framework by critically examining the validity of current testing procedures when applied to increasingly integrated system architectures. In particular, emerging studies focus on configurations where the heat pump and the ventilation subsystem are thermodynamically coupled—a condition that challenges the independence assumptions underlying existing standards and reveals significant methodological gaps.

The limits of current standards were clearly demonstrated by Hunt et al. [89], who critically evaluated the EN 16573:2017 standard against advanced configurations where the heat pump directly influences the heat recovery exchanger. Their findings showed that the standard's subtractive method fails to accurately capture coupled system behaviour—particularly when the evaporator actively enhances heat recovery by pre-conditioning the airstream. This evidence underscores that measurement strategies relying on the superposition of separate subsystem performances are fundamentally ill-suited for highly integrated units.

To overcome the inherent deficiencies of this subsystem separation methodology, Wemhoener et al. [90], within the framework of IEA HPP Annex 28, established a holistic "black-box" assessment methodology. Unlike standard protocols that attempt to isolate

subsystems, this approach treats the unit as a single thermodynamic control volume. Their methodology defined key operating modes—such as ventilation-only, combined space heating, and domestic hot water (DHW) modes—to explicitly capture the interaction between ventilation and heat pump operation. Furthermore, seasonal performance was calculated using a bin method weighted by climate-specific outdoor temperature distributions, utilizing enthalpy-balance corrections to isolate the contribution of heat recovery without the need to physically decouple the subsystems.

2.3.1. Performance metrics

Standardized testing evaluates key performance indicators to ensure ventilation units and heat pumps operate efficiently and reliably. These metrics are measured under controlled conditions for accuracy and comparability:

- **Airflow rate** ($m^3\ h^{-1}$): measures the volume of air supplied and exhausted at rated static pressure. Tests often include pressure-flow curves and calculate Specific Fan Power (SFP), expressing energy used per volume of air moved.
- **Heat/moisture recovery efficiency** (%): indicates how effectively heat/moisture is transferred from exhaust to supply air. For passive exchangers, effectiveness follows AHRI 1060 standards [91], while units with heat pumps use energy balance methods to capture additional thermal gains.
- **Heating/cooling capacity** (W): represents the thermal capacity delivered by the unit under standardized temperature conditions.
- **Coefficient of Performance/Energy Efficiency Ratio** (COP/EER)(-): ratio of heating or cooling output to electrical input, showing system efficiency under test conditions.
- **Electric power input** (W): total electrical consumption of fans, compressors, and any electric heaters, essential for calculating efficiency metrics.
- **Sound power level** (dB): measures noise emissions to ensure products meet acoustic comfort and regulatory limits.
- **Additional efficiency ratios** (%): additional metrics as the Energy Factor (EF) provide further insight into energy consumption and cost-effectiveness.

Testing instruments accuracy. To ensure compliance with standards, laboratory testing must be carried out under tightly controlled conditions using instrumentation that satisfies defined accuracy requirements. In particular, temperature and airflow measurements are subject to strict uncertainty limits: ±0.2 K for dry-bulb temperature, ±0.3

K for wet-bulb temperature, and a maximum of 3 m^3 h^{-1} or 3% of the measured flow rate for airflow. Measurements are performed in ducts at prescribed locations to ensure representativeness, with the temperature variation across the duct section limited to 0.1 K.

Tests must be conducted under steady-state conditions maintained for at least one hour, with deviations from set values not exceeding ±0.3 K (mean) or ±1 K (instantaneous) for temperature, ±5% (mean) and ±10% (instantaneous) for airflow, and ±1% for voltage. All significant data must be recorded continuously for a minimum of 30 minutes. These strict criteria ensure that reported performance values are reliable, comparable, and suitable for regulatory compliance and product benchmarking.

CHAPTER 3

Development of the Digital Twin

In this chapter, the comprehensive development of the model for the analyzed HVAC system is presented. The formulation of governing conservation equations and auxiliary physical correlations is detailed for key components, including the enthalpy and sensible recovery exchangers, fans, filters, the check valve, the electric pre-heater, T-junctions, fin-and-tube heat exchangers, the suction line accumulator, the compressor, the four-way valve, and the electronic expansion valve. Particular emphasis is placed on capturing complex thermodynamic phenomena such as coupled heat and mass transfer, two-phase flow dynamics, and frost formation mechanisms.

3.1. Mathematical framework and implementation

The modeling framework developed in this work follows a system-level approach based on a combination of lumped-parameter and distributed-parameter representations. Each physical component of the system is described by one or more one-dimensional control volumes, where flow variables are assumed uniform across the cross-section and vary only along the main flow direction. This assumption allows the governing equations to be expressed as a set of ordinary differential and algebraic equations (DAEs). Components with nearly uniform conditions, are represented using a single control volume, while components exhibiting significant spatial gradients, such as the heat exchangers in the refrigerant lines, are discretized into multiple control volumes to capture local variations more accurately. This hybrid modeling strategy ensures a good compromise between model accuracy and computational efficiency.

For each component, the conservation equations of mass, energy, and mechanical energy are formulated. These equations are then combined into a single global system that represents the behavior of the entire network. Because the components are interconnected, the resulting formulation takes the form of a differential-algebraic system that

describes the evolution of pressures, mass flow rates, and other state variables. At each simulation time step, the corresponding system matrix is solved iteratively to update all variables consistently across the network.

The implementation is performed within the MATLAB® Simulink® [92] environment using the Simscape toolbox, which provides a modular representation of each component and automates the assembly and numerical solution of the coupled system. Moreover, the current control logic of the unit, developed as well in Simulink®, is directly integrated into the model. This coupling ensures that the digital twin accurately reproduces the dynamic interaction between physical processes and control actions under a wide range of operating conditions.

3.2. Component-level modeling

In this section, the modeling approach adopted for the main components of the system is presented. Each model is formulated so as to reproduce the relevant thermal and dynamic behavior of the component within the analyzed system, with a level of detail consistent with system-level simulations and control-oriented applications.

Given that the direction of mass and energy flows may vary depending on the operating conditions, a consistent sign convention is adopted across all component models: flows entering the control volume are defined as positive, while flows exiting are defined as negative. This convention allows the conservation equations to be expressed in a more compact and coherent manner, thereby facilitating numerical implementation and the solution of the resulting system of differential-algebraic equations (DAEs).

3.2.1. Recovery exchanger

3.2.1.1. Finite volume for moist air

The component is modeled using two finite volumes, each representing one side of the heat exchanger: the ETA-EHA side (“EE”) and the ODA-SUP side (“OS”). For each finite volume, a set of conservation equations is applied to determine the thermodynamic state of the control volume and, consequently, the outlet conditions of the corresponding stream. In this work, the reference state for moist-air mixture enthalpy is defined by setting the enthalpy of liquid water at 0 °C to zero (0 J kg^{-1}). To ensure the model is as general as possible, both the compressibility and the thermal capacity of the moist air within each control volume are not neglected. Wall surface condensation at the heat transfer surface is considered only in the case of sensible-only recovery exchangers, as, in enthalpy recovery exchangers, it rarely occurs under typical (non-extreme) operating conditions due to the moisture recovery process, which significantly reduces the potential for condensation [93]. In both recovery exchanger models, a frost-free operating condition is assumed, as the unit is equipped with an electric pre-heater that warms the incoming air, preventing frost formation in the exchanger (Section 1.4).

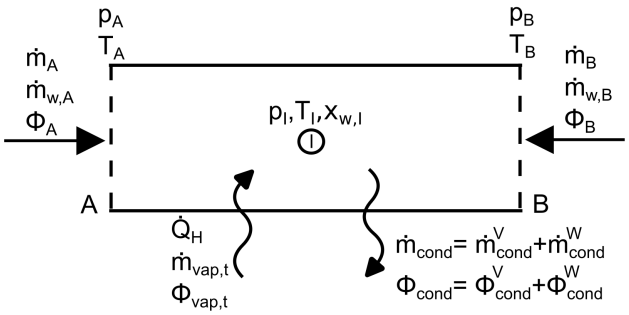

Figure 3.1: Finite volume for the air stream.

Figure 3.1 illustrates the finite volume for each moist air streams and defines the positive direction of the relevant variables: moist air mass flow rates $\dot{m}_A$ and $\dot{m}_B$, water vapor mass flow rates $\dot{m}_{w,A}$ and $\dot{m}_{w,B}$, total energy inflows at the control volume ports Φ_A and Φ_B (sum of enthalpy and kinetic energy), water condensation rate $\dot{m}_{cond}$ (sum of volume and wall condensation $= \dot{m}^V_{cond} + \dot{m}^W_{cond}$), the energy associated with the removal of this condensate Φ_{cond} $(= \Phi^V_{cond} + \Phi^W_{cond})$, the exchanged water vapor mass flow rate between the two control volumes $\dot{m}_{vap,t}$, its corresponding energy $\Phi_{\text{vap,t}}$ $(= \dot{m}_{vap,t} h_{vap,t})$, and the total inlet heat flow rate to the control volumes, $\dot{Q}_H$ (in this case, resulting from heat recovery). An internal node, denoted as 'I', is introduced to represent the state of the fluid within the control volume. The moist air domain is defined by three state variables: pressure (p), temperature (T), and specific humidity (x_w), and accordingly, the state of the fluid inside each control volume is represented by p_I, T_I, and $x_{w,I}$. In this section, $\dot{Q}_H$, $\dot{m}_{vap,t}$ and $\Phi_{vap,t}$ are considered known quantities. Their modeling will be addressed in a subsequent section.

The net flow rates into the control volume rapresented in Figure 3.1 are defined as:

$$\text{Total mass:} \quad \dot{m}_{net} = \dot{m}_A + \dot{m}_B - \dot{m}_{cond} + \dot{m}_{vap,t} \tag{3.1}$$

$$\text{Water mass:} \quad \dot{m}_{w,net} = \dot{m}_{w,A} + \dot{m}_{w,B} - \dot{m}_{cond} + \dot{m}_{vap,t} \tag{3.2}$$

$$\text{Energy:} \quad \Phi_{net} = \Phi_A + \Phi_B + \dot{Q}_H - \Phi_{cond} + \Phi_{vap,t} \tag{3.3}$$

Mass balances

The water vapor mass conservation for the control volume reads as:

$$\frac{dM_w}{dt} = \dot{m}_{w,net} \tag{3.4}$$

with M_w the mass of water vapor in the control volume. Observing that the water vapor density is $\rho_w = \rho_I x_{w,I}$ and then expanding the time derivative and rearranging, one obtains:

$$\frac{d}{dt}(\rho_I x_{wI} V) = \dot{m}_{w,net} \Rightarrow \boxed{\frac{dx_{w,I}}{dt}\rho_I V + x_{w,I}\dot{m}_{net} = \dot{m}_{w,net}} \tag{3.5}$$

with V the geometrical dimension of the control volume.

In the same way the overall mixture mass conservation equation can be recovered:

$$\frac{dM}{dt} = \dot{m}_{net} \Rightarrow \frac{d\rho_I}{dt} V = \dot{m}_{net} \tag{3.6}$$

where M is the mass of moist air in the control volume. Recalling that the moist air density can be expressed using the ideal gas law as $\rho_I = \frac{p_I}{R_I T_I}$, its time derivative can be written as:

$$\frac{d\rho_I}{dt} = \frac{1}{R_I T_I}\frac{dp_I}{dt} - \frac{p_I}{R_I^2 T_I}\frac{dR_I}{dt} - \frac{p_I}{R_I T_I^2}\frac{dT_I}{dt} = \rho_I\left(\frac{1}{p_I}\frac{dp_I}{dt} - \frac{1}{T_I}\frac{dT_I}{dt} - \frac{1}{R_I}\frac{dR_I}{dt}\right) \tag{3.7}$$

The specific gas constant of the moist air mixture (R_I) is given by the weighted average of the component-specific gas constants [94]:

$$R_I = (1 - x_{w,I})R_{dry} + x_{w,I}R_w = R_{dry} + (R_w - R_{dry})x_{w,I} \tag{3.8}$$

where R_{dry} is the specific gas constant of dry air and R_w is the specific gas constant of water vapor. Deriving the Equation (3.8) with respect to time leads to:

$$\frac{dR_I}{dt} = (R_w - R_{dry})\frac{dx_{w,I}}{dt} = \frac{(R_w - R_{dry})}{\rho_I V}(\dot{m}_{w,net} - x_{w,I}\dot{m}_{net}) \tag{3.9}$$

Finally substituting Equation (3.9) and (3.7) into Equation (3.6), yields the final form of the mixture conservation equation:

$$\boxed{\left(\frac{1}{p_I}\frac{dp_I}{dt} - \frac{1}{T_I}\frac{dT_I}{dt}\right)\rho_I V + \frac{R_{dry} - R_w}{R_I}\left(\dot{m}_{w,net} - x_{w,I}\dot{m}_{net}\right) = \dot{m}_{net}} \tag{3.10}$$

Energy conservation

The energy conservation for the control volume can be derived from the first law of thermodynamics:

$$\frac{d}{dt}\left(\rho_I u_I V\right) = \Phi_{net} \tag{3.11}$$

Expanding the time derivative:

$$\frac{d}{dt}\left(\rho_I u_I V\right) = \rho_I V\frac{du_I}{dt} + u_I\frac{dV\rho_I}{dt} = \rho_I V\frac{du_I}{dt} + u_I\dot{m}_{net} = \Phi_{net} \tag{3.12}$$

The specific internal energy of a mixture is defined as [94]:

$$u_I = (1 - x_{w,I})u_{dry,I} + x_{w,I}u_{w,I} = u_{dry,I} + (u_{w,I} - u_{dry,I})x_{w,I} \tag{3.13}$$

Differentiating Equation (3.13) with respect to time, and using the definitions of the specific heat at constant volume for dry air ($c_{v,dry}$) and for water vapor ($c_{v,w}$), one obtains:

$$\frac{du_I}{dt} = x_a c_{v,dry} \frac{dT_I}{dt} + x_{w,I} c_{v,w} \frac{dT_I}{dt} + \left(u_{w,I} - u_{dry,I}\right) \frac{dx_{w,I}}{dt} = c_{v,I} \frac{dT_I}{dt} + \left(u_{w,I} - u_{dry,I}\right) \frac{dx_{w,I}}{dt} \tag{3.14}$$

with $c_{v,I} = x_{dry} c_{v,dry} + x_{w,I} c_{v,w}$. Extracting $\frac{dx_{w,I}}{dt}$ from Equation (3.5) and substituting it into Equation (3.14) yields:

$$\frac{du_I}{dt} = c_{v,I} \frac{dT_I}{dt} + \frac{u_{w,I} - u_{dry,I}}{\rho_I V} \left(\dot{m}_{w,net} - x_{w,I} \dot{m}_{net}\right) \tag{3.15}$$

Finally, by substituting Equation (3.15) into Equation (3.12), and by using the relation $c_{v,I} = c_{p,I} - R_I$, we can recover the complete energy conservation equation for the moist air control volume:

$$\boxed{\rho_I (c_{p,I} - R_I) V \frac{dT_I}{dt} + (u_{w,I} - u_{dry,I})(\dot{m}_{w,net} - x_{w,I} \dot{m}_{net}) + u_I \dot{m}_{net} = \Phi_{net}} \tag{3.16}$$

with $c_{p,I} = (1 - x_{w,I}) c_{p,dry} + x_{w,I} c_{p,w}$. The specific heat at constant pressure for dry air ($c_{p,dry}$) and water vapor ($c_{p,w}$), as well as the specific enthalpy for dry air (h_{dry}) and water vapor (h_w), are stored in lookup tables (for simplicity, at standard ambient pressure), and retrieved as functions of T_I during the simulation run time.

Mechanical energy balance

The pressure loss for the control volume can be simply determinated from:

$$p_A - p_B = \Delta p_{loss} \tag{3.17}$$

Δp_{loss} represents the total pressure drop across the recovery exchanger, including both momentum flux and viscous losses. This value, in this case, is experimentally determined as a function of the average mass flow rate ($\dot{m}_{avg}$) on each side of the exchanger:

$$\Delta p_{loss} = a |\dot{m}_{avg}| \dot{m}_{avg} + b \dot{m}_{avg} \tag{3.18}$$

where a and b are empirical coefficients supplied by the manufacturer's datasheet.

Considering the sign convention defined in Figure 3.1, the average inflow mass flow rate is defined as:

$$m_{avg} = \frac{\dot{m}_A - \dot{m}_B}{2} \tag{3.19}$$

According to Equation (3.18), Δp_{loss} can be either positive or negative depending on the sign of $\dot{m}_{avg}$, and it is therefore always consistent with the flow direction. To close the system of equations, an intermediate pressure (p_I) is defined at the control volume

node 'I':

$$p_I = \frac{p_A + p_B}{2} \tag{3.20}$$

Volume condensation

During the cooling of a moist air volume, the specific humidity of the air may reach or even exceed the saturation humidity corresponding to the local air temperature T_I. As a result, water vapor begins to condense within the volume. This phenomenon is known as *volume condensation* or *bulk-flow condensation*. This process is accounted for by the term $\dot{m}^V_{cond}$ calculated as:

$$\dot{m}^V_{cond} = \begin{cases} 0, & \text{if } x_{w,I} \leq x_{w,sat,I} \\ \frac{x_{w,I} - x_{w,sat,I}}{\tau_{cond}} \rho_I V, & \text{if } x_{w,I} > x_{w,sat,I} \end{cases} \tag{3.21}$$

In the above equation, $x_{w,sat,I}$ is the saturation specific humidity evaluated at temperature T_I, and τ_{cond} is the time constant associated with the condensation process. The energy term associated with the condensed water in the bulk-flow is:

$$\Phi^V_{cond} = \dot{m}^V_{cond} h^V_{wl,cond} \tag{3.22}$$

which is subtracted in the net energy flow rate (Equation (3.3)). This formulation accounts for the enthalpy of the liquid water leaving the control volume, while the latent heat released during condensation (associated with this condensate) remains within the control volume. Here, $h^V_{wl,cond}$ is the specific enthalpy of the condensed water in the bulk-flow, evaluated at the control volume temperature T_I.

3.2.1.2. Heat and mass transfer

To reduce the complexity of the modeling procedure, the aggregate heat and mass transfer characteristics of the exchanger are derived by employing a single-channel analysis (as illustrated in Figure 3.2) within the counter-flow region. Subsequently, these findings are extrapolated to encompass the entire recovery exchanger. By convention, the direction of heat and moisture transfer is considered positive from the control volume 1 (C1) to control volume 2 (C2).

Sensible heat recovery

Concerning the sensible heat recovered in the exchanger, the effectiveness-NTU method has been employed [95].

The heat transfer rate exchanged between two channels ($\dot{Q}^{ch}$) is:

$$\dot{Q}^{ch}_s = \varepsilon_s \dot{Q}^{ch}_{s,\max} = \varepsilon_s (\dot{m}^{ch} c_p)_{\min} (T_{11} - T_{21}), \qquad \varepsilon_s = \frac{1 - \exp[-\mathrm{NTU}_s(1 - C_r)]}{1 - C_r \exp[-\mathrm{NTU}_s(1 - C_r)]} \tag{3.23}$$

where T_{11} denotes the inlet C1 flow temperature, T_{21} refers to the inlet C2 flow temper-

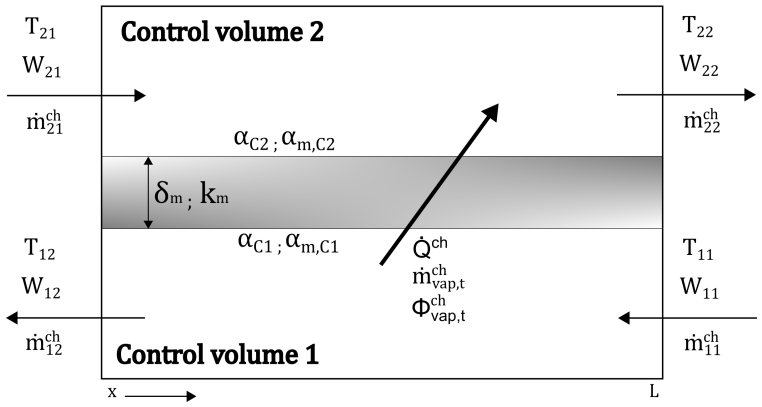

Figure 3.2: Control volumes for the single-channel analysis.

ature, ε_s represents the sensible effectiveness for a counter-flow type exchanger, $\dot{Q}^{ch}_{s,\max}$ is the maximum recoverable heat flow rate per channel, $C_r = \frac{(\dot{m}^{ch}cp)_{\min}}{(\dot{m}^{ch}cp)_{\max}}$ is the inlet heat capacity ratio and $\dot{m}^{ch}_{11}$ and $\dot{m}^{ch}_{21}$ are the inlet mass flow rates per channel.

If $C_r = 1$ the sensible effectiveness is calculated as:

$$\varepsilon_s = \frac{\mathrm{NTU}_s}{1 + \mathrm{NTU}_s} \tag{3.24}$$

The Number of Transfer Units for sensible heat transfer (NTU_s) is:

$$\mathrm{NTU}_s = \frac{U_s A^{ch}}{C_{\min}} \tag{3.25}$$

with the overall heat transfer conductance per channel ($U_s A^{ch}$) defined as:

$$U_s A^{ch} = \left(\frac{1}{\alpha_{C1} A^{ch}} + \frac{\delta_m}{k_m A^{ch}} + \frac{1}{\alpha_{C2} A^{ch}} \right)^{-1} \tag{3.26}$$

where U_s is the global heat transfer coefficient, A^{ch} is the total heat-transfer area per channel, α_{C1} and α_{C2} are the average convective heat-transfer coefficients of the two control volumes, δ_m is the membrane thickness, and k_m is the membrane thermal conductivity.

To simplify the model, Equation (3.26) includes only the intrinsic conductive thermal resistance, and is therefore insensitive to mass transfer. Min et al. [96] showed that neglecting the latent heat effect in the sensible effectiveness calculation always results in a marginal error on the sensible effectiveness (less than 2%), while its impact on the moisture effectiveness is always negligible.

Given the small hydraulic diameter of the channels, the flow regime within this type of exchanger is predominantly laminar [53,97]. For this reason, the correlation proposed by Muzychka and Yovanovich [98] is adopted in the present work to estimate the convective heat transfer coefficients (α_{C1} and α_{C2}). This correlation is applicable to both uniform wall temperature (UWT) and uniform wall heat flux (UWF) boundary conditions,

as it is derived from a generalized analytical framework. It is among the most comprehensive correlations available, as it accounts for both thermally and hydrodynamically developing laminar flow in non-circular ducts. This level of detail is particularly relevant in the context of vertical plate-type enthalpy exchangers, such as the one analyzed in this work, where the entrance regions can represent a significant portion of the channel length. Indeed, Zhang et al. [99] showed that the combined hydrodynamic, thermal, and concentration entry lengths may extend up to 30% of the total duct length in such configurations.

The correlation proposed by Muzychka and Yovanovich consists of three terms: the first two describe the developing flow region (entry effects), while the third represents the fully developed Nusselt number. The correlation can be expressed as follows:

$$\mathrm{Nu}_{\sqrt{A}}(z^*) = \left[\left(\frac{C_4 f(\mathrm{Pr})}{\sqrt{z^*}} \right)^m + \left\{ \left(C_2 C_3 \left(\frac{f\,\mathrm{Re}_{\sqrt{A}}}{z^*} \right)^{1/3} \right)^5 + \left(C_1 \frac{f\,\mathrm{Re}_{\sqrt{A}}}{8\sqrt{\pi}\epsilon^{1/10}} \right)^5 \right\}^{m/5} \right]^{1/m} \tag{3.27}$$

All quantities with the subscript $\sqrt{A}$ refer to a characteristic length ($L_{\sqrt{A}}$), defined as the square root of the channel cross-sectional area. In Equation (3.27), ϵ is the aspect ratio of the channel and z^* is defined as the dimensionless axial length:

$$z^* = \frac{z/L_{\sqrt{A}}}{\mathrm{Re}_{\sqrt{A}}\mathrm{Pr}} \tag{3.28}$$

m is a blending parameter, function of the Prandtl number:

$$m = 2.27 + 1.65\mathrm{Pr}^{1/3} \tag{3.29}$$

and $f\,\mathrm{Re}_{\sqrt{A}}$ is the product of the friction factor and Reynolds number, which is given by the same authors in a previous work [98]:

$$f\,\mathrm{Re}_{\sqrt{A}} = \frac{12}{\sqrt{\epsilon}(1+\epsilon)\left[1 - \frac{192\epsilon}{\pi^5}\tanh\left(\frac{\pi}{2\epsilon}\right)\right]} \tag{3.30}$$

In the present study, given that the developed model adopts a lumped-parameter approach, the calculation of interest is the average Nusselt number. Consequently, the axial length z is set equal to the total duct L and the constant C_2 and C_4 are equal to 1.5 and 2, respectively, as recommended by Muzychka and Yovanovich [98].

The constants C_1 and C_3 depend on the type of correlation (UWT or UWF) as well as $f(\mathrm{Pr})$:

- UWT: $C_1 = 3.24$, $C_3 = 0.409$, $f(\mathrm{Pr}) = \frac{0.564}{[1+(1.664\mathrm{Pr}^{1/6})^{9/2}]^{2/9}}$
- UWF: $C_1 = 3.86$, $C_3 = 0.501$, $f(\mathrm{Pr}) = \frac{0.886}{[1+(1.909\mathrm{Pr}^{1/6})^{9/2}]^{2/9}}$

The heat transfer coefficients (α_{C1} and α_{C2}) can now be evaluated from the Nusselt Number:

$$\alpha = \frac{\mathrm{Nu}_{\sqrt{A}} k_{air}}{L_{\sqrt{A}}} \tag{3.31}$$

k_{air} is the air thermal conductivity in the respective control volume.

It is worth to note that correlations based on the uniform wall temperature (UWT) boundary condition generally yield lower Nusselt number predictions compared to those assuming uniform wall heat flux (UWF). Zhang et al. [99] demonstrated that the actual boundary condition experienced by heat exchanger surfaces typically falls between the idealized UWT and UWF scenarios. In this work, the UWT correlation is adopted for the ERV model, while the UWF correlation is used for the HRV model. The motivation behind this choice will be further elaborated in Section 5.2.

If we now consider the total number of channels per side (n^{ch}), it is possible to compute the overall recovered sensible heat ($\dot{Q}_s$):

$$\dot{Q}_s = n^{ch} \dot{Q}_s^{ch} \tag{3.32}$$

and if wall surface condensation is neglected (i.e., in the case of an enthalpy recovery exchanger), at steady state we have:

$$\dot{Q}^{std} = \dot{Q}_s \tag{3.33}$$

Moisture recovery

The equations for moisture recovery are derived mainly from the works of Min et al. [100], Križo et al. [101] and Zhang et al. [102].

Analogously to Equation (3.23) it is possible to define the moisture exchanged between two channels ($\dot{m}_{vap,t}^{ch}$) as:

$$\dot{m}_{vap,t}^{ch} = \varepsilon_x (\dot{m}_{dry}^{ch})_{\min} (W_{11} - W_{21}) \tag{3.34}$$

W_{11} and W_{21} indicate the humidity ratios of the two streams and $\dot{m}_{dry}^{ch}$ is the mass flow rate of dry air per channel. Consequently, the moisture effectiveness (ε_x) can be computed as:

$$\varepsilon_x = \frac{1 - \exp[-\mathrm{NTU}_x(1-R)]}{1 - R\exp[-\mathrm{NTU}_x(1-R)]}, \qquad R = \frac{\dot{m}_{\min}^{ch}}{\dot{m}_{\max}^{ch}}, \qquad \mathrm{NTU}_x = \frac{U_x A^{ch}}{\dot{m}_{\min}^{ch}} \tag{3.35}$$

If $R = 1$, moisture effectiveness is redefined as:

$$\varepsilon_x = \frac{\mathrm{NTU}_x}{1 + \mathrm{NTU}_x} \tag{3.36}$$

The overall moisture transfer conductance per channel ($U_x A^{ch}$) can be calculated in a similarly to Equation 3.26:

$$U_x A^{ch} = \left(\frac{1}{\alpha_{m,C1} A^{ch}} + \frac{\delta_m}{P_m A^{ch}} + \frac{1}{\alpha_{m,C2} A^{ch}} \right)^{-1} \tag{3.37}$$

Unlike the overall heat transfer resistance, which is typically dominated by convective effects and where neglecting the conductive resistance usually implies a reasonable approximation, the overall mass transfer resistance is primarily influenced by the conductive term. Therefore, an accurate evaluation of the membrane's conductive resistance, and consequently of its permeability (P_m) is essential. To this aim, in the present work, the membrane permeability is modeled following the references [100], [101], [102]:

$$P_m = \frac{C D_{wm} \omega_{\max} \exp(5294/\overline{T}_m)}{10^6 \left(1 - C + \frac{C}{\overline{RH}_m}\right)^2 \overline{RH}_m^2} \tag{3.38}$$

where D_{wm} is the moisture diffusivity within the membrane, $\omega_{\max}$ denotes the maximum moisture content (i.e., the water uptake limit) of the membrane material and C is a constant describing the shape of the sorption isotherm. $\overline{T}_m$ is the average membrane temperature, while $\overline{RH}_m$ represents the average relative humidity of the air adjacent to the membrane surface, which can be estimated from $\overline{T}_m$ and the average humidity ratio at the membrane surface, $\overline{W}_m$. The calculation of $\overline{T}_m$ will be better detailed at the end of this section, and is treated for now as a known value, while a simplified procedure for estimating $\overline{W}_m$ is presented below.

Assuming a balanced ventilation unit and quasi-steady-state moisture transport, referring to Figure 3.2, the water mass flow rates at the outlets of the two channels can be expressed as:

$$\dot{m}^{ch}_{w,12} = \dot{m}^{ch}_{w,11} - \dot{m}^{ch}_{vap,t}, \qquad \dot{m}^{ch}_{w,22} = \dot{m}^{ch}_{w,21} + \dot{m}^{ch}_{vap,t} \tag{3.39}$$

Since the unit is balanced, dividing both equations by the dry mass flow rate per channel ($\dot{m}^{ch}_{dry}$) yields:

$$W^b_{12} = W^b_{11} - \Delta W, \qquad W^b_{22} = W^b_{21} + \Delta W \tag{3.40}$$

where $\Delta W = \frac{\dot{m}^{ch}_{vap,t}}{\dot{m}^{ch}_{dry}}$ represents the shift in humidity ratio due to the moisture exchanged across the membrane. Assuming a linear variation of humidity ratio along each channel, the average bulk humidity ratios ($\overline{W}^b_{C1}, \overline{W}^b_{C2}$) in control volumes 1 and 2 (C1 and C2) are:

$$\overline{W}^b_{C1} = \frac{W^b_{11} + W^b_{12}}{2} = \frac{2W^b_{11} - \Delta W}{2}, \qquad \overline{W}^b_{C2} = \frac{W^b_{21} + W^b_{22}}{2} = \frac{2W^b_{21} + \Delta W}{2} \tag{3.41}$$

Following [42] the mean surface membrane humidity ratios on the two sides can be

expressed as:

$$\overline{W}_{m,C2} = \overline{W}^{b}_{C2} + \frac{J}{\alpha_{m,C2}\overline{\rho}_{air}}, \qquad \overline{W}_{m,C1} = \overline{W}^{b}_{C1} - \frac{J}{\alpha_{m,C1}\overline{\rho}_{air}} \tag{3.42}$$

where $J = \frac{\dot{m}^{ch}_{vap,t}}{A^{ch}}$ is the recovered water mass flux and $\overline{\rho}_{air}$ is the average air density in the exchanger. Finally, by averaging again one has:

$$\boxed{\overline{W}_{m} = \frac{\overline{W}_{m,C2} + \overline{W}_{m,C1}}{2} = \overline{W} + \frac{J}{2\overline{\rho}_{air}}\left(\frac{1}{\alpha_{m,C2}} - \frac{1}{\alpha_{m,C1}}\right)} \tag{3.43}$$

with:

$$\overline{W} = \frac{\overline{W}^{b}_{C2} + \overline{W}^{b}_{C1}}{2} = \frac{W^{b}_{12} + W^{b}_{11}}{2} \tag{3.44}$$

which rapresents the average average humidity ratio in the recovery exchanger. Regarding membrane permeability, the data provided by Abadi et al. [42] in the form of a lookup table can be directly used to obtain the product $D_{wm}\omega_{max}$ under different temperatures and membrane activities, provided that the membrane material is known and the corresponding sorption constant C is available.

The convective moisture transfer coefficient α_m appearing in Equation 3.37, is estimated according to the Chilton-Colburn analogy, from the convective heat-transfer coefficient, the Lewis number (Le=0.9 [103]), the density ρ and specific heat capacity c_p of the respective air streams:

$$\alpha_m = \frac{\alpha}{\mathrm{Le}^{2/3}\rho c_p} \tag{3.45}$$

Finally, the overall exchanged moisture between the two streams is:

$$\dot{m}_{vap,t} = n^{ch}\dot{m}^{ch}_{vap,t} \tag{3.46}$$

Integration of the cross-flow section

As previously discussed and illustrated in Figure 1.2, the actual flow arrangement of these exchangers is typically cross-counter-flow. Since a significant portion of the total exchange area operates in a cross-flow configuration, it is essential to account for it. Unfortunately, an effectiveness formula for this kind of flow arrangement does not exist and assuming a purely counter-flow configuration or neglecting the cross-flow portion may lead to a significant underestimation or overestimation, respectively, of the heat and mass transfer. Following Siegele et al. [53], a simplified methodology that balance accuracy and computational cost, is introduced in this work. This method provides an effective way to account for the contribution of the cross-flow section in terms of both heat and mass transfer, helping to reduce the cumulative modeling error in the context

of integrated HVAC system simulations.

The method simply consist in calculating an equivalent cross-counter effectiveness ($\varepsilon_{s,cc}$ and $\varepsilon_{x,cc}$), starting from the effectiveness values of the pure counter-flow ($\varepsilon_{s,count}$ and $\varepsilon_{x,count}$) and pure cross-flow ($\varepsilon_{s,cross}$ and $\varepsilon_{x,cross}$) configuration, calculated assuming the entire surface operates under that specific flow arrangement. The overall effectiveness is then estimated through a weighted average, using the heat transfer area (A_{count}, A_{cross}) associated with each flow pattern:

$$\varepsilon_{s,cc} = \frac{A_{count}\,\varepsilon_{s,count} + A_{cross}\,\varepsilon_{s,cross}}{A_{count} + A_{cross}}, \qquad \varepsilon_{x,cc} = \frac{A_{count}\,\varepsilon_{x,count} + A_{cross}\,\varepsilon_{x,cross}}{A_{count} + A_{cross}} \tag{3.47}$$

For the cross-flow exchange the effectivenesses are:

$$\begin{aligned} \varepsilon_{s,cross} &= 1 - \exp\left[\frac{\exp\left(-C_r\,\mathrm{NTU}_{s,cross}^{0.78}\right) - 1}{C_r\,\mathrm{NTU}_{s,cross}^{-0.22}}\right], \\ \varepsilon_{x,cross} &= 1 - \exp\left[\frac{\exp\left(-R\,\mathrm{NTU}_{x,cross}^{0.78}\right) - 1}{R\,\mathrm{NTU}_{x,cross}^{-0.22}}\right] \end{aligned} \tag{3.48}$$

In the previous equations, the NTUs are calculated with respect to the heat and mass transfer coefficients associated with the respective configuration.

Observations on HRV modeling

The model of the sensible-only recovery exchanger (HRV) differs from that of the enthalpy recovery exchanger (ERV) for two main aspects. The first difference concerns moisture effectiveness, which in the case of the HRV is set to zero, since the membrane is impermeable to water vapor and no moisture exchange occurs between the two air streams. The second difference is the inclusion of a wall condensation model. Unlike enthalpy exchangers, where the membrane permeability prevents wall condensation under most operating conditions, condensation is a common and significant phenomenon in sensible-only heat exchangers. Accurately accounting for this effect is therefore essential. Neglecting it may lead to substantial errors in the predicted heat transfer, due to the unaccounted latent heat, and to inaccurate estimation of the outlet air moisture content.

A commonly adopted formulation to estimate the condensation rate on a surface held at uniform temperature is reported in [62]. In that framework, the condensation rate ($\dot{m}_{w,cond}$) is expressed as:

$$\dot{m}_{w,cond} = |\dot{m}_{dry}|(W_{in} - W_{wall})\left[1 - \exp\left(-\frac{\alpha_m A}{|\dot{m}|}\right)\right] \tag{3.49}$$

where $|\dot{m}_{dry}|$ is absolute value of the mass flow rate of dry air per side, A is the surface

area, $\dot{m}$ is the mass flow rate, α_m is the average mass transfer coefficient, W_{in} is the inlet humidity ratio and W_{wall} is the humidity ratio at the wall, defined as:

$$W_{wall} = \min(W_{in}, W_{sat,wall}) \tag{3.50}$$

with $W_{sat,wall}$ the saturation humidity ratio based on wall temperature. The min function in Equation (3.50) provides the switch between "dry" and "wet" heat transfer:

- when wall temperature is above the dew point, then $W_{sat,wall} > W_{in}$, therefore, condensation is not occurring;
- when wall temperature is below the dew point, then $W_{sat,wall} < W_{in}$, therefore, condensation is occurring.

Although this formulation is appropriate for surfaces maintained at a uniform temperature, it cannot be directly applied to sensible-only heat recovery exchangers. The combination of low wall thermal conductivity, relatively large wall thickness, and the temperature variations of both air streams along the device causes the mean wall temperature to vary significantly with the flow direction. Since the condensation rate depends strongly on the local wall temperature, replacing this spatial distribution with a single average value, as implicitly required by Equation (3.49), leads to a severe underprediction of the condensate.

To address this limitation, a linear variation of the wall mean temperature from the outdoor to the indoor side is assumed. This effectively corresponds to adopting the Uniform Wall Heat Flux (UWF) hypothesis under fully developed flow conditions, for which the energy balance yields a linear wall temperature profile along the exchanger length. To capture this spatial variation, the exchanger is discretized in segments (Figure 3.3). For each segment, a local mean wall temperature is extracted from the linear profile, and the corresponding wall saturation humidity ratio is evaluated. Equation (3.49) is then applied segment by segment, while the inlet humidity ratio is updated step by step to account for the progressive removal of water vapor. The condensation contributions from all segments are finally summed to obtain the total condensation rate ($\dot{m}^W_{cond}$) and the associated latent heat flow rate ($\dot{Q}_l$) and liquid water energy removed (Φ^W_{cond}):

$$\dot{m}^W_{cond} = \sum_{i=1}^{n_{seg}} \dot{m}_{w,cond,i}, \quad \dot{Q}_l = \sum_{i=1}^{n_{seg}} \dot{m}_{w,cond,i} \Delta h_{vap_i}, \quad \Phi^W_{cond} = \sum_{i=1}^{n_{seg}} \dot{m}_{w,cond,i} h_{wl,cond,i} \tag{3.51}$$

where $\Delta h_{vap,i}$ is the latent heat of vaporization and $h_{wl,cond,i}$ is the removed liquid water specific enthalpy both evaluated at the average local wall temperatures.

Different condensation rates along the exchanger length are generally expected and may lead to a non-uniform wall heat flux, so that the UWF assumption is not strictly valid. However, since the latent heat contribution usually represents only a small fraction of the

total heat transfer, approximating it as uniformly distributed along the exchanger length (thus preserving the validity of the UWF assumption) provides a practical compromise. This assumption preserves computational efficiency and model simplicity while maintaining adequate physical accuracy.

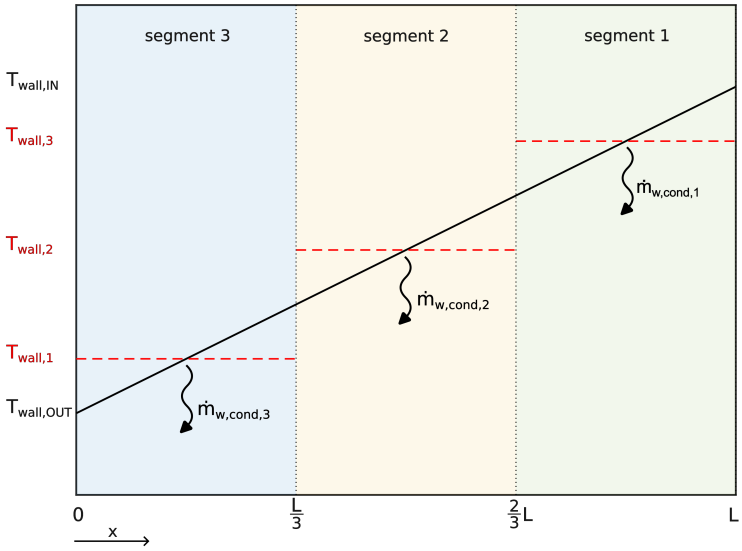

Figure 3.3: Discretization of the average wall temperature profile using thee segments (winter condition).

With reference to Figure 3.2, the average wall temperatures on the indoor side (IN) and outdoor side (OUT) of the exchanger are approximated as:

$$T_{wall,IN} \approx \frac{T_{11}\alpha_{EE} + T_{22}\alpha_{OS}}{\alpha_{EE} + \alpha_{OS}}, \qquad T_{wall,OUT} \approx \frac{T_{12}\alpha_{EE} + T_{21}\alpha_{EE}}{\alpha_{EE} + \alpha_{OS}} \tag{3.52}$$

and since $T_{wall,IN}$ and $T_{wall,OUT}$ are calculated from the outlet temperatures of the two sides, they are also influenced by the heat transfer mechanism. In the above equations, the mean convective heat transfer coefficients (α_{EE} and α_{OS}) are obtained as a weighted average of the contributions from the counter-flow and cross-flow portions of the surface, as for the overall effectiveness:

$$\alpha_{EE} = \frac{A_{count}\,\alpha_{EE,count} + A_{cross}\,\alpha_{EE,cross}}{A_{count} + A_{cross}} \tag{3.53}$$

$$\alpha_{OS} = \frac{A_{count}\,\alpha_{OS,count} + A_{cross}\,\alpha_{OS,cross}}{A_{count} + A_{cross}} \tag{3.54}$$

At steady state, the overall total exchanged heat flow rate between the two control volume is:

$$\dot{Q}^{std} = \dot{Q}_s + \dot{Q}_{l,EE} - \dot{Q}_{l,OS} \tag{3.55}$$

where $\dot{Q}_s$ is the predicted sensible heat flow rate by the effectiveness-NTU method, $\dot{Q}_{l,EE}$

is the latent heat flow rate due to condensation that occurs on the EE side and $\dot{Q}_{l,OS}$ is the latent heat flow rate due to condensation that occurs on the OS side.

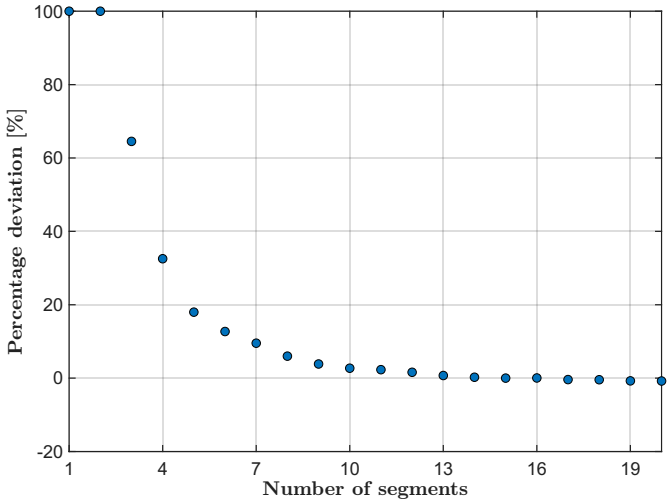

Figure 3.4: Convergence of the latent heat flow rate in the HRV model.

As with all discrete models, also in this case a convergence is expected by increasing the number of segments. Figure 3.4 shows the convergence of the latent heat flow rate as a function of the number of segments. The results show that a discretization into ten segments is, in this case, sufficient to achieve a good approximation of the total latent heat flow rate, with deviation below 3% compared to the converged value. The above convergence test is made by simulating the following typical winter condition:

- $T_{ETA} = 22°\text{C}$, $RH_{ETA} = 40\%$, $\dot{m}_{ETA} = 400$ kg hr^{-1}
- $T_{ODA} = 2°\text{C}$, $RH_{ODA} = 70\%$, $\dot{m}_{ODA} = 400$ kg hr^{-1}

Re-evaporation of the condensed water

During winter operation, when warm and humid indoor air flows through the exhaust side of a sensible heat recovery exchanger, water vapor may condense on the cold surface of the separating wall. If the exchanger has limited drainage capability, part of the condensate tends to accumulate and remain temporarily retained within the channels instead of being efficiently drained away. This retained water can subsequently re-evaporate due to the heat transferred from the adjacent warm air stream or the wall itself, even under nearly steady operating conditions. The re-evaporation phenomenon alters the local humidity temperature distributions as well as the latent heat transfer due to wall condensation. Although its overall magnitude is generally small, insufficient drainage can enhance re-evaporation effects and lead to measurable deviations in the outlet air temperature and humidity, in both sides of the exchanger.

In the present work, the phenomenon is represented through a simplified, lumped formulation that preserves overall energy and mass balance without introducing additional spatial resolution or transient states. The effective condensate flow rate is simply reduced by a factor (f_e) accounting for the portion of condensed water that is assumed to re-evaporate:

$$\dot{m}^W_{cond,eff} = (1 - f_e)\dot{m}^W_{cond} \tag{3.56}$$

Consequently, both the associated latent heat flow rate ($\dot{Q}_l$) and the energy removed as liquid water (Φ^W_{cond}) are scaled by the same term $(1 - f_e)$. This approach provides a computationally efficient way of representing the partial re-evaporation of condensate while maintaining consistency with the global energy balance of the system; however, it implicitly assumes that the re-evaporated fraction uniformly affects the exhaust-side thermodynamic state, thereby neglecting localized or transient phenomena such as film accumulation, uneven wetting, or delayed moisture release.

The parameter f_e represents the fraction of condensate assumed to re-evaporate and was calibrated using certified laboratory data presented in Section 5.4. A value of $f_e = 0.2$ was found to provide the best agreement for the case under analysis.

Transient operations

Under transient operating conditions, the total heat flow rates entering the two moist-air finite volumes ("EE" and "OS") can differ. This discrepancy arises from the thermal inertia of the heat exchanger wall, which temporarily stores or releases energy. As a result, a perturbation on one side of the exchanger is not instantaneously transferred to the other side. To represent this behavior, a two-node thermal model of the wall is adopted. The wall is conceptually divided into two thermal masses, each representing the portion of wall material adjacent to one moist-air finite volume. These two wall nodes are connected by conductive heat transfer through the wall material. The labels "EE" and "OS" simply indicate the side of the exchanger to which each wall node is adjacent.

The energy balances for the wall nodes are:

$$\frac{M_{wall}\, c_{wall}}{2} \frac{dT_{wall,EE}}{dt} = -\dot{Q}_{H,EE} - \dot{Q}^{std} \tag{3.57}$$

$$\frac{M_{wall}\, c_{wall}}{2} \frac{dT_{wall,OS}}{dt} = -\dot{Q}_{H,OS} + \dot{Q}^{std} \tag{3.58}$$

where M_{wall} is the total wall mass, c_{wall} is the specific heat capacity of the wall material, and $T_{wall,EE}$ and $T_{wall,OS}$ are the temperatures of the wall portions adjacent to EE and OS, respectively.

The terms $\dot{Q}_{H,EE}$ and $\dot{Q}_{H,OS}$ represent the convective heat exchange between the wall

surface and the moist-air stream in each finite volume:

$$\dot{Q}_{H,EE} = \alpha_{EE} A_{EE} \left(T_{wall,EE} - T_{EE} \right) \tag{3.59}$$

$$\dot{Q}_{H,OS} = \alpha_{OS} A_{OS} \left(T_{wall,OS} - T_{OS} \right) \tag{3.60}$$

where A_{EE} and A_{OS} are the heat transfer surface areas on each side, and T_{EE} and T_{OS} are the average bulk air temperatures in each finite volume, obtained as the arithmetic mean of the corresponding inlet and outlet temperatures. The term $\dot{Q}^{std}$ denotes the steady-state net conductive heat transfer rate through the wall between the two nodes, as calculated in the previous sections. Its sign is taken as positive when heat flows from the wall node adjacent to "EE" to the wall node adjacent to "OS".

The average wall temperature of the membrane ($\overline{T}_m$) used for moisture transfer calculations, in the enthalpy recovery exchanger model, can now be simply calculated as the arithmetic mean of the two wall node temperatures:

$$\overline{T}_m = \frac{T_{wall,EE} + T_{wall,OS}}{2} \tag{3.61}$$

At steady state, no energy is stored in the wall, and the model reduces to:

$$\dot{Q}_{H,EE} = \dot{Q}_{H,OS} = \dot{Q}^{std} \tag{3.62}$$

Heat and mass transfer decoupling in the HRV

In the proposed modelling framework, heat and mass transfer are treated as coupled and mutually dependent processes. The global exchange of sensible heat between the two moist-air streams is first computed using the standard effectiveness-NTU method. Based on this heat transfer rate, the outlet conditions of both streams are updated and an average wall temperature profile is estimated under the assumption of a linear temperature distribution. This wall profile is then used to evaluate the overall condensate formation on each side, from which the associated latent heat is calculated. Afterwards, the latent contribution is added to the sensible part to obtain the total heat transfer, and the outlet states of the streams are recalculated accordingly. The wall temperature profile and the sensible heat transfer (since the averages heat transfer coefficients varies) are subsequently updated, as prescribed by the governing equations, and the entire procedure is repeated iteratively until convergence of wall temperature, condensate mass flow, and outlet conditions in general. In this way, the model consistently captures the inherent interdependence between sensible and latent heat transfer.

A reasonable simplification in this context is to evaluate the convective heat transfer coefficients at the inlet conditions of the two air streams. Since property variations along the flow are relatively small, they do not significantly affect the heat transfer coefficients

or, consequently, the model predictions. Moreover, for hydrodynamically and thermally fully developed laminar flow, the Nusselt number is constant for a given geometry and thermal boundary condition, so the heat transfer coefficients depend only on the geometry, thus further justifying this simplification. Under this assumption, only the latent heat calculation remains iterative and dependent on the sensible part, thereby substantially reducing the computational cost of the model.

3.2.2. Fans and other auxilary components

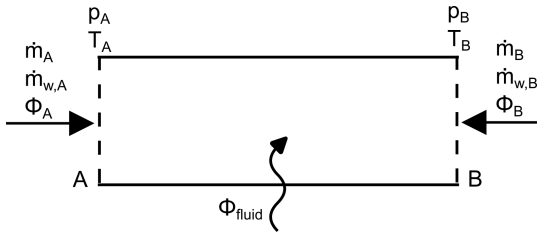

Figure 3.5: Control volume for the fan component.

Fans are modeled as one-dimensional, quasi-steady-state devices, with constant mass flow rate. Their behavior is characterized by the pressure rise (Δp_{fan}) and the electric power consumption (PC_{fan}), both expressed as functions of the volumetric flow rate ($\dot{V}$) and the fan rotational speed (ω). The pressure rise, defined as the difference between outlet and inlet pressures, is calculated according to the classical similarity laws:

$$p_B - p_A = \Delta p_{ref}(\dot{V}_{ref}) \left(\frac{\overline{\rho}}{\rho_{ref}} \right) \left(\frac{\omega}{\omega_{ref}} \right)^2 \tag{3.63}$$

and analogously, the electric power consumption is given by:

$$PC_{fan} = PC_{ref}(\dot{V}_{ref}) \left(\frac{\overline{\rho}}{\rho_{ref}} \right) \left(\frac{\omega}{\omega_{ref}} \right)^3 \tag{3.64}$$

where $\Delta p_{ref}(\dot{V}_{ref}(\omega_{ref}))$ is the reference pressure rise at the reference volumetric flow rate $\dot{V}_{ref}(\omega_{ref})$, $PC_{ref}(\dot{V}_{ref})$ is the reference power consumption at $\dot{V}_{ref}(\omega_{ref})$, ω_{ref} is the reference rotational speed, ρ_{ref} is the reference air density and $\overline{\rho}$ is the average air density between inlet and outlet. The reference pressure rise and power consumption is typically provided by the manufacturer in the form of a performance curve, which can be approximated using a polynomial fit or a piecewise linear function. The reference volumetric flow rate ($\dot{V}_{ref}$) is:

$$\dot{V}_{ref} = \dot{V} \left(\frac{\omega_{ref}}{\omega} \right) \tag{3.65}$$

with $\dot{V} = \frac{\dot{m}_A}{\rho_{out}}$ the actual volumetric flow rate and ρ_{out} the air density at the outlet. The

energy balance of the component is:

$$\Phi_A + \Phi_B + \Phi_{fluid} = 0, \qquad \Phi_{fluid} = \dot{V}(p_B - p_A) \tag{3.66}$$

while moist-air and vapor mass balances are:

$$\dot{m}_A + \dot{m}_B = 0, \qquad \dot{m}_{w,A} + \dot{m}_{w,B} = 0 \tag{3.67}$$

Considering the overall momentum balance of the moist air network, the system of equations is closed either by imposing the actual fan speed (ω) as a boundary condition, which represents the case of the additional OEA fan in the alternative MFRBV configuration, or by specifying the mass flow rate ($\dot{m}_A$) or volumetric flow rate ($\dot{V}$) through the fan, as in the case of the fans in the MVHR unit.

Other auxiliary components of the moist-air network, such as filters, the pre-heater, and the check valve, are modeled as one-dimensional lumped elements with a constant mass flow rate across the device. Their pressure drop is expressed through relations of the same form as Equation (3.18).

In the case of the electric pre-heater, an additional heat input term ($\dot{Q}_{in}$) is included in the energy balance to account for the thermal energy added to the fluid:

$$\Phi_A + \Phi_B + \dot{Q}_{in} = 0 \tag{3.68}$$

where $\dot{Q}_{in}$ is the rate of heat added to the fluid, and since the pre-heater is an electric device, the electric power consumption is approximately equal to the heat added to the fluid.

For the check valve, flow is allowed only from port A to port B. This is modeled by assigning a finite pressure loss for $\dot{m}_A > 0$, while for $\dot{m}_A < 0$ a pressure loss tending to infinity is imposed. To guarantee a smooth transition at flow reversal, a cubic Hermite polynomial centered at $\dot{m}_A = 0$ is applied.

3.2.3. T-junction

The T-junction is a component that allows to model the associated pressure losses derived from the merging or splitting of two moist air streams. In the model developed in this work, T-junctions are included only in the alternative MFRBV configuration, where they are used to connect the additional OEA line to the main air line.

The mixture mass conservation equation for the T-junction, referring to Figure 3.6, is expressed as:

$$\dot{m}_A + \dot{m}_B + \dot{m}_C = 0 \tag{3.69}$$

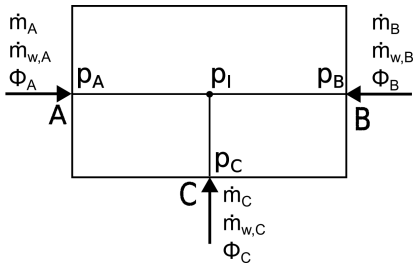

Figure 3.6: Control volume for the T-junction component.

and similarly for the water vapor:

$$\dot{m}_{w,A} + \dot{m}_{w,B} + \dot{m}_{w,C} = 0 \tag{3.70}$$

The energy balance for the component is given by:

$$\Phi_A + \Phi_B + \Phi_C = 0 \tag{3.71}$$

And finally the mechanical energy balances, which accounts for the pressure losses due to the flow configuration, are expressed as:

$$p_A - p_I = \frac{K_A}{(\rho_A + \rho_I)A_{\text{main}}^2}\,\dot{m}_A|\dot{m}_A| \tag{3.72}$$

$$p_B - p_I = \frac{K_B}{(\rho_B + \rho_I)A_{\text{main}}^2}\,\dot{m}_B|\dot{m}_B| \tag{3.73}$$

$$p_C - p_I = \frac{K_C}{(\rho_C + \rho_I)A_{\text{side}}^2}\,\dot{m}_C|\dot{m}_C| \tag{3.74}$$

where A_{main} is the main branch cross-section area (A-B) and A_{side} is the side branch area (C-I). The coefficients K_A, K_B, and K_C are empirical loss coefficients that depend on the specific geometry and flow configuration of the T-junction.

The loss coefficients are introduced to represent the pressure losses in the main and side branches of the junction. Their formulation is designed to automatically capture changes in the flow configuration within the component, such as transitions between diverging and converging flow at each port.

$$K_A = m_A^+\left(m_B^+ m_C^- \frac{K_{\text{main}}}{2} + m_B^- m_C^+ K_{\text{main}}\right) + m_A^-\left(m_B^+ m_C^+ K_{\text{main}} + m_B^- m_C^- \frac{K_{\text{main}}}{2}\right) \tag{3.75}$$

$$K_B = m_A^+\left(m_B^+ m_C^- \frac{K_{\text{main}}}{2} + m_B^- m_C^+ K_{\text{main}}\right) + m_A^-\left(m_B^+ m_C^+ K_{\text{main}} + m_B^- m_C^- \frac{K_{\text{main}}}{2}\right) \tag{3.76}$$

$$K_C = \left(m_A^+ m_B^- + m_A^- m_B^+\right)\left(m_C^+ K_{\text{side}} + m_C^- K_{\text{side}}\right) \tag{3.77}$$

Here:

- K_{main} is the loss coefficient for the main branch.
- K_{side} is the loss coefficient for the side branch.

Using correlations by Crane [104], the loss coefficients for the main and side branches can be calculated as:

$$K_{\text{main}} = 20 f_{t,\text{main}}, \qquad K_{\text{side}} = 60 f_{t,\text{side}} \tag{3.78}$$

where $f_{t,\text{main}}$ and $f_{t,\text{side}}$ are the friction factors for the main and side branches, respectively. These friction factors are determined, based on the nominal hydraulic diameter, as provided in Table 3.1.

The positive mass flow direction at each port is computed as:

$$m^{+}_{\text{port}} = \frac{1 + \tanh\left(\frac{4\dot{m}_{\text{port}}}{\dot{m}_{\text{thresh}}}\right)}{2}, \tag{3.79}$$

while the negative mass flow direction is given by:

$$m^{-}_{\text{port}} = \frac{1 - \tanh\left(\frac{4\dot{m}_{\text{port}}}{\dot{m}_{\text{thresh}}}\right)}{2}. \tag{3.80}$$

Here $\dot{m}_{\text{thresh}}$ represents a small reference threshold for the mass flow rate, that is used to ensure a smooth transition between the change in flow configuration and so pressure losses in the component. The use of Equations 3.75 to 3.77 allows for a continuous and differentiable representation of the pressure losses in the T-junction, and provides an automatic adjustment of the loss coefficients based on the actual flow directions and magnitudes at each port. Indeed, for example, in the case of converging flows to port B (i.e, $\dot{m}_A > 0$, $\dot{m}_B < 0$, $\dot{m}_C > 0$), the loss coefficients reduce to $K_A = K_{\text{main}}$, $K_B = 0$, and $K_C = K_{\text{side}}$, which are the expected values for this flow configuration.

Nominal size [in]	f_t
1/2	0.027
3/4	0.025
1	0.023
$1\frac{1}{4}$	0.022
$1\frac{1}{2}$	0.021
2	0.019
$2\frac{1}{2}$–3	0.018
4	0.017
5	0.016
6	0.015
8–10	0.014
12–16	0.013
18–24	0.012

Table 3.1: Friction factor vs nominal hydraulic diameter (inches), from Crane [104]

3.2.4. Fin and tube heat exchanger

3.2.4.1. Refrigerant finite volume

To develop a physically accurate yet computationally efficient model of moist air (MA) to two-phase flow (2P) heat exchanger, the refrigerant side is discretized into a sequence of finite control volumes (segments) along the main flow direction. This spatial discretization is a key modeling choice, as it allows for the local resolution of thermodynamic variables such as pressure, temperature, enthalpy, and vapor quality. In systems involving phase-change fluids, such as refrigerants in heat pumps, these quantities can vary significantly over short distances, due to evaporation and condensation. By dividing the flow path into smaller segments, the model can accurately capture the progression of phase change, determine the local flow regime (subcooled, two-phase, or superheated), and compute the associated pressure drops and heat transfer coefficients accordingly. This discretized approach enables the implementation of state-dependent correlations for frictional pressure losses and convective heat transfer, which are strongly influenced by the local thermodynamic state and flow conditions. For instance, two-phase pressure drops and heat transfer are highly non-linear and depend on parameters such as vapor quality, mass flux, and channel geometry. A lumped-parameter model would be unable to capture these local effects, leading to inaccurate predictions, especially under transient conditions or when the working fluid undergoes partial phase changes. Each segment is treated as a fixed volume (control volume) of fluid in which the mass, momentum, and energy balance equations are solved. To simplify the model and reduce computational cost, a one-dimensional flow assumption is made, focusing on axial variations and neglecting radial and circumferential gradients. In addition, the model explicitly accounts for the dynamic compressibility and thermal inertia of the refrigerant as well as

the thermal inertia of the heat exchanger wall. These properties are especially important in transient simulations, where rapid changes of the fluid state variables occur. Accurately capturing these dynamic responses is essential for predicting the time-dependent behavior of the real system.

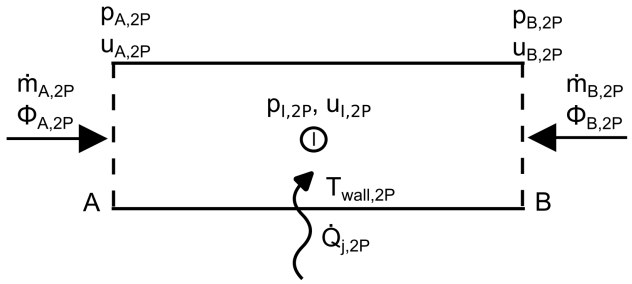

Figure 3.7: Finite volume for the refrigerant stream.

Figure 3.7 illustrates the refrigerant finite volume, showing the positive direction of relevant variables: mass flow rates $\dot{\mathbf{m}}$, total energy $\mathbf{\Phi}$ (sum of enthalpy and kinetic energy), and $\dot{\mathbf{Q}}_\mathbf{j}$ is the total heat flow rate that enters in the segment. An internal node, labeled as '**I**', is defined within the segment, and the state variables describing the fluid's state (p and u) of the control volume are associated with this node.

Mass balance

In heat pump systems involving phase-changing refrigerants, local variations in pressure and enthalpy can cause also significant density changes, especially during phase transitions. For this reason, dynamic compressibility is taken into account, allowing the mass conservation equation to reflect transient mass accumulation within the segment. Consequently, the inlet and outlet mass flow rates may differ during dynamic conditions. Neglecting this effect would lead to inaccurate predictions of the system's transient behavior. The mass conservation equation for the refrigerant, under the one-dimensional flow assumption, in a segment, reads as:

$$\frac{dM_{2P}}{dt} = \dot{m}_{A,2P} + \dot{m}_{B,2P} \tag{3.81}$$

where $M_{2P} = \rho_{I,2P} V_{2P}$ is the refrigerant mass in the control volume. Applying then the chain rule to express the time derivative of the fluid volume density ($\rho_{I,2P}$), as a function of pressure and specific internal energy, an expression for the rate of mass accumulation within the segment is obtained:

$$\frac{dM_{2P}}{dt} = \frac{d\rho_{I,2P}}{dt} V_{2P} = \left[\left(\frac{\partial \rho_{I,2P}}{\partial p_{I,2P}} \right)_{u_{I,2P}} \dot{p}_{I,2P} + \left(\frac{\partial \rho_{I,2P}}{\partial u_{I,2P}} \right)_{p_{I,2P}} \dot{u}_{I,2P} \right] V_{2P} \tag{3.82}$$

The first term in the square brackets describes how the internal fluid density varies with respect to pressure at constant specific internal energy, and the second term describes how the fluid density varies with respect to specific internal energy at constant pressure. The partial derivatives of density with respect to pressure and specific internal energy in Equation (3.82) are treated as state properties of the two-phase fluid domain, and, as such, are calculated *a priori* and conveniently stored in a lookup table.

Energy balance

The energy conservation equation for the refrigerant control volume is:

$$\frac{d(M_{2P}u_{I,2P})}{dt} = \Phi_{A,2P} + \Phi_{B,2P} + \dot{Q}_{j,2P} \tag{3.83}$$

Applying the product rule to the left-hand side of Equation (3.83), the final energy balance equation of the segment becomes:

$$\boxed{M_{2P}\frac{du_{I,2P}}{dt} + u_{I,2P}\left(\dot{m}_{A,2P} + \dot{m}_{B,2P}\right) = \Phi_{A,2P} + \Phi_{B,2P} + \dot{Q}_{j,2P}} \tag{3.84}$$

Heat transfer from the wall to the fluid is expressed by Newton's law of cooling:

$$\dot{Q}_{j,2P} = \alpha_{2P}A_{2P}\left(T_{wall,2P} - T_{I,2P}\right) \tag{3.85}$$

where A_{2P} is the segment surface area at the refrigerant side. The refrigerant heat transfer coefficient (α_{2P}) strongly depends on the fluid state, therefore the following specific approach is used to improve the accuracy of the results, especially for transitional segments (i.e., segments where phase change occurs).

If the flow is in a single-phase state (subcooled liquid or superheated vapor):

$$\alpha_{2P} = \frac{k_{I,2P}\mathrm{Nu}_{S,2P}}{D_h} \tag{3.86}$$

where $k_{I,2P}$ is the fluid's thermal conductivity. The Nusselt number (Nu_{2P}) is computed in this case using the Gnielinski correlation [105]:

$$\mathrm{Nu}_{s,2P} = \frac{\frac{f}{8}(\mathrm{Re}_{I,2P} - 1000)\mathrm{Pr}_{I,2P}}{1 + 12.7\sqrt{\frac{f}{8}}(\mathrm{Pr}_{I,2P}^{2/3} - 1)} \tag{3.87}$$

The Reynolds number $\mathrm{Re}_{I,2P} = \frac{|\dot{m}_{avg}|D_h}{S_{2P}\mu_{I,2P}}$ depends on the average mass flow rate $\dot{m}_{avg} = \frac{\dot{m}_{A,2P} - \dot{m}_{B,2P}}{2}$ passing through the segment.

On the other hand, if the flow is in a two-phase state, the heat transfer coefficient is:

$$\alpha_{2P} = \frac{k^*_{SL,2P}\mathrm{Nu}_{M,2P}}{D_h} \tag{3.88}$$

The thermal conductivity of the saturated liquid ($k^*_{SL,2P}$) is used in the above formula, since heat transfer in two-phase flow is typically dominated by the liquid phase, which maintains contact with the tube wall and governs the convective heat transfer mechanism. The Nusselt number of the two-phase flow mixture is computed by means of the Cavallini-Zecchin equation [106]:

$$\mathrm{Nu}_{M,2P} = 0.05\left[\left(1 - x_I + x_I\sqrt{\frac{\nu_{SV}}{\nu_{SL}}}\right)\mathrm{Re}_{SL}\right]^{0.08}\mathrm{Pr}_{SL}^{0.33} \tag{3.89}$$

Since the previous correlation generally applies to condensation, a more realistic and accurate simulation of evaporation can be achieved by employing a dedicated correlation for the specific phase-change mechanism to evaluate the Nusselt number of the two-phase mixture. An example of a suitable correlation is the one proposed by Shah [107]:

$$\mathrm{Nu}_{2P} = 1.8\frac{0.023\left[\mathrm{Re}_{SL}(1-x_I)\right]^{0.8}\mathrm{Pr}_{SL}^{0.4}}{\left[\left(\frac{1}{x_I}-1\right)^{0.8}\left(\frac{\nu_{SL}}{\nu_{SV}}\right)^{0.5}\right]^{0.8}} \tag{3.90}$$

where $\mathrm{Re}_{SL} = \frac{|\dot{m}_{avg}|D_h}{S_{2P}\mu_{SL}}$ is the Reynolds number of the saturated liquid, calculated using the dynamic viscosity of the saturated liquid (μ_{SL}), ν_{SV} and ν_{SL} are the specific volume of the saturated vapor and liquid respectively, and (Pr_{SL}) is the Prandtl number of the saturated liquid. Saturated fluid properties are all evaluated at the fluid volume pressure ($p_{I,2P}$). Although heat transfer correlations for calculating the Nusselt number in two-phase flow

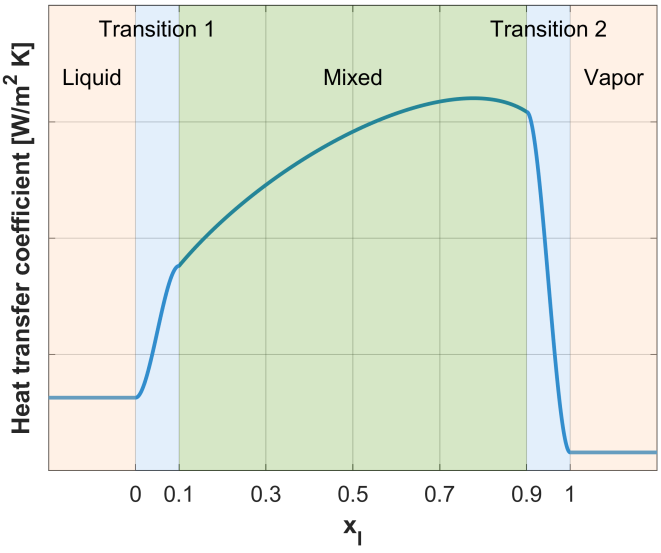

Figure 3.8: Blending of the heat transfer coefficient.

are generally applicable to single-phase conditions (except Shah, which is undefined at extreme vapor quality values), the results they provide often exhibit significant errors, as demonstrated by Sánta [108]. Therefore, when the fluid volume is entirely in the liquid or vapor phase, a more accurate single-phase heat transfer correlation (such as the

Gnielinski correlation) can be used. However, this introduces a discontinuity in the convective heat transfer coefficient, leading to numerical challenges. To mitigate this issue, a blending function can be used to ensure a smooth transition between the two coefficients. This requires defining transition zones where the blending function is applied. In this work, as shown in Figure 3.8, a cubic Hermite spline is used as the blending function over the vapor quality ranges of 0 to 0.1 and 0.9 to 1. Within these transition regions, the resulting convective heat transfer coefficient is defined as:

$$\begin{aligned}\alpha = &\left[1-3\left(\frac{x_I-x_1}{x_2-x_1}\right)^2-2\left(\frac{x_I-x_1}{x_2-x_1}\right)^3\right]\alpha_{2P}(x_1)\\ &+\left[3\left(\frac{x_I-x_1}{x_2-x_1}\right)^2-2\left(\frac{x_I-x_1}{x_2-x_1}\right)^3\right]\alpha_{2P}(x_2)\end{aligned} \tag{3.91}$$

where x_1 and x_2 represent the extreme of vapor qualities in the transition region (e.g., 0 and 0.1 in case of the first transition region and 0.9 and 1 for the second), while $\alpha_{2P}(x_1)$ and $\alpha_{2P}(x_2)$ are the heat transfer coefficients evaluated using the single-phase correlation or the two-phase correlation, associated with x_1 and x_2.

3.2.4.2. Mechanical energy balance

Since the inlet and outlet mass flow rates may differ during dynamic conditions due to mass accumulation, the segment itself is subdivided into two parts, and the pressure losses are calculated separately for each section, assuming the flow rates in the two sections are $\dot{m}_{A,2P}$ and $\dot{m}_{B,2P}$, respectively. For the half adjacent to port side (A or B) the mechanical energy balance equation is:

$$p_{i,2P}-p_{I,2P}=\frac{\dot{m}_{i,2P}}{S_{2P}}\left|\frac{\dot{m}_{i,2P}}{S_{2P}}\left(v_{I,2P}-v_{i,2P}\right)\right|+\Delta p_{visc,i,2P} \tag{3.92}$$

The first terms on the right-hand side represent momentum flux losses from mass entering at port i and the second term the viscous friction losses (Δp_{visc}) within the first or second half of the segment. Here, S_{2P} is the segment cross-sectional area at the refrigerant side, p the pressure and v the specific fluid volume. As for the heat transfer coefficient, viscous friction losses may vary significantly depending on the fluid state [109]. Also in this case, the discretization approach allows for a more precise estimation of the total pressure drop.

In the context of phase-change flows, two distinct modeling approaches are commonly found in the literature: the homogeneous flow model and the separated flow model.

The homogeneous flow model assumes that the liquid and vapor phases are perfectly mixed and move at the same velocity, effectively treating the two-phase mixture as a single pseudo-fluid with average properties. In contrast, the separated flow model treats the liquid and vapor phases as distinct, each with its own velocity and flow characteristics,

requiring more complex modeling techniques.

In case of the homogeneous model, viscous friction losses can be readily evaluated using the classical Darcy-Weisbach equation as follows:

$$\Delta p_{visc,i,2P} = \frac{\dot{m}_{i,2P}|\dot{m}_{i,2P}|f_{i,2P}L_{eff}v_{I,2P}}{4D_{h,2P}S_{2P}} \tag{3.93}$$

L_{eff} is the effective length of the segment (sum of the geometric length plus an aggregate equivalent length that accounts for the local resistance of the segment), $D_{h,2P}$ is the hydraulic diameter. Where the Darcy friction factors $f_{i,2P}$ can be calculated, for example, using the Haaland correlation [110]:

$$f_{i,2P} = \left\{-1.8\log\left[\left(\frac{6.9}{\mathrm{Re}_{i,2P}}\right)+\left(\frac{\varepsilon_r}{3.7}\right)^{1.11}\right]\right\}^{-2} \tag{3.94}$$

where ε_r is the relative roughness of the pipe and $\mathrm{Re}_{i,2P} = \frac{|\dot{m}_{i,2P}|D_h}{S_{2P}\mu_{i,2P}}$ the Reynolds number of the equivalent single-phase flow at the respective port.

In contrast, under the separated flow model, viscous pressure losses are often evaluated using the Lockhart-Martinelli correlation [111]:

$$\Delta p_{visc,i,2P} = \phi_{SL}^2 \Delta p_{SL} \tag{3.95}$$

where ϕ_{SL}^2 is the two-phase frictional multiplier for the liquid phase, defined as:

$$\phi_{SL}^2 = 1 + \frac{K}{X} + \frac{1}{X^2} \tag{3.96}$$

$X^2 = \frac{\Delta p_{SL}}{\Delta p_{SV}}$ is the ratio between single-phase liquid (Δp_{SL}) and vapor (Δp_{SV}) pressure drops, better known as the Lockhart-Martinelli parameter. K is the Chisholm parameter, a factor used to account for the interfacial pressure drop between the liquid and gas phases, determined based on the flow regimes of the liquid and gas phases:

$$K = \begin{cases} 5 & \text{for } \mathrm{Re}_{SL}^* < 1500 \text{ and } \mathrm{Re}_{SV}^* < 1500 \\ 10 & \text{for } \mathrm{Re}_{SL}^* \geq 1500 \text{ and } \mathrm{Re}_{SV}^* < 1500 \\ 12 & \text{for } \mathrm{Re}_{SL}^* < 1500 \text{ and } \mathrm{Re}_{SV}^* \geq 1500 \\ 20 & \text{for } \mathrm{Re}_{SL}^* \geq 1500 \text{ and } \mathrm{Re}_{SV}^* \geq 1500 \end{cases} \tag{3.97}$$

The pressure drops Δp_k of each individual phase are calculated, again, using the Darcy-Weisbach equation:

$$\Delta p_k = \frac{\dot{m}_{i,k}|\dot{m}_{i,k}|f_{i,k}L_{eff}v_{I,k}}{4D_h S_{2P}} \tag{3.98}$$

$\dot{m}_{i,k}$ is the mass flow rate of the k-th phase (i.e., liquid or vapor) entering the i-th port. For

instance, in the case of the vapor phase, it is expressed as: $\dot{m}_{i,SV} = \dot{m}_i x_i$ where x_i is the inlet vapor quality at port i. $f_{i,k} = \left\{-1.8\log\left[\left(\frac{6.9}{\mathrm{Re}^*_{i,k}}\right)+\left(\frac{\varepsilon_r}{3.7}\right)^{1.11}\right]\right\}^{-2}$ is the friction factor of the k-th phase with the phase Reynolds number defined as $\mathrm{Re}^*_{i,k} = \frac{|\dot{m}_{i,k}|D_h}{S_{2P}\mu_{I,k}}$, and $v_{I,k}$, $\mu_{I,k}$ are the specific volume and dynamic viscosity of the k-th phase at saturation, respectively, evaluated at the fluid volume pressure $p_{I,2P}$. Similarly to the approach used for the heat transfer coefficient in the previous section, the separated flow model, specifically the Lockhart-Martinelli correlation, remains applicable across the full vapor quality range. However, as observed in [109] a simpler homogeneous flow model may yield more accurate results at the vapor quality extremes. This is because the assumption of a well-mixed flow becomes increasingly valid as the flow approaches these limits. To improve accuracy, the separated flow model is therefore blended with the homogeneous model in the transition regions (vapor quality between 0-0.1 and 0.9-1), following Equation (3.91), as was done for the heat transfer coefficient. If the fluid volume is in a subcooled liquid or superheated vapor state (i.e., $x_i = 0$ or $x_i = 1$), viscous pressure losses are instead evaluated using the homogeneous model, Eq. (3.93), which corresponds to the conventional approach for modeling viscous friction losses in single-phase flows.

3.2.4.3. Moist air side

On the moist-air side, a finite volume analogous to the one on the 'Recovery exchanger' section is defined. The same positive directions for mass flow and energy flow rates, shown in Figure 3.1, are adopted for this control volume.

The net flow rates in this case are defined as:

$$\text{Total mass:} \quad \dot{m}_{net,MA} = \dot{m}_{A,MA} + \dot{m}_{B,MA} - \dot{m}_{cond} \tag{3.99}$$

$$\text{Water mass:} \quad \dot{m}_{w,net,MA} = \dot{m}_{w,A} + \dot{m}_{w,B} - \dot{m}_{cond} \tag{3.100}$$

$$\text{Energy:} \quad \Phi_{net,MA} = \Phi_{A,MA} + \Phi_{B,MA} + \dot{Q}_{j,MA} - \Phi_{cond} \tag{3.101}$$

The mixture conservation equations for each segment on the moist air side is then given by:

$$\left(\frac{1}{p_{I,MA}}\frac{dp_{I,MA}}{dt} - \frac{1}{T_{I,MA}}\frac{dT_{I,MA}}{dt}\right)\rho_{I,MA}V_{MA} + \frac{R_{dry}-R_w}{R_{I,MA}}\left(\dot{m}_{w,net} - x_{w,I,MA}\dot{m}_{net,MA}\right) = \dot{m}_{net,MA} \tag{3.102}$$

the water mass conservation equation is:

$$\frac{dx_{w,I,MA}}{dt}\rho_I V_{MA} + x_{w,I}\dot{m}_{net,MA} = \dot{m}_{w,net,MA} \tag{3.103}$$

the energy conservation equations is:

$$\begin{aligned}&\rho_{I,MA}(c_{p,I,MA}-R_{I,MA})V_{MA}\frac{dT_{I,MA}}{dt}\\&+(u_{w,I,MA}-u_{dry,I,MA})(\dot{m}_{w,net,MA}-x_{w,I,MA}\dot{m}_{net,MA})\\&+u_{I,MA}\dot{m}_{net,MA}=\Phi_{net,MA}\end{aligned} \tag{3.104}$$

and finally the air side pressure loss across each segment (Δp_{MA}), is calculated using the Kays and London equation [112]:

$$\Delta p_{j,MA}=\frac{G_{MA}^2}{2\rho_{in,MA}}\left[f_{MA}\frac{A_0}{A_c}\frac{\rho_{in,MA}}{\rho_{avg,MA}}+(1+\sigma^2)\left(\frac{\rho_{in,MA}}{\rho_{out,MA}}-1\right)\right] \tag{3.105}$$

where G_{MA} is the moist air mass flux per segment ($G_{MA}=\dot{m}_{in,MA}/A_c$), $\rho_{in,MA}$ is the segment inlet air density, $\rho_{out,MA}$ is segment outlet air density, $\rho_{avg,MA}$ is their arithmetic mean, σ is the segment ratio of the minimum free flow area (A_c) to the segment heat exchange frontal-area and A_0 is the total segment surface area on the air side. The segment moist air Fanning friction factor ($\tilde{f}_{MA}$) is obtained, from the correlations of Wang for plain [113] or louvered fins [114]. Here for brevity is reported only the correlation for plain finned tubes:

$$\tilde{f}_{MA}=0.0267\,\mathrm{Re}_{D_{c,MA}}^{F1}\left(\frac{P_t}{P_l}\right)^{F2}\left(\frac{F_p}{D_c}\right)^{F3} \tag{3.106}$$

where P_t is the transverse tube pitch, P_l is the longitudinal tube pitch, D_c is the tube outer diamater incremented by the fin thickness, F_p is the fin spacing, $\mathrm{Re}_{D_{c,MA}}$ is the segment Reynolds number based on D_c and $F1$,$F2$ and $F3$ are correlation parameters defined in the reference article [113].

Water vapor condensation

As outlined in the Recovery Exchanger model the total water vapor condensation on the moist air side ($\dot{m}_{cond}$, Φ_{cond}) is given by the sum of the volume condensation contribution ($\dot{m}_{cond}^V$, Φ_{cond}^V), calculated as in Section 3.2.1.1, and the wall surface condensation ($\dot{m}_{cond}^W$, Φ_{cond}^W), which accounts for the latent heat transfer. The rate of water vapor condensing on the wall surface for each segment is evaluated under the assumption of uniform wall temperature:

$$\dot{m}_{cond}^W=|\dot{m}_{dry,MA}|(W_{in,MA}-W_{wall,MA})\left\{1-\exp\left[-\frac{\alpha_{m,MA}(A_{tube,MA}+\eta_{fin,MA}A_{fin})}{|\dot{m}_{MA}|}\right]\right\} \tag{3.107}$$

with $A_{tube,MA}$ the tube surface area on the MA side and $A_{fin,MA}$ the fin surface area. This condensate is assumed to be removed from the segment control volume. The energy

term associated with the removal of this condensate is calculated as:

$$\Phi^{W}_{cond} = \dot{m}^{W}_{cond}\, h_{wl,cond} \tag{3.108}$$

where $h_{wl,cond}$ is the specific enthalpy of the removed liquid water evaluated at the average local wall temperature ($T_{wall,MA}$).

Heat and mass transfer coefficients

For each segment the Nusselt number on the moist air side is calculated using the standard Colburn equation:

$$\mathrm{Nu}_{MA} = j_{MA}\,\mathrm{Re}_{D_h,MA}\,\mathrm{Pr}^{1/3}_{MA} \tag{3.109}$$

with the Reynolds number ($\mathrm{Re}_{D_h,MA}$) based on the hydraulic diameter (D_h) of the minimum flow area of the segment. The segment moist air Colburn j-factor (j_{MA}) is obtained from the correlations of Wang for plain fin [115]:

for $N_r = 1$

$$j_{MA} = 0.108\,\mathrm{Re}^{-0.29}_{D_{c,MA}} \left(\frac{P_t}{P_l}\right)^{P1} \left(\frac{F_p}{D_c}\right)^{-1.084} \left(\frac{F_p}{D_h}\right)^{-0.786} \left(\frac{F_p}{P_t}\right)^{P2} \tag{3.110}$$

for $N_r \geq 1$

$$j_{MA} = 0.086\,\mathrm{Re}^{P3}_{D_{c,MA}}\, N_r^{P4} \left(\frac{F_p}{D_c}\right)^{P5} \left(\frac{F_p}{D_h}\right)^{P6} \left(\frac{F_p}{P_t}\right)^{-0.93} \tag{3.111}$$

where N_r is the numeber of tube row and $P1, \ldots, P6$ are correlation parameters defined in the reference article [113]. Similar correlations are also implemented to determine the j-factor for the case of louvered fin [114].

The segment heat transfer coefficient on the air side can now be easily determined from the definition of the Nusselt number:

$$\alpha_{MA} = \frac{\mathrm{Nu}_{MA}\, k_{MA}}{D_h} \tag{3.112}$$

Assuming the validity of the heat and mass transfer analogy, an estimation of the segment mass transfer coefficient is given by:

$$\alpha_{m,MA} = \frac{\alpha_{MA}}{c_{p,MA}\,\rho_{MA}\,\mathrm{Le}^{2/3}} \tag{3.113}$$

where Le=0.9 [103]. The heat and mass transfer coefficients are both evaluated at the internal node, that rapresents the state of the MA fluid volume.

3.2.4.4. Overall segment heat transfer

At steady state, the sensible heat flow rate ($\dot{Q}_{j,s}$) from the MA to the 2P side is computed for each segment using the effectiveness-NTU method:

$$\dot{Q}_{j,s} = \varepsilon C_{\min}\left(T_{in,MA} - T_{in,2P}\right) \tag{3.114}$$

where $C_{\min} = (\dot{m}c_p)_{\min}$ is the segment minimum heat capacity rate, $T_{in,MA}$ is the moist air inlet temperature and $T_{in,2P}$ is the segment two-phase fluid inlet temperature. The effectiveness (ε) is calculated according to the flow arrangement and in the case of a fin and tube heat exchangers, the flow arrangement is *cross-flow* with both fluids unmixed:

$$\varepsilon = \begin{cases} 1 - \dfrac{\exp\left(C_r\,\mathrm{NTU}^{0.78} - 1\right)}{C_r^{0.22}\exp\left(-\mathrm{NTU}\right)} & \text{if single-phase} \\ 1 - \exp\left(-\mathrm{NTU}\right) & \text{if two-phase} \end{cases} \tag{3.115}$$

with $C_r = \frac{C_{\min}}{C_{\max}}$ where $C_{\max}$ is the maximum heat capacity rate and $\mathrm{NTU} = \frac{1}{R_{tot}\,C_{\min}}$. The same blending approach based on the vapor quality of the fluid volume (x_I), previously introduced for heat transfer and momentum balance on the refrigerant side, is also applied here to ensure a smooth transition between single-phase and two-phase effectiveness. This treatment enhances the numerical robustness of the model and improves simulation accuracy in transitional segments (i.e., segments where $0 \leq x_I \leq 0.1$ or $0.9 \leq x_I \leq 1$).

The total thermal resistance between the two flows (R_{tot}) is:

$$R_{tot} = R_{conv,2P} + R_{wall} + R_{conv,MA} \tag{3.116}$$

Thermal resistances are defined as:

$$R_{conv,2P} = \frac{1}{\alpha_{2P} A_{tube,2P}}, \qquad R_{wall} = \frac{\ln\left(\frac{OD}{ID}\right)}{2\pi k_{tube} L_{tube}}, \qquad R_{conv,MA} = \frac{1}{\alpha_{MA}(A_{tube,MA} + \eta_{fin} A_{fin,MA})}$$

for internal convective resistance ($R_{conv,2P}$), wall resistance (R_{wall}) and external convective resistance ($R_{conv,MA}$), respectively. Here OD is the outer tube diameter, ID is the inner tube diameter, k_{tube} is the thermal conductivity of the tube material and L_{tube} is the length of the tube segment. The fin efficiency (η_{fin}) is computed in this work using the approximated formula by Schmidt [116] for annular circular fins:

$$\eta_{fin} = \frac{\tanh\left[m\left(R_e - \frac{OD}{2}\right)\right]}{m\left(R_e - \frac{OD}{2}\right)} \tag{3.117}$$

where R_e is the equivalent fin external radius that can be determined using a 1D-SERF model [117], $m = \sqrt{\frac{\alpha_{MA}}{0.5\,k_{fin}\,\delta_{fin}}}$ with k_{fin} the fin thermal conductivity and δ_{fin} the

fin thickness.

Finally, the total heat flow rate transferred from moist air to the refrigerant, at steady state, is:

$$\dot{Q}_j^{std} = \dot{Q}_{j,MA} = \dot{Q}_{j,2P} = \dot{Q}_{j,s} + \dot{Q}_{j,l} \tag{3.118}$$

where $\dot{Q}_{j,l} = \dot{m}_{cond}^{W} \Delta h_{vap}$ is the latent heat flow rate due to condensation that occurs on the moist air side, and Δh_{vap} is the latent heat of vaporization of water evaluated at the wall temperature ($T_{I,MA}$) of the segment.

As for the Recovery exchanger model, to simulate the dynamic behavior of the heat exchanger resulting from energy accumulation in the solid wall, a two-node thermal model is used. The wall is conceptually divided into two thermal masses, each representing the portion of wall material adjacent to moist-air (MA) and refrigerant (2P) finite volumes.

The energy balances for the wall nodes reads as follows:

$$\frac{M_{wall}\bar{c}_{wall}}{2}\frac{dT_{wall,2P}}{dt} = -\dot{Q}_{j,2P} - \dot{Q}_j^{std} \tag{3.119}$$

$$\frac{M_{wall}\bar{c}_{wall}}{2}\frac{dT_{wall,MA}}{dt} = -\dot{Q}_{j,MA} + \dot{Q}_j^{std} \tag{3.120}$$

where M_{wall} is the total wall mass, $\bar{c}_{wall}$ is the average specific heat capacity of the wall material, and $T_{wall,2P}$ and $T_{wall,MA}$ are the temperatures of the wall portions adjacent to two-phase and moist air finite volumes, respectively.

The terms $\dot{Q}_{j,2P}$ and $\dot{Q}_{j,MA}$ represent the convective heat exchange between the wall surface and the two-phase and moist-air stream in each finite volume:

$$\dot{Q}_{j,2P} = \alpha_{2P} A_{tube,2P} \left(T_{wall,2P} - T_{I,2P}\right) \tag{3.121}$$

$$\dot{Q}_{j,MA} = \alpha_{MA}(A_{tube,MA} + \eta_{fin} A_{fin,MA})\left(T_{wall,MA} - T_{I,MA}\right) \tag{3.122}$$

The term $\dot{Q}_j^{std}$ denotes the steady-state net conductive heat transfer rate through the wall between the two nodes in the segment, as calculated in the previous sections. Its sign is taken as positive when heat flows from the wall node adjacent to "MA" to the wall node adjacent to "2P".

Solution of the coupled heat and mass transfer problem

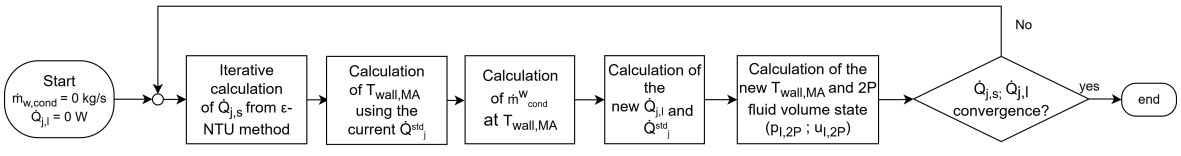

Figure 3.9: Iterative algorithm for the calculation of the overall segment heat and mass transfer.

As previously discussed for the wall condensation in the 'Recovery exchanger' model, the set of equations presented above emphasizes the strong interdependence between sensible heat exchange, condensation processes, and the thermal response of the solid wall. In the present case, this coupling becomes even more pronounced, since both sensible and latent heat transfer are influenced by the thermodynamic state of the refrigerant fluid volume. Consequently, it is not possible to reduce the complexity of the problem by calculating the heat transfer coefficients and the effectiveness solely from the refrigerant inlet conditions, as this would introduce a substantial error. On the other hand, such an approximation can be reasonably applied to the moist air side with respect to the heat and mass transfer coefficients.

To accurately capture these coupled mechanisms within the model, an iterative solution strategy is therefore required. The non linear solver implemented in Simulink® is already capable of handling such problems, without the need for additional user intervention. However, to facilitate the understanding of the solution process and the coupled problem, a solution algorithm is proposed and presented in Figure 3.9. The iterative algorithm is presented in its simplified form, assuming negligible thermal mass of the segment ($M_{wall} = 0\,\text{kg}$), which corresponds to the quasi-steady-state heat transfer case.

The algorithm begins with an initial guess for the condensed water mass flow rate and the associated latent heat transfer, both initially set to zero. The sensible heat transfer rate for each segment is then computed using the ε–NTU method. Since the segment effectiveness (ε) depends on the refrigerant fluid state, which is itself influenced by the sensible heat transfer, this step requires iteration itself to be solved. Subsequently, the wall temperature on the moist air side ($T_{wall,MA}$) is determined based on the current total heat transfer rate ($\dot{Q}_j^{std}$), and subsequently used to evaluate the condensed water mass flow on the heat transfer surface ($\dot{m}_{cond}^W$). $\dot{Q}_j^{std}$ is then updated as the sum of the sensible heat ($\dot{Q}_{j,s}$) and the new latent heat released during condensation ($\dot{Q}_{j,l}$). Following this step, both $T_{wall,MA}$ and the thermodynamic state of the refrigerant fluid volume ($p_{l,2P}$ and $u_{l,2P}$) are recalculated. The process must be repeated iteratively until both $\dot{Q}_{j,l}$ and $\dot{Q}_{j,s}$ converge, due to the coupling between heat and mass transfer.

3.2.4.5. Overall heat transfer

The individual heat exchanger segments can then be assembled to reconstruct the complete device under analysis. The process is first illustrated for a single-row heat exchanger, followed by the multi-row configuration. As shown in Figure 3.10, the geometry of the single-row heat exchanger is simply built by connecting the refrigerant fluid volumes of the segments in series, while the corresponding MA volumes are arranged in parallel. As a result, the total heat flow rate exchanged ($\dot{Q}_{tot,2P}$) and the overall pressure drop ($\Delta p_{tot,2P}$), on the refrigerant side, for this configuration, are given by the sum of the individual heat flow rates $\dot{Q}_{j,2P}$ and pressure drops $\Delta p_{j,2P}$ of the various segments.

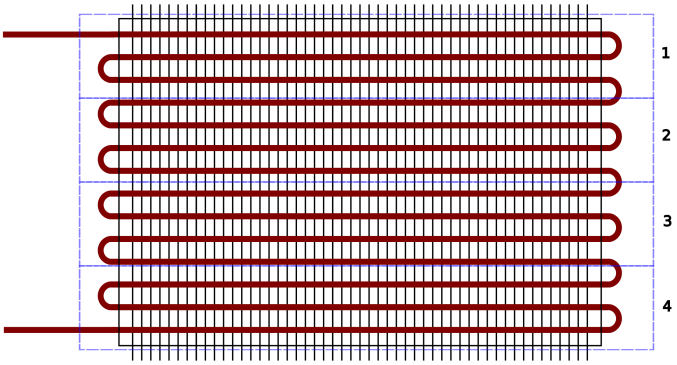

Figure 3.10: Reconstruction of the single-row heat exchanger.

On the other hand, for the moist air side, the total heat flow rate exchanged ($\dot{Q}_{tot,MA}$) is likewise given by the sum of the individual heat flow rates ($\dot{Q}_{j,MA}$), while the overall pressure drop is approximated as:

$$\Delta p_{tot,MA} = \frac{\sum_{j=1}^{n_{seg,row}} \Delta p_{j,MA}}{n_{seg,row}} \tag{3.123}$$

with $n_{seg,row}$ the number of segment per row. Equation (3.123) is an approximation, as variations in air density caused by different heat flow rates across the segments would, according to Equation (3.105), lead to different pressure drops on the air side of each segment. Since these segments are arranged in parallel on the air side, this would cause a redistribution of the airflow across the heat exchanger face to equalize the pressure drops [61]. However, because density variations on the air side are relatively small, the resulting redistribution effect is limited and is neglected in the context of frost-free heat exchangers, to reduce complexity. To complete the heat exchanger reconstruction, the previously built single-row unit can be connected in series on both the air and refrigerant sides to form the multi-row, multi-pass configuration. Alternatively, for a multi-row single-pass configuration, the single-row unit can be connected in parallel on the refrigerant and in series on the air sides.

In the context of this work, to simplify the model, an adiabatic mixing is applied at the end of each row to compute an aggregate air outlet state of the single-row unit, which then serves as the inlet condition for the subsequent row. This approach allows different discretization levels to be adopted across the rows, enabling finer discretization only where needed while still capturing the temperature and humidity gradients along the moist-air side of the heat exchanger. Since the objective is a system-level simulation of the entire unit rather than a detailed high-fidelity simulation of individual components, this assumption offers an effective compromise between numerical accuracy, model robustness, and computational cost.

Modelling considerations for multi-circuit heat exchangers

Fin-and-tube heat exchangers are often designed with multiple circuits to improve thermal performance and reduce pressure drop. However, splitting the refrigerant flow into parallel paths can lead to maldistribution of the refrigerant, affecting the overall effectiveness. This issue is often caused by non-uniform airflow distribution across the heat exchanger, which leads to uneven thermal loads among the circuits. To mitigate this, flow distributors, optimized header geometries, and balancing devices such as orifices or capillary tubes are commonly used by manufacturers. To keep the computational cost of the model low, uniform airflow at the heat exchanger frontal face and symmetry among the refrigerant paths in multi-circuit heat exchangers are assumed. This allows for a highly simplified modeling approach for this type of geometry: it is sufficient to evaluate heat transfer performance and pressure drops using the air and refrigerant mass flow rates divided by the number of parallel circuits (multi-circuit approximation).

In the global energy balances of the heat exchanger block, the calculated exchanged heat, for the single heat exchanger, must then be multiplied by the number of parallel circuits. On the other hand, for pressure drops, the values calculated for a single parallel circuit are used directly in the global balances, since the composite circuit behaves as hydraulic resistances in parallel in both air and refrigerant side. If a balancing device is used it is sufficient to adjust L_{eff}, on the refrigerant side, to account for the associated local resistance.

3.2.4.6. Frost formation

Accurate prediction of heat exchanger performance during winter operation requires accounting for potential frost accumulation on the air side. To achieve this, a frost formation model has been integrated into the segment model, enabling the simulation of frost layer growth and its effects on heat transfer, pressure drop, and the resulting performance degradation over time.

Frost initiation and termination

Frost forms on the evaporator surface when the frost point temperature at the heat exchanger (HX) wall is reached. The DP calculation in the model is based on a formula presented by Górnicki et al. [118]:

$$DP = \frac{A\log_{10}(RH_d) + \frac{BT}{A+T}}{B - \log_{10}(RH_d) - \frac{BT}{A+T}} \tag{3.124}$$

where DP is the dew point temperature °C, RH_d is the relative humidity in decimal form, and $A = 237$ °C and $B = 7.5$ are empirical constants. Both RH_d and T are continuously evaluated during runtime at the exposed surface (wall or frost) to verify whether frost

growth can continue.

When the frost-layer surface temperature rises to the frost-point temperature, further frost accumulation is assumed to stop. At that moment, any additional moisture condensing on the surface is removed from the segment control volume, following the same assumption used for wall condensation (Section 3.2.4.3).

Frost surface energy balances

To simplify the modeling approach, thermal capacity of the frost layer is neglected here,

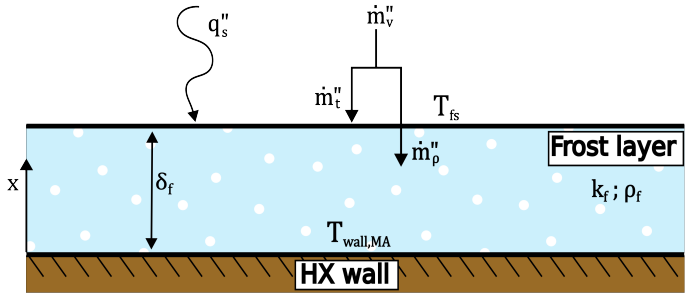

Figure 3.11: Energy and mass transport within the frost control volume.

therefore, the developed model is quasi steady-state. Padhmanabhan [77] demonstrated the validity of the quasi steady-state hypothesis in his work.

If a uniform frost layer is assumed (Figure 3.11), at the frost surface the steady-state energy balance can be expressed as:

$$k_f \frac{(T_{fs} - T_{wall,MA})}{\delta_f} = q"_s + (\dot{m}"_v - \dot{m}"_\rho)\Delta h_{sub} \tag{3.125}$$

with k_f the frost layer average thermal conductivity and δ_f the frost layer thickness. The sensible heat flux ($q"_s$) at the frost surface is calculated by assuming an uniform frost surface temperature (T_{fs}) over each segment, which leads to an exponential air temperature distribution along the segment:

$$q"_s = \frac{|\dot{m}_{MA}| c_{p,MA} (T_{in,MA} - T_{fs}) \left\{1 - \exp\left[-\frac{\alpha_{MA}(A_{tube,MA} + \eta_{fin} A_{fin,MA})}{|\dot{m}_{MA}| c_{p,MA}}\right]\right\}}{A_{fin,MA} + A_{tube,MA}} \tag{3.126}$$

where $\dot{m}"_v$ is the total water mass flux, $\dot{m}"_\rho$ is the diffusive mass flux, Δh_{sub} is the latent heat of sublimation and δ_f is the frost thickness. Equation (3.125) is solved each time step as the frost grows in time, to calculate frost surface temperature (T_{fs}).

Frost growing and densification

The total water vapor mass flux desublimated ($\dot{m}"_w$) from the air stream to the frost surface can be evaluated again using the uniform wall (frost surface) temperature as-

sumption over the segment:

$$\dot{m}"_w = \frac{|\dot{m}_{dry,MA}|(W_{in,MA} - W_{fs,MA})\left\{1 - \exp\left[-\frac{\alpha_{m,MA}(A_{tube,MA}+\eta_{fin,f}A_{fin,MA})}{|\dot{m}_{MA}|}\right]\right\}}{A_{fin,MA} + A_{tube,MA}} \tag{3.127}$$

where $W_{fs,MA} = \min(W_{in,MA}, W_{sat,fs,MA})$, with $W_{sat,fs,MA}$ the saturation humidity ratio at the frost surface. The total water vapor mass flux can be divided over two contributions:

$$\dot{m}"_w = \frac{d}{dt}(\overline{\rho}_f \delta_f) = \dot{m}"_t + \dot{m}"_\rho = \overline{\rho}_f \frac{d\delta_f}{dt} + \delta_f \frac{d\overline{\rho}_f}{dt} \tag{3.128}$$

where $\dot{m}"_t$ is the water mass flux responsible for frost thickening, $\dot{m}"_\rho$ is the water mass flux responsible for frost densification and $\overline{\rho}_f = \frac{1}{\delta_f}\int_0^{\delta_f} \rho_f dx$ is the average density of the frost layer. So, if $\dot{m}"_w$ and $\dot{m}"_\rho$ are known $\dot{m}"_t$ can be determined from equation (3.128).

Molecular diffusion of water vapor into the frost layer is mainly due to Fickian diffusion caused by the vapor partial pressure gradient [76]:

$$\dot{m}"_\rho = D_{eff}\left(\frac{M_w}{RT}\right)\left(\frac{p_{I,MA}}{p_{I,MA} - p_v}\right)\frac{dp_w}{dx} \tag{3.129}$$

where D_{eff} is the effective diffusion coefficient, M_w is the molecular weight of water, R is the universal gas constant, T is the temperature, $p_{I,MA}$ is the total pressure of the MA volume and p_w is the partial pressure of water vapor. According to the local thermodynamic equilibrium hypothesis ($p_w = p_{w,sat}$), and in combination with the perfect gas law and Clausius-Clapeyron equation [119], $\dot{m}"_\rho$ can be also expressed in terms of a temperature gradient. At the frost surface:

$$\dot{m}"_\rho = D_{eff}\left(\frac{M_w^2 \Delta h_{sub}}{R^2 T_{fs}^3}\right)\left[\frac{p_{I,MA} p_{w,sat}}{p_{I,MA} - p_{w,sat}}\right]\frac{dT}{dx}\Big|_{fs} \tag{3.130}$$

where $p_{w,sat}$ is the saturation pressure of water vapor. The temperature gradient at the frost surface is given by the Fourier's law:

$$\frac{dT}{dx}\Big|_{fs} = \frac{q"_t}{k_f} \tag{3.131}$$

with $q"_t = q"_s + (\dot{m}"_v - \dot{m}"_\rho)\Delta h_{sub}$, where $q"_t$ is the total heat flux sum of the sensible and latent heat fluxes at the frost surface. The average frost layer thermal conductivity, could be determined from the Sanders's correlation [69] based on average frost density ($\overline{\rho}_f$):

$$k_f = 0.001202\overline{\rho}_f^{0.963} \tag{3.132}$$

Finally, from equation (3.128) the time evolution of the average density and thickness of

the frost layer are:

$$\delta_f(t) = \int_0^t \frac{\dot{m}"_t}{\overline{\rho}_f} dt \tag{3.133}$$

$$\overline{\rho}_f(t) = \int_0^t \frac{\dot{m}"_\rho}{\delta_f} dt \tag{3.134}$$

The initial conditions for the frost formation model are set to $\delta_{f,0} = 1 \cdot 10^{-5}$ m for the frost thickness and $\rho_{f,0} = 25$ kg m^{-3} for the frost density. These initial conditions ensure consistency at the start of the simulation while introducing a negligible initial conductive thermal resistance, thus having no significant impact on the heat transfer calculations.

Diffusion coefficient

The diffusion path of water vapor follows the pore structure within the porous frost layer; consequently, the actual path length is greater than the geometric displacement due to the inherent tortuosity of the porous medium. Hence, the effective diffusion coefficient is redefined [78]:

$$D_{eff} = D_{AB} \frac{\epsilon}{\tau} \tag{3.135}$$

with $\epsilon = 1 - \frac{\overline{\rho_f}}{\rho_{ice}}$, $\tau = \frac{\epsilon}{1-(1-\epsilon)^{0.5}}$, where ϵ, τ are the porosity and the tortuosity of the porous medium respectively and ρ_{ice} is the ice density. An empirical equation for the binary diffusion coefficient (D_{AB}) [120] for water vapor diffusion in the frosting process is adopted:

$$D_{AB} = 2.6 \cdot 10^{-5} \left(\frac{T_{film}}{T_0} \right)^{1.75} \tag{3.136}$$

where $T_{film} = \frac{T_{MA}+T_{fs}}{2}$ with $T_0 = 298$ K.

Fin efficiency: frost integration

Fin efficiency strongly decreases as frost grows on the evaporator surface [121]. This effect can be considered by modelling the frost layer as a low conductivity coating layer [122]:

$$\eta_{fin,f} = \left[cos(m\delta_f) - \frac{mk_{fin}\delta_{fin}}{2k_f} sin(m\delta_f) \right] \eta_{fin} \tag{3.137}$$

where $m = \sqrt{\frac{\alpha_{MA} k_f}{\delta_f k_f^2 + 0.5\delta_f h_{MA} k_{fin} \delta_{fin} + 0.5 k_{fin} k_f \delta_{fin}}}$.

Pressure loss correction and air flow redistribution

The presence of a frost layer on the heat exchanger surface increases the pressure drop across each segment because the frost reduces the effective flow area. As the frost thickness (δ_f) increases, the free flow area becomes progressively smaller, which in turn

causes a higher pressure drop across the segment. The pressure drop is calculated again using the Kays and London Equation (3.105), but modified to account for three main effects: the reduction in flow area, the variation of the surface area due to frost growth and the resulting change in the friction factor. Specifically, the geometric parameters of each elementary heat exchanger segment are updated by incorporating the frost thickness, and the correlations for the friction factor are recalculated based on the new geometry.

The non-uniform frost growth on the heat exchange surface, caused by the subdivision into segments, leads to various degrees of blockage across the different segments. This varying blockage leads to an uneven distribution of flow resistance across the heat exchanger face. As a direct consequence, the total air mass flow ($\dot{m}_{in,MA}$) must be divided according to the classical parallel arrangement so that the pressure drop ($\Delta p_{j,MA}$) across each segment remains the same, as described by equations (3.138). Considering the single-row unit this reads as:

$$\begin{cases} \dot{m}_{j,MA}^2 R_{j,MA} = \Delta p_{j,MA} \\ \dot{m}_{in,MA} = \sum_{j=1}^{n} \dot{m}_{j,MA} \\ R_{j,MA} = \dfrac{1}{2\rho_{in,MA} A_{c,MA}^2} \left[f \dfrac{A_{0,MA}}{A_{c,MA}} \dfrac{\rho_{in,MA}}{\rho_{avg,MA}} + (1+\sigma^2) \left(\dfrac{\rho_{in,MA}}{\rho_{out,MA}} - 1 \right) \right] \end{cases} \tag{3.138}$$

Heat transfer correction

The sensible heat flow rate ($\dot{Q}_{j,s}$) at steady-state, from the MA to the 2P fluid volume, is calculated for each segment using a modified ε-NTU method to consider the effect of frost layer on the heat transfer surface. The differences with respect to the standard ε-NTU method stands on the calculation of the total heat transfer resistance where, the heat transfer coefficient on the air side (α_{MA}) is replaced by the frost corrected value ($\alpha_{MA,f}$), the fin efficiency on the air side ($\eta_{fin,MA}$) is replaced by the frosted fin efficiency ($\eta_{fin,f,MA}$) and an additional thermal resistance (R_f) is added to account for the frost layer conductive thermal resistance:

$$R_{tot} = R_{conv,2P} + R_{wall} + R_f + R_{conv,f,MA} \tag{3.139}$$

The thermal resistances are defined as: $R_{conv,2P} = \frac{1}{\alpha_{2P} A_{tube,2P}}$, $R_{wall} = \frac{\ln\left(\frac{OD}{ID}\right)}{2\pi k_{tube} L_{tube}}$, $R_f = \frac{\ln\left(\frac{OD+2\delta_f}{OD}\right)}{2\pi k_f L_t}$, $R_{conv,f,MA} = \frac{1}{\alpha_{f,MA}\left(A_{tube,MA} + \eta_{fin,f,MA} A_{fin,MA}\right)}$ for internal convective, wall, frost, and external convective resistances, respectively. Similarly to the correction applied to the friction factor correlations, the correlations used to calculate the j-factor, and therefore the corrected heat transfer coefficient $\alpha_{f,MA}$, are also modified to account for frost growth on the heat exchange surface. This is achieved by updating the geometric parameters of

each elementary heat exchanger segment to include the frost thickness (δ_f).

3.2.5. Accumulator

The suction line accumulator prevents liquid refrigerant from entering the compressor, ensuring stable operation and protecting it from liquid slugging. In this work, the accumulator is modeled as an adiabatic constant-volume chamber (V_{acc}) with two ports: an inlet (A) and an outlet (B). At port A, the refrigerant enters from the evaporator in any thermodynamic state. At port B, provided the chamber is not completely filled with liquid, the refrigerant leaves the accumulator as either saturated or superheated vapor. Energy and mass flow are assumed positive when entering the control volume, in both ports.

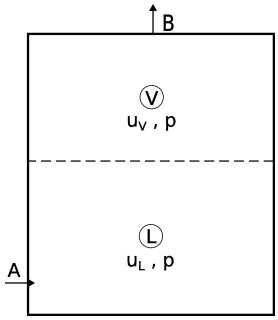

Figure 3.12: Schematic of the accumulator model.

The accumulator is conceptually divided into two control volumes: a liquid region at the bottom and a vapor region at the top, separated by an interface (3.12). Internal nodes, denoted as L and V, are assigned to the liquid and vapor control volumes, respectively, and represent their thermodynamic states. No flow resistance is modeled and the pressure is assumed uniform throughout the control volume and equal to the pressure at the inlet and outlet ports ($p_L = p_V = p_A = p_B = p$).

The mass balance for the liquid control volume is given by:

$$\frac{dM_L}{dt} = \dot{m}_{L,in} - \dot{m}_{L,out} + \dot{m}_{cond} - \dot{m}_{evap} \tag{3.140}$$

where M_L is the liquid mass, $\dot{m}_{L,in} = \dot{m}_{A,L}$ is the liquid mass flow rate entering the chamber at port A, $\dot{m}_{L,out} = -\dot{m}_{B,L}$ is the liquid mass flow rate leaving the chamber at port B. In general $\dot{m}_{L,out}$ is set to zero, only in the case the chamber is completely filled with liquid this quantity is nonzero and corresponds to the outlet mass flow rate from the accumulator.

When the liquid specific enthalpy is lower than the saturated liquid specific enthalpy, no vaporization occurs, and $\dot{m}_{evap} = 0$. Conversely, if the liquid specific enthalpy exceeds the saturated liquid specific enthalpy, vaporization occurs, and $\dot{m}_{evap} = \frac{M_L(h_L - h_{L,sat})/(h_V - h_{V,sat})}{\tau}$. Similarly, when $h_V \geq h_{V,sat}$, no condensation occurs, and $\dot{m}_{cond} = 0$, on the other hand

if $h_V < h_{V,sat}$, condensation occurs, and $\dot{m}_{cond} = \frac{M_V(h_{V,sat}-h_V)/(h_{V,sat}-h_{L,sat})}{\tau}$. In these expressions, τ is a time constant associated to the specific phase-change process (evaporation or condensation).

The liquid mass accumulation rate can be expressed again in terms of the main state variabiles of the refrigerant as:

$$\frac{dM_L}{dt} = \frac{d\rho_L}{dt} V_L = \left[\left(\frac{\partial \rho_L}{\partial p} \right)_{u_L} \dot{p} + \left(\frac{\partial \rho_L}{\partial u_L} \right)_p \dot{u}_L \right] V_L \tag{3.141}$$

where $V_L = V_{acc} z_L$ is the liquid volume, that can be expressed in terms of the liquid volume fraction $z_L = \frac{f_{M,L} v_L}{f_{M,L} v_L + (1-f_{M,L}) v_V}$, with $f_{M,L} = \frac{M_L}{M_L + M_V}$.

The energy balance for the liquid control volume is given by:

$$M_L \frac{du_L}{dt} + (\dot{m}_{L,in} - \dot{m}_{L,out} + \dot{m}_{cond} - \dot{m}_{evap}) u_L = \Phi_{L,in} - \Phi_{L,out} + \Phi_{cond} - \Phi_{evap} \tag{3.142}$$

where the energy associated to vaporization and condensation processes are defined as $\Phi_{evap} = \dot{m}_{evap} h_{V,sat}$ and $\Phi_{cond} = \dot{m}_{cond} h_{L,sat}$, respectively, with $h_{V,sat}$ and $h_{L,sat}$ the saturated vapor and liquid specific enthalpy at the chamber pressure, respectively. $\Phi_{L,in} = \Phi_{A,L}$ is the inlet liquid energy flow rate at port A, and $\Phi_{L,out} = -\Phi_{B,L}$ is the outlet liquid energy flow rate at port B.

For the vapor control volume, instead, the mass balance is given by:

$$\frac{dM_V}{dt} = \dot{m}_{V,in} - \dot{m}_{V,out} - \dot{m}_{cond} + \dot{m}_{evap} \tag{3.143}$$

where M_V is the liquid mass, $\dot{m}_{V,in} = \dot{m}_{A,V}$ is the vapor mass flow rate entering the chamber at port A, $\dot{m}_{V,out} = -\dot{m}_{B,V}$ is the vapor mass flow rate leaving the chamber at port B. In normal operating conditions $\dot{m}_{V,out}$ is nonzero and corresponds to the outlet mass flow rate from the accumulator, only in the case the chamber is completely filled with liquid this quantity becomes zero.

The vapor mass accumulation rate can be expressed again in terms of the main state variabiles of the refrigerant as:

$$\frac{dM_V}{dt} = \frac{d\rho_V}{dt} V_V = \left[\left(\frac{\partial \rho_V}{\partial p} \right)_{u_V} \dot{p} + \left(\frac{\partial \rho_V}{\partial u_V} \right)_p \dot{u}_V \right] V_V \tag{3.144}$$

where $V_V = V_{acc} - V_L$ is the vapor volume.

The energy balance for the vapor control volume is given by:

$$M_V \frac{du_V}{dt} + (\dot{m}_{V,in} - \dot{m}_{V,out} - \dot{m}_{cond} + \dot{m}_{evap}) u_V = \Phi_{V,in} - \Phi_{V,out} - \Phi_{cond} + \Phi_{evap} \tag{3.145}$$

where $\Phi_{V,in} = \Phi_{A,V}$ is the inlet vapor energy flow rate at port A, and $\Phi_{V,out} = -\Phi_{B,V}$ is the

outlet vapor energy flow rate at port B.

If the liquid volume fraction lies between 0 and 1, the refrigerant outlet state from the accumulator is assumed to be purely vapor:

$$\Phi_{out} = \Phi_{V,out} \tag{3.146}$$

$$\dot{m}_{out} = \dot{m}_{V,out} \tag{3.147}$$

Conversely, if $z_L = 0$ or $z_L = 1$, meaning that the chamber is entirely filled with either vapor or liquid, the refrigerant outlet state at port B is set equal to the corresponding inlet values at port A:

$$\Phi_{out} = -\Phi_A \tag{3.148}$$

$$\dot{m}_{out} = -\dot{m}_A \tag{3.149}$$

3.2.6. Compressor

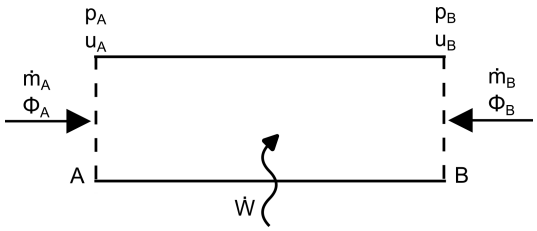

Figure 3.13: Control volume for the compressor component.

The compressor is the source of momentum in the 2P network, and its main function is to increase the pressure and temperature of the refrigerant vapor exiting the evaporator. In this work, a simplified model based on the isentropic efficiency (η_{ise}) is adopted. The compressor is modeled using a quasi-steady lumped formulation. Referring to the control volume shown in Figure 3.13, the governing equations for mass and energy conservation of the refrigerant are given as follows:

$$\dot{m}_A + \dot{m}_B = 0 \tag{3.150}$$

$$\Phi_A + \Phi_B + \dot{W} = 0 \tag{3.151}$$

with $\dot{W}$ is the work that the compressor does on the refrigerant (i.e., fluid power). Using an isentropic efficiency model it is defined as:

$$\dot{W} = \dot{m}_A(h_{out} - h_{in}) \tag{3.152}$$

From the definition of isentropic efficiency, the outlet specific enthalpy (h_{out}) can be

expressed as:

$$h_{out} = h_{in} + \frac{h_{out,ise} - h_{in}}{\eta_{ise}} \tag{3.153}$$

where h_{in} is the inlet specific enthalpy, which correspond to the outlet state computed by the accumulator, and $h_{out,ise}$ is the outlet specific enthalpy for an isentropic compression process, which can be determined from the inlet specific entropy (s_{in}) and the outlet pressure (p_{out}).

In vapor-compression systems, the compressor is typically a volumetric machine, therefore, the mass flow rate through the compressor is related to its displacement volume (V_{disp}) and rotational speed (ω) by the following equation:

$$\dot{m}_A = \rho_{in} V_{disp} \omega \eta_v \tag{3.154}$$

where ρ_{in} is the refrigerant density at the compressor inlet and η_v is the volumetric efficiency, which accounts for the losses due to re-expansion of the refrigerant in the clearance volume and leakage flows.

Regarding the power consumption of the compressor, in addition to the compressor work ($\dot{W}$), it is necessary to consider the motor efficiency, the drive efficiency and electrical efficiency to convert the compressor work into power consumption (PC_{comp}). Separating these contributions could be difficult in practice. Therefore, in this work, a 20-coefficient model of the compressor power consumption is adopted, which directly relates the power consumption to the compressor speed and the evaporating and condensing temperatures (T_{evap} and T_{cond}, respectively):

$$\begin{aligned} PC_{comp} = {} & C_1 + C_2 T_{evap} + C_3 T_{cond} + C_4 \omega + C_5 T_{evap} T_{cond} + C_6 T_{evap}\, \omega + C_7 T_{cond}\, \omega \\ & + C_8 T_{evap}^2 + C_9 T_{cond}^2 + C_{10} \omega^2 + C_{11} T_{evap} T_{cond}\, \omega + C_{12} T_{evap}^2 T_{cond} \\ & + C_{13} T_{evap}^2 \omega + C_{14} T_{evap}^3 + C_{15} T_{evap} T_{cond}^2 + C_{16} T_{cond}^2 \omega + C_{17} T_{cond}^3 \\ & + C_{18} T_{evap} \omega^2 + C_{19} T_{cond} \omega^2 + C_{20} \omega^3 \end{aligned} \tag{3.155}$$

where C_1 to C_{20} are the empirical coefficients that can be determined from a multivariate regression of experimental data provided by the manufacturer.

The 20-coefficient model can, in principle, also be applied to the compressor mass flow rate and isentropic efficiency. However, at near-zero or low compressor speeds, it may produce non-physical mass flow rate values and is generally not available for the isentropic efficiency. For this reason, in this work, the 20-coefficient model is used only for power consumption, whereas the mass flow rate is computed with the physical model described above, which ensures robustness and physical consistency at low speeds.

Nonetheless, a 20-coefficient representation of the mass flow rate is extracted from the manufacturer data and employed to generate a volumetric efficiency map η_v as a

function of pressure ratio $\left(\frac{p_{out}}{p_{out}}\right)$ and compressor speed (ω) (this can be done by using the known V_{disp} and equating Equation 3.154 with the mass flow predicted by the 20-coefficient model). This map is interpolated and extrapolated linearly during the simulation to obtain η_v under any operating condition. The combination of Equation 3.154 with the 20-coefficient mass flow rate model allows the mass flow rate to be predicted across the entire operating range, including near-zero and low speeds, while remaining consistent with the manufacturer data. The isentropic efficiency, instead in this work, is determined experimentally as described later.

On the other hand, since power consumption does not appear in the compressor conservation equations, it does not need to be accurate outside the operating range for the sake of simulation robustness. Therefore, when computing power consumption, saturation temperatures and compressor speed are limited to the manufacturer's data range, and PC_{comp} is set to zero when the speed is zero. From zero speed to the minimum speed available in the manufacturer data, a linear interpolation is performed to ensure continuity of the power consumption curve.

During the simulation routine, the compressor component receives as input a smoothed rotational speed signal, computed by the system control logic based on the current operating conditions. This control logic not only determines the speed set-point for capacity regulation but also integrates several protection strategies to maintain the compressor within its operating envelope. Specifically, speed limitations are imposed to prevent excessive discharge temperatures, while additional constraints on the condensation temperature in winter and on both condensation and evaporation temperatures in summer are enforced to ensure safe operating conditions.

At each simulation time step, the smoothed compressor speed is then used to calculate the refrigerant mass flow rate (from Equation 3.154) and the fluid power (from Equation 3.152), which defines the energy transfer at the compressor outlet. The rotational speed smoothing itself is performed using a first-order transfer function, to both improve the numerical stability of the model and reproduce the mechanical inertia of the compressor rotor.

3.2.7. Four-ways valve

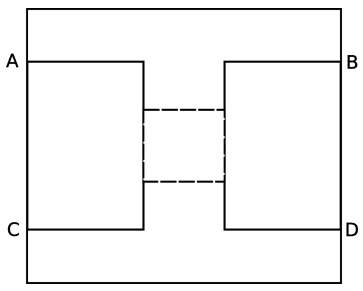

Figure 3.14: Four-ways valve schematic.

The four-ways valve is a key component in heat pump systems, enabling the reversal of the refrigeration cycle for switching between heating (winter operation) and cooling (summer operation) modes. The valve has four ports: one connected to the compressor discharge in the high-pressure side (C), one to the indoor coil (B), one to the outdoor coil (A), and one to the accumulator on the low-pressure side (D). By changing the internal flow path, the valve directs the refrigerant flow to either the indoor coil or outdoor coil, depending on the desired mode of operation. In the simplified modelling framework adopted in this work, the component is modeled as a simple switch with two positions and the associated pressure drops for the two flow paths in the component.

Considering the schematic in Figure 3.14 and adopting the convention that mass and energy flow rates are positive when entering the ports, when the component operates in cooling mode, the governing equations for mass and energy conservation of the refrigerant are given as follows:

$$\dot{m}_A + \dot{m}_C = 0, \qquad \dot{m}_B + \dot{m}_D = 0 \tag{3.156}$$

$$\Phi_A + \Phi_C = 0, \qquad \Phi_B + \Phi_D = 0 \tag{3.157}$$

Assuming negligible flow compressibility and adopting the conventional valve flow coefficient K_v (commonly provided by manufacturers in $\mathrm{m^3\,h^{-1}}$), the pressure drops across the two flow paths are expressed as:

$$p_C - p_A = a\frac{\dot{m}_C|\dot{m}_C|}{K_v^2\overline{\rho}}, \qquad p_B - p_D = a\frac{\dot{m}_B|\dot{m}_B|}{K_v^2\overline{\rho}} \tag{3.158}$$

where $a = 100$ Pa $\mathrm{m^3\,kg^{-1}}$ and $\overline{\rho}$ is the average density of the refrigerant between the two ports of each flow path.

If the component is in the heating mode position, the governing equations for mass and energy conservation are:

$$\dot{m}_A + \dot{m}_D = 0, \qquad \dot{m}_C + \dot{m}_B = 0 \tag{3.159}$$

$$\Phi_A + \Phi_D = 0, \qquad \Phi_C + \Phi_B = 0 \tag{3.160}$$

and in the same way as the cooling mode, the pressure drops across the two flow paths are given by:

$$p_A - p_D = a\frac{\dot{m}_A|\dot{m}_A|}{K_v^2\overline{\rho}}, \qquad p_C - p_B = a\frac{\dot{m}_C|\dot{m}_C|}{K_v^2\overline{\rho}} \tag{3.161}$$

3.2.8. Electronic expansion valve

The electronic expansion valve (EEV) is a variable restriction device that regulates the refrigerant flow into the evaporator, thereby controlling the outlet superheating.

In this work, the EEV is modeled as a quasi-steady-state component with negligible internal volume. Referring to the lumped control volume in Figure 3.15, let S denote the upstream and downstream cross-sectional areas and S_R the throat area, with $\sigma = S_R/S$ as the area ratio. For an inlet flow (in), a restriction flow (R), and an outlet flow (out), we can further define the corresponding flow velocities w_{in}, w_R, and w_{out}, and the specific-volume ratios $r_{in} = v_{in}/v_R$ and $r_{out} = v_{out}/v_R$, where v_R is the specific volume at the throat.

From continuity we have:

$$w_{in} = \frac{\dot{m}\, v_{in}}{S} = w_R\, r_{in}\, \sigma, \qquad w_{out} = \frac{\dot{m}\, v_{out}}{S} = w_R\, r_{out}\, \sigma, \qquad \dot{m} = \rho_R\, w_R\, S_R \tag{3.162}$$

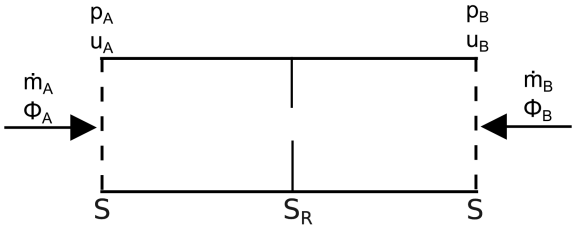

Figure 3.15: Control volume for the electronic expansion valve component.

Dividing the control volume into two parts, the contraction ($in \rightarrow R$) and the expansion ($R \rightarrow out$), and applying momentum and mechanical energy balances to each part, with the assumption of no wall friction and adiabatic component, we obtain the following equations:

Contraction ($in \rightarrow R$).

$$\text{Momentum:} \quad p_{in}S - p_R S_R = \dot{m}\,(w_R - w_{in}) \tag{3.163}$$

$$\text{Mechanical energy:} \quad p_{in} + \tfrac{1}{2}\rho_{in} w_{in}^2 = p_R + \tfrac{1}{2}\rho_R w_R^2 \tag{3.164}$$

Expansion ($R \rightarrow out$).

$$\text{Momentum:} \quad p_R S_R - p_{out} S = \dot{m}\,(w_{out} - w_R) \tag{3.165}$$

$$\text{Mechanical energy:} \quad p_R + \tfrac{1}{2}\rho_R w_R^2 = p_{out} + \tfrac{1}{2}\rho_{out} w_{out}^2 \tag{3.166}$$

By solving Equation (3.163) and (3.165) for p_R and substituting the result into Equation (3.164)-(3.166), and using $S = \dot{m}\, v_{in}/w_{in}$, $S_R = \dot{m}\, v_R/w_R$ together with the continuity relations (Equations 3.162), the pressure losses across contraction ($\Delta p_{in-R} = p_A - p_R$) and expansion ($\Delta p_{R-out} = p_R - p_{out}$) become:

$$\Delta p_{in-R} = \frac{\rho_R w_R^2}{2}\Big[(1+\sigma)(1-r_{in}\sigma)\Big], \quad \Delta p_{R-out} = -\frac{\rho_R w_R^2}{2}\Big[2\sigma(1-r_{out}\sigma)\Big] \tag{3.167}$$

The total pressure drop across the valve is then the sum of the contraction and expansion losses:

$$\Delta p_{tot} = \Delta p_{in-R} + \Delta p_{R-out} = \frac{\rho_R w_R^2}{2} K_T \tag{3.168}$$

with:

$$K_T = (1+\sigma)\big(1 - r_{in}\sigma\big) - 2\sigma\big(1 - r_{out}\sigma\big), \quad \sigma = \frac{S_R}{S}, \quad r_{in} = \frac{v_{in}}{v_R}, \quad r_{out} = \frac{v_{out}}{v_R}$$

From the definition of the throat velocity then we have:

$$w_R = \frac{\dot{m}}{\rho_R S_R} \tag{3.169}$$

and substituting Equation 3.169 into the total pressure drop expression (Equation (3.168)) gives:

$$\Delta p = \frac{K_T}{2\,\rho_R\, S_R^2}\,\dot{m}^2 \tag{3.170}$$

Finally, solving for $\dot{m}$ and multiplying the result by a discharge coefficient C_d, a tunable parameter used to account for non-ideal flow conditions, the valve equation is obtained:

$$\boxed{\dot{m} = C_d S_R \Delta p \sqrt{\frac{2\,\rho_R}{|\Delta p| K_T}}} \tag{3.171}$$

For solving Equation (3.171), the refrigerant state at the restriction is obtained by enforcing both the isenthalpic relation:

$$u_A + p_A v_A + \frac{w_A^2}{2} = u_R + p_R v_R + \frac{w_R^2}{2} = u_B + p_B v_B + \frac{w_B^2}{2} \tag{3.172}$$

which ensures conservation of specific total enthalpy across the valve, and the pressure relation:

$$p_R = p_{in} - \Delta p_{in-R} = p_{in} - \frac{w_R^2}{2 v_R}\Big[(1+\sigma)(1 - r_{in}\sigma)\Big] \tag{3.173}$$

which provides the pressure needed to fully determine the thermodynamic state at the restriction. The conservation equations for mass, energy and momentum for the EEV control volume finally are:

$$\dot{m}_A + \dot{m}_B = 0 \tag{3.174}$$

$$\Phi_A + \Phi_B = 0 \tag{3.175}$$

$$\dot{m}_A = C_d S_R (p_A - p_B) \sqrt{\frac{2\rho_R}{|p_A - p_B| K_T}} \tag{3.176}$$

In the case of our specific model, the throat area S_R is modulated by the control logic to achieve the desidered operating condition.

CHAPTER 4

Experimental analysis

In this chapter, the experimental campaign conducted to characterize the performance of the analyzed HVAC system is presented. The laboratory infrastructure, consisting of climatic chambers designed to simulate indoor and outdoor environmental, is described alongside the standard and additional onboard instrumentation integrated for high-fidelity model validation. A comprehensive test matrix is defined to map the system behavior under a wide range of operating conditions, covering both winter and summer scenarios. Finally, the test procedure is outlined.

4.1. Experimental setup

4.1.1. Test rig

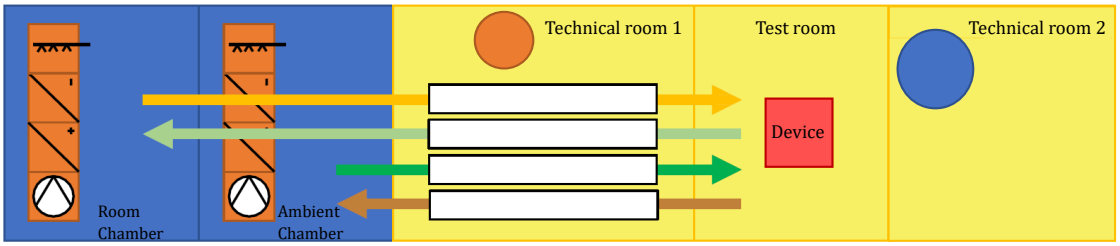

Figure 4.1: Full schematic of the laboratory setup. Source: [123].

The experimental campaign was conducted at the *Kompaktgeräteprüfstand* laboratory, located at the *Unit of Energy Efficient Building* of the University of Innsbruck. An overview of the facility layout is shown in Figure 4.1. The laboratory, which extends over a surface area of approximately 90 m^2, is specifically designed for the performance testing of compact ventilation and heat pump units and consists of five interconnected rooms:

- **Room**: a climatic chamber reproducing indoor conditions, with a capacity of up to 8.0 kW in cooling at 21 °C and 3.5 kW in heating.
- **Ambient**: a climatic chamber reproducing outdoor conditions, with a capacity of up to 8.0 kW in cooling at +2 °C (or 6.5 kW in cooling at −7 °C) and 9.4 kW in heating.
- **Technical room 1**: a service room housing the air ductwork, flow measurement devices, auxiliary fans, and part of the instrumentation.
- **Test room**: a thermally stable chamber where the unit under test is installed and connected to the ductwork leading to the climatic chambers; it is also acoustically treated to enable noise measurements under controlled conditions.
- **Technical room 2**: a service room containing additional technical equipment and system control devices.

Both climatic chambers allow precise regulation of temperature and humidity, ensuring inlet conditions to the unit under test with an accuracy of ±0.05 °C and ±2 % RH, respectively. This is achieved by dedicated PI-PID in cascade controllers acting on the climatic chambers.

Airflow and psychrometric quantities are measured inside the air ducts to capture representative flow properties:

- **Volumetric airflow rates** are measured using calibrated orifice plates, with the pressure drop across each plate acquired by differential pressure sensors and converted into volumetric flow rates through the corresponding calibration curves.
- **Humidity measurements** are performed using capacitive sensors, positioned sufficiently downstream of the unit outlets to ensure well-mixed conditions before sampling.
- **Temperature measurements** are carried out directly at the duct cross-sections close to the unit connections. Each cross-section is instrumented with five temperature sensors: four type-K thermocouples equally distributed circumferentially and positioned away from the duct walls to avoid boundary layer effects, and one PTC thermistor at the duct centerline. This arrangement is specifically designed to provide a realistic measurement of the mean air temperature over the entire duct cross-section rather than at a single point.
- An **ambient pressure sensor** is installed in the test room to measure the static absolute pressure of the surrounding air. Since the climatic chambers are not airtight, the ambient pressure inside the test room is representative of the pressure conditions in the climatic chambers.

Additionally, auxiliary fans are installed in each duct and controlled via PID loops to regulate the static pressure directly at the unit openings, enabling the simulation of realistic and controlled installation conditions.

Finally, the laboratory is equipped with power meters that continuously monitor the electrical consumption of the tested unit, providing the data required to evaluate its energy efficiency under different operating conditions.

The complete list of sensors together with their measurement accuracies is reported in Table 4.2.

Table 4.1: Measurement devices and accuracies of the test rig sensors.

Measurement value	SI unit	Measurement device	Measurement accuracy
Temperature	°C	1 × Pt100 4-wire with NI 9217; 4 × type-K thermocouples with NI 9213	Pt100: ±0.05 °C; TC: ±0.10 °C
Relative humidity	°C, %	Pt100 and capacitive humidity sensors (E+E EE210)	T: ±0.10 °C; RH: ±1.5 %
Volume flow	m^3/h	FläktWoods MR; Huba Control 699	±5.0 %
Absolute pressure	Pa	THIES Clima Barogeber	±25 Pa
Differential pressure	Pa	Huba Control 699	±2 Pa
Electrical power consumption	W	Iskra MT 400	±0.5 %

4.1.2. Unit

The unit analyzed in the experimental campaign corresponds to the standard configuration described in Section 1.4 and equipped with an ERV. In principle, the performance of the two subsystems (heat pump and ventilation unit) could therefore be decoupled and tested according to EN 16573:2017, with the existing test rig already allowing such tests without additional instrumentation. However, since the objective of this work was to develop a high-fidelity digital model, as already discussed, standard boundary measurements alone were insufficient to capture the amount of data required for calibration and validation. Additional measurements were necessary to resolve internal states and reproduce accurately the system behavior.

To extend the information beyond the standard boundary measurements, additional onboard instrumentation was integrated into the unit, as illustrated in Figure 4.2. The placement and function of these sensors can be summarized as follows:

- **Refrigerant-side temperature sensors (red)**: resistance thermometer were mounted on the external surface of the copper tubes of the refrigeration circuit, ensuring

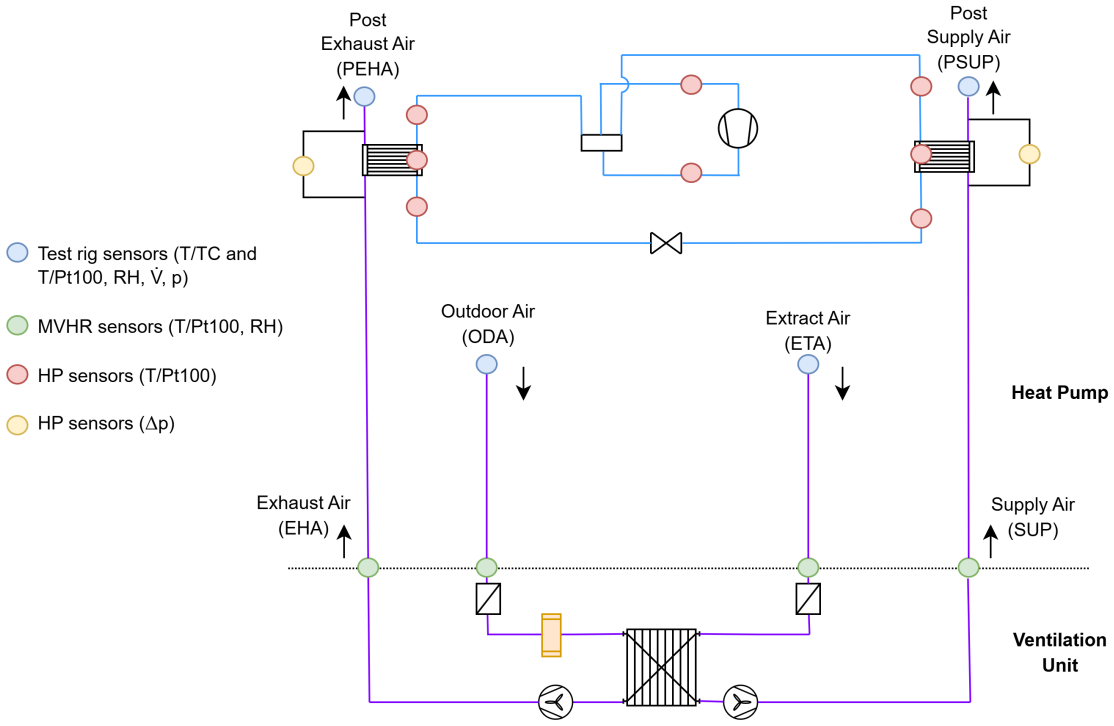

Figure 4.2: Schematic of the unit, with the additional sensors position.

thermal coupling with a conductive paste and insulated with 1 cm of flexible elastomeric foam to limit heat losses. Sensors were placed at the inlets and outlets of the condenser and evaporator, and at the compressor suction and discharge ports. Additional probes (resistance thermometer) were installed on central return bends

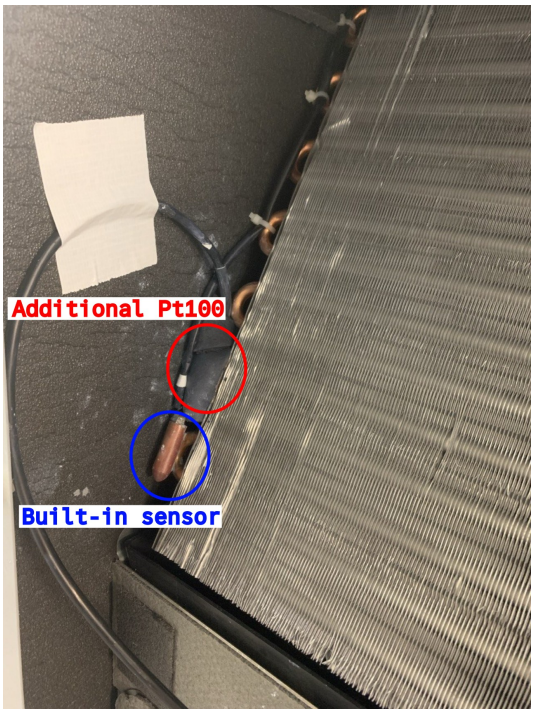

Figure 4.3: Installation of refrigerant-side temperature sensor on the coil, for saturation temperature measurement.

of the heat exchangers, in positions shielded from the air stream, so as to provide representative condensation and evaporation temperatures (Figure 4.3). The discharge sensor and those used to derive evaporation and condensation temperatures were deliberately positioned close to the built-in sensors of the unit, which feed the internal heat pump control logic (Section 1.4). This arrangement ensures consistency between the experimental data and the machine's reference signals, allowing a direct assessment of the control strategy and guaranteeing that the digital twin validation reflects the actual control-driven behavior.

- **Air-side differential pressure sensors (yellow)**: positioned across the condenser and evaporator air channels to quantify the pressure losses on the air side of the heat pump heat exchangers. This information is of particular relevance during frosting events at the evaporator, where the progressive increase in flow resistance forces the fans to operate at higher rotational speeds to maintain the nominal airflow rate. As a result, the electrical power consumption of the fans increases. In extreme cases, the available fan head may no longer be sufficient to overcome the additional pressure drop, ultimately leading to a reduction in airflow through the heat exchanger. Monitoring these variables is therefore essential to quantify the interaction between frost growth, fan performance, and overall system efficiency.
- **MVHR sensors (green)**: placed at the inlets and outlets of the ventilation unit, positioned at the center of the air ducts to avoid wall effects and ensure representative measurements. These sensors serve two main purposes. First, they enable an accurate characterization of the air conditions entering the heat pump, which is critical for evaluating the coupling between the ventilation and refrigeration cycles. Second, they make it possible to avoid performing the tests in two separate stages, as required by EN 16573:2017.

This enhanced experimental setup allows the accurate calibration and validation of the digital model under steady-state, off-design, and transient conditions, thereby ensuring its robustness and predictive capability across the full operational envelope of the unit.

No additional insulation was applied to the unit beyond the factory configuration, in order to preserve realistic operating conditions. The casing of the unit was already insulated, as was most of the refrigerant circuit; only the compressor body and a short section of the discharge line—from the compressor outlet to the four-way valve—were left exposed. Maintaining this layout ensured that the tests remained representative of real installations. A full overview of the experimental testbench is shown in Figure 4.7.

4.2. Test procedure

Figure 4.4 reports the test matrix adopted to characterize the unit. Two families of boundary conditions were investigated, representative of winter and summer operation.

Table 4.2: Measurement devices and accuracies of the additional sensors placed in the unit.

Measurement value	SI unit	Measurement device	Measurement accuracy
Temperature	°C	Pt100 4-wire with NI 9217	±0.05 °C
Relative humidity	°C, %	Pt100 and capacitive humidity sensors (KFFT/M-X/S)	T: ±0.30 °C; RH: ±2 %
Differential pressure	Pa	Huba Control 699	±2 Pa

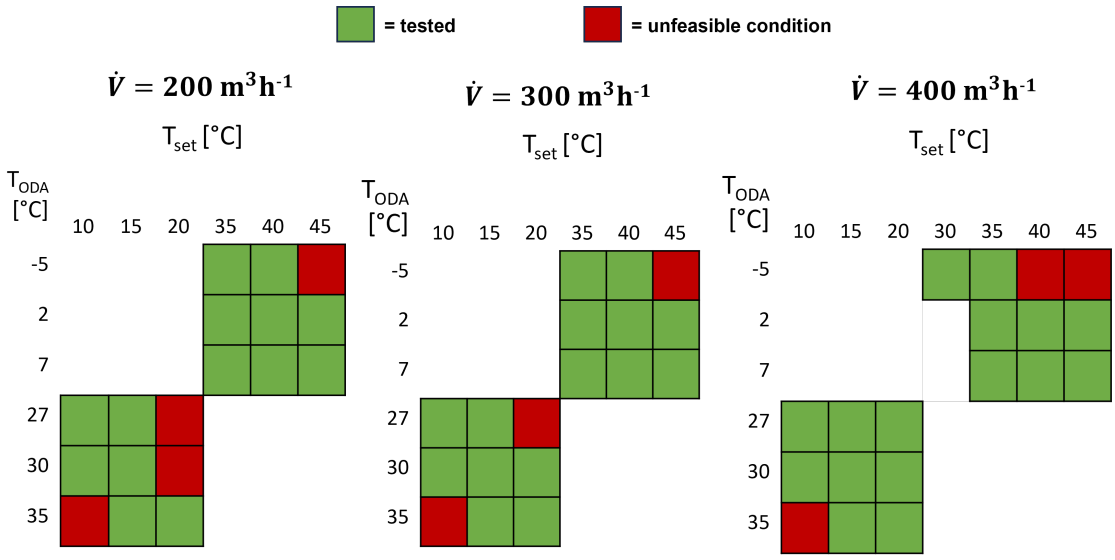

Figure 4.4: Test matrix for the system equipped with an MVHR/ERV.

The "ambient" chamber, representing the outdoor environment, was set to $T_{ODA} = -5$, 2 and 7°C for winter tests, and to $T_{ODA} = 27$, 30 and 35°C for summer tests. The relative humidity in the outdoor chamber was fixed at 70 % in winter and 50 % in summer. The "room" chamber, representing the indoor environment, was maintained at 20°C and with a relative humidty of 50 % during winter tests, and at 22°C and 50 % during summer tests.

As illustrated in Figure 4.5, the experimental test matrix was designed to provide a comprehensive mapping of the possible operating conditions of the unit in terms of airflow rates and outdoor air temperatures. In the winter experimental campaign, the minimum outdoor temperature tested (−5°C) was limited to the activation threshold of the electric pre-heater installed in the duct connected to the outdoor air intake (Figure 1.7). The electric pre-heater is a factory-integrated component used to protect the recovery exchanger from frosting. For the ventilation unit equipped with the enthalpy recovery exchanger, the pre-heater turns on when the outdoor air temperature drops below −5°C, supplying controlled heating power to raise the air temperature to this threshold and thus

prevent frost formation on the exchanger core. In contrast, for the unit with the sensible recovery exchanger, the pre-heater is activated at 0°C. As a result, operating points below these thresholds are effectively equivalent to the corresponding limit conditions (−5°C or 0°C, respectively) and were therefore not included in the test matrix. The summer experimental campaign, by contrast, explored outdoor conditions up to 35°C, which are representative of high-load scenarios in warm climates.

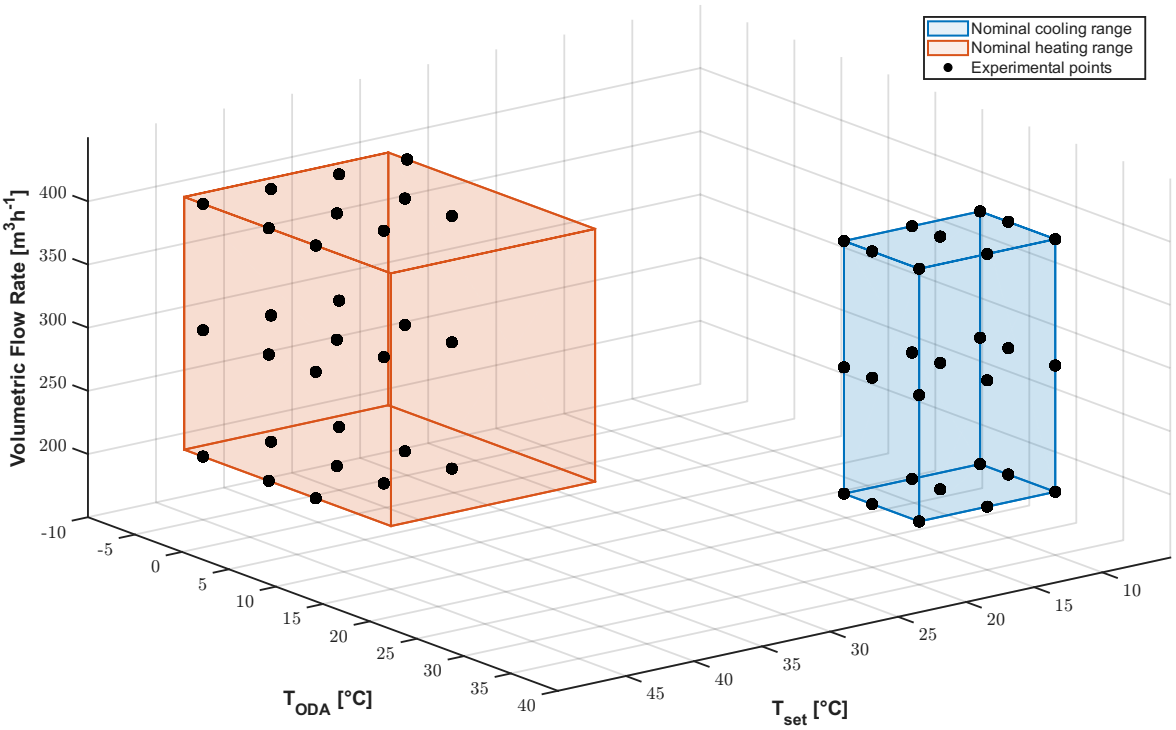

Figure 4.5: Experimental test matrix plotted against nominal heating and cooling boundaries.

For each outdoor temperature, the compressor frequency was manually adjusted to approach the prescribed post-supply temperature set-points T_{set}, within the limits of the unit's allowable frequency range. A test point was considered unfeasible and therefore excluded only if, at the immediately preceding set-point, the compressor was already operating at either its maximum or minimum permissible frequency. For example, at a supply airflow of 200 m^3h^{-1} and an outdoor temperature of 35 °C, the point corresponding to $T_{set} = 10$°C was not tested because at $T_{set} = 15$°C the compressor was already running at the maximum allowed frequency. Conversely, at the same airflow but with an outdoor temperature of 30 °C, the point at $T_{set} = 20$°C was not tested because at $T_{set} = 15$°C the compressor was already running at the minimum allowed frequency. In cooling mode (summer tests), the set-points were $T_{set} = 10, 15$ and 20°C, whereas in heating mode (winter test) they were $T_{set} = 35, 40$ and 45°C. These sets of values span, respectively, the minimum and maximum post-supply temperatures that can be imposed by the unit in summer and winter, thereby covering the entire operating range of the

compressor in both seasons. This approach was deliberately adopted to decouple the measurements from the internal control logic of the heat pump and to ensure stable and repeatable operating points, which is particularly critical under frosting conditions. Indeed, under these operating conditions, the built-in control would progressively increase the compressor speed in order to compensate for the performance degradation of the evaporator caused by frost accumulation, thereby continuously chasing the post-supply temperature set-point.

In addition, one further operating point was investigated at $T_{\mathrm{ODA}} = -5°\mathrm{C}$, $\dot{V} = 400\ \mathrm{m^3h^{-1}}$, and $T_{\mathrm{set}} = 30°\mathrm{C}$, to provide at least two reference conditions with identical outdoor temperature and airflow rate. Each $(T_{\mathrm{ODA}}, T_{\mathrm{set}})$ combination was subsequently tested at three values of ventilation flow rate: $\dot{V} = 200, 300$ and $400\ \mathrm{m^3h^{-1}}$.

In both winter and summer scenarios, data logging was initiated only after the ventilation unit had reached steady-state conditions, at which point the heat pump was also switched on. In summer tests and in frost-free winter tests, each operating point was then maintained for a duration of one hour, which proved sufficient for the heat pump itself to reach steady-state. In winter tests affected by frosting, instead, data were recorded continuously over a period covering three complete operating cycles of the heat pump, each consisting of a heating phase followed by a defrost phase. This allowed the transient behavior associated with frost accumulation and removal to be fully captured.

To obtain a reliable mapping of the fan power consumption, the unit was operated with a constant external pressure difference of 50 Pa applied to each duct relative to the ambient. This boundary condition was imposed in both heating and cooling tests, so that the measured fan energy demand reflects realistic installation scenarios and can be consistently reproduced in the model.

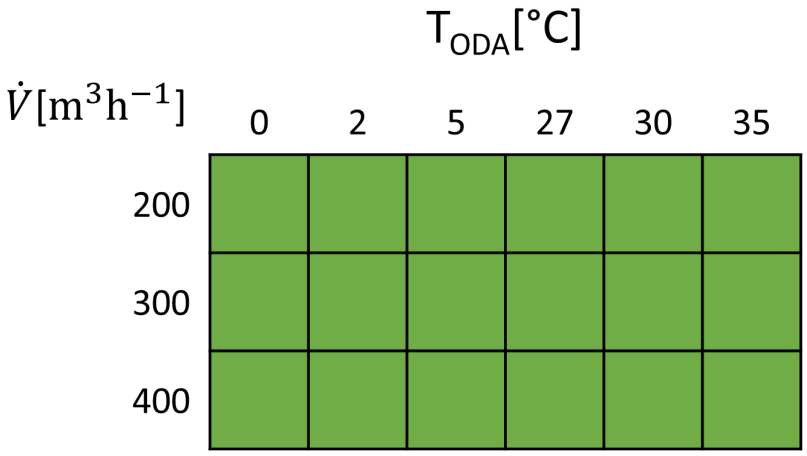

Figure 4.6: Additional test matrix for the MVHR/HRV unit.

Besides to the complete-unit tests, a set of complementary measurements (Figure 4.6) was performed on the ventilation subsystem alone, with the heat pump deactivated. In

particular, tests with the MVHR/HRV configuration (sensible-only recovery) were conducted at outdoor air temperatures of $0, 2, 5, 27, 30$ and $35°C$, each repeated at airflow rates of $200, 300$ and $400\ m^3h^{-1}$.

Moreover, six additional measurement points were available from previous campaigns conducted in the same laboratory for the MVHR/ERV configuration (enthalpy recovery). These measurements were performed at a lower airflow rate of $150\ m^3h^{-1}$ at outdoor air temperatures of $-5, 2, 7, 27, 30$ and $35°C$. In all of these additional tests, the thermo-hygrometric conditions of the "ambient" chamber were fixed at 70% relative humidity (RH) for winter and 50% RH for summer, while the "room" chamber was kept at 20°C and 50% RH in winter, and 22°C and 50% RH in summer.

Figure 4.7: Overview of the experimental testbench.

CHAPTER 5

Experimental outcomes and model validation

In this chapter, the experimental outcomes and the validation of the developed digital twin are presented. Preliminary findings regarding compressor heat losses and pressure estimation are applied to refine the model and verify measurement reliability. The validation process is then detailed, encompassing the component-level verification of recovery exchangers against data from a notified body and the numerical validation of fin-and-tube heat exchangers against a reference software. Finally, the predictive accuracy of the complete system is assessed against experimental datasets under both summer and winter regimes, with specific focus on performance under frosting conditions and the validation of the simplified defrost model.

5.1. Experimental outcomes

During the experimental campaign, two main findings were obtained that are relevant for the validation and refinement of the model.

Heat loss correction. The first finding concerns the compressor characterization. In order to achieve a consistent agreement between measured and simulated discharge temperatures, it was evident that additional heat losses were taking place downstream of compressor. As a matter of fact, the experimental data often suggested isentropic compressione efficiencies apparently higher than one, which is obviously unrealistic. This discrepancy was traced back to thermal losses occurring through the compressor shell and the uninsulated portion of the discharge line, which lowered the temperature measured at the discharge port even compared to the ideal adiabatic prediction. To quantify this effect, a dedicated series of measurements was conducted under summer conditions,

which ensure stable operating points. In these tests, the compressor body and the entire discharge line were additionally insulated with a 1 cm layer of flexible elastomeric foam. Figure 5.1 shows the resulting discharge temperatures as a function of the cooling load (defined according to Equation (6.1)), a quantity used to defined the specific operating point. From these measurements, realistic values of isentropic efficiency ranging from 0.80 to 0.67 were obtained, depending on the operating point. Based on these data, a lookup table of isentropic efficiency as a function of pressure ratio (pr) and compressor rotational speed (ω) was derived, with values linearly interpolated within the operating domain.

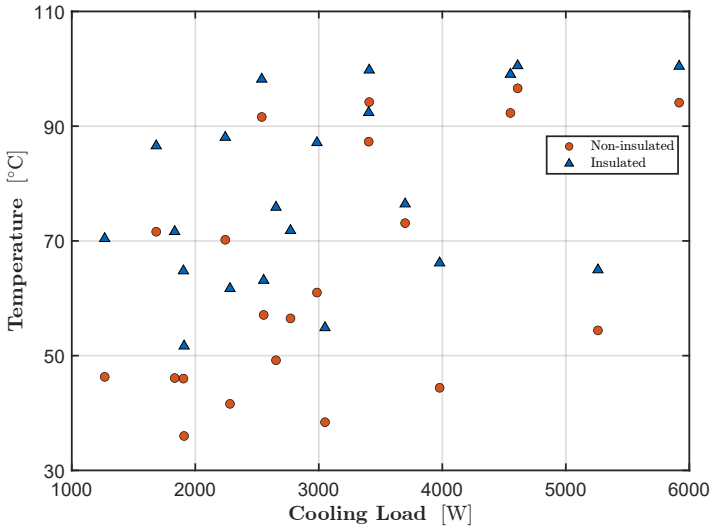

Figure 5.1: Discharge temperatures recorded with the discharge line insulated and non-insulated.

The heat losses in the non-insulated configuration of the real system were subsequently identified by matching the measured discharge temperatures against the values predicted using the isentropic efficiency map. This led to the introduction of an empirical heat loss model, expressed as:

$$\dot{Q}_{loss} = K(pr, \omega)\dot{W}_{comp} \tag{5.1}$$

where $K(pr, \omega)$ is the heat-loss factor, stored in tabulated form and linearly interpolated across the operating domain. In this formulation, the heat loss is treated as a system-specific characteristic, inherently linked to the compressor and to its installation within the unit. The same procedure was also applied to the heating mode, where $K(pr, \omega)$ was derived starting from a realistic constant isentropic efficiency of 0.75, corresponding to the average value obtained from the summer tests, as no measurements with an insulated discharge line were collected during winter operation.

Saturation pressure estimation. The second finding relates to the validation of the condensation and evaporation temperature readings. A central objective of the experimental campaign was to obtain a model validated against measurements on a unit as close as possible to its original factory configuration, without introducing alterations that could compromise its intrinsic characteristics. For this reason, direct pressure measurements could not be performed on the primary system, since the installation of refrigerant-side pressure probes requires invasive modifications to the circuit. These operations involve evacuating the refrigerant, cutting the piping, and brazing the sensor connections, which would have inevitably altered the state of the machine under investigation. To overcome this limitation, the validation was carried out on a secondary heat pump unit of the same type as the analyzed one, where Wurm DAR60 pressure transducers were installed at the suction and discharge ports of the compressor component. These sensors provide an accuracy of ±1% at 0 °C (±0.8% at 20 °C and ±1.2% at −20°C). The comparison between the saturation pressures derived from the embedded temperature sensors located within the heat exchanger circuits and the pressures measured by the transducers is reported in Figure 5.2. Several operating points were tested under both winter and summer conditions. However, only the most critical case is shown, corresponding to an unstable winter operating point where the compressor control logic was let to repeatedly adjusted the rotational speed and the evaporator was also affected by frosting, with three consecutive defrost cycles clearly visible. Despite these conditions, an excellent agree-

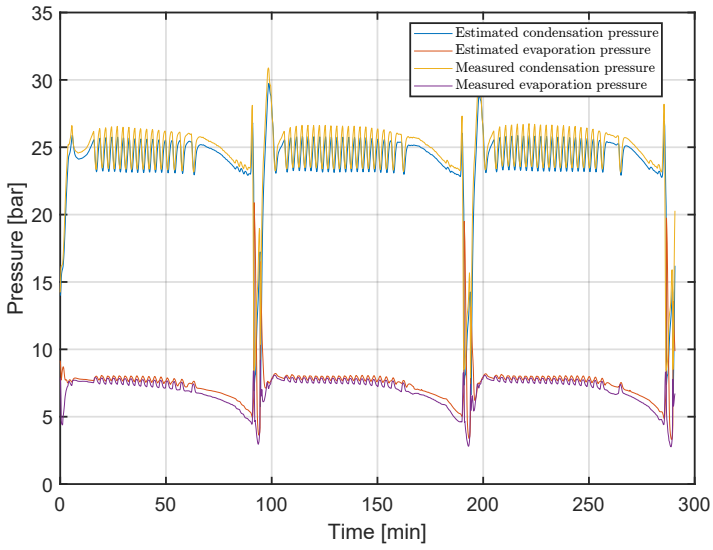

Figure 5.2: Estimated versus measured saturation pressures.

ment was observed between the two datasets. On average, the estimated high pressure was 0.6 bar lower than the measured value, while the low pressure was overestimated by about 0.3 bar. These deviations are expected and justified, as the pressure transducers were installed across the compressor and therefore did not account for the pressure drops in the connecting line and in the four-way valve. A significant discrepancy was

found only during the initial start-up transient, which can be attributed to the thermal inertia of the refrigerant circuit and metallic components. Overall, the results confirm that the saturation pressures estimated from the refrigeration temperature sensors, both the additional ones installed for the tests and the built-in sensors of the unit, provide sufficiently accurate estimates of the actual condensation and evaporation conditions.

5.2. Model validation

5.2.1. Preliminary validation of the recovery exchanger model

A first validation of the recovery exchanger model was conducted using experimental data provided by a notified body. The two types of recovery cores were analyzed: the enthalpy exchanger and the sensible-only exchanger. Both components were tested according to the EN 13141-7 [84] standard, which specifies the performance testing methods for heat and energy recovery systems used in residential ventilation units.

For the enthalpy exchanger, experimental data were available under two reference sets of boundary conditions, representative of typical winter and summer operation:

- Winter: $RH_{ODA} = 70\%$, $T_{ODA} = 5$ °C; $RH_{ETA} = 50\%$, $T_{ETA} = 25$ °C
- Summer: $RH_{ODA} = 50\%$, $T_{ODA} = 35$ °C; $RH_{ETA} = 60\%$, $T_{ETA} = 25$ °C

For the sensible-only exchanger, experimental measurements were available only for winter conditions, at the following operating points:

- $RH_{ODA} = 80\%$, $T_{ODA} = 7$ °C; $RH_{ETA} = 40\%$, $T_{ETA} = 20$ °C
- $RH_{ODA} = 80\%$, $T_{ODA} = 2$ °C; $RH_{ETA} = 60\%$, $T_{ETA} = 20$ °C

The deviations reported in the subsequent figures were expressed as normalized percentage deviations with respect to a reference values (X_{ref}):

$$\text{Percentage deviation} = \frac{X_{meas} - X_{sim}}{X_{ref}} \cdot 100 \tag{5.2}$$

A reference temperature of 35 °C and a reference relative humidity of 100% were adopted for normalization.

For the enthalpy exchanger (Figure 5.3), the model reproduced the experimental behavior across the full operating range with very high accuracy and without incorporating any calibration coefficients. The agreement remained consistently strong in both winter and summer operation and for all outlet thermo-hygrometric conditions. This outcome demonstrated the robustness of the underlying formulation and confirmed its applicability across a wide range of boundary conditions.

For the sensible-only exchanger (Figure 5.4), the predictive accuracy remained good, although slightly larger deviations were observed. These differences primarily reflected

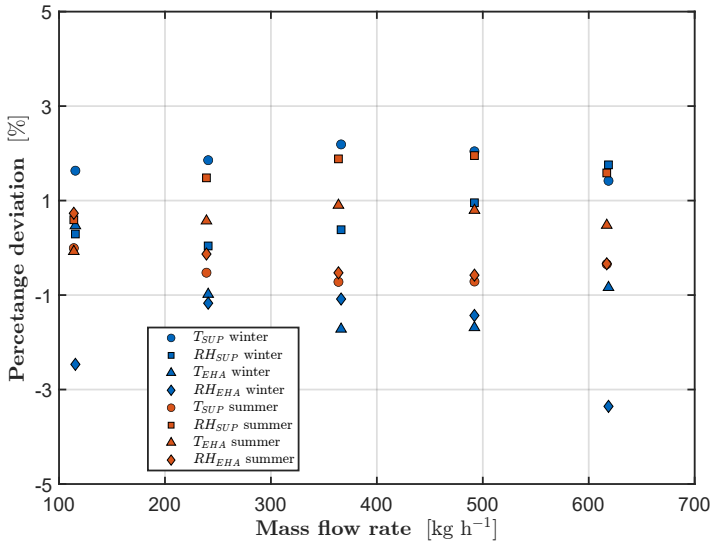

Figure 5.3: Percentage deviations for the air outlet conditions of the MVHR/ERV unit.

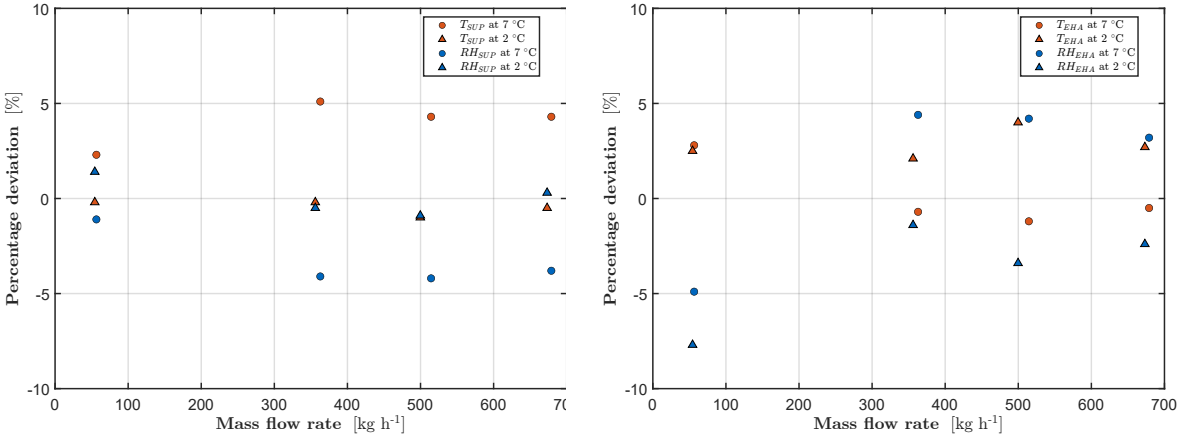

(a) Supply air conditions. **(b)** Exhaust air conditions.

Figure 5.4: Percentage deviations for the air outlet conditions of the MVHR/HRV unit under winter operation.

the heightened sensitivity of the HRV performance to condensation, which strongly influences both heat transfer and the outlet conditions. Consequently, small inaccuracies in predicting the onset and magnitude of condensate formation can lead to more noticeable discrepancies. A minor contribution also stems from the simplified, calibrated treatment of condensate re-evaporation. Even so, the model reliably reproduced the experimental trends across all tested operating points.

Overall, the comparison confirms that the model provides a physically consistent and sufficiently accurate representation of both sensible and enthalpy recovery processes. A broader experimental verification will be presented later on, including additional measurements under summer operation for the sensible-only exchanger, to further corroborate the assessment of the model across different regimes.

5.2.2. Numerical validation of the fin and tube HX model

A first validation of the fin-and-tube heat exchanger was performed via simulation. A heat exchanger with 3 tube rows and 15 tubes per row, composed of two parallel refrigerant circuits, was simulated. R32 was selected as the working fluid. The results of the developed model were compared against those obtained using EVAP-COND 5.0, a widely used steady-state simulation tool for air-to-refrigerant heat exchangers. EVAP-COND, developed by NIST, is based on a detailed segment-by-segment modeling of the heat exchanger geometry, accounting for refrigerant flow distribution, phase-change phenomena, and heat and mass transfer processes on both the air and refrigerant sides. To support the validity of the multi-circuit approximation, a uniform air velocity distribution was assumed across the frontal surface of the heat exchanger. Two different operating conditions for the heat exchanger were tested:

- **Condenser operating condition:** on the refrigerant side, inlet mass flow rate of $40\,\mathrm{kg\,h^{-1}}$, inlet saturation temperature of 45 °C, and 30 °C of superheating. On the air side, volumetric flow rate of $450\,\mathrm{m^3h^{-1}}$ (based on a standard air density of $1.204\,\mathrm{kg\,m^{-3}}$, as defined in the EVAP-COND software), with inlet air conditions of 22 °C and 50 % relative humidity.

- **Evaporator operating condition:** on the refrigerant side, inlet mass flow rate of $40\,\mathrm{kg\,h^{-1}}$, inlet saturation temperature of 7 °C, and 0.2 of vapor quality. On the air side, volumetric flow rate of $450\,\mathrm{m^3h^{-1}}$ (based on a standard air density of $1.204\,\mathrm{kg\,m^{-3}}$, as defined in the EVAP-COND software), with inlet air conditions of 26 °C and 50 % relative humidity.

Since the developed model uses a *segment-by-segment* approach, the comparison was performed by varying the number of segments. The coarsest discretization corresponded to the minimum resolution required to capture the temperature gradient on the moist air (MA) side, using only one segment per row. The number of segments was then increased by one per row in sequence, starting from the air inlet row. Conversely, within the EVAP-COND software, the discretization method was set to the finest resolution.

As shown in Figures 5.5a and 5.5b, the accuracy of the proposed model improved as the number of segments increased, gradually converging toward the EVAP-COND reference solution. For the condenser, the sensible heat flow rate deviation at convergence was approximately 2.7% compared to EVAP-COND. In contrast, under the evaporator operating condition, the model underestimated the sensible heat transfer by approximately 2.4% and overestimated the latent heat transfer by 6.8% at convergence. Despite these deviations, the compensating effect between sensible and latent contributions limited the total heat transfer error to 0.18%, as the sensible heat was roughly twice the latent heat in this specific case. The larger discrepancy in latent heat was likely attributable to differences in the air-side condensation model and the use of different correlations for the

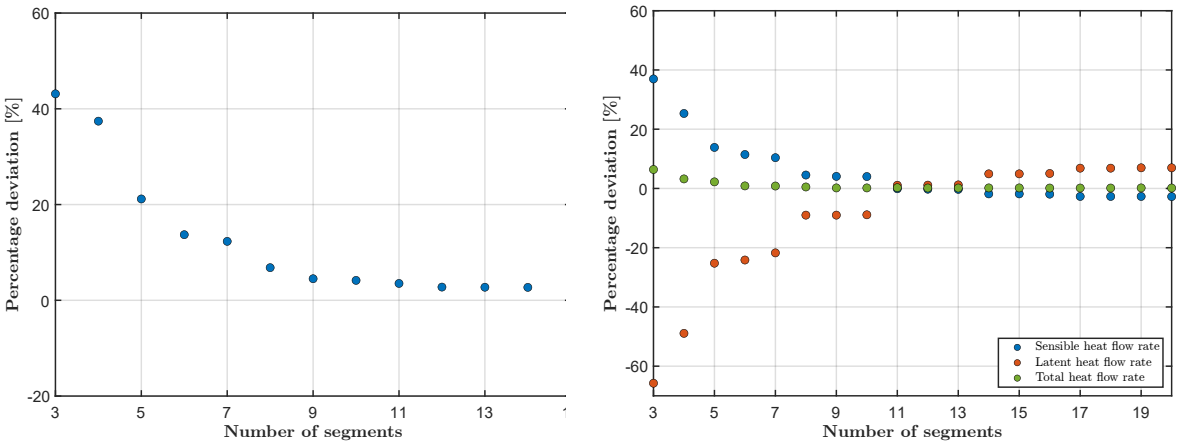

(a) Condenser **(b)** Evaporator

Figure 5.5: Heat flow rate percentage deviation in condenser (a) and evaporator (b) operating condition.

heat transfer coefficients on both the air and refrigerant sides. A 9-segment discretization was found to be sufficient to achieve a satisfactory convergence error for the condenser case, while a finer discretization of 14 segments was required for the evaporator case.

It is worth noting that, for the evaporator case (Fig. 5.5b), when more than five segments were used (specifically, two segments in each of the first two rows and one in the third), the accuracy improved only if the discretization of the second row was further refined. In contrast, the results remained almost insensitive to the number of segments in the first and third rows. To better illustrate this, Fig. 5.6 shows the same convergence analysis, but with additional discretization applied exclusively to the second row, while the first and third rows were kept coarser (three and one segment, respectively).

This behavior is dictated by the local thermodynamics of the heat exchanger. In the specific case considered, the transition from two-phase to superheated vapor occurs within the second row, triggering a sharp spatial variation in the refrigerant-side heat transfer coefficient. In addition, because the inlet temperature difference between the two-phase refrigerant and the moist air remains substantial at this stage, significant sensible heat transfer persists. The coupling of these effects generates a steep wall temperature gradient along the second row, making both condensation and latent heat transfer highly sensitive to spatial discretization. Physically, a similar requirement for refinement arises in the first row when the refrigerant mass flow rate is low relative to the moist air flow rate. Conversely, while such conditions could theoretically occur in the third row if the refrigerant mass flow rate were disproportionately high, the reduced inlet temperature difference at that stage typically limits the wall temperature gradient. Consequently, further refinement in the third row is often computationally unjustified.

These findings suggest that a non-uniform discretization strategy is more efficient for the evaporator under analysis. By selectively refining only the first and second rows, a

9-segment discretization (configured as 3, 5, and 1 segments for the respective rows) was found to be sufficient to achieve a satisfactory convergence error. This optimized scheme reduced the computational cost by approximately 36% compared to a uniform 14-segment discretization without compromising too much the accuracy.

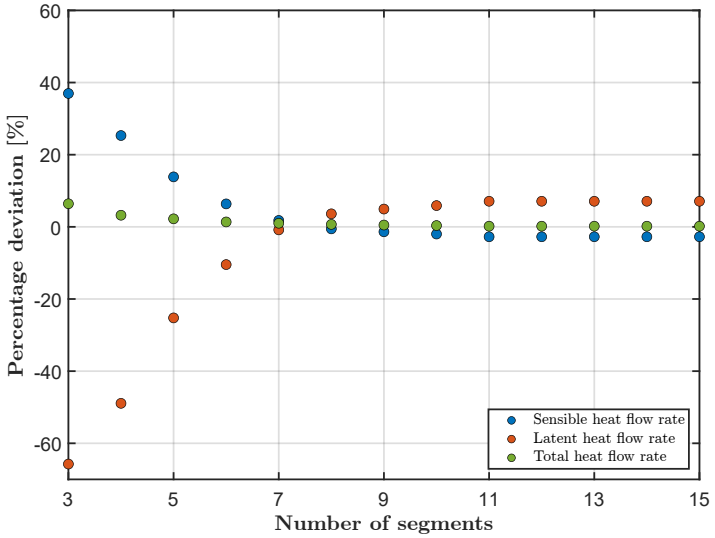

Figure 5.6: Evaporator percentage deviation with respect to the refinement of the second row discretization.

In terms of computational performance, EVAP-COND 5.0 required 5.8 seconds to reach the steady-state solution for both the condenser and evaporator cases. Conversely, the proposed converged models—configured with 9 segments for the condenser and 9 segments for the evaporator (using the optimized discretization scheme)—simulated 2000 seconds (enough to reach a steady-state solution) in approximately 1.20 seconds for the condenser case and 1.77 seconds for the evaporator case, resulting in a run-to-simulation time ratio of about 0.6 and 0.885 milliseconds respectively. Simulations were performed using an Intel® Core Ultra 7-265K processor.

5.2.3. Model validation using recorded experimental data

5.2.3.1. Summer operating conditions

Ventilation unit

Figures 5.7 and 5.8 present the relative deviations between simulated and measured thermo-hygrometric conditions at the ventilation unit outlets: *SUP* and *EHA*. No calibration procedure was applied to compensate for potential inaccuracies in the heat and mass transfer modelling. The percentage deviations are defined also in this case by Equation (5.2). For temperature, a fixed reference of 35 °C was adopted for normalization, while for relative humidity the saturation value of 100 % was used as reference.

For the unit equipped with an enthalpy exchanger (MVHR/ERV, Figure 5.7), the convective heat transfer coefficient (and the corresponding mass transfer coefficient, since

it was derived from the heat transfer coefficient through the heat-mass transfer analogy) was estimated using the Muzychka-Yovanovich correlations under the uniform wall temperature (UWT) boundary condition. The adoption of the UWT formulation resulted in a closer agreement with the experimental data, which is consistent with the findings of Zhang et al. [49], who showed that for enthalpy plate exchangers with a high channel aspect ratio (as in the case of the enthalpy exchanger analyzed here), the actual boundary condition can be reliably approximated by assuming a uniform wall temperature.

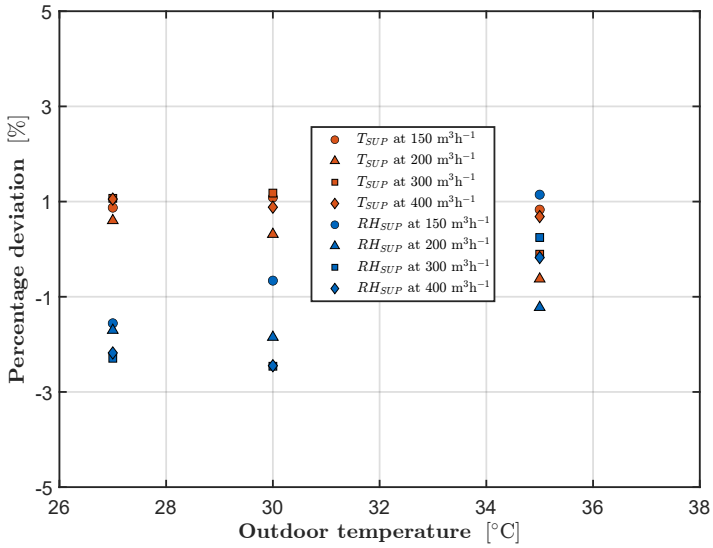

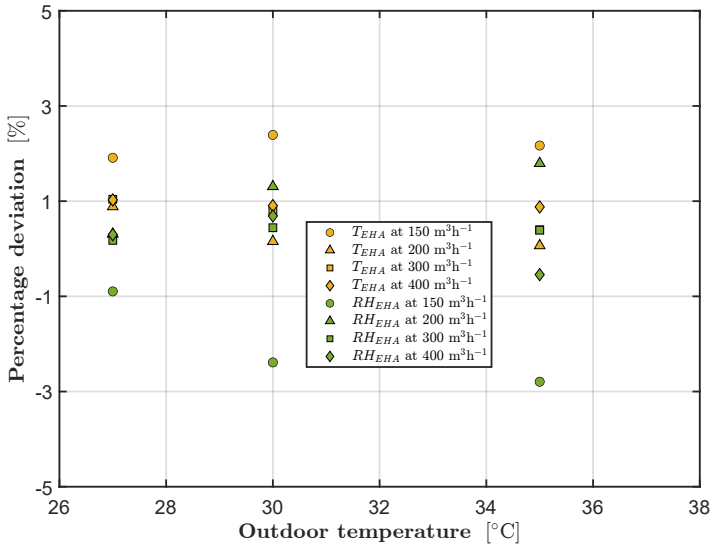

(b) EHA side

Figure 5.7: percentage deviations for temperatures and relative humidities of the MVHR/ERV unit.

In contrast, for the unit operating with a sensible-only exchanger (MVHR/HRV, Fig. 5.8), the Muzychka-Yovanovich correlations under a uniform wall heat-flux (UWF) assumption yielded a better match with the experimental data. This result can be explained by the structural characteristics of the exchanger under consideration, which features a thicker

separating wall, a channel aspect ratio close to unity, and a wall material with limited thermal conductivity. These aspects make the uniform wall-flux assumption more physically consistent.

Overall, in both configurations the relative deviations remained within ±5% for temperatures and within ±10% for relative humidities at both the *SUP* and *EHA* outlets, thereby confirming the robustness of the modelling approach.

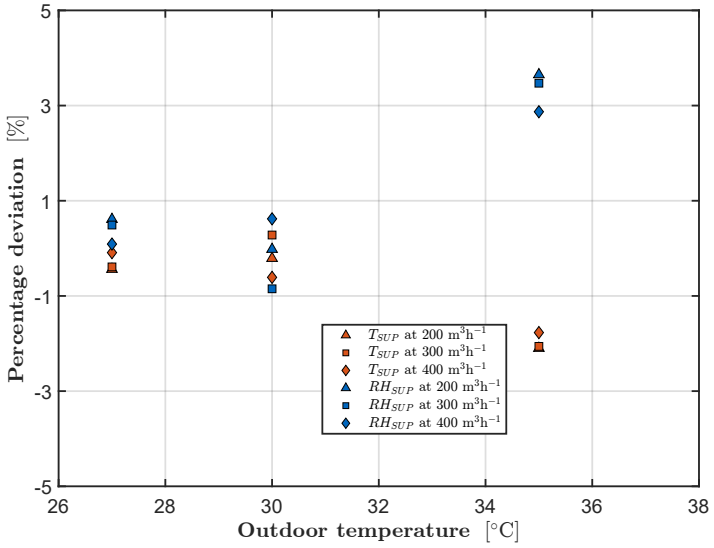

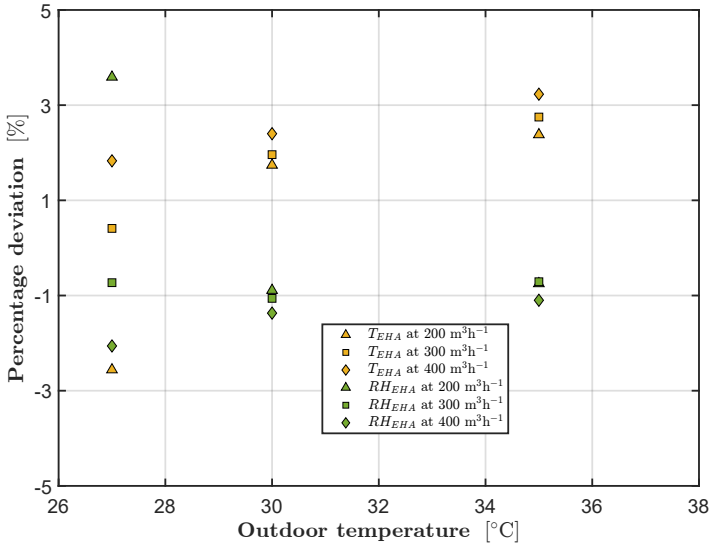

(b) EHA side

Figure 5.8: Percentage deviations for temperatures and relative humidities of the MVHR/HRV unit.

In addition to validating the predicted outlet air conditions, the developed model was evaluated with respect to the electrical power consumption of the ventilation unit. The data referred to the MVHR system equipped with an enthalpy recovery exchanger, yet they were equally representative of the sensible-only configuration, since both types of heat-recovery devices involved comparable air-side pressure losses. This comparison en-

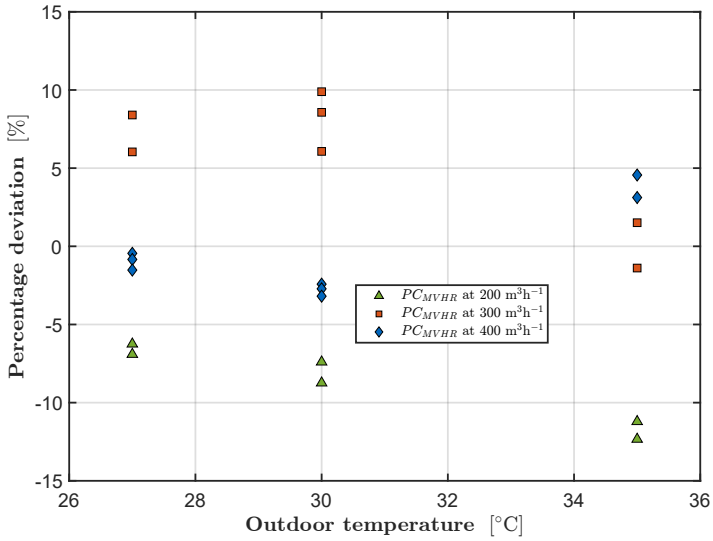

Figure 5.9: Percentage deviation for power consumption of the MVHR.

abled both a direct validation of the predicted fan-power consumption and an indirect assessment of the accuracy of the unit's pressure-drop representation, which was not directly measured during the experimental campaign. The deviations reported in Fig. 5.9 remained within ±12%, confirming the robustness of the adopted modelling strategy. In this case, the main source of uncertainty was associated with the filter resistance, whose pressure drops are strongly influenced by fouling. Progressive clogging of the filter medium increases airflow resistance, thereby shifting the fan operating point and raising the corresponding electrical-power demand.

Overall unit

Figures 5.10 and 5.11 present the validation results for the complete unit. Figure 5.10 reports the relative deviations of the main system-level performance indicators, including the total cooling capacity ($\dot{Q}_{sys}$) and the total energy efficiency ratio (EER_{sys}). Conversely, Figure 5.11 provides a detailed analysis of the operational parameters and is composed of three distinct parts. First, Figure 5.11a illustrates the percentage deviations of the outlet air conditions, which correspond to the thermo-hygrometric states of the PSUP and PEHA streams. Second, Figure 5.11b presents the percentage deviations of the air-side pressure drops across the two fin-and-tube heat exchangers of the heat pump. Finally, Figure 5.11c focuses on the percentage deviations of the refrigerant-cycle control temperatures, specifically the condensation, evaporation, and discharge temperatures. For these quantities, a modified scaling approach was adopted using a reference value of 50 °C. This reference represents the maximum condensation temperature physically permitted by the system before triggering a protection state. Its application ensures a consistent normalization of the relative deviations, properly accounting for the significantly higher magnitude of the refrigerant-side temperatures compared to the air-side conditions.

A minor calibration step was introduced exclusively for the modelling of the air-side pressure drops. Specifically, the friction factor predicted by the correlations of Wang et al. [114], discussed in Chapter 3, was multiplied by a correction factor of 0.9. This adjustment is physically justified by the actual geometry of the unit, where the heat exchangers are installed with an inclined orientation relative to the airflow, in contrast to the orthogonal configuration considered in the experimental dataset of Wang et al. [114]. The inclination reduces the effective flow resistance, leading to lower measured pressure drops and explaining the need for a correction.

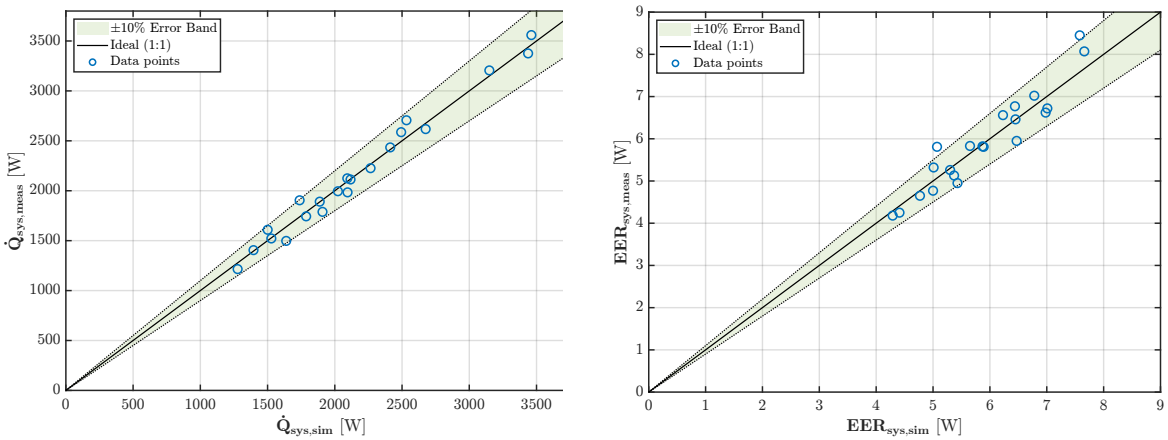

(a) System Capacity **(b)** System EER

Figure 5.10: Percentage deviations of overall system performance indicators.

Overall, the model demonstrates excellent agreement with the experimental data. Both the global performance indicators and the outlet air thermo-hygrometric conditions are predicted with an accuracy of approximately ±10%, while comparable precision is achieved for air-side pressure drops and refrigerant-cycle temperatures. The strong consistency with the measurements, combined with the minimal calibration required, confirms that the model accurately captures the dominant physical phenomena of the system. As a result, the developed digital twin can be regarded as a reliable predictive tool not only under tested operating points but also for extrapolation to untested scenarios, providing a robust foundation for further analyses and system-level investigations.

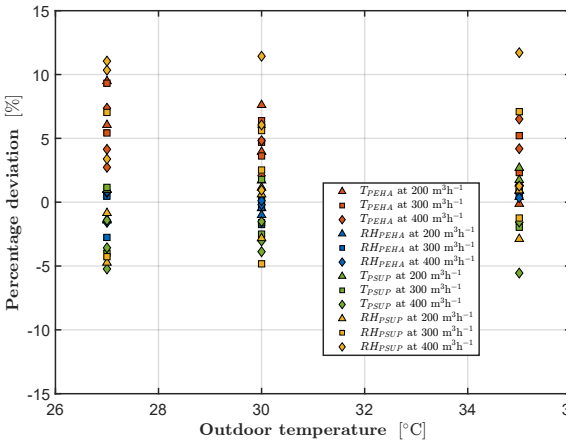

(a) Outlet air conditions

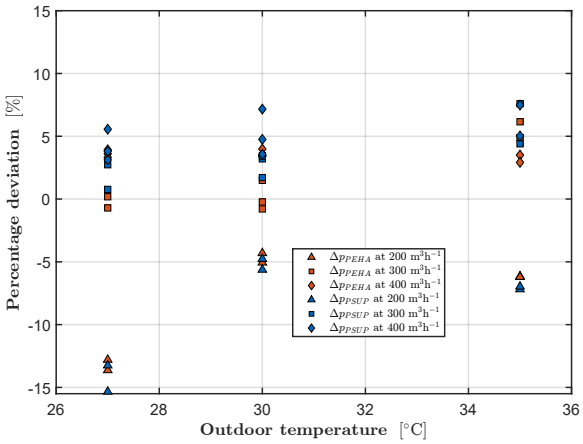

(b) HP pressure losses

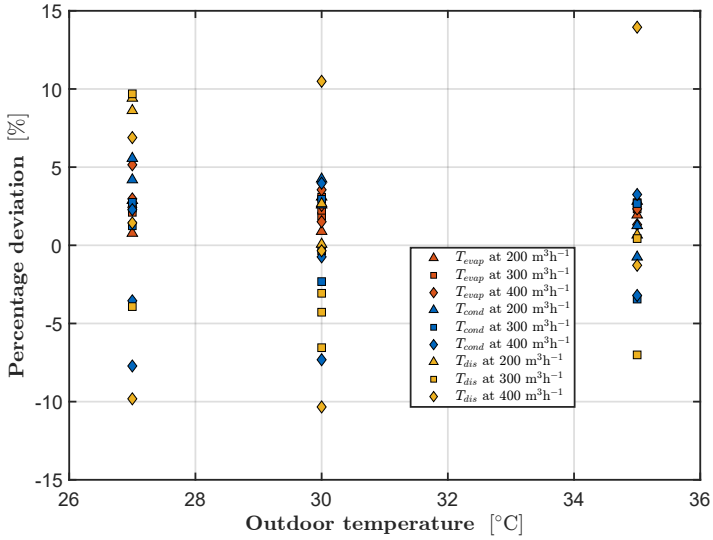

(c) Refrigeration cycle temperatures

Figure 5.11: Percentage deviations for the main system operating parameters.

5.2.3.2. Winter operating conditions

Ventilation unit

The validation of the ventilation unit under winter operating conditions is presented in Figures 5.12, 5.13, and 5.14. For the MVHR/ERV configuration (Figure 5.12), the comparison between experimental and simulated data revealed a systematic underestimation of the supply-air temperature by approximately 2.5%, which resulted in a corresponding overestimation of the supply relative humidity. A similar consistent error was also observed during the comparison with notified body data (presented in Section 5.3), suggesting that the observed bias can therefore be attributed to a slight underestimation of the sensible effectiveness of the enthalpy exchanger under winter conditions.

For the MVHR/HRV configuration (Figure 5.13), a similar pattern was observed on the exhaust side. In this case, however, the deviation is more plausibly associated with the simplified formulation adopted to model the re-evaporation of condensed water within

the recovery exchanger. The current representation assumes an instantaneous and spatially uniform re-evaporation process, whereas in reality the phenomenon is transient and spatially heterogeneous, depending on local wall temperature and air-humidity conditions. Such simplification may therefore lead to small residual discrepancies in the predicted exhaust-air temperature and relative humidity. Nonetheless, these deviations remain minor and do not compromise either the reliability of the experimental dataset or the overall validity of the numerical model.

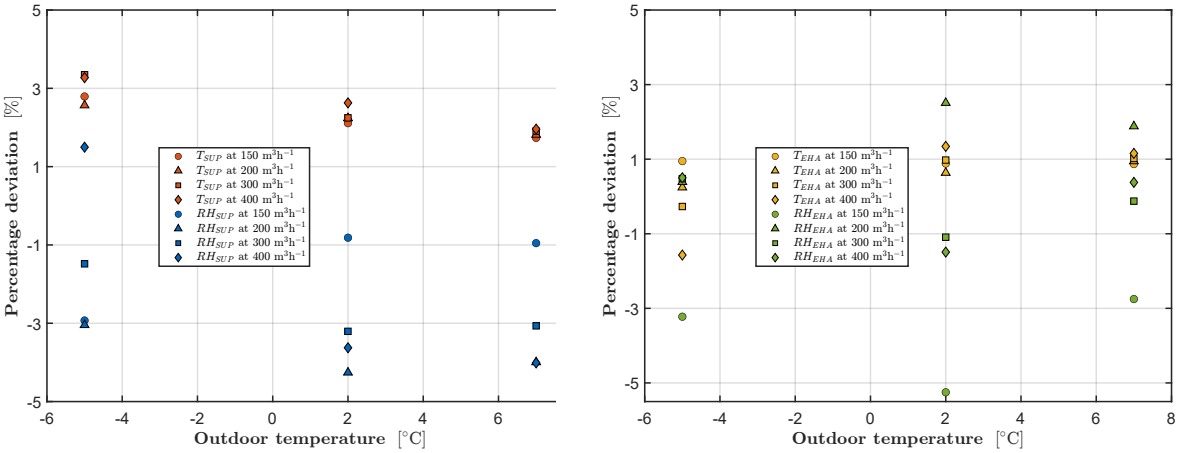

(a) SUP side **(b)** EHA side

Figure 5.12: Percentage deviations for temperatures and relative humidities of the MVHR/ERV unit.

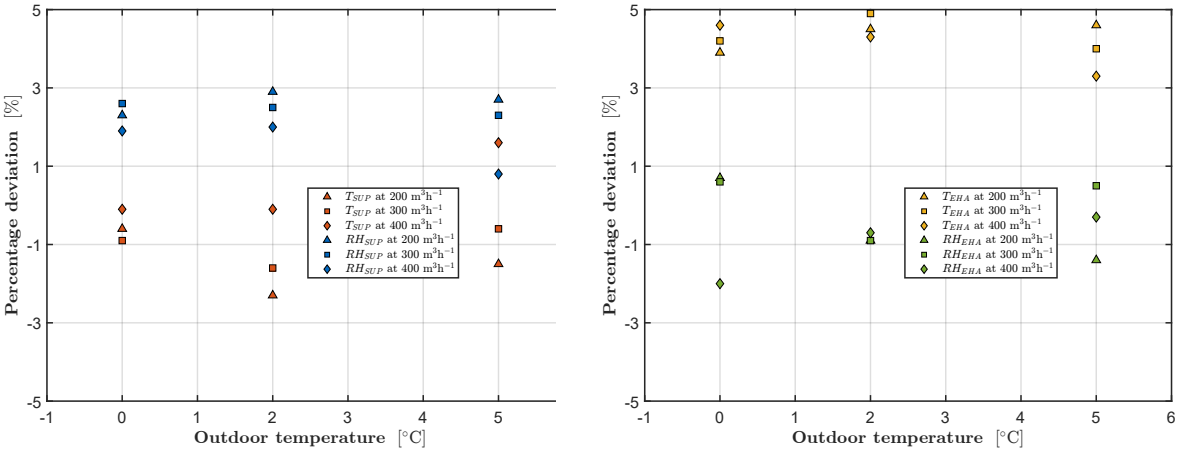

(a) SUP side **(b)** EHA side

Figure 5.13: Percentage deviations for temperatures and relative humidities of the MVHR/HRV unit.

Regarding the electrical power consumption (Figure 5.14), the model shows a generally good agreement with the experimental data, with percentage deviations typically within ±10 %. The largest positive deviations (up to 13 %) are observed at the lowest outdoor temperature (around $-5\ ^{\circ}C$), where the frosting dynamics on the heat pump

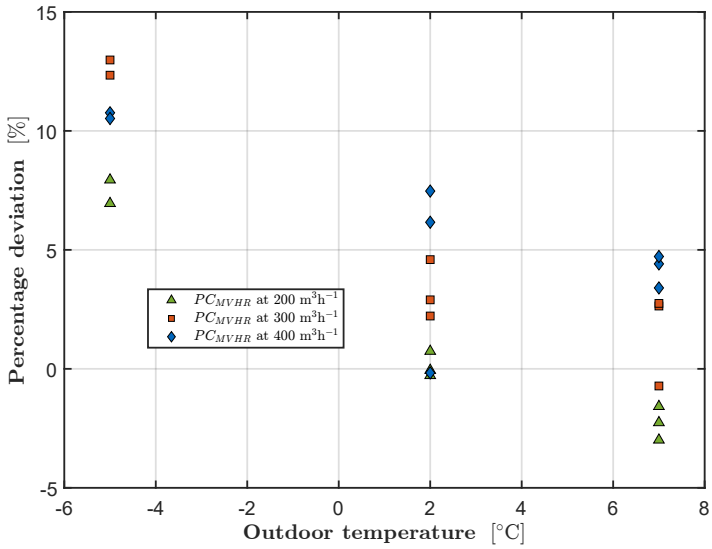

Figure 5.14: Percentage deviations for power consumption of the MVHR.

evaporator strongly affect the fan power demand of the ventilation unit, particularly at high air flow rates. This behavior should be interpreted in conjunction with the results presented in Figure 5.16b, which reports the percentage deviations on the predicted air-side pressure losses of the heat pump. Indeed, this pressure loss error also influences the predicted power consumption of the ventilation unit.

Overall, these results confirm that the numerical model reliably reproduces both thermodynamic and electrical performance also across the winter operating range.

Overall unit

The overall system validation under winter conditions is detailed in Figures 5.16 and 5.15a, highlighting the predictive accuracy of the model during active heating operations. The validation was performed using time-averaged quantities of air conditions and system performance, calculated over three consecutive heating cycles (i.e., intervals between defrost events). This methodological approach allows for an accurate representation of the system behavior while still capturing the progressive degradation of performance induced by frost accumulation. The defrost periods are excluded from this analysis and are discussed separately in the subsequent section.

To achieve a satisfactory agreement between the predicted and measured air-side pressure losses on the exhaust side of the heat pump, a local restriction was introduced and modeled in parallel with the outdoor coil, following the same formulation presented in Section 3.2.8. This restriction represents the free-flow area available for the air stream to bypass the heat exchanger without effectively passing through it. In the investigated unit, this bypass path corresponds to the small clearance around the bypass flap of the heat pump, which is mechanically actuated during the defrost phase to isolate the outdoor coil from the ventilation airflow. The flap cannot be perfectly sealed against the

surrounding wall, since a small gap must be maintained to allow its movement and prevent mechanical jamming. This design feature results in a residual bypass section that, although negligible under normal (i.e., frost-free) conditions due to its high pressure drop, may become relevant under severe frosting when the evaporator pressure losses increase significantly. In such cases, a non-negligible portion of the airflow may be diverted through this preferential path.

It is worth noting that, for both the evaporator and condenser of the heat pump, the same correction factor of 0.9 applied to the air-side friction factor under summer conditions was also applied in this case.

Overall, the model exhibits robust agreement with the experimental measurements. The system heating capacity (Figure 5.15a) and system COP (Figure 5.15b) are accurately predicted, with deviations generally lying within ±10%. A similar level of accuracy is observed for the errors in the outlet air thermo-hygrometric conditions (Figure 5.16a). Deviations in the refrigerant-side temperatures (Figure 5.16c) fall within comparable bounds, confirming that the main thermodynamic cycle is well reproduced. By contrast, the air-side pressure drop across the evaporator (Figure 5.16b) shows larger deviations, reaching up to ±20%. This discrepancy is mainly due to the interplay between the heat exchanger geometry and non-uniform frost growth, as well as the extrapolation of friction-factor correlations beyond their nominal range of validity. Nevertheless, the consistent agreement across the main system performance indicators demonstrates that the digital twin reliably captures the system behavior also under winter conditions.

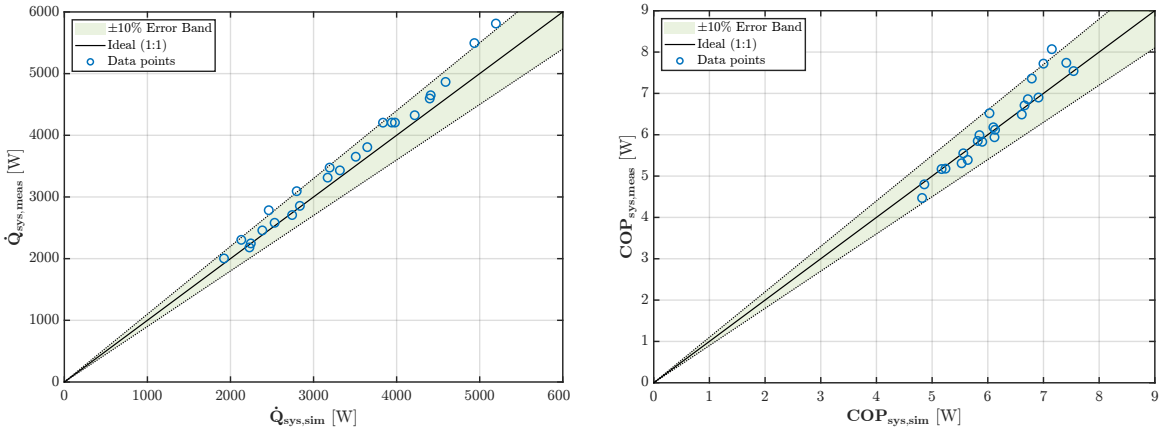

(a) System heating capacity **(b)** System COP

Figure 5.15: Percentage deviations of overall system performance indicators.

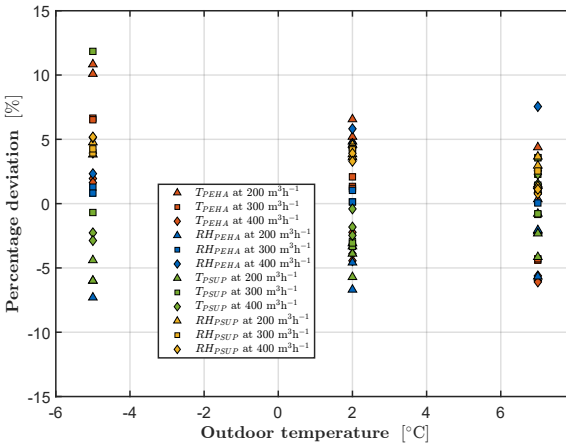

(a) Outlet air conditions

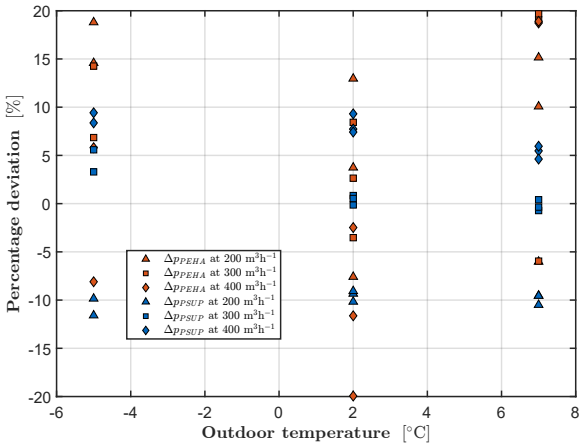

(b) HP pressure drop

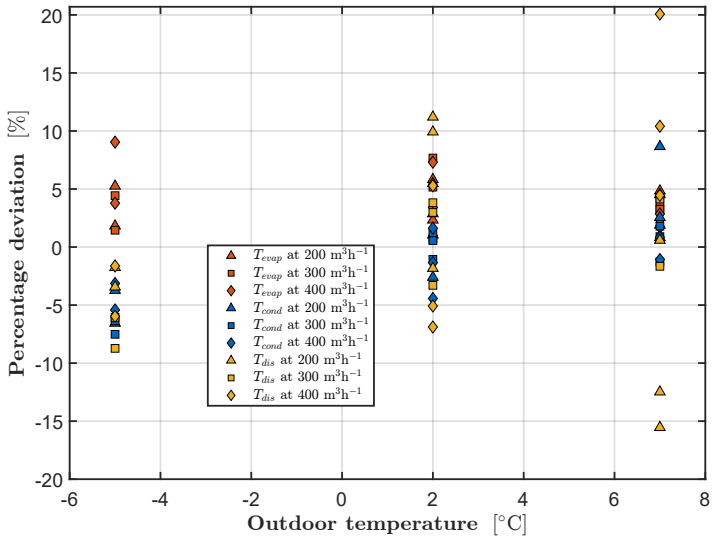

(c) Refrigeration cycle temperatures

Figure 5.16: Percentage deviations for the main system operating parameters.

Defrost operations

Building on the previously described frost formation model (Section 3.2.4.6), the digital twin incorporates a simplified representation of the defrost process, which restores the outdoor coil to frost-free conditions after each cycle. The model does not aim to reproduce the detailed physics of frost melting but instead estimates, in a coherent and computationally efficient manner, the quantities most relevant to system-level performance for the defrost phase: the duration of the defrost phase and the corresponding electrical energy consumption. This simplified formulation enables a consistent description of the complete frost-defrost sequence while maintaining low computational cost, which is essential for long-term and seasonal simulations. After each defrost event, the state variables defining the frost layer—thickness (δ_f) and average density ($\overline{\rho}_f$)—are reset to their initial values, allowing the model to reproduce the cyclic accumulation and removal behavior of frost.

In the unit under investigation, defrost initiation and termination are governed by a time–temperature logic embedded in the onboard controller, consistent with the strategy described by [124]. The same control sequence was implemented in the digital twin to reproduce the actual operating behavior of the system. A defrost cycle is triggered only after a minimum compressor runtime and once the evaporating temperature has remained below a predefined threshold for a specified time interval. The defrost cycle terminates after the compressor has operated for a defined duration and the temperature of the external coil has exceeded its release threshold for a sustained period.

As detailed above, to assess the seasonal impact of defrosting, the model had to predict the duration and energy demand of each defrost cycle. Since a fully physical simulation of the frost melting process would have been computationally prohibitive and unnecessary for system-level analyses, a simplified empirical formulation was developed using data from the winter test campaign. This approach provides an accurate yet efficient representation of the process dynamics.

The total defrost duration, $t_{tot,def}$, can be expressed as the sum of a passive phase ($t_{pass,def}$) and an active phase ($t_{act,def}$):

$$t_{tot,def} = t_{act,def} + t_{pass,def} \tag{5.3}$$

The passive phase includes the time intervals immediately before and after the active defrost operation. During this phase, the unit transitions from standard heating to reversed-cycle operation and then restores normal heating mode once the frost has been removed. Specifically, the heat pump bypasses the airflows through the heat exchangers to prevent the air from crossing the coils during the defrost, switches the four-way valve to invert the cycle, and performs routine control and safety checks. Although the corresponding electrical power demand is minimal, the duration of this phase represents a relevant portion of the total defrost period, during which the system provides no active heating. The passive phase time is therefore explicitly included in the total defrost duration and is assumed constant, as it mainly depends on the unit's internal control sequence rather than on external boundary conditions.

The active phase corresponds to the actual frost removal process, starting with compressor activation and ending when the evaporator is fully defrosted. Its duration depends on the amount, distribution, and structure of the frost layer accumulated during the preceding heating operation. To capture this dependency, a multivariate linear regression was developed to correlate the active defrost time with integral mean values of selected operating variables computed over the entire heating phase preceding the defrost. These quantities are assumed to influence or reflect the amount and characteristics of the frost accumulated on the external heat exchanger, and therefore to determine the

effort required for its removal:

$$t_{act,def} = C_0 + C_1\overline{T}_{EHA} + C_2\overline{RH}_{EHA} + C_3\overline{\Delta p}_{PEHA} + C_4\overline{T}_{evap} + C_5\overline{\dot{V}}_{MVHR} \tag{5.4}$$

The above regression achieved a correlation coefficient of $R^2 = 0.88$, confirming its suitability for system-level performance analyses.

The total electrical energy consumed during defrost, E_{def}, was then correlated with the total cycle duration through a linear regression:

$$E_{def} = C_0 + C_1 t_{tot,def} \tag{5.5}$$

This captures the nearly linear dependence between energy consumption and defrost duration, providing a simple yet effective way to estimate the associated energy penalty. The regression achieved a correlation coefficient of $R^2 = 0.93$.

The proposed simplified model was then verified by directly comparing the predictions of the digital twin with experimental measurements collected during the winter campaign. Each defrost event in the simulation was reproduced using the empirical correlations 5.4 and 5.5. Figure 5.17 presents the comparison between modeled and measured values for the two key metrics—cycle duration and electrical energy consumption. Deviations remained within ±10 %, indicating that the simplified formulation provides a reliable estimation of the aggregated impact of defrost events under the tested conditions.

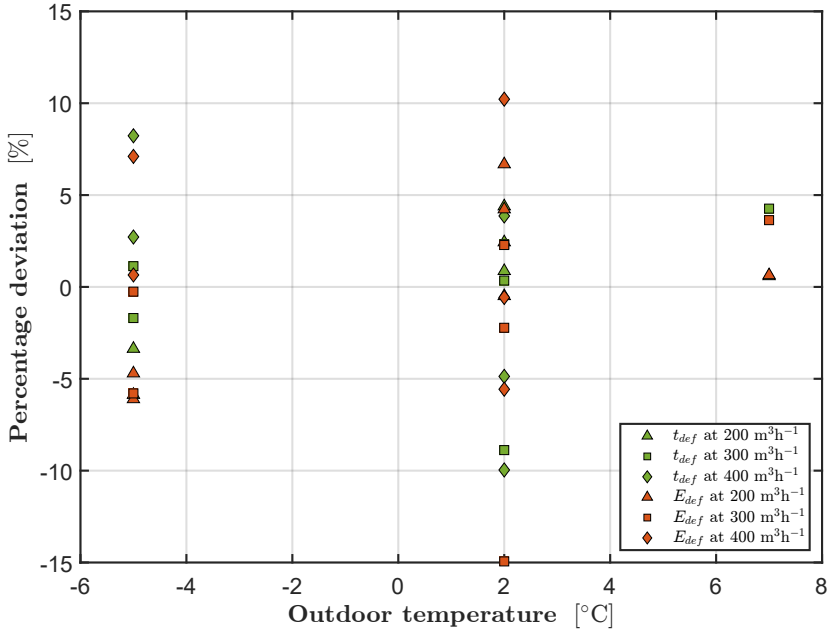

Figure 5.17: Percentage deviations for defrost operations.

CHAPTER 6

Predictive capability of the Digital Twin

In this chapter is evaluated the capability of the digital twin to predict system behavior under varying operating conditions through a series of analyses addressing the research questions introduced in Chapter 1. The investigation first compares the standard configuration of the unit with an alternative variant integrating an auxiliary Outdoor Exhaust Air (OEA) fan in the HP unit. The analysis then considers the influence of different heat-recovery technologies—enthalpy-based versus sensible-only (ERV vs. HRV)—and subsequently examines the role of bypassing strategies applied to the recovery exchanger. These configurations are assessed to quantify their impact on system performance and on the post-supply air conditions required to meet the desidered set-point. After establishing predictive capability of the model in cooling operations, the analysis shifts to heating operations, where frost formation on the outdoor heat exchanger introduces additional physical complexity. Frost accumulation alters heat-transfer and pressure-drop characteristics, degrades performance, and triggers defrost cycles that must be represented accurately.

6.1. Summer conditions

In this section, each analysis was carried out in two modes. The first focused on fixed-frequency operation of the compressor. In this case, the simulations were run under exactly the same boundary conditions as those adopted in the experimental campaign described previously, including the indoor and outdoor thermo-hygrometric conditions, the airflow rates, and the compressor speed. In the second mode, the same boundary conditions were applied, but the compressor frequency was no longer fixed. Instead, the unit's control logic was enabled, allowing the compressor speed to adjust dynamically in order to satisfy the post-supply temperature set-point. This two-step procedure

established a consistent evaluation framework. Fixed-frequency tests isolated the effect of each unit configuration on the refrigeration cycle, at identical operating conditions. This allowed a direct assessment of architecture-driven changes in system performance. Control-driven tests, instead, captured how the operating point shifted once the compressor logic governed the system response.

Results are presented as a function of the Cooling Load (CL), which represents the total cooling capacity that the unit must provide to bring the outdoor air stream to the prescribed post-supply set-point conditions. It is defined as:

$$\mathrm{CL} = \dot{m}_{PSUP}\,(h_{ODA} - h_{set}) \tag{6.1}$$

where the set-point enthalpy (h_{set}) is evaluated at the post-supply temperature set-point (T_{set}) and the corresponding humidity ratio (W_{set}). The latter is defined as the extract-air humidity ratio, limited by the saturation value at T_{set} to ensure physically consistent conditions.

6.1.1. Standard configuration vs Alternative configuration

The impact of introducing an auxiliary Outdoor to Exhaust Air (OEA) recirculation fan on overall system performance was assessed. Two configurations were compared, identical in all respects except for the inclusion of this auxiliary fan. In the modified configuration, the fan recirculates outdoor air, thereby increasing the airflow through the external heat exchanger, which acts as the condenser in summer mode. The full schematic of this configuration is shown in Fig. 1.7. Although not part of the present experimental campaign, this solution has been implemented in practice, and both the fan geometry and performance characteristics are well established and have been incorporated into the model.

In present analysis, the unit is assumed to operate ideally (i.e., no external ducting), hence the airflow provided by the OEA fan depends solely on the internal losses of the unit, which scale with the ventilation flow rate. Under the investigated conditions, the OEA fan was set to its maximum speed, corresponding to the highest achievable airflow. The analysis therefore focuses on whether this additional airflow enhances heat rejection and cycle efficiency, or whether the concurrent rise in condenser air inlet temperature offsets the expected benefits, ultimately leading to a deterioration in system performance.

6.1.1.1. Fixed-frequency analysis

The results are presented for each tested airflow rate and classified according to outdoor temperature, providing a systematic framework for interpreting the unit's operating behavior. Figure 6.2 shows that, even under the same cooling load, the system may follow different operating paths depending on the imposed boundary conditions, since the

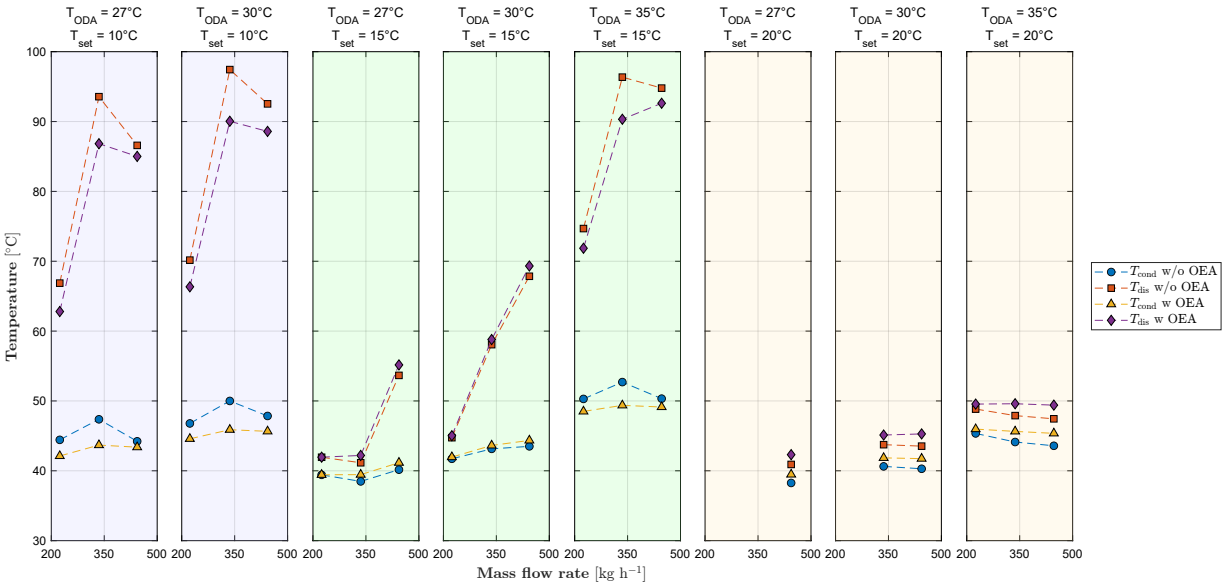

Figure 6.1: Effect of OEA fan on refrigeration cycle temperatures on the high pressure side at fixed compressor frequencies.

capacity limits are strongly influenced by them. In particular, the maximum compressor frequency is constrained by the control logic as a function of both the condenser air inlet temperature and the airflow processed by the ventilation unit. This constraint safeguards the compressor from both excessive condensing and discharge temperatures, thereby preventing frequent activation of protection modes. Since the same cooling load can be achieved through different combinations of (T_{ODA}, $\dot{m}_{SUP}$,T_{set}) the maximum admissible compressor frequency may vary for identical loads. For this reason, performance trends can only be consistently interpreted within a defined pair of boundary conditions (T_{ODA}, $\dot{m}_{SUP}$), thus underlining the importance of a digital twin capable of reproducing the control logic to realistically simulate the system's operation.

The first outcomes of this analysis are reported in Figure 6.1. The figure highlights that, at sufficiently high refrigerant mass flow rates (for instance, when the unit was tested near $T_{set} = 10$°C at outdoor conditions of 27°C and 30°C, or near $T_{set} = 15$°C at 35°C), the condenser airflow becomes the bottleneck for heat rejection. In these cases, the additional airflow provided by the OEA fan lowers both condensation and discharge temperatures, suggesting that the compressor could be driven to higher speeds to better meet the post-supply set-point. Conversely, at lower refrigerant flow rates (corresponding to higher post-supply set-points), the temperature of the air entering the condenser becomes the dominant factor. When the inlet air temperature rises, the refrigerant must condense at a higher saturation temperature in order to reject the required heat load. This increase in condensation temperature directly raises compressor discharge pressure and, consequently, compressor power consumption.

These dynamics are further illustrated in Figure 6.3, which reports the system response at fixed operating conditions. In summer operation, the recirculation of outdoor

air produced only a modest reduction in post-supply temperature, resulting in a limited increase in cooling capacity. The overall effect strongly depends on the cooling load relative to the specific boundary conditions defined by the pair (T_{ODA}, $\dot{m}_{SUP}$). The most relevant improvement was obtained at high cooling loads and at the intermediate airflow rate ($\dot{m}_{SUP} = 339\,\mathrm{kg\ h^{-1}}$). Under these conditions, the additional airflow lowered the condensation temperature and thereby reduced the compressor's energy requirement, while the increase in cooling capacity compensated for the extra power consumption of the auxiliary fan, leading to a net increase in system EER. At low cooling loads, by contrast, the temperature of the air entering the condenser became the dominant factor relative to airflow rate. In this case, the higher inlet air temperature penalized heat rejection, raised the condensation temperature, worsened the cycle performance, and increased compressor power consumption, while the auxiliary fan added further electrical demand. As a result, the system EER decreased. Depending on the operating point, the trade-off between auxiliary fan consumption and compressor energy savings can therefore result in either an improvement or a deterioration in overall efficiency.

Overall, these results indicate that, at sufficiently high cooling loads, the compressor can be safely operated at higher frequencies to achieve higher cooling capacity. In such conditions, the auxiliary airflow provided by the OEA fan effectively lowers condensation and discharge temperatures, which are the key variables monitored by the control logic to prevent overheating.

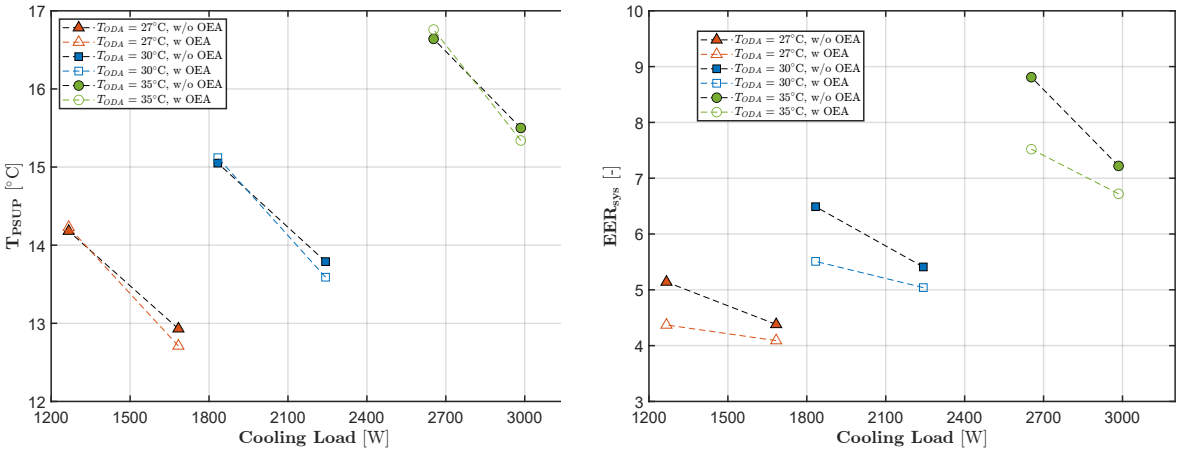

(a) Results at $\dot{m}_{PSUP} = 227$ kg h^{-1}, $\dot{m}_{PEHA} = 565$ kg h^{-1}

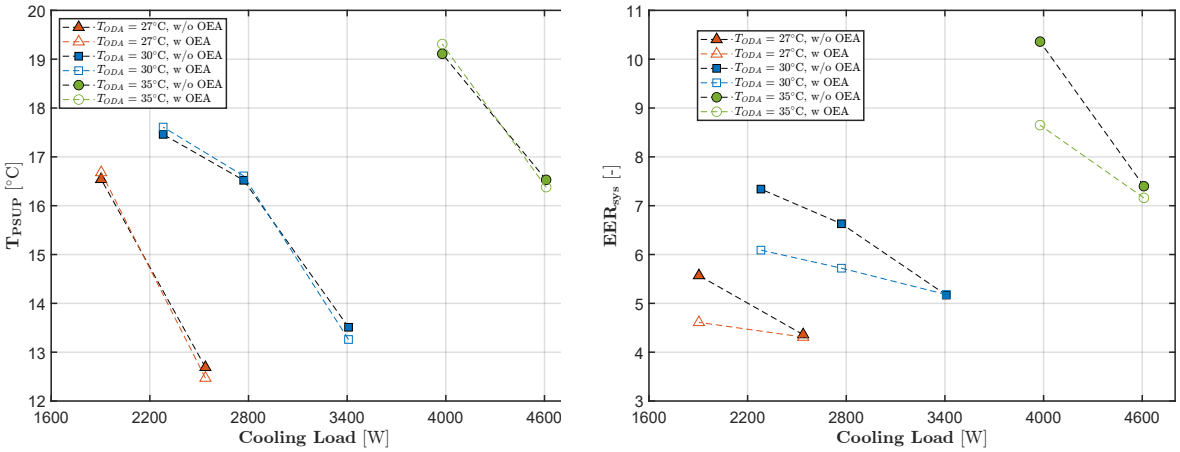

(b) Results at $\dot{m}_{PSUP} = 339$ kg h^{-1}, $\dot{m}_{PEHA} = 650$ kg h^{-1}

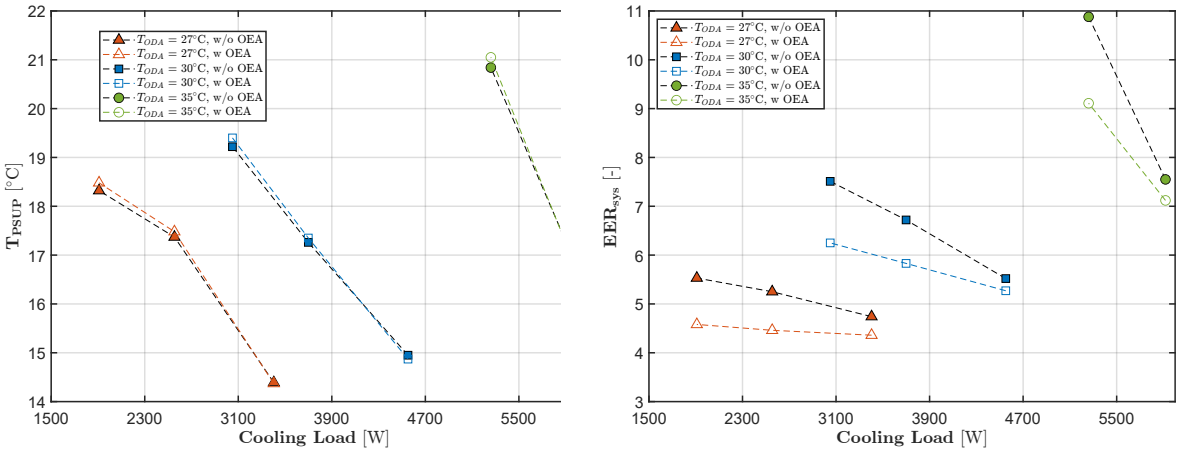

(c) Results at $\dot{m}_{PSUP} = 447$ kg h^{-1}, $\dot{m}_{PEHA} = 724$ kg h^{-1}

Figure 6.2: Post supply temperature and overall EER at fixed compressor frequency with and without auxilary OEA recirculation.

6.1.1.2. Control-driven analysis

The analysis with the compressor frequency governed by the unit's internal control logic provides further insight into the role of the auxiliary OEA recirculation fan. As shown in Figure 6.3, at high cooling loads relative to the specific operating conditions defined by the pair (T_{ODA}, $\dot{m}_{SUP}$), the baseline capacity of the unit was sometimes insufficient to reach the prescribed set-point. In these cases, the activation of the auxiliary fan yielded a significant boost in cooling capacity. A maximum increase of 25% was recorded for the operating point characterized by the highest cooling load at $T_{ODA} = 27°C$ and $\dot{m}_{SUP} = 447\,kg\,h^{-1}$. This improvement arose primarily because the additional airflow allowed the compressor to operate at higher maximum frequencies, as both condensation and discharge temperatures were more effectively controlled under these conditions. In addition, as already highlighted in the fixed-frequency analysis, a smaller further increase in capacity was obtained from the modified thermodynamic cycle of the heat pump itself.

This capacity gain, however, came at the expense of the overall system EER. The deterioration in efficiency was mainly due to the increased electrical consumption of the compressor, which operated at higher speeds, compounded by the power demand of the auxiliary fan. Moreover, the presence of the fan increased internal pressure drops on the air side of the system, thereby raising the power consumption of the main ventilation fans for the same processed airflow. Under the operating conditions that yielded the maximum increase in cooling capacity, the system EER decreased by 15.6%.

At low cooling loads, again relative to the specific operating conditions, and in particular when the system tended to undershoot the set-point (i.e., when the available capacity exceeded the demand), the effect of the OEA loop was reversed. Here, the additional airflow provided by the OEA fan worsened the thermodynamic performance of the heat pump, reducing the available capacity and thereby bringing the outlet temperature closer to the set-point. Under these conditions, however, the auxiliary power consumption from the OEA fan, combined with the additional power required for the MVHR fans to overcome the extra pressure drop introduced by the recirculation loop, became comparable to that of the compressor, which operated close to its minimum speed. As a result, the system EER was significantly penalized.

In summary, the use of the OEA recirculation fan proves beneficial only at high cooling demands with respect to the defined operating conditions, whereas in all other cases the additional electrical consumption largely outweighs the performance gains. The analysis also highlights a scenario that could be further investigated: lowering the minimum airflow of the heat pump and relying on the auxiliary fan to keep condensation and discharge temperatures under control, which would otherwise rise beyond acceptable limits at very low baseline airflows.

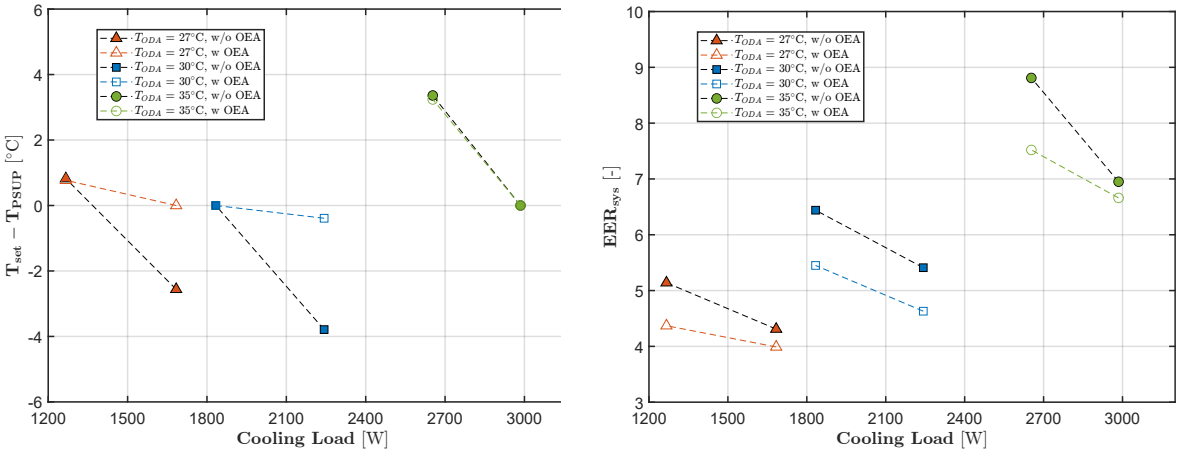

(a) Results at $\dot{m}_{PSUP} = 227$ kg h^{-1}, $\dot{m}_{PEHA} = 565$ kg h^{-1}

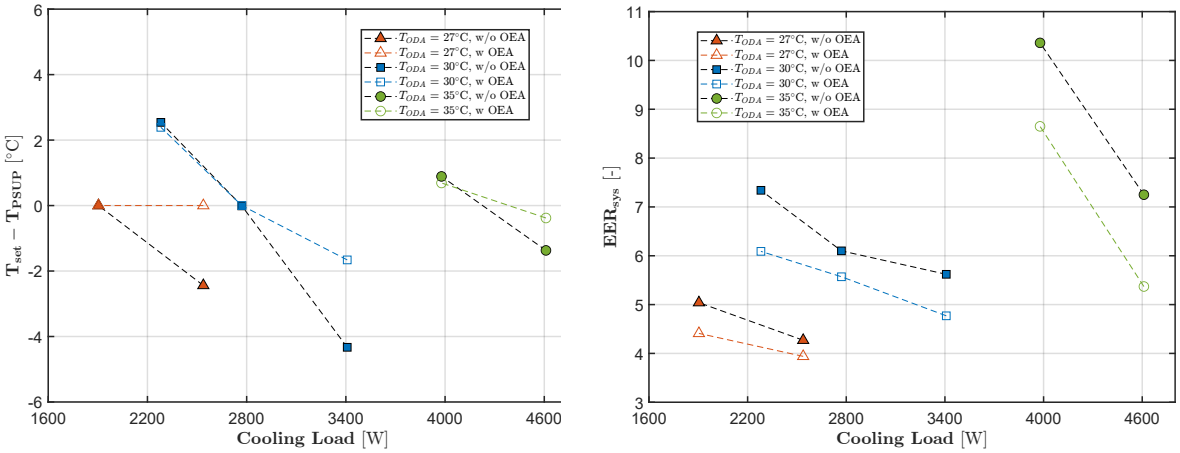

(b) Results at $\dot{m}_{PSUP} = 339$ kg h^{-1}, $\dot{m}_{PEHA} = 650$ kg h^{-1}

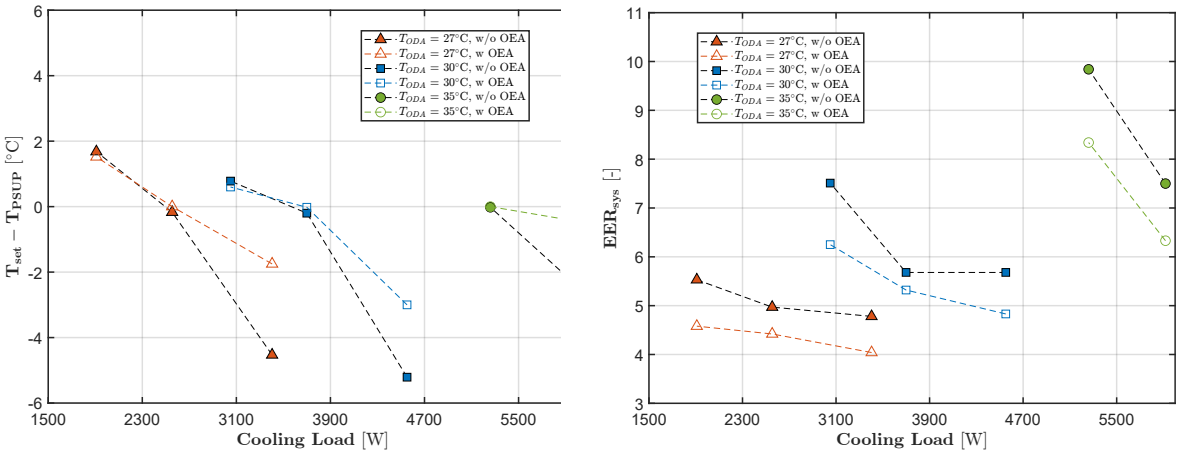

(c) Results at $\dot{m}_{PSUP} = 447$ kg h^{-1}, $\dot{m}_{PEHA} = 724$ kg h^{-1}

Figure 6.3: Post supply temperature and overall EER with and without auxilary OEA recirculation.

6.1.2. Enthalpy recovery vs Heat recovery

The effect of the recovery principle on the coupled ventilation-heat pump system was analyzed by comparing two recovery exchangers with identical external dimensions and core volume, both designed with a quasi-counter-flow configuration. Within this common framework, the counter-flow sections differ in their internal construction and channel geometry: the sensible-only exchanger (HRV) consists of homogeneous polymer plates forming square channels (Figure 1.3a), whereas the enthalpy exchanger (ERV) employs a membrane with polymer spacers that create rectangular passages (Figure 1.3b). As shown in Figure 6.4, the HRV supplied air at a lower dry-bulb temperature and higher relative humidity, while the ERV provided warmer and drier supply air. Conversely, on the exhaust side, the ERV discharged colder and more humid air compared with the HRV. These outlet conditions define the boundary states for the heat pump and are expected to markedly affect both its operation and the overall system performance.

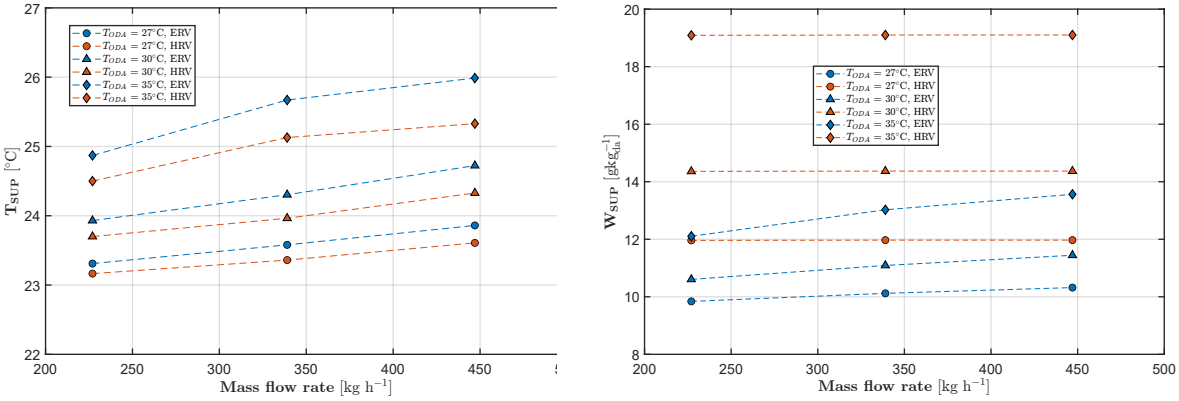

(a) Supply side

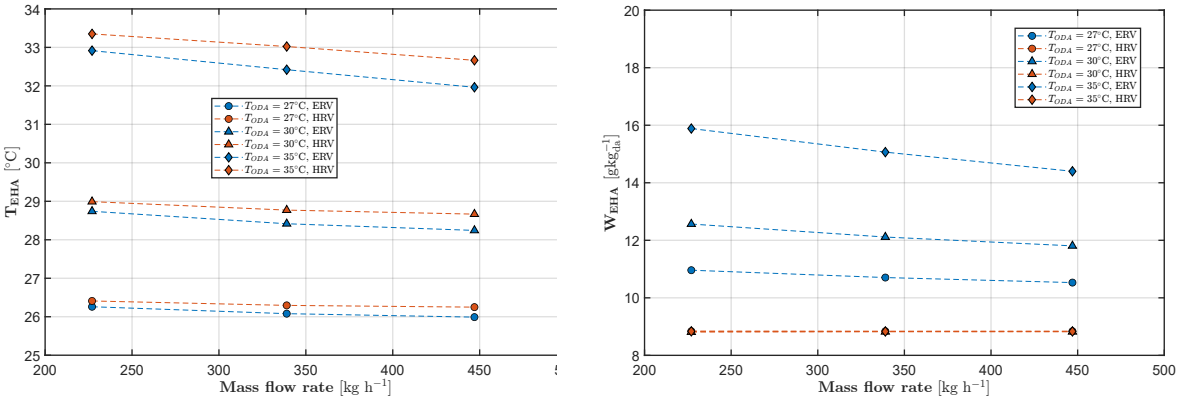

(b) Exhaust side

Figure 6.4: MVHR air outlet conditions, ERV vs HRV.

Cycle-level analysis at fixed compressor frequencies indicated that the HRV configuration operated with higher evaporating and condensing temperatures. The higher dew point of the supply air led to earlier water condensation on the coil and increased the evaporating pressure. Simultaneously, the stronger sensible recovery of the HRV unit

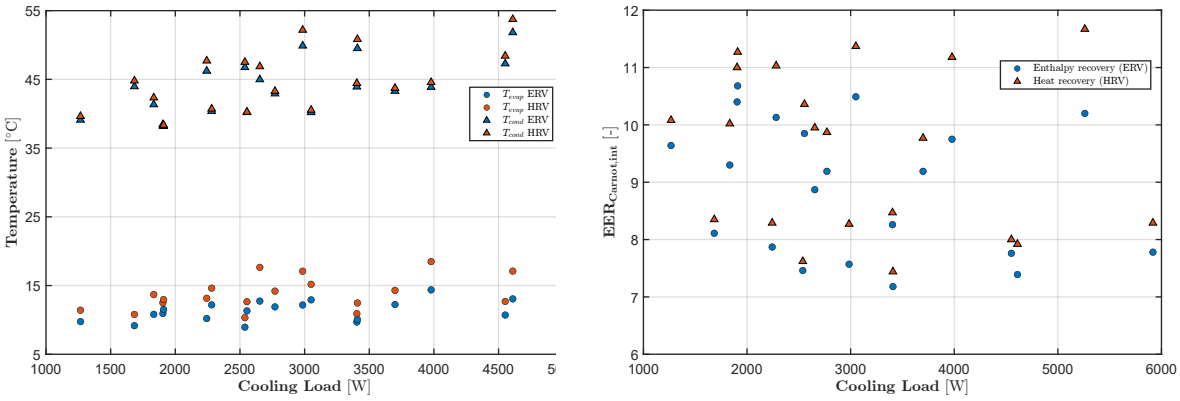

(a) Saturation temperatures **(b)** Carnot EER

Figure 6.5: Impact of the recovery strategy on the refrigeration cycle at fixed compressor frequencies.

raised the temperature of the exhaust stream that served as the heat-rejection sink, and the condenser was therefore required to operate at higher saturation temperature (Figure 6.5a). As shown in Figure 6.5b, the increase in evaporating temperature outweighed the rise in condensing temperature, so the Carnot reference efficiency for the cycle was higher with the HRV in all operating points tested. From the viewpoint of the refrigerant cycle alone, this represented a thermodynamic advantage.

When the coupled system was considered, a different conclusion emerged. Figure 6.6 shows that the system coupled with an ERV consistently achieved lower post-supply temperatures and higher system EER than the HRV configuration, under identical boundary conditions and at the same compressor speed. The HRV unit supplied air to the heat pump that was colder but significantly more humid than the ERV. As a result, a larger share of the cooling effect produced by the heat pump was used as latent cooling to remove moisture, leaving less sensible capacity available to reduce the air temperature. In contrast, the ERV partly transferred this latent load through the membrane to the exhaust stream, so that the ventilation unit itself provided a higher total cooling capacity while at the same time reducing the latent load on the heat pump. This shift increased the share of sensible cooling, resulting in lower post-supply temperatures and higher overall system EER. An average of 28% greater cooling capacity and 25% higher EER for the MFRBV/ERV system, relative to the MFRBV/HRV system, was recorded.

With the compressor control logic active, the difference between the two configurations became even clearer. As shown in Figure 6.7, the higher humidity of the supply air in the HRV case reduced the sensible effect achievable at the post-supply, so the compressor had to operate at higher frequencies to reach the same temperature set-point. This further increased electrical consumption and confirmed that the ERV ensures superior overall system performance also when the control logic is active.

From the standpoint of thermohygrometric comfort, the different moisture content

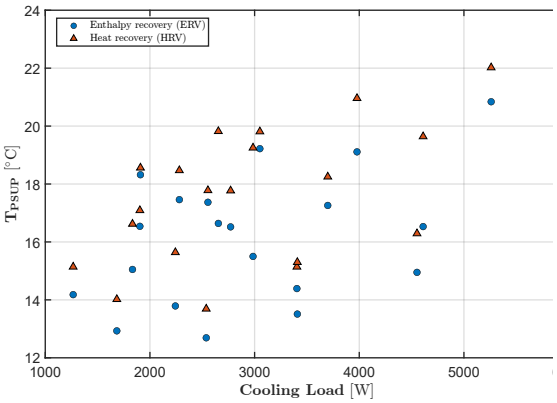

(a) Post-supply temperature

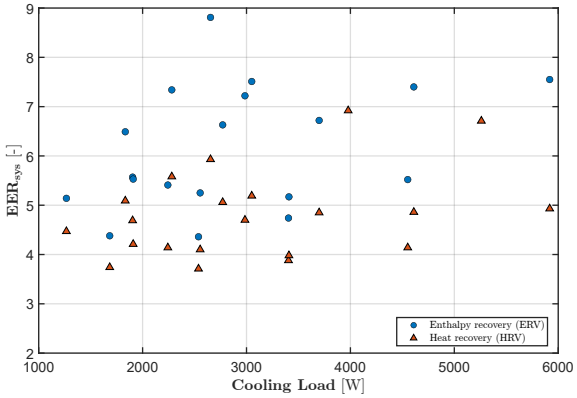

(b) Overall EER

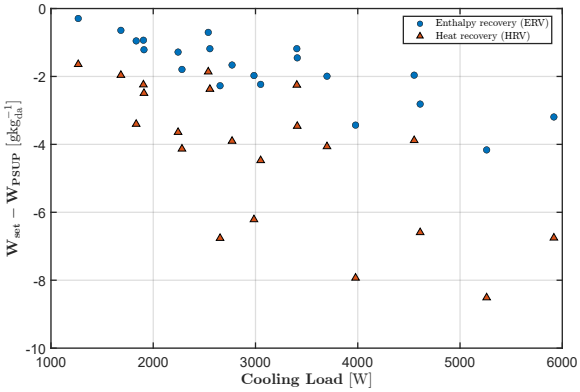

(c) Post-supply humidity ratio deviation

Figure 6.6: Post-supply temperature, overall EER, and humidity ratio deviation at fixed compressor frequencies; ERV vs HRV.

of the supply air further distinguishes the two solutions. The HRV delivers air that is noticeably more humid and farther from the target humidity ratio (W_{set}), whereas the ERV maintains conditions much closer to the desired set-point. Consequently, the ERV not only enhances thermodynamic performance but also provides supply air conditions more conducive to comfort, limiting indoor humidity levels within the optimal range.

In short, although the HRV enhances the theoretical efficiency of the refrigeration cycle by yielding a higher Carnot EER and provides lower supply-air temperatures at the ventilation level, the system coupled with the ERV unit (MFRBV/ERV) achieves lower post-supply temperatures, lower post-supply humidity ratios and higher system EER. These practical advantages make the MFRBV/ERV the more favorable configuration under summer operating conditions, when overall system performance is the relevant metric.

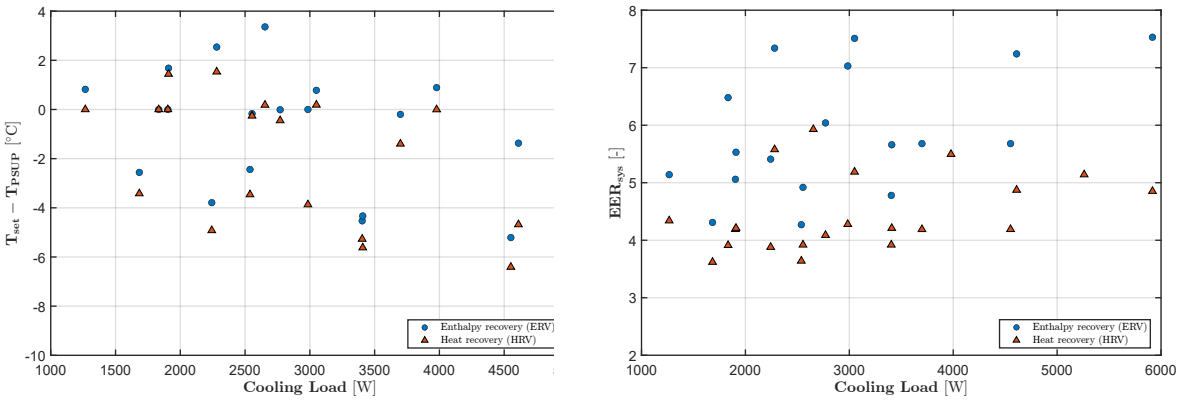

Figure 6.7: Post-supply temperature deviation and overall EER, with compressor logic; ERV vs HRV.

6.1.3. Bypass of the recovery exchanger

6.1.3.1. Fixed-frequency analysis: implications on system performance

The digital twin was employed to investigate the impact of different bypass levels of the recovery exchanger on the performance of the coupled ventilation-heat pump system. The motivation for this study arose from the hypothesis that, as the fraction of bypass increases, the air streams entering the heat pump become thermodynamically more favorable, leading to higher cycle efficiencies. In principle, a higher evaporating temperature and a lower condensing temperature should enhance the energy efficiency ratio (EER) of the heat pump. At the same time, however, bypassing the exchanger implies that the system would lack the pre-conditioning effect provided by heat (and moisture in case of an ERV) recovery, i.e. the reduction of sensible (and latent in case of an ERV) loads before the air flow reaches the indoor coil. This raises the question of whether the overall efficiency of the coupled system would improve or deteriorate.

Four bypass configurations were simulated: 0%, 30%, 50%, and 100% of the airflow bypassing the heat recovery exchanger. The 100% bypass case represented a limiting scenario, effectively corresponding to a system coupled with a ventilation unit without heat (and moisture in case of an ERV) recovery. This analysis was carried out for both ERV- and HRV-based systems, though here the focus is on the general trends, since the detailed comparison between the two recovery principles was already discussed in the previous section.

The results, summarized in Figures 6.8-6.9, confirmed the expected trend: the internal cycle EER of the heat pump increased with the degree of bypass and reached its maximum when the exchanger was fully bypassed. However, this apparent advantage at the heat pump level did not translate into an overall benefit. At fixed compressor frequencies, the system-level performance consistently decreased with increasing bypass, as the contribution of the recovery unit to lowering the cooling demand more than outweighed the moderate efficiency gains observed at the heat pump level. Within the tested range

of operating conditions, the increase in cycle EER was never sufficient to compensate for the energy recovery that was lost.

The post-supply temperature profiles (Figures 6.8c-6.9c) further highlighted this behavior, showing a progressive reduction of available sensible cooling capacity as the bypass fraction grew. This effect was particularly evident when considering the enthalpy recovery case, which again underlined the positive role of latent energy exchange in alleviating the evaporator load. Overall, the findings demonstrate that bypassing the exchanger in summer conditions should not be regarded as a viable performance-enhancing strategy. Instead, exchanger bypass should be restricted to specific scenarios such as free cooling, where its benefits are unambiguous. More broadly, the analysis illustrates the importance of system-level evaluation: strategies that appear advantageous at the subsystems scale may prove counterproductive when the full interactions between subsystems are accounted for.

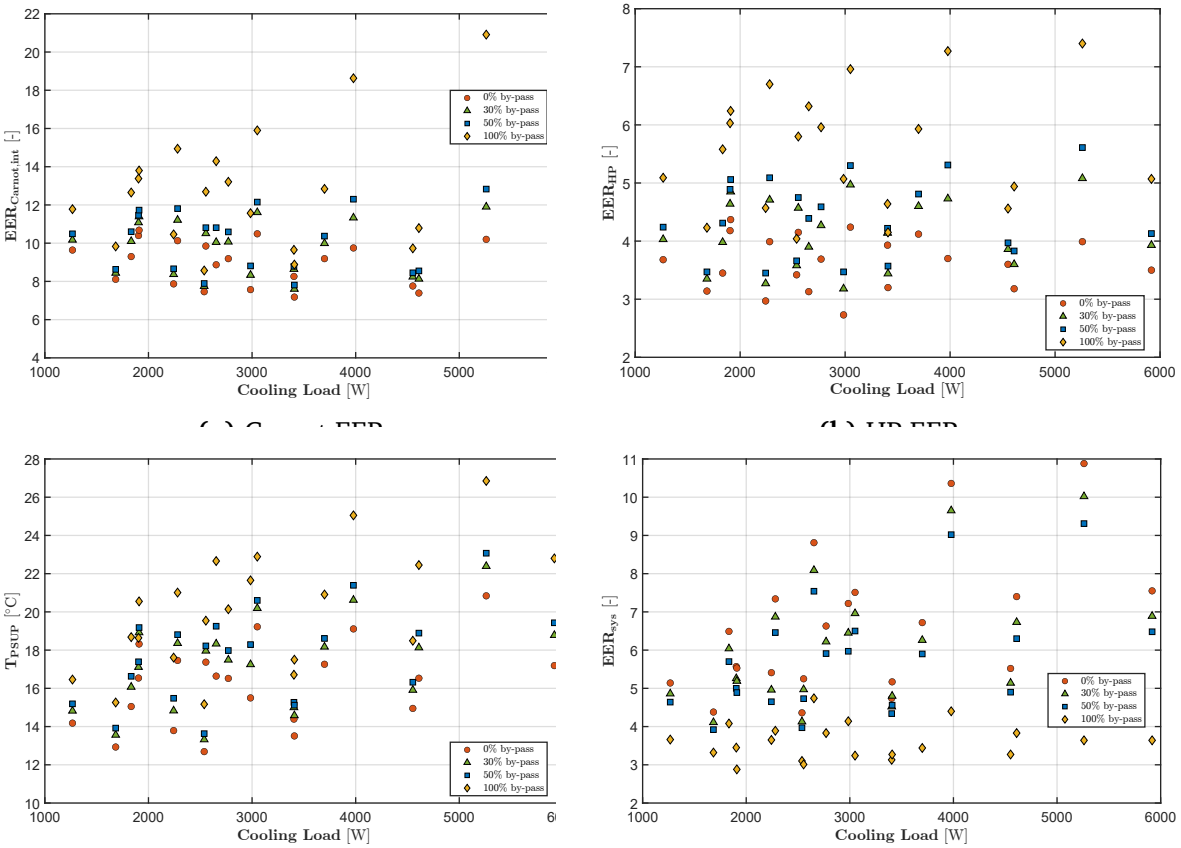

(c) Post-supply temperature

(d) System EER

Figure 6.8: Performance indicators under different bypass levels of the enthalpy recovery exchanger (ERV).

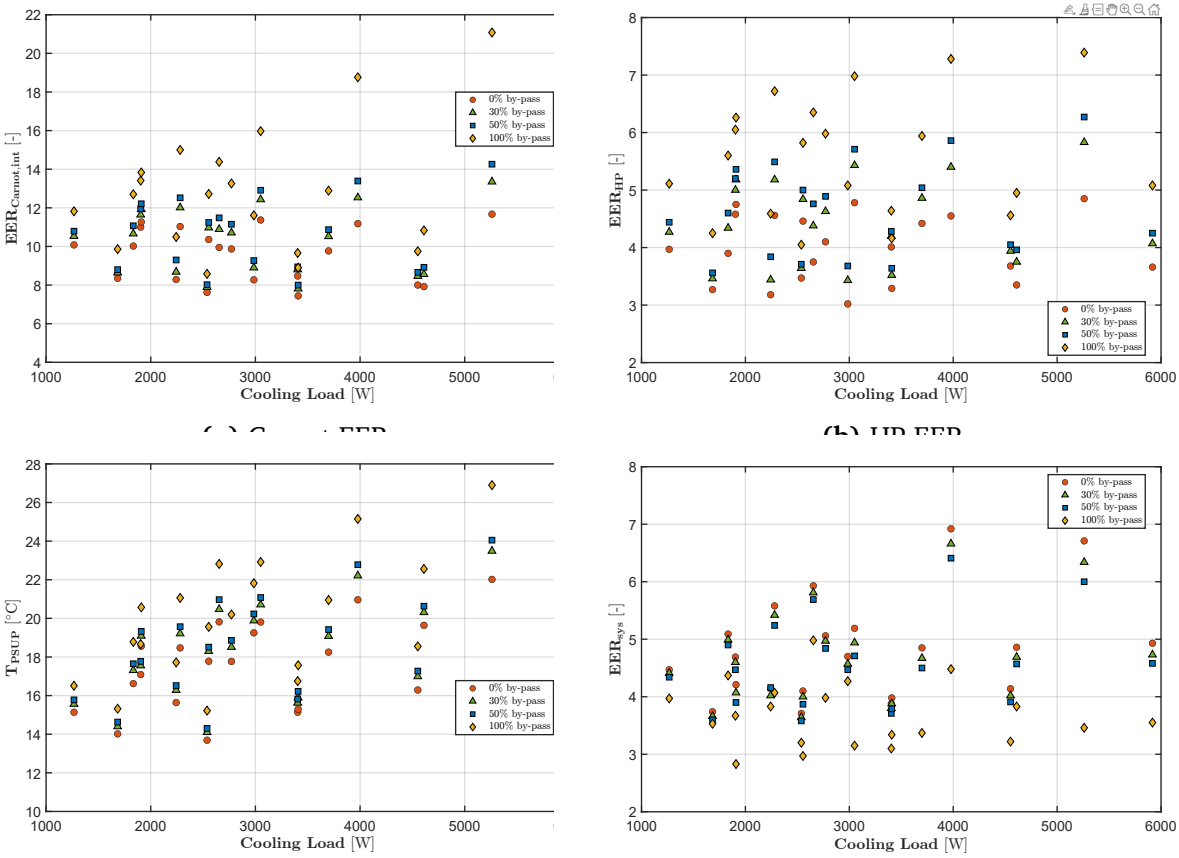

(c) Post-supply temperature

(d) System EER

Figure 6.9: Performance indicators under different bypass levels of the heat recovery exchanger (HRV).

6.1.3.2. Control-driven analysis: Implications on fullfilment of the requirements

The same bypass analysis was repeated with the compressor frequency governed by the internal control logic of the unit, instead of being fixed at prescribed values. The corresponding results are shown in Figures 6.10 and 6.11. As in the fixed-frequency case, a general decrease in system performance was observed for both ERV- and HRV-based configurations when the bypass fraction was increased. This confirms the fundamental role of the recovery unit, regardless of the adopted control strategy.

However, an additional effect emerged when considering conditions with low cooling loads. In these operating regions, the heat pump tended to overshoot the post-supply temperature set-point, since its minimum available capacity still exceeded the actual demand. Under such circumstances, bypassing the recovery exchanger modified the source and sink conditions in a way that effectively reduced the mismatch between capacity and load. As a result, the system operated closer to the desired post-supply set-point, with a larger number of operating points showing lower or no deviation.

This finding indicates that, at low cooling loads, partial bypass of the recovery exchanger may improve the fulfilment of post-supply air temperature requirements, although this occurs at the expense of a lower system EER. In practice, the bypass thus

introduces a trade-off: it reduces energy efficiency but can enhance set-point tracking under part-load conditions where the compressor's minimum modulation is insufficient.

A conventional solution to this mismatch is on-off compressor cycling, which effectively reduces the delivered capacity by intermittently switching the heat pump on and off. While this approach can restore set-point tracking, it is accompanied by well-known drawbacks: frequent start-stop sequences increase mechanical wear on the compressor, lead to transient inefficiencies during each restart, and can compromise thermal comfort due to the pulsed nature of capacity delivery. By contrast, exchanger bypass achieves a comparable modulation effect continuously, without imposing additional mechanical stress or introducing cycling-induced inefficiencies. These considerations suggest that exchanger bypass, beyond its traditional role for free cooling, may also represent a valuable control lever under part-load conditions. Although it entails a measurable efficiency penalty, its ability to continuously reshape operating conditions offers a smoother and potentially more durable alternative to on-off cycling. From a broader perspective, this highlights the opportunity to integrate bypass operation into advanced control frameworks, where it can be dynamically combined with compressor modulation to balance energy efficiency, equipment durability, and comfort requirements.

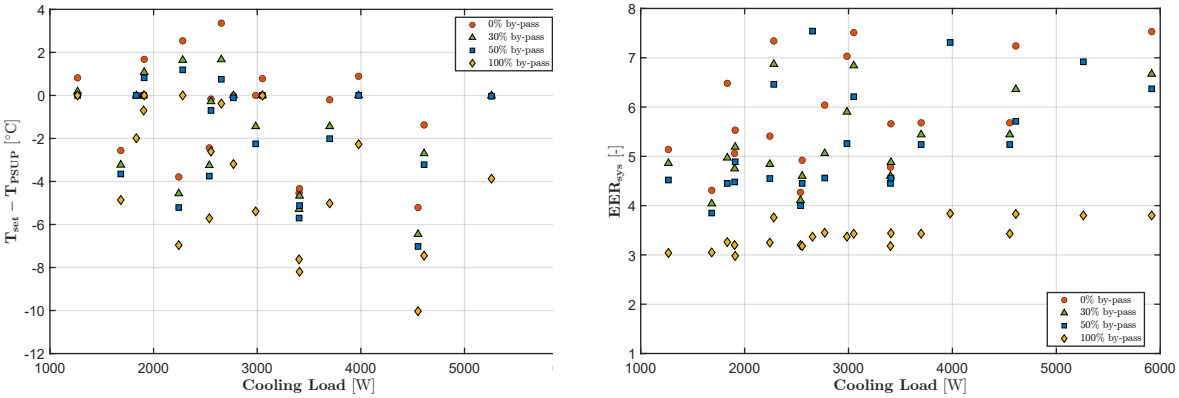

Figure 6.10: Post-supply temperature deviation and overall EER under different degree of bypass of the enthalpy recovery exchanger (ERV).

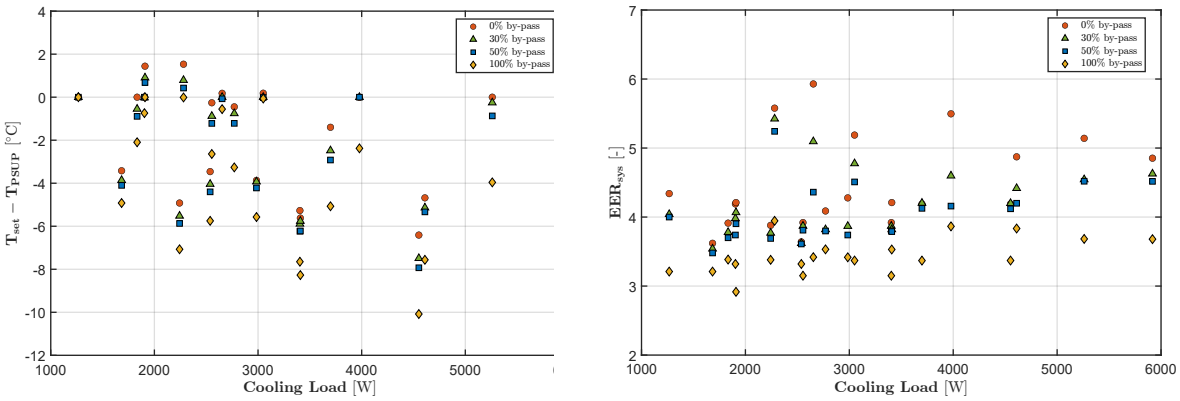

Figure 6.11: Post-supply temperature deviation and overall EER under different degree of bypass of the heat recovery exchanger (HRV).

6.2. Winter conditions

For each winter operating condition, simulations utilizing the digital twin were conducted over a total duration of three hours, including both the active heating operation and the defrost periods required to restore frost-free conditions. The choice of a three-hour operating period follows the reference duration adopted in the relevant European standards for performance assessment of multifunctional ventilation unit (EN 13141-7 [84] and EN 16573:2017 [86]), which prescribe a minimum test length sufficient to include at least one complete frost-defrost sequence and to obtain statistically representative average values of the system performance.

In the following analysis, the variables associated with the refrigeration cycle (T_{evap}, T_{cond}, and T_{dis}) were averaged only over the active heating phase (i.e., excluding defrost phases), in order to highlight the effect of the configuration variant on the thermodynamic cycle of the heat pump. Conversely, the system-level quantities (PC_{sys}, COP_{sys}, $\dot{Q}_{sys}$, and T_{PSUP}) were averaged over the entire three-hour operation (i.e., including the defrost events), in order to represent the actual impact of each configuration on the average overall winter performance of the unit. As described in Section 5.2.3.2, the defrost process was not explicitly simulated in the digital model. Instead, its duration and energy consumption were computed in the simulation run time, at the end of each heating cycle, using the empirical correlations reported in Equations 5.4 and 5.5. These quantities were accumulated during the simulated period to obtain the total defrost time and total defrost energy consumption. The simulation was stopped when the cumulative active heating time plus the accumulated defrost time reached a total of three hours. As a result, the model provided directly the temporal evolution of the system variables throughout the active heating operation ($PC_{act,sys}(t)$, $\dot{Q}_{act,sys}(t)$, $COP_{act,sys}(t)$, and $T_{act,PSUP}(t)$). The time-averaged values over the active cycle ($PC_{act,sys}$, $\dot{Q}_{act,sys}$, $COP_{act,sys}$, and $T_{act,PSUP}$) were then derived from these temporal data, and finally, the overall three-hour averages were derived by combining the active heating and defrost contributions as follows:

$$PC_{sys} = \frac{PC_{act,sys}\, t_h + \left(PC_{MVHR,def} + E_{def}/t_{tot,def}\right) t_{tot,def}}{t_h + t_{tot,def}} \tag{6.2}$$

$$\dot{Q}_{sys} = \frac{\dot{Q}_{act,sys}\, t_h + \dot{Q}_{MVHR,def}\, t_{tot,def}}{t_h + t_{tot,def}} \tag{6.3}$$

$$COP_{sys} = \frac{\dot{Q}_{sys}}{PC_{sys}} \tag{6.4}$$

Here, t_h is the active heating time, $PC_{MVHR,def}$ and $\dot{Q}_{MVHR,def}$ represent respectively the electrical power consumption and the supply heat flow rate of the MVHR unit, operating alone during the defrost phases, i.e., with the heat pump turned off. Since the airflow during defrost is markedly lower than during the active heating phase, a simple time average of T_{PSUP} would not be physically meaningful. To obtain a representative mean temperature consistent with the corresponding average heating capacity (Equation 6.3), a mass-time weighted average was therefore adopted:

$$T_{PSUP} = \frac{T_{act,PSUP}\, \dot{m}_{PSUP}\, t_h + T_{MVHR,def}\, \dot{m}_{MVHR,def}\, t_{tot,def}}{\dot{m}_{PSUP}\, t_h + \dot{m}_{MVHR,def}\, t_{tot,def}} \tag{6.5}$$

with $T_{MVHR,def}$ and $\dot{m}_{MVHR,def}$ the post-supply air temperature and the mass airflow rate processed by the ventilation unit during the defrost phase. Here $\dot{m}_{MVHR,def}$ was fixed at 120 kg h^{-1}, consistent with the real system behavior. This formulation ensures full energetic consistency between the mean air temperature and the mean heat flow rate supplied by the system. The consistency is demonstrated below, for a simplified case with a sensible-only heat recovery and constant c_p.

Let $T_{SUP,def}$ denotes the supply-air temperature of the ventilation unit during the defrost phase. Assuming sensible-only heat transfer and constant air specific heat, the average system heat flow rate over the total operating time (Equation 6.3) can be rewritten as:

$$\dot{Q}_{sys} = \frac{c_p\left[\dot{m}_{PSUP}(T_{act,PSUP} - T_{ODA})\, t_h + \dot{m}_{MVHR,def}(T_{SUP,def} - T_{ODA})\, t_{tot,def}\right]}{t_h + t_{tot,def}} \tag{6.6}$$

If we now define the time-averaged mass flow rate as:

$$\overline{\dot{m}} = \frac{\dot{m}_{PSUP}\, t_h + \dot{m}_{MVHR,def}\, t_{tot,def}}{t_h + t_{tot,def}} \tag{6.7}$$

the mean sensible heating capacity of the system can be formulated in the conventional form:

$$\dot{Q}_{sys} = c_p\, \overline{\dot{m}}\left(T_{PSUP} - T_{ODA}\right) \tag{6.8}$$

Equating Equations 6.6 and 6.8 and isolating T_{PSUP} yields again to Equation 6.5. This

demonstrates that the mass-weighted temperature definition guarantees complete energetic consistency between the averaged air-side temperature difference and the corresponding mean sensible heat flow rate. Hence, the adopted formulation for T_{PSUP} provides a physically meaningful and mathematically consistent representation of the average post-supply temperature over mixed heating and defrost operation.

In analogy with the analysis performed under summer conditions, the winter results are presented as a function of the *Heating Load* (HL), defined as:

$$HL = \dot{m}_{PSUP}(h_{set} - h_{ODA}) \tag{6.9}$$

where the set-point enthalpy h_{set} was computed from the supply air temperature set-point (T_{set}) and the humidity ratio of the extract air flow used as a humidity set-point ($W_{set} = W_{ETA}$).

Simulations were run under exactly the same boundary conditions as those adopted in the experimental campaign described in Chapter 4, including the indoor and outdoor thermo-hygrometric conditions, the airflow rates, and the compressor speed.

6.2.1. Standard configuration vs Alternative configuration

In winter operation, the effect of integrating an auxiliary Outdoor to Exhaust Air (OEA) recirculation fan was assessed to determine its influence on the performance of the multifunctional ventilation unit. The modelling framework and the fan characterization adopted in the summer analysis were retained. In this configuration, the auxiliary fan operated at its maximum rotational speed, and the corresponding mass flow rate through the frost-free external coil was denoted as $\dot{m}^*_{PEHA}$. This flow rate gradually decreased during operation because the growing frost layer increased the coil pressure losses and limited the airflow that the additional fan could deliver. The resulting time-dependent airflow through the evaporator modified the boundary conditions that determine the evaporating temperature, the initiation and progression of frosting, and the sequence of heating and defrost phases.

The analysis focused on whether this altered, and progressively declining, airflow could enhance the overall heating performance of the unit or, alternatively, intensify frost formation and reduce the time-averaged heating capacity.

The influence of the additional recirculation flow provided by the OEA fan on the average thermodynamic cycle is illustrated in Figure 6.12. The increased airflow across the outdoor coil generally led to higher evaporating temperatures across most operating conditions. This effect was particularly pronounced at medium and low ventilation rates and for operating points characterized by relatively high heating loads within the same boundary condition defined by the pair ($T_{ODA}, \dot{m}_{PSUP}$). Under these conditions, the larger mass flow rate enhanced the heat transfer on the evaporator side, resulting in a noticeable

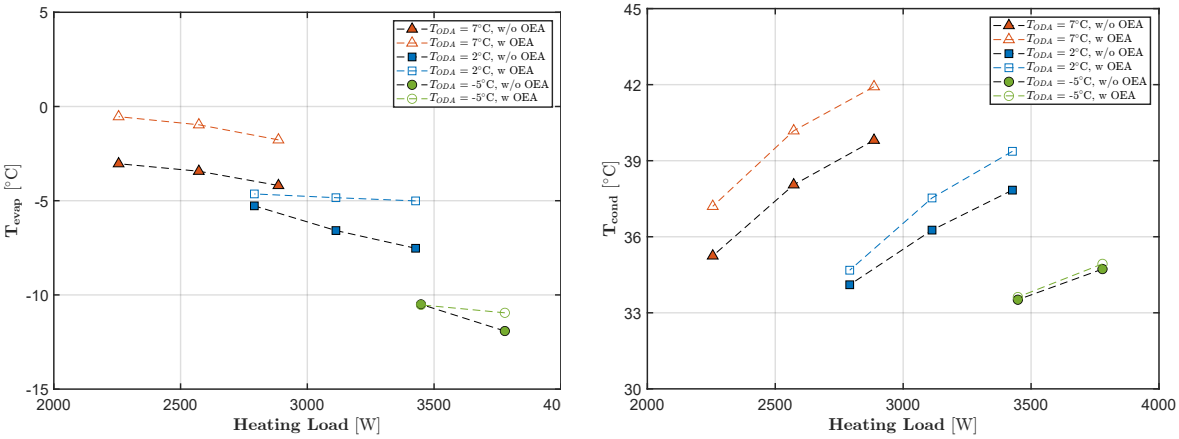

(a) Results at $\dot{m}_{PSUP} = 227$ kg h^{-1}, $\dot{m}^*_{PEHA} = 565$ kg h^{-1}

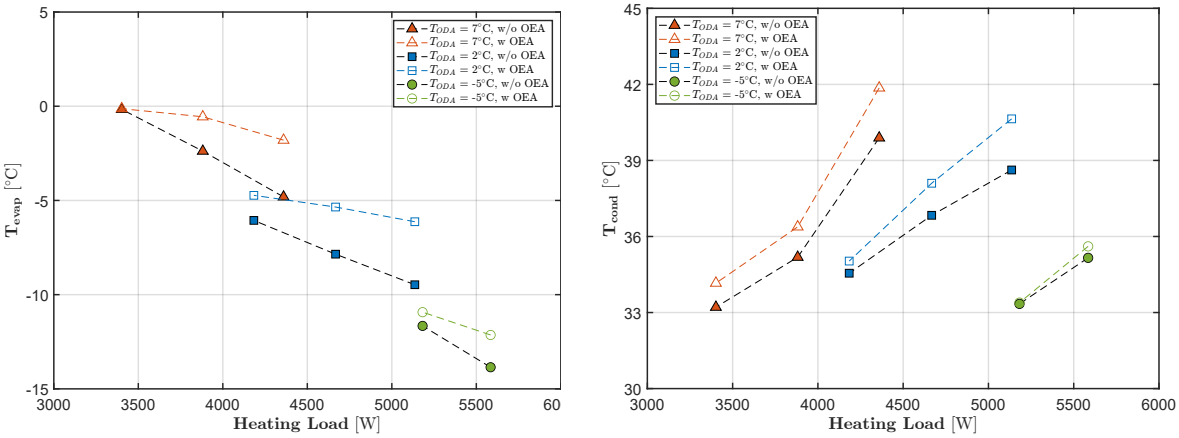

(b) Results at $\dot{m}_{PSUP} = 339$ kg h^{-1}, $\dot{m}^*_{PEHA} = 650$ kg h^{-1}

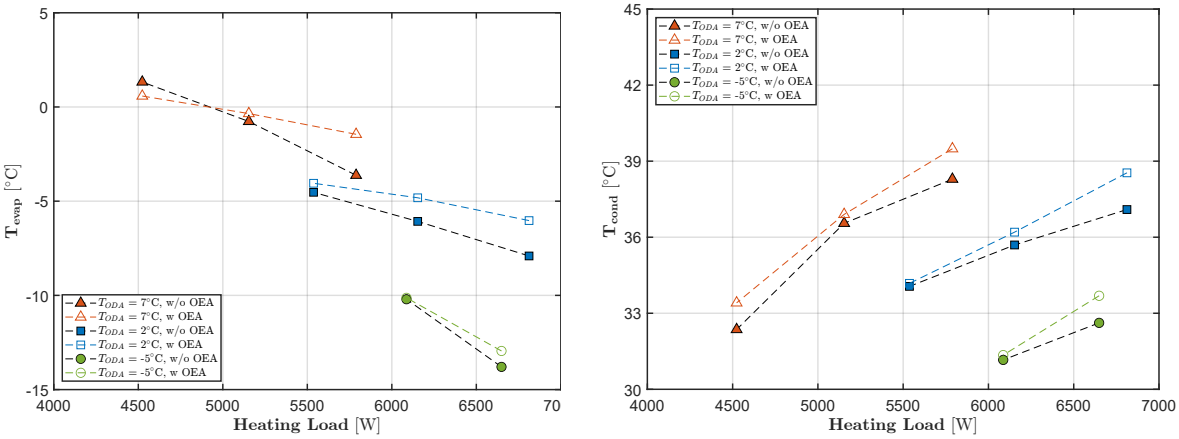

(c) Results at $\dot{m}_{PSUP} = 447$ kg h^{-1}, $\dot{m}^*_{PEHA} = 724$ kg h^{-1}

Figure 6.12: Evaporation and condensation temperatures.

rise in the average evaporating temperature.

At lower heating loads, however, the impact of the additional recirculated airflow became less evident and, in some cases, negligible or even slightly adverse (e.g., at $T_{\text{ODA}} = 7°\text{C}$, $\dot{m}_{\text{PSUP}} = 447$ kg h^{-1} and $T_{\text{set}} = 35°\text{C}$). This behavior mirrored the mech-

anism previously discussed in the summer analysis: when the system operated under low or mild heating load relative to the specific boundary condition, the quality of the heat transfer—driven by the inlet air temperature to the outdoor coil—played a more decisive role than the quantity of air crossing the heat exchanger. Specifically, although the OEA fan increased the airflow and thereby improved the convective heat transfer coefficient on the air side, it simultaneously lowered the inlet air temperature at the coil, an effect which could offset or even exceed the benefit produced by the higher mass flow rate.

Regarding the condensing temperature, it was generally higher when the OEA fan was active. This outcome followed directly from the larger amount of heat absorbed at the evaporator: the additional energy entering the refrigerant loop required a higher condensing temperature to be transferred to the supply-air stream. Since the inlet conditions and airflow rate on the condenser side were identical for both configurations—being fixed by the operating point of the ventilation unit—the increase in condensing temperature simply reflected the higher load imposed on the cycle when the OEA fan was operating.

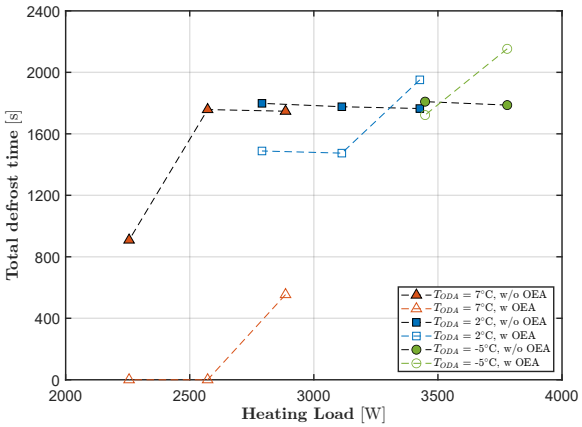

(a) $\dot{m}_{PSUP} = 227$ kg h^{-1}, $\dot{m}^{*}_{PEHA} = 565$ kg h^{-1}

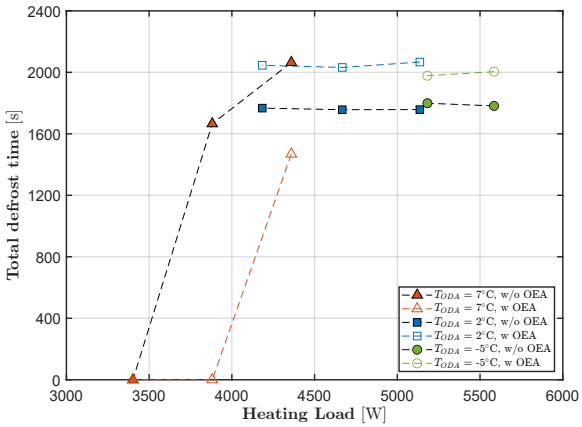

(b) $\dot{m}_{PSUP} = 339$ kg h^{-1}, $\dot{m}^{*}_{PEHA} = 650$ kg h^{-1}

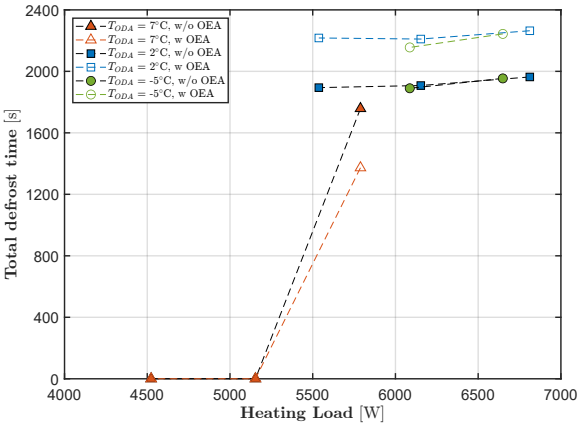

(c) $\dot{m}_{PSUP} = 447$ kg h^{-1}, $\dot{m}^{*}_{PEHA} = 724$ kg h^{-1}

Figure 6.13: Total defrost time.

The increase in evaporator airflow also affected how frost accumulated on the out-

door coil. Figure 6.13 summarizes these changes by comparing the total defrost time under for the two configurations. At 7°C, the activation of the OEA recirculation fan consistently reduced the total defrost time across all ventilation rates. This improvement was primarily driven by a lower amount of frost deposited on the coil, as the higher evaporating temperature reduced the overall moisture condensation rate.

At 2°C, a beneficial effect emerged exclusively for medium and low heating loads at the minimum ventilation rate (227 kg h^{-1}). In this specific condition, the impact of the OEA fan reflected a critical balance between two opposing mechanisms:

i. **Increased airflow:** the higher mass flow delivered more moisture to the coil, inherently increasing the total frost mass.

ii. **Higher evaporating temperature:** the increased evaporating temperature promoted the formation of a denser and more conductive frost layer.

As illustrated by the variations in frost nature (Figure 6.14), in these operating points the higher density mitigated the insulating effect of the accumulated frost. Under these favorable conditions, heat transfer performance degraded more gradually, allowing for longer operational periods between defrost events and reduced the total defrost time compared with the standard configuration (Figure 6.13).

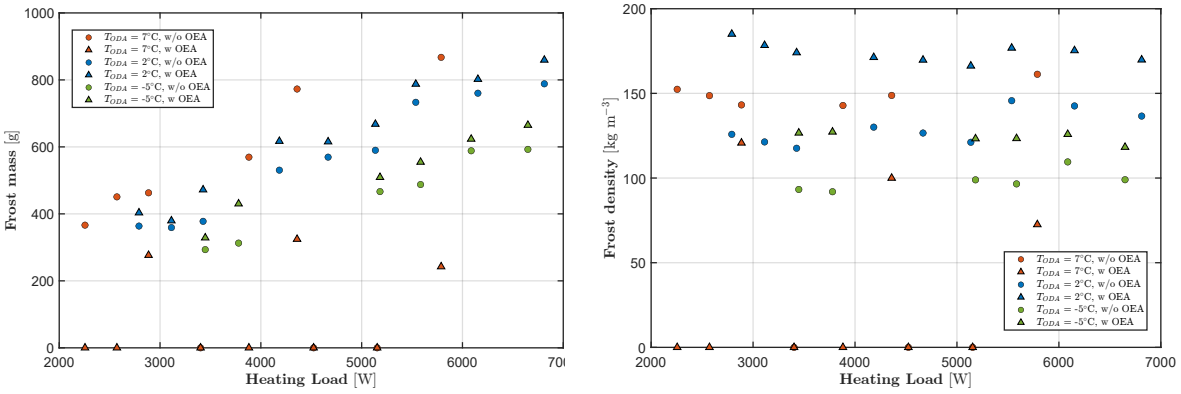

(a) Accumulated frost mass **(b)** Average frost density

Figure 6.14: Frost build-up metrics.

For all other conditions at 2°C, and for all operating points at −5°C, this balance shifted unfavourably. The additional airflow again significantly increased the amount of frost formed. Although the frost developed was denser than in the standard case (as evidenced in Figure 6.14b), the resulting increase in diffusive water mass flux (responsible for frost density growth) was insufficient to counteract the much larger convective moisture flux reaching the coil. Frost therefore accumulated rapidly and formed highly insulating layers that obstructed the coil more quickly. This accelerated the deterioration of heat-transfer performance and consequently led to longer or more frequent defrost events relative to the standard configuration.

The direct consequences of these thermodynamic changes, together with the modified defrost behavior, are clearly reflected in the time-averaged system performance (Figure 6.15). The integration of the OEA recirculation fan generally resulted in a higher average post-supply air temperature, with increases reaching up to 4°C (corresponding to an approximate 21.2% increase in heating capacity). This maximum benefit was recorded at $T_{\mathrm{ODA}} = 7°\mathrm{C}$ and $\dot{m}_{\mathrm{PSUP}} = 227\ \mathrm{kg\ h^{-1}}$ at a mild heating load, a condition where frost formation was entirely suppressed. Overall, the largest benefits consistently appeared at high heating loads (relative to the boundary condition) and at medium or low ventilation rates, a distribution which closely followed the positive trends observed in the evaporating temperature.

Conversely, under harsher ambient conditions, such as at −5°C and minimum ventilation rate, the benefit was minimal. This performance deterioration resulted from an unfavorable combination of factors: a significant reduction in the air temperature entering the evaporator (which penalizes heat transfer effectiveness) and the increased total time spent in defrost. This latter condition arose because, despite the much higher airflow rate across the evaporator compared to the standard configuration, the increased moisture flux led to the rapid formation of highly insulating frost layers (as previously discussed), thus accelerating system performance degradation.

With respect to the system COP (Figure 6.15), the higher airflow through the evaporator increased the heating capacity but also raised the electrical consumption. This occurred because the auxiliary fan required additional power and, in addition, the MVHR fans had to operate at a higher load in order to overcome the extra pressure drop introduced by the recirculation loop, thereby increasing their electrical consumption. The compressor power also rose due to the modified thermodynamic cycle. Overall, a small reduction in COP was observed at nearly all operating points (typically around 0.5 points), with the most pronounced effect at low heating loads. At the specific operating points where the maximum heating capacity increase was achieved ($T_{\mathrm{ODA}} = 7°\mathrm{C}$, $\dot{m}_{\mathrm{PSUP}} = 227\ \mathrm{kg\ h^{-1}}$ at a mild heating load), the corresponding reduction in COP was approximately 8.3%.

In conclusion, the comparison between the standard and alternative configuration indicates that the benefits of increased airflow depend strongly on the resulting evaporating temperature and the associated frost-formation dynamics. When the auxiliary fan raises the evaporating temperature sufficiently, frost accumulation decreases, which in turn slows the deterioration of heat-transfer performance, reduces or eliminates defrost events, and increases both average heating capacity and operational stability. When the evaporating temperature remains low, however, the inevitably larger water vapor mass flow supplied to the outdoor coil, under these colder conditions, rapidly forms low-density, highly insulating frost layers, consequently leading to longer or more frequent defrost phases. The increased airflow consistently yields a higher time-averaged

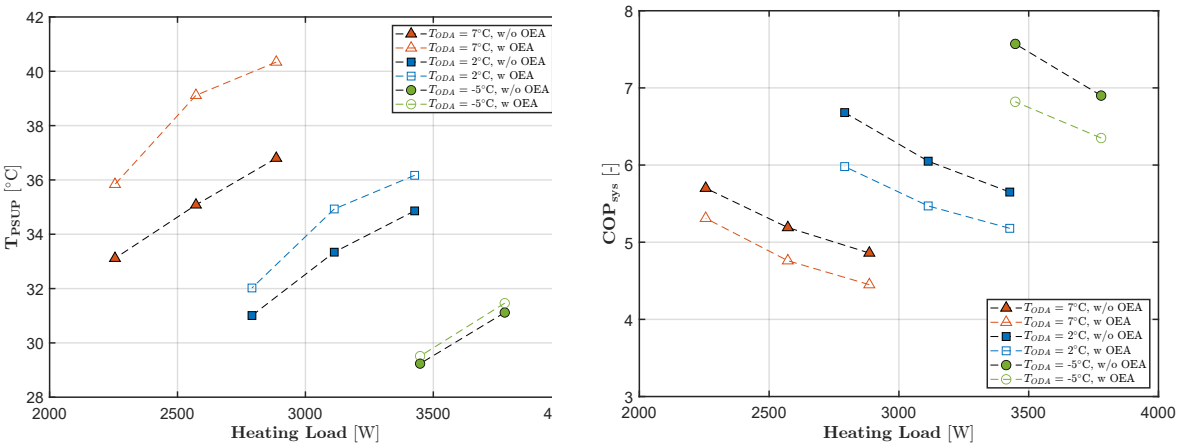

(a) Results at $\dot{m}_{PSUP} = 227$ kg h^{-1}, $\dot{m}^*_{PEHA} = 565$ kg h^{-1}

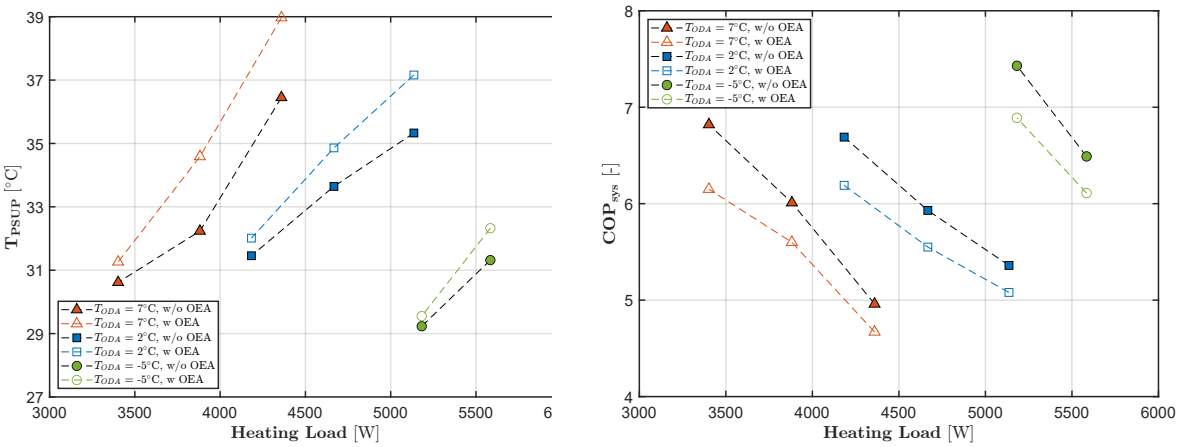

(b) Results at $\dot{m}_{PSUP} = 339$ kg h^{-1}, $\dot{m}^*_{PEHA} = 650$ kg h^{-1}

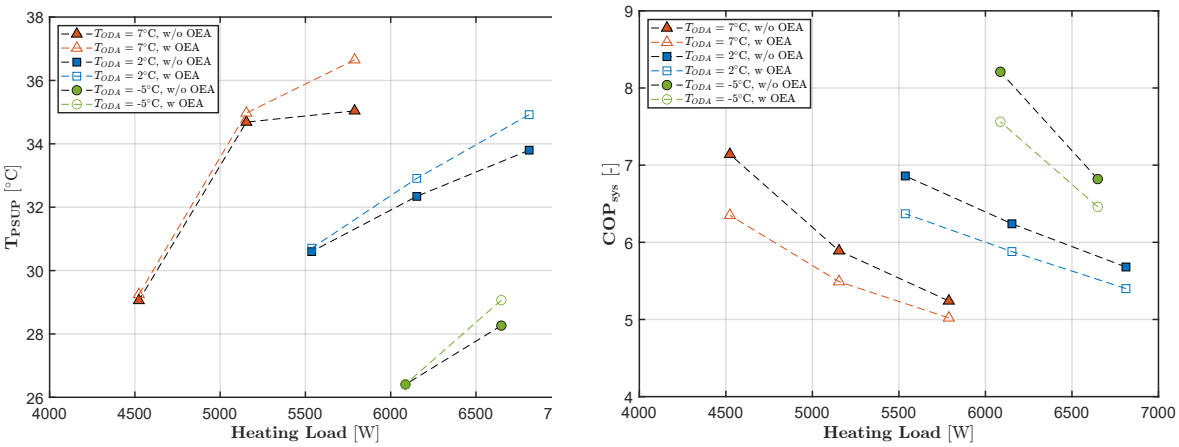

(c) Results at $\dot{m}_{PSUP} = 447$ kg h^{-1}, $\dot{m}^*_{PEHA} = 724$ kg h^{-1}

Figure 6.15: Average post-supply temperature and system COP with defrost losses with and without auxilary OEA recirculation.

post-supply temperature, which can be favourable from a comfort perspective; yet in operating points where defrost durations become longer and the system becomes more unstable, this advantage may be partially offset by stronger temperature fluctuations and

by more frequent exposure to colder supply air during defrost.

These results also suggest a viable control strategy. Under moderately cold outdoor conditions—such as the 7 °C case studied here—the auxiliary recirculation flow can be safely activated to raise the evaporating temperature just enough to suppress or significantly reduce defrost operation. In this regime the system experiences a moderate increase in electrical consumption due to the additional fan, but this is largely compensated by the marked reduction in the time spent in defrost and by the improvement in thermal comfort, as the post-supply air temperature remains warmer and its fluctuations are significantly reduced. Under more severe outdoor conditions—such as the 2 and −5°C cases studied here-however, the recirculation fan should be used only when the system must deliver a heating capacity that exceeds the baseline limits without recirculation. In these cases the additional air flow can indeed provide additional capacity, but at the cost of more frequent defrost cycles, slightly lower COP, and a more noticeable increase in electrical consumption.

6.2.2. Enthalpy recovery vs Heat recovery

The performance of the multifunctional ventilation unit was evaluated for two configurations: one coupled with an enthalpy recovery exchanger (ERV) and one with a sensible-only heat recovery exchanger (HRV). The resulting supply air conditions are shown in Figure 6.16. The ERV delivered lower supply temperatures and higher humidity ratios due to moisture transfer, whereas the HRV, which recovers only sensible heat, provided higher supply temperatures but resulted in much drier supply air, since the humidity ratio remained unchanged through the exchanger.

At low outdoor temperatures (2°C and −5°C in this case), condensation inside the HRV introduced an additional latent heat contribution that simultaneously affected both the supply and the exhaust streams. Two distinct mechanisms governed this behavior: water vapor condensing on the wall released latent heat that was conducted through the plate and increased the supply-air temperature, while water vapor condensing within the bulk-flow released latent heat directly to the exhaust stream, raising its temperature. These combined effects became particularly evident at an outdoor temperature of 2 °C, where the pre-heater was inactive and the HRV configuration yielded both higher supply and higher exhaust temperatures compared to the ERV. In this condition, the higher supply temperature was primarily associated with wall condensation on the heat transfer surfaces, while the higher exhaust temperature reflected bulk-flow condensation on the exhaust side. At −5 °C, the same condensation mechanisms were still active, but their influence was superimposed on the action of the pre-heater, which raised the outdoor-air temperature to approximately 0 °C before the sensible core; the resulting supply and exhaust temperatures therefore reflected the combined contribution of pre-heating and condensation. The ERV, by contrast, did not require pre-heating at any outdoor condition,

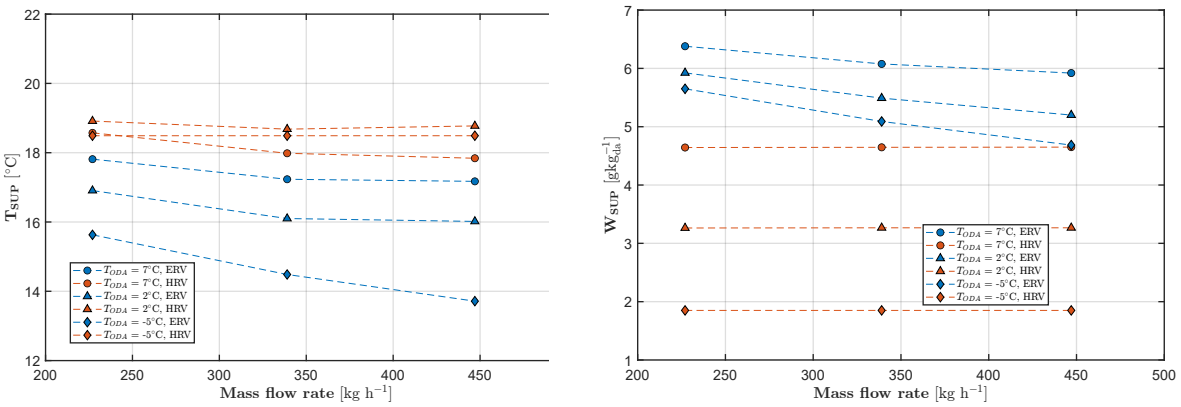

(a) Supply side

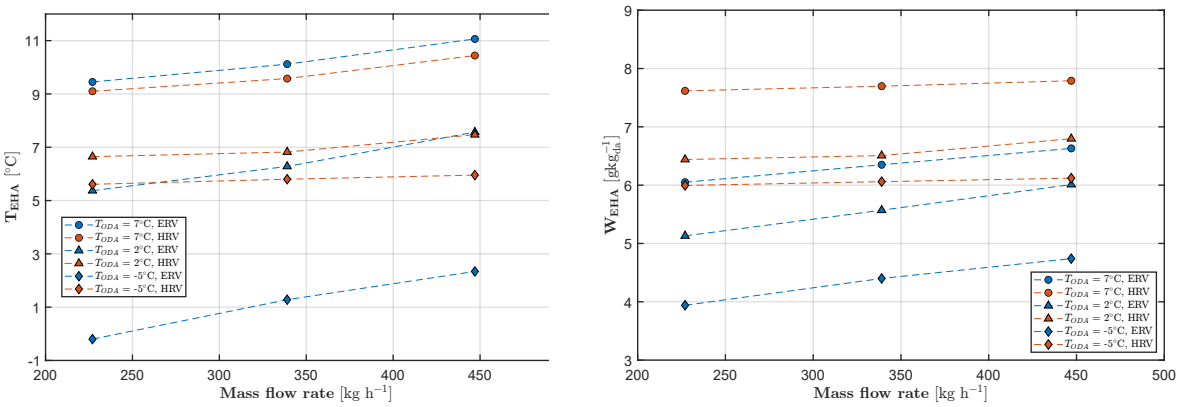

(b) Exhaust side

Figure 6.16: MVHR air outlet conditions, ERV vs HRV.

since membrane-based moisture transfer prevented the onset of condensation regimes prone to frosting, thereby avoiding both wall and bulk-flow condensation and producing a consistently drier exhaust stream, in winter conditions.

These effects were reflected in the computed exhaust-air temperatures. At an outdoor temperature of 7 °C, both exchangers operated in dry conditions and the HRV produced a colder exhaust stream than the ERV, consistent with its higher sensible effectiveness. At 2 °C, the HRV had already entered in a partially wet regime. Bulk-flow condensation became significant and the associated latent heat release increased the exhaust temperature, so that the exhaust air leaving the HRV was warmer than that of the ERV. At −5 °C, the inlet temperature increase imposed by the pre-heater further altered the HRV exhaust conditions and amplified the difference between the two recovery exchangers.

Given the marked differences in both the supply and exhaust conditions produced by the two recovery units, a significant impact on the global system performance was expected, particularly with regard to the dynamics of frost formation on the evaporator.

The variation of the average thermodynamic cycle during the heating phase, expressed in terms of evaporating and condensing temperatures, is shown in Figure 6.17. Overall, the configuration equipped with the sensible-only exchanger (HRV) exhibited

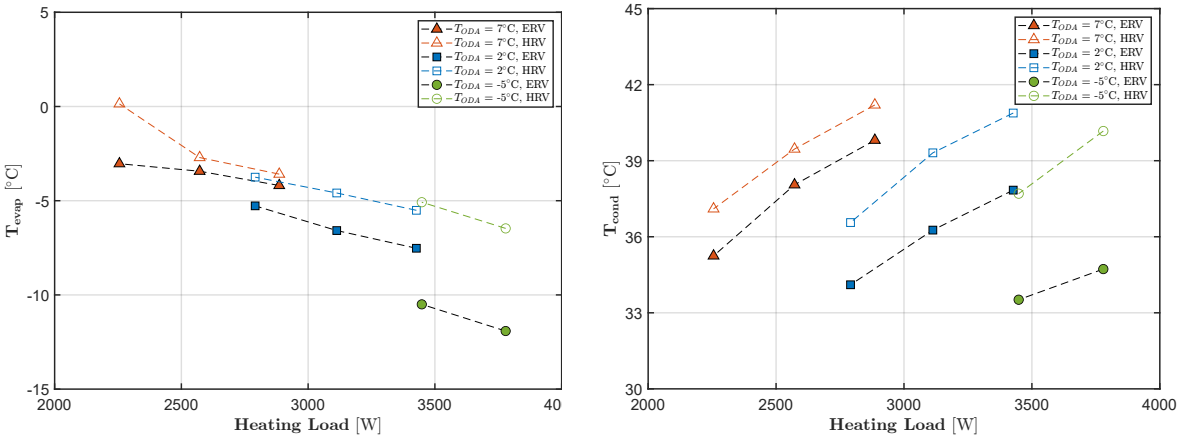

(a) Results at $\dot{m}_{MVHR} = 227$ kg h^{-1}

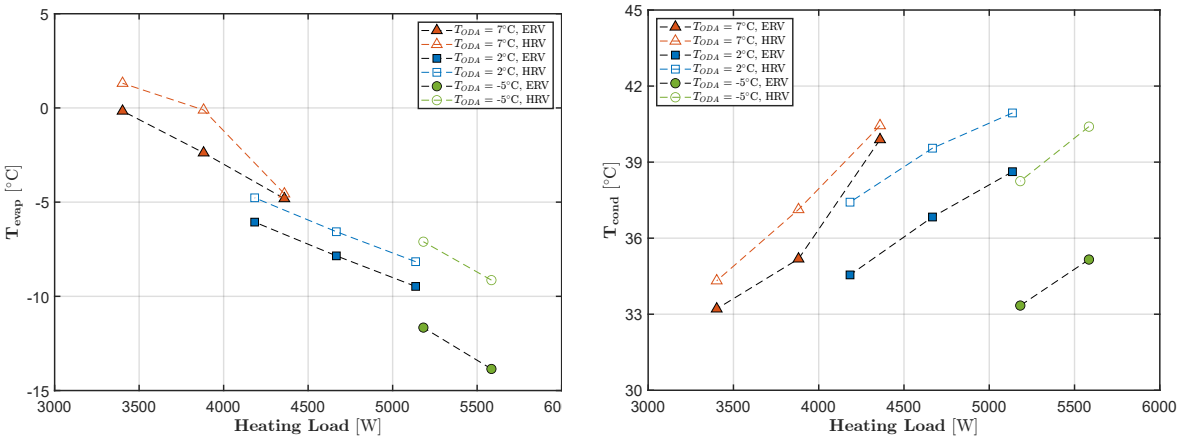

(b) Results at $\dot{m}_{MVHR} = 339$ kg h^{-1}

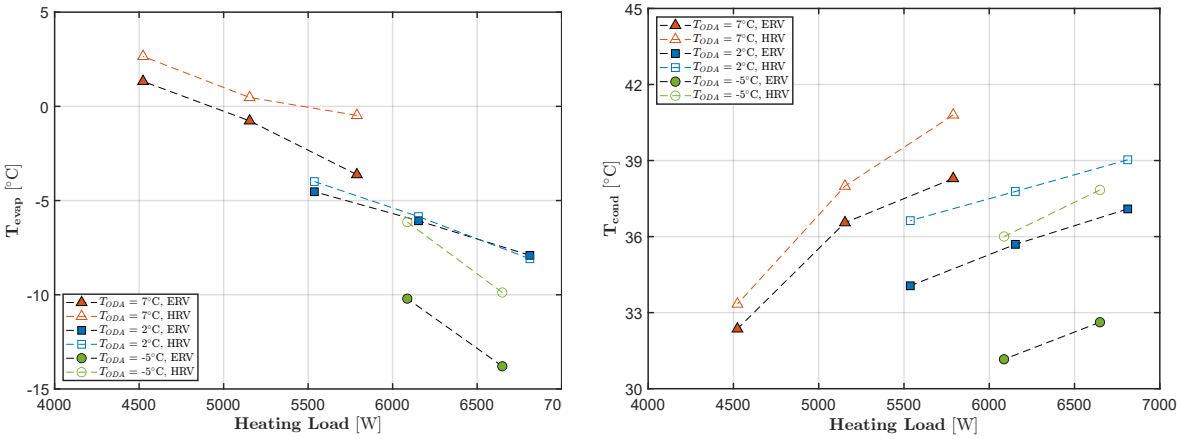

(c) Results at $\dot{m}_{MVHR} = 447$ kg h^{-1}

Figure 6.17: Evaporation and condensation temperatures.

both higher evaporating and higher condensing temperatures than the configuration with the enthalpy exchanger (ERV), indicating an upward shift of the refrigeration cycle consistent with the different boundary conditions imposed by the two recovery units. The increase in condensing temperature was observed at all operating points because the air

entering the condenser was always significantly warmer in the HRV configuration (Figure 6.16a). The evaporating temperature was also higher in the HRV case, for two main reasons. First, the humidity ratio of the air entering the evaporator was always higher with the HRV, and—as discussed in the summer analysis (Section 6.1.2)—an increased inlet humidity tends to raise the evaporating temperature. This effect was particularly evident at 7 °C and under low heating loads, where no frosting occurred and the evaporating temperature was not deteriorated by frost accumulation; in these conditions, the air entering the evaporator was even slightly colder in the HRV configuration (Figure 6.16), yet the higher humidity more than compensated for this, raising the evaporation temperature. Second, at lower outdoor temperatures (2°C and −5°C) the evaporator inlet air was also generally warmer in the HRV configuration, as already discussed. This systematic increase in evaporating temperature had direct implications for frosting behavior: the first operating point above the frosting threshold for the ERV remained completely frost-free when the system was equipped with the HRV, for all the values of airflow rate. As a result, the HRV configuration achieved a higher average heating capacity at these specific operating points, since no defrost cycle was required, and under these conditions it outperformed the ERV configuration (Figure 6.18). Specifically, a maximum improvement in average heating capacity of 15.4% was achieved by the MFRBV/HRV system relative to the MFRBV/ERV configuration (at the operating point $T_{ODA} = 7$°C, $\dot{m}_{MVHR} = 447$ kg h^{-1}, and $T_{set} = 45$°C), while COP decreased by about 6.1%.

For all other operating points not located at the transition between frosting and non-frosting conditions, the ERV configuration generally exhibited higher average system heating capacities (Figure 6.19), despite delivering lower average post-supply temperatures (Figure 6.21). This behavior confirmed the positive impact of moisture transfer to the supply stream: the specific enthalpy of the post-supply air was higher in the ERV configuration even though its temperature was lower, because the air stream was substantially more humid; as shown in Figure 6.16, the humidity ratio at the supply side—and maintained across the condenser—was consistently higher for the ERV.

At operating points where frosting developed on the evaporator, the HRV configuration yielded noticeably longer defrost cycles (Figure 6.18). This resulted from the higher moisture content of the exhaust air, which produced greater frost accumulation on the evaporator surface and therefore extended the duration and frequency of defrost events. The longer defrost times further penalized the average heating capacity of the HRV system relative to that of the ERV. The same trends were reflected in the time-averaged system COP (including defrost losses). The ERV configuration achieved consistently higher COP values (Figure 6.21), owing to its greater average heating capacity combined with similar electrical consumption. Furthermore, with the outdoor temperature at −5 °C, the HRV configuration exhibited a marked reduction in COP due to the additional energy demand of the pre-heater, which remained inactive in the ERV configuration.

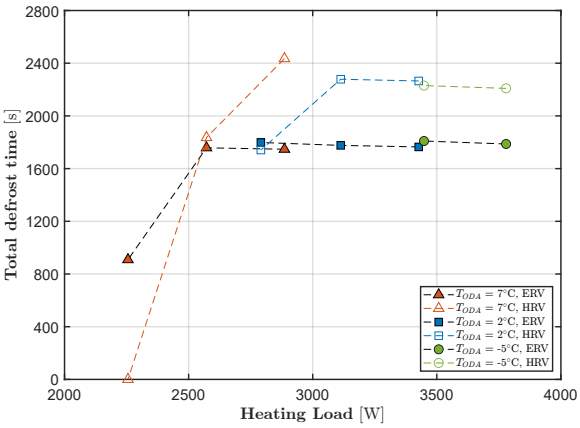

(a) $t_{tot,def}$ at $\dot{m}_{MVHR} = 227$ kg h^{-1}

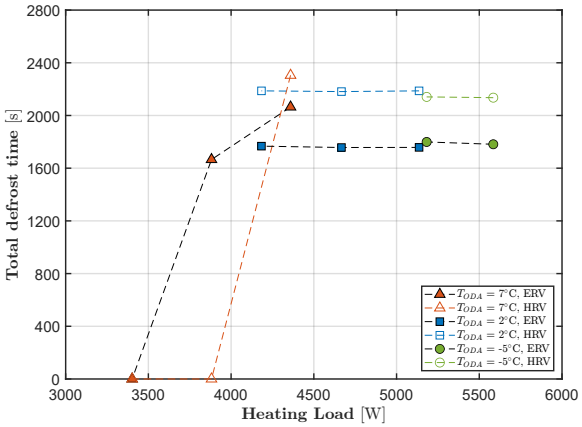

(b) $t_{tot,def}$ at $\dot{m}_{MVHR} = 339$ kg h^{-1}

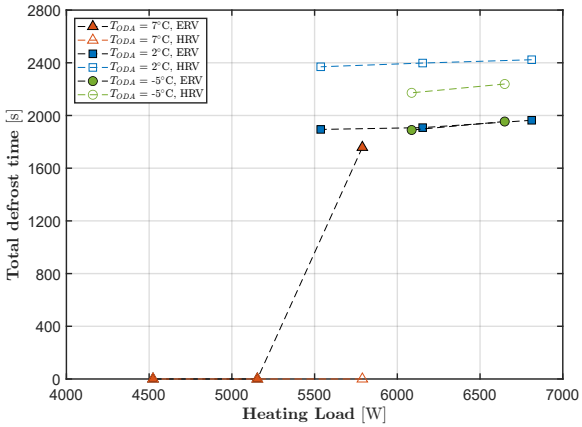

(c) $t_{tot,def}$ at $\dot{m}_{MVHR} = 447$ kg h^{-1}

Figure 6.18: System heating capacity in relation to defrost time for ERV and HRV configurations.

Overall, the comparison shows that the moisture-transfer capability of the ERV mitigates the conditions that promote evaporator frosting, leading to a more stable operation of the heat-pump cycle. The ERV lowers the evaporator frosting potential, stabilizes the heating capacity (less defrost events), and improves the time-averaged COP. By contrast, the HRV supplies warmer air and reduce the frosting risk, but at the cost of longer defrost cycles, and a more extensive pre-heating requirement. As a result, the ERV generally enhances the winter performance of the coupled system, except at specific operating points where the HRV benefits from an elevated evaporating temperature and completely avoids frosting (Figure 6.20). From a comfort perspective, the advantage of the warmer post-supply air delivered by the HRV becomes relevant only when sufficient free indoor moisture sources are available to counteract lower humidity level of the supply flow; otherwise, the more stable post-supply conditions associated with the ERV may be preferable.

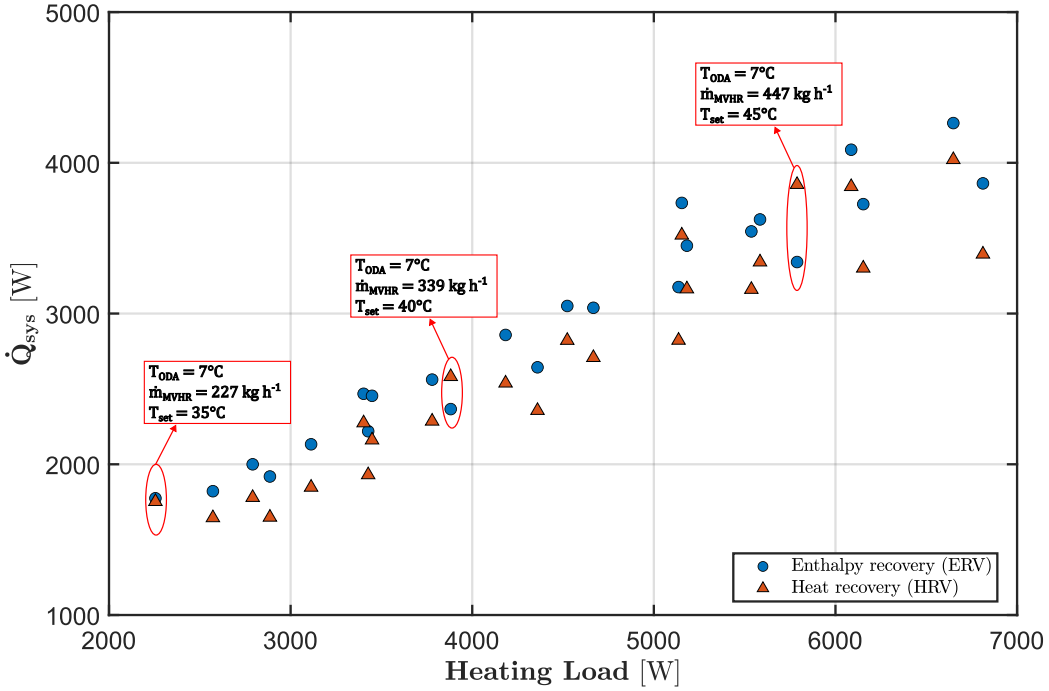

Figure 6.19: Heating capacity with defrost losses, ERV vs HRV.

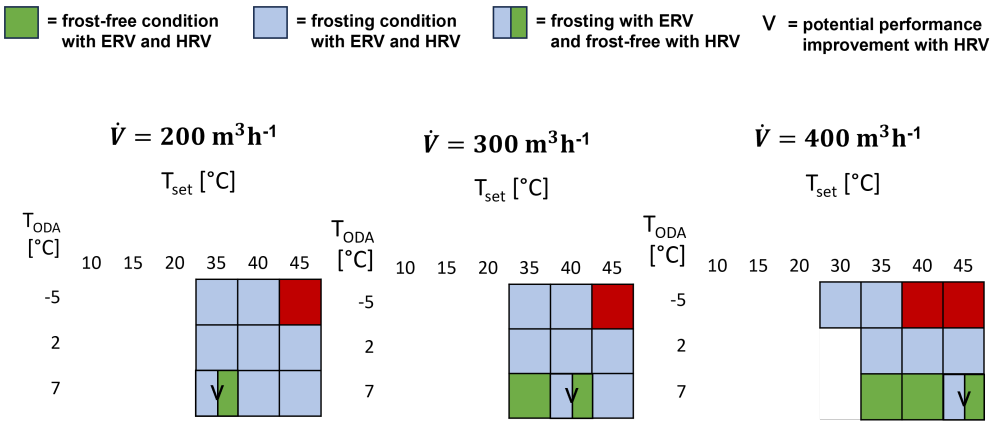

Figure 6.20: Performance impact map, ERV vs HRV.

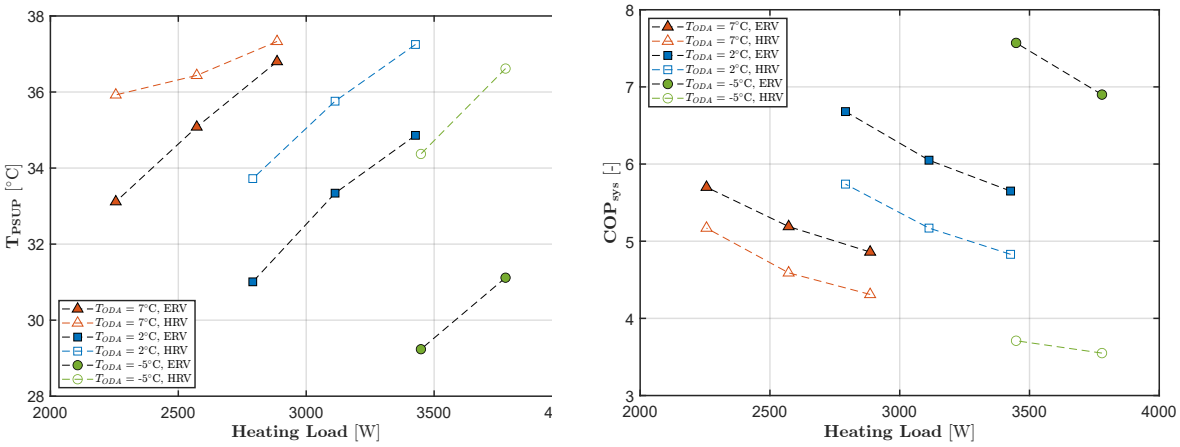

(a) Results at $\dot{m}_{MVHR} = 227$ kg h^{-1}

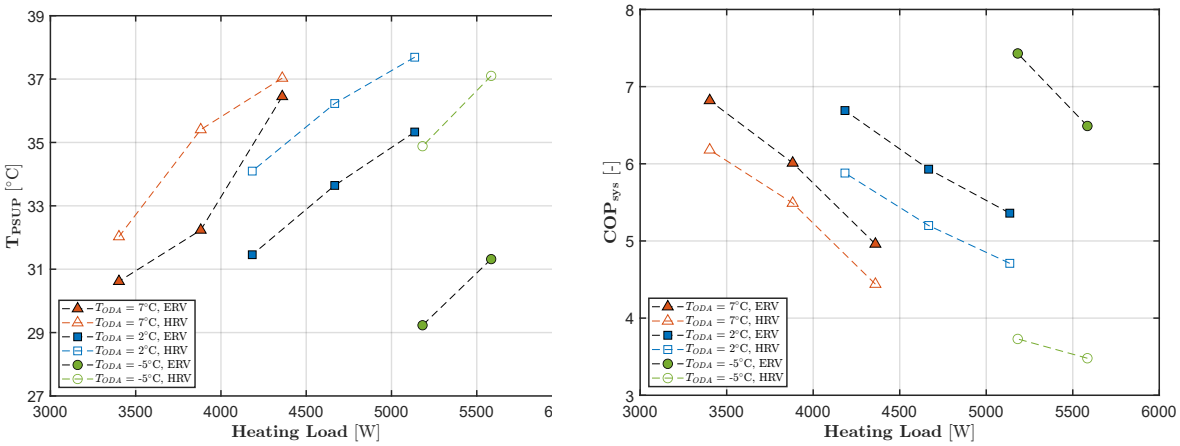

(b) Results at $\dot{m}_{MVHR} = 339$ kg h^{-1}

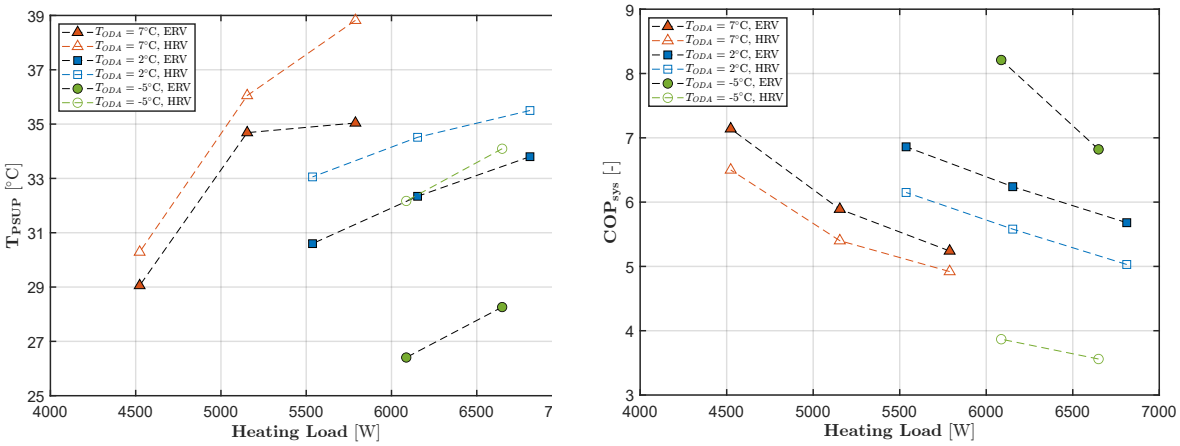

(c) Results at $\dot{m}_{MVHR} = 447$ kg h^{-1}

Figure 6.21: Post-supply temperature and system COP with defrost losses, ERV vs HRV.

6.2.3. Bypass of the recovery exchanger

Analogously to the summer analysis, the winter operating performance of the multifunctional system was assessed as a function of the bypass opening fraction of the recovery exchanger, varied between 0 % (no bypass) and 100 % (full bypass). This anal-

ysis was motivated by the hypothesis that, also under heating conditions, modifying the interaction between the heat pump and the recovery section could affect both the thermodynamic performance and the defrost behavior of the system. It should be noted that during the defrost phase the bypass of the recovery exchanger was assumed to remain closed, as activating it would lose physical meaning once the heat pump circuit was already bypassed. Under this condition, the recovery exchanger continued to transfer heat between the exhaust and outdoor air streams, preventing excessive cooling of the supply air during defrost and ensuring smoother temperature variations.

When only the active heating periods were considered, the system-level indicators—the active heating capacity, the active post-supply temperature, the active overall COP and the active post-supply humidity ratio—showed that the best performance was achieved when the recovery exchanger was not bypassed (Figures 6.22 and 6.23). These findings confirmed and extended the trends observed in summer operation, highlighting that the recovery of heat (and moisture, in the ERV configuration) provided clear benefits to the coupled system whenever the heat pump operated continuously without interruptions.

However, when the performance indicators were recalculated over the full operating period, including the defrost losses, a different conclusion emerged. At the same compressor speed, certain operating points exhibited a higher average heating capacity when the recovery exchanger was partially bypassed, both for the MFRBV/ERV configuration (Figure 6.22b) and for the MFRBV/HRV configuration (Figure 6.23b). This outcome can be explained by the reduction in total defrost time, which increased the fraction of operation under active heating and thus enhanced the time-averaged heating capacity over the entire operating cycle. Depending on the combined effect of the shorter defrost duration and the lower post-supply temperature during heating (resulting from the partial bypass of the recovery exchanger), two distinct behaviors were identified. In some operating points, the reduced defrost duration governed the overall average: because the system spent less time in the defrost phase — during which the ventilation unit continues to supply air at markedly lower temperatures — both the average heating capacity and the average post-supply temperature increased (red-circled points in Figures 6.22 and 6.23). In other points, the effect of the shorter defrost period was offset by the lower post-supply temperature during the heating phase. As a result, although the average heating capacity still increased due to the reduced defrost time, the post-supply temperature decreased because the air delivered during heating was significantly colder (blue-circled points in Figures 6.22 and 6.23). These latter conditions indicated an improvement in energetic performance that could entail a reduction in thermal comfort.

From the point of view of comfort, a slightly lower average supply temperature does not necessarily imply degraded conditions, provided it remains above the comfort threshold and the time spent below it is negligible. Moreover, the shorter defrost time improves the thermal stability perceived by occupants, while a modest temperature decrease at the

diffusers can promote better air mixing and prevent local overheating. Therefore, system assessment should jointly consider energy and comfort indicators to ensure that efficiency gains do not compromise indoor comfort.

The operating points showing a potential improvement in system performance with a partial bypass were typically located near the transition between frosting and non-frosting conditions of the outdoor coil (Figures 6.24a and 6.24b). Under these borderline conditions, partially bypassing the recovery exchanger produced a warmer and more humid exhaust airflow entering the outdoor coil, for both the ERV and HRV configurations (in the HRV case, the exhaust air could also be slightly more humid because less condensation occurred within the sensible core). These modified boundary conditions increased the evaporating temperature of the heat pump, reducing the frequency and total duration of defrost cycles (Figures 6.22h and 6.23h). The decrease in total defrost time could be explained by the frost growth dynamics on the outdoor coil: a higher evaporating temperature enhanced the diffusive mass flux of frost formation, generating denser frost that grew more slowly in thickness. This denser layer remained more thermally conductive, delaying the performance degradation of the coil and thus postponing the defrost trigger. Consequently, fewer defrost events occurred within the same operating period, although the frost mass accumulated per cycle was larger due to the higher moisture content of the exhaust air. A maximum improvement in the average heating capacity of 9.15% was achieved for the MFRBV/ERV system (for the operating point at $T_{ODA} = 7$°C, $\dot{m}_{MVHR} = 447$ kg h^{-1} at $T_{set} = 45$°C), while the MFRBV/HRV system attained a peak enhancement of 19.1% (for the operating point at $T_{ODA} = 7$°C, $\dot{m}_{MVHR} = 339$ kg h^{-1} at $T_{set} = 45$°C).

The magnitude of this improvement depends strongly on the recovery type. The system coupled with the ERV showed a more limited benefit, with reductions in defrost time confined to specific operating points. When bypassing the ERV, the exhaust air entering the evaporator became warmer and more humid due to reduced sensible and latent transfer across the membrane. The warmer inlet conditions increased the evaporating temperature and tended to delay frost formation, while the additional moisture promoted it. Under severe frosting conditions, the increase in humidity outweighed the rise in evaporating temperature, resulting in longer defrost durations. The same reduction in heat and moisture transfer also caused the supply air downstream of the recovery stage to become colder and drier, which further reduced the effectiveness of the bypass strategy in heating mode. In contrast, bypassing the HRV increased the exhaust-air temperature entering the outdoor coil while causing only minimal changes in exhaust humidity due to the limited condensation capability of the sensible core (Figure 6.23g), so the bypass did not introduce additional hygrometric penalties compared to the ERV configuration. Therefore, in this case, the warmer exhaust airflow consistently improved the operating conditions of the heat pump, producing a more pronounced and widespread reduction

in defrost time across the operating map and, consequently, a smaller penalty on the average system heating capacity as the bypass opening fraction increased (Figure 6.23b), for all operating points.

Regarding the average system COP, over the full operating period it remained generally lower—or at best equal—to that of the non-bypassed configuration. The improvement in heating capacity achieved through shorter defrost phases was counterbalanced by the higher electrical consumption associated with longer compressor operation and the additional fan power required to overcome the increased pressure losses in the bypass line of the ventilation unit. For the point where the maximum heating capacity improvement was observed, the overall COP decreased by 6.2% for the MFRBV/ERV system and by 1.79% for the MFRBV/HRV system, when the optimal bypass fraction was applied.

Overall, the results confirm that the optimal bypass strategy cannot be defined solely on the basis of thermodynamic efficiency. The interaction between energy performance, defrost behavior, and thermal comfort must be considered as a whole. Partial bypassing of the recovery exchanger proves to be a potentially beneficial control action in borderline frosting conditions, as it mitigates defrost penalties and thereby increases the average heating capacity, while also enhancing overall operational stability and improving the perceived thermal comfort by reducing temperature fluctuations. These benefits are most evident in the HRV configuration, where the bypass more effectively improves the inlet conditions of the outdoor coil across a wider range of operating points. In the ERV system, instead, the same strategy yields comparatively smaller energetic benefits and comes at the expense of reduced moisture transfer toward the supply air, leading to drier indoor conditions and a slight reduction in hygrometric comfort.

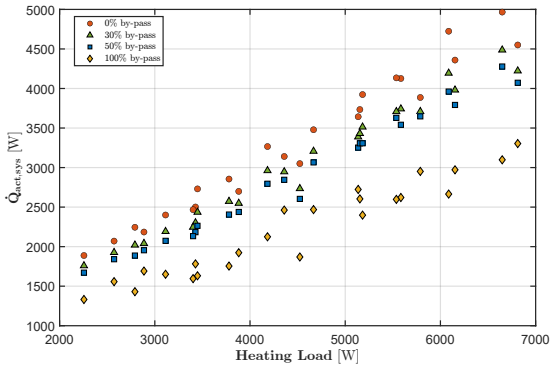

(a) Active heating capacity

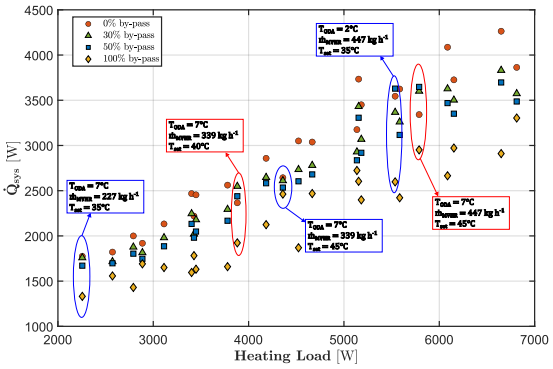

(b) Heating capacity with defrost losses

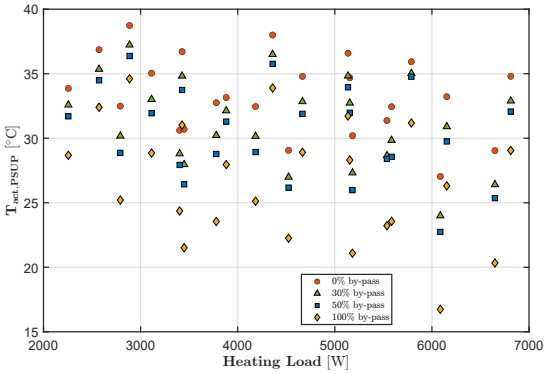

(c) Active PSUP temperature

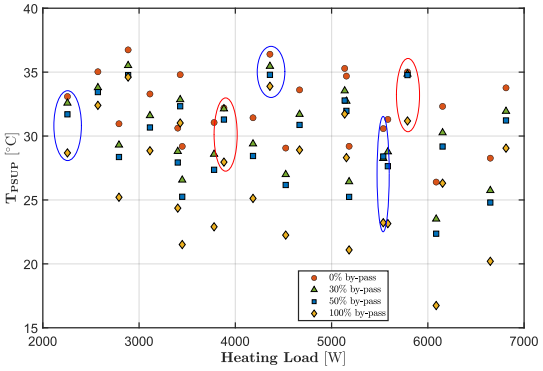

(d) PSUP temperature with defrost losses

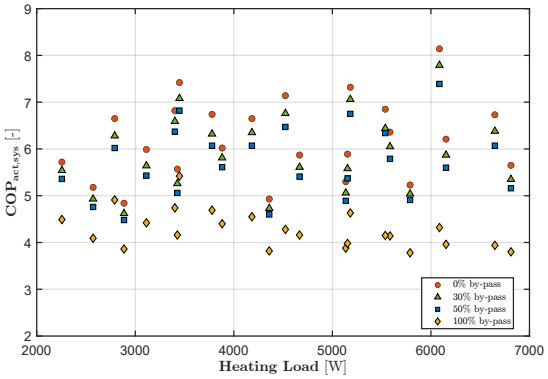

(e) Active system COP

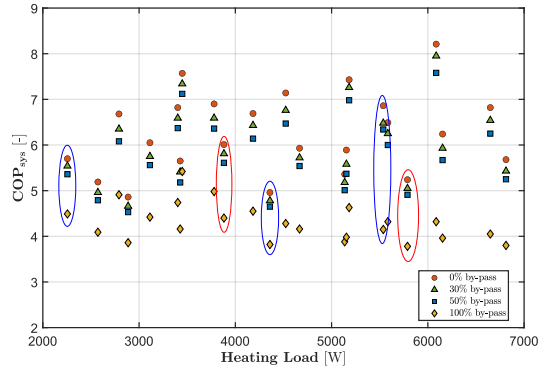

(f) Overall COP with defrost losses

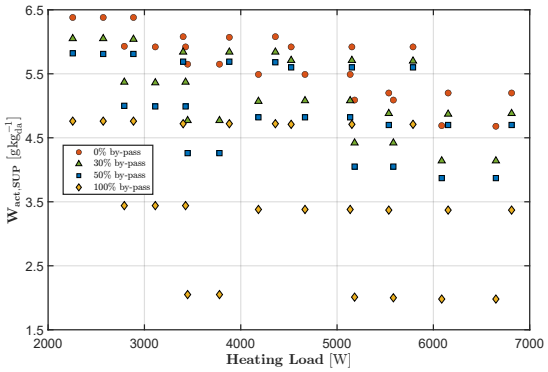

(g) Active PSUP humidity ratio

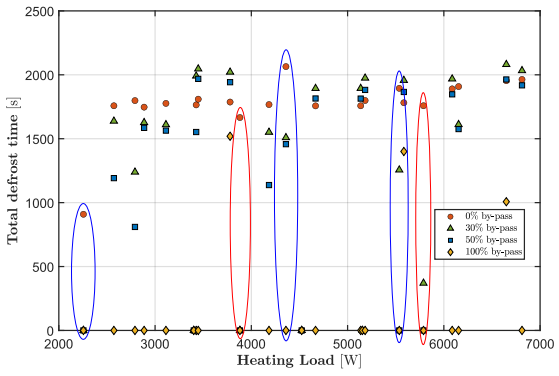

(h) Total defrost time

Figure 6.22: Performance indicators under different bypass levels of the enthalpy recovery exchanger (ERV).

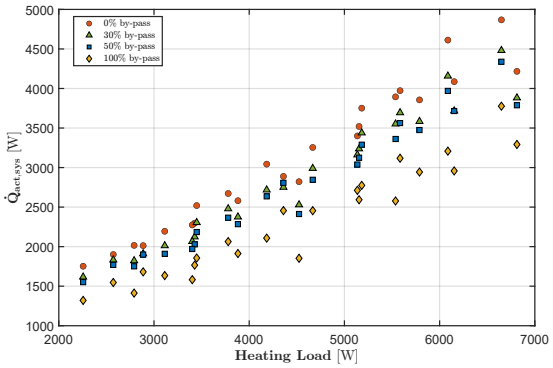

(a) Active heating capacity

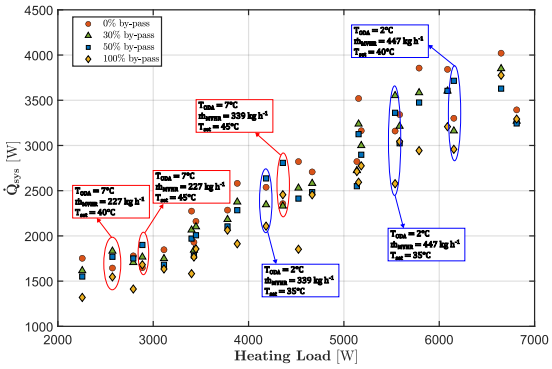

(b) Heating capacity with defrost losses

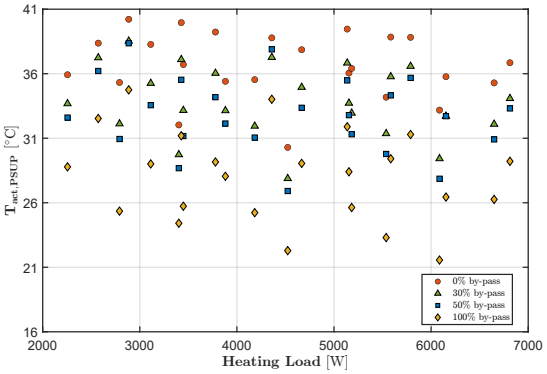

(c) Active PSUP temperature

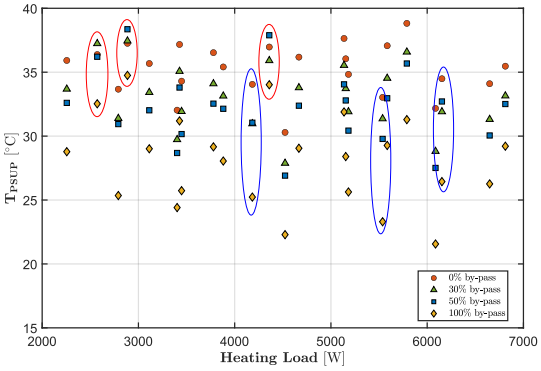

(d) PSUP temperature with defrost losses

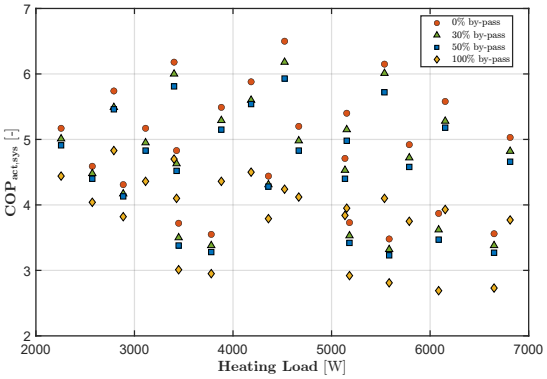

(e) Active system COP

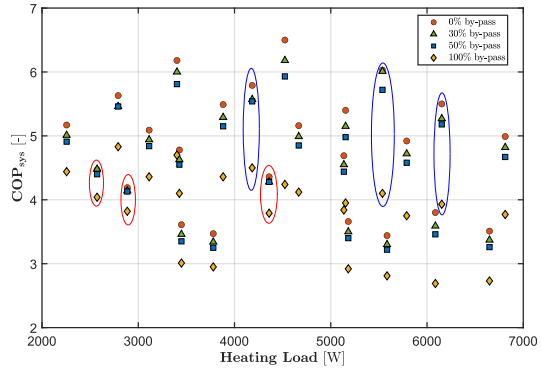

(f) System COP with defrost losses

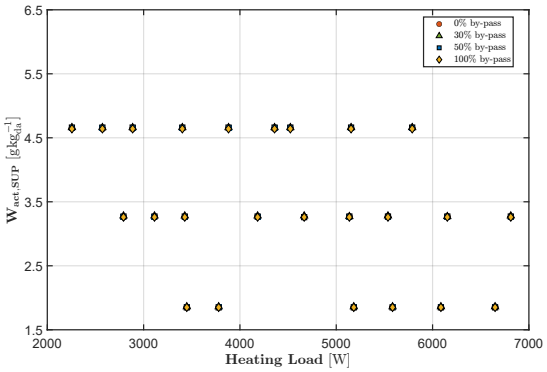

(g) Active PSUP humidity ratio

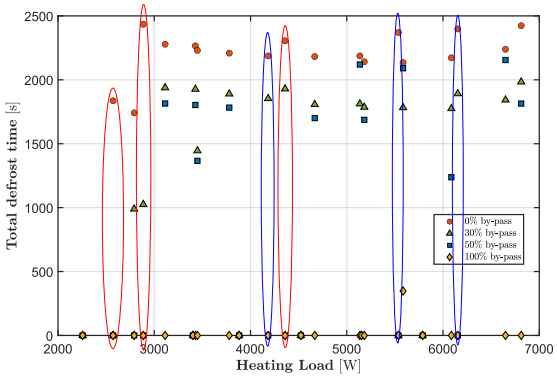

(h) Total defrost time

Figure 6.23: Performance indicators under different bypass levels of the sensible-only recovery exchanger (HRV).

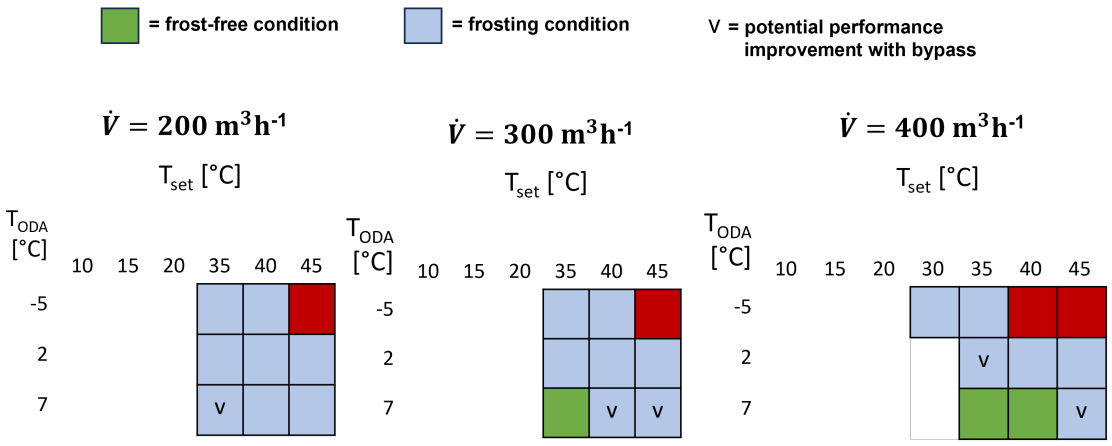

(a) MFRBV/ERV unit.

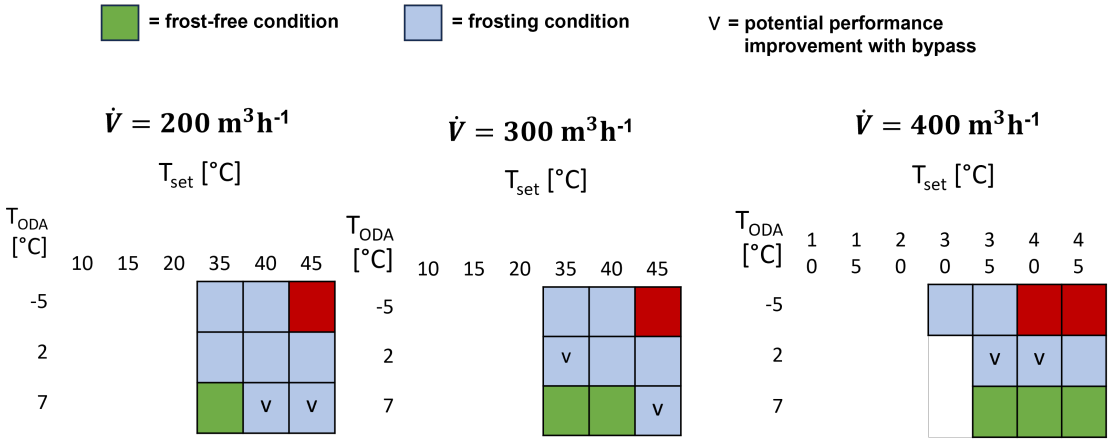

(b) MFRBV/HRV unit.

Figure 6.24: Bypass impact maps.

CHAPTER 7

Conclusions

In this work, a physics-based dynamic digital twin of a multifunctional balanced ventilation unit integrating an air-to-air heat pump was developed and experimentally validated. The model is able to capture the main physical mechanisms governing the operation of these systems through a detailed representation of the heat exchangers and all major components, using a combination of lumped and distributed parameter formulations to balance accuracy and computational cost. In heating mode, the modelling framework was further extended to explicitly represent evaporator frosting through a physics-based formulation, enabling the model to reproduce performance degradation mechanisms that are typically overlooked or oversimplified in conventional HVAC models.

The comparison with 45 experimentally characterized operating points, covering the full range of operating conditions for the unit analyzed, showed that the model replicates system behavior with high accuracy. All major performance metrics were captured reliably, including heating/cooling capacity, electrical power input, and COP/EER, as well as key state variables such as outlet air conditions, air-side pressure drops, and refrigerant temperatures. Summer points were validated against steady-state measurements, whereas winter points were validated using time-averaged system performance to account for the transient performance degradation induced by frost accumulation on evaporator surface. For most operating points, deviations between predictions and measurements remained within ±10%, with only a few outliers. Therefore, the digital twin provides a robust and reliable representation of the real system and can be used as a predictive tool beyond the specific operating range explored experimentally.

Following the validation, the digital twin was subsequently used to evaluate the performance of three system configuration variants under both cooling and heating conditions.

The analysis of the system integrating an external air recirculation loop (OEA) showed

that the impact of the additional airflow depends strongly on the operating regime. In summer, the additional recirculated flow enhances heat transfer on the condenser side and helps to keep system overheating under control, allowing the compressor to operate at higher speeds and resulting in increased cooling capacity at medium and high loads, although this benefit is partly offset by lower EER due to the additional electrical consumption of both the auxiliary fan and the compressor. In the most favourable case, cooling capacity increased by up to 25%, while the EER decreased by 15.6%. In winter, the impact of the additional recirculated airflow depends on how it modifies the evaporating temperature, since this directly influences frost formation and the associated performance degradation. When the enhanced airflow raises the evaporating temperature sufficiently, frost accumulation decreases and the system delivers higher time-averaged heating capacity with more stable operation and fewer or no defrost events. Indeed, the implementation of this recirculation loop enabled a peak increase in heating capacity of 21.2%, achieved through a 4°C rise in the average post-supply air temperature. When the evaporating temperature remains low, instead, the larger moisture flux promotes rapid formation of insulating frost layers and leads to longer or more frequent defrost phases, reducing the net gain in heating performance. In these operating points, the benefit of a higher time-averaged post-supply temperature may also be offset at the comfort level, as frost-induced instabilities lead to larger temperature fluctuations and more frequent exposure to colder supply air during defrost. From an energy-efficiency perspective, a general decrease in COP is observed, also in this case, due to the extra electrical demand of the auxiliary fan and the increased compressor power consumption; specifically, a reduction in COP of approximately 8.3% was recorded at the point of maximum heating capacity improvement.

In addition to that, the comparison between the system equipped with an enthalpy-based exchanger (ERV) and the system equipped with a sensible-only exchanger (HRV) shows distinct seasonal behaviours. In summer, the ERV lowers the humidity of the air entering the evaporator, reducing the latent load and allowing a larger share of the cooling capacity to be used for sensible cooling, which results in lower post-supply temperatures at the system level and higher overall unit EER, whereas the HRV configuration delivers colder but more humid air at the ventilation-unit level, increasing the latent load on the heat pump and forcing a larger fraction of the cooling capacity to be spent on dehumidification, ultimately yielding warmer final supply air and lower overall performance. On average, the system equipped with the ERV unit delivered a 28% higher cooling capacity and a 25% higher EER than the system equipped with the HRV unit. In winter, the ERV again yields more favourable behavior: by reducing the humidity of the airflow entering the evaporator, it reduces frost accumulation, shortens defrost cycles, and leads to higher time-averaged COP and heating capacity compared to the HRV configuration. Conversely, the HRV configuration supplies warmer and drier post-supply air, while the higher hu-

midity at the evaporator inlet promotes faster frost formation, causing longer or more frequent defrost phases, thus worsening system performance. The HRV configuration offers more stable operation only at operating points very close to the frosting threshold, where the specific thermo-hygrometric conditions of the air entering the evaporator can raise the evaporating temperature just enough to reduce or eliminate frost formation; however, this behavior is limited to a narrow operating boundary region. In this narrow region, the HRV configuration delivered 15.4% higher time-averaged heating capacity compared to the ERV configuration, but this comes at the cost of a 6.1% reduction in average COP. Outside this limited range, the ERV configuration consistently outperforms the HRV configuration.

Finally, the parametric bypass fraction analysis of the recovery exchanger showed that, in summer conditions, increasing the bypass opening improves the intrinsic cycle EER of the heat pump by providing more favourable evaporator inlet conditions. However, the overall system EER consistently decreases because bypassing reduces the sensible and latent recovery available at the ventilation unit, outweighing the modest gains achieved at the heat pump level for both ERV and HRV configurations. Although bypass penalizes full-load performance in summer, the analysis showed that it plays a different role under part-load conditions. In these conditions, partial bypass helps the system meet the post-supply temperature set-point more smoothly when the minimum compressor speed still provides more cooling capacity than required. By modulating the bypass opening fraction, the unit alters the thermo-hygrometric conditions of the supplied air (for instance, raising its temperature and humidity), thereby reducing the total effective cooling capacity delivered by the system. This allows the system to better match the load through a continuous adjustment of supply conditions, avoiding the abrupt regulation associated with on-off compressor cycling. On the other side, in winter conditions, increasing the bypass fraction of the recovery exchanger raises both the temperature and the humidity of the air entering the evaporator. This change in inlet conditions causes the refrigerant to evaporate at a higher temperature. For the operating points near the frosting threshold, this increase reduces the time spent in defrost and, in some cases, eliminates the need for defrost. At these specific operating conditions, the balance between the loss of heating capacity attributable to the partial bypass of heat recovery and the reduction in defrost time becomes favourable, resulting in higher time-averaged heating capacity, an effect notably pronounced in the HRV configuration. Regarding the average system efficiency, however, the COP generally remained comparable to or lower than that of the non-bypassed configuration, as the thermal gains were offset by the increased compressor consumption and the additional fan power required to overcome higher pressure drops in the bypass circuit. The use of the optimal bypass fraction yielded a maximum improvement of 9.15% in average heating capacity for the MFRBV/ERV system and 19.1% for the MFRBV/HRV system, with a concurrent reduction in the overall

COP of 6.2% and 1.79%, respectively. Conversely, outside these transitional conditions, bypassing the exchanger leads to lower performance because the loss of sensible and latent recovery outweighs the thermodynamic benefits at the heat pump level.

Overall, these results show that airflow management, recovery strategy, and bypass operation interact in complex and non-linear ways with the thermodynamic cycle and with the moisture loads that govern condensation in summer and frost formation in winter. Interventions that are beneficial under cooling conditions may become neutral or even detrimental in winter, and strategies that enhance the heat pump cycle often fail to improve the performance of the coupled system. The digital twin thus provides a comprehensive framework for identifying when and why each configuration delivers performance advantages, and under which boundary conditions these strategies should be deployed.

More broadly, the study demonstrates the value of physics-based digital twins in extending the scope of conventional experimental testing. By enabling systematic exploration of coupled thermodynamic and control phenomena that would be difficult or impractical to assess experimentally, the modelling framework provides deeper insight into how recovery, airflow management, and compressor operation shape system performance across the full operating envelope. At the same time, it offers a robust foundation for the design and optimization of next-generation multifunctional ventilation units aimed at achieving higher energy efficiency and improved indoor comfort in low-energy buildings.

Acknowledgements

I want to express my gratitude to my family, my girlfriend, and my friends for their support and patience throughout this journey. Their encouragement has been essential during the most demanding phases of this work.

I would also like to thank my colleagues and my supervisors for their guidance, feedback, and collaboration. Their insight helped shape the direction and quality of this research.

Finally, I want to acknowledge the Zehnder Group - Competence Center Campogalliano (MO) and my colleagues at the University of Innsbruck for their support and for providing the resources necessary to carry out the research and experimental activities needed to complete this project.

Doctoral dissertation funded by the European Union - NextGenerationEU, Mission 4, Component 2 “Dalla Ricerca all’Impresa” - Investment 3.3 “Introduzione di dottorati innovativi che rispondono ai fabbisogni di innovazione delle imprese e promuovono l’assunzione dei ricercatori dalle imprese”.

Bibliography

[1] U. SBCI. Sustainable buildings & climate initiative. *Buildings and Climate Change: Summary for Decision-Makers*, 2009.

[2] J. Seppälä, I. Mäenpää, S. Koskela, T. Mattila, A. Nissinen, J.M. Katajajuuri, T. Härmä, M.R. Korhonen, M. Saarinen, and Y. Virtanen. An assessment of greenhouse gas emissions and material flows caused by the finnish economy using the envimat model. *Journal of Cleaner Production*, 19(16):1833–1841, 2011. Promoting Transformation towards Sustainable Consumption and Production in a Resource and Energy Intensive Economy - the Case of Finland.

[3] L.G. Swan and V.I. Ugursal. Modeling of end-use energy consumption in the residential sector: A review of modeling techniques. *Renewable and Sustainable Energy Reviews*, 13(8):1819–1835, 2009.

[4] M.K. Mattinen, J. Heljo, J. Vihola, A. Kurvinen, S. Lehtoranta, and A. Nissinen. Modeling and visualization of residential sector energy consumption and greenhouse gas emissions. *Journal of Cleaner Production*, 81:70–80, 2014.

[5] Eurostat. Energy consumption in households, 2025. Accessed: 2026-01-28.

[6] K. S, G. O, B. J, D. D, and P. D. Promoting healthy and energy efficient buildings in the european union: National implementation of related requirements of the energy performance buildings directive (2010/31/eu). Scientific analysis or review KJ-1A-27665-EN-N (online),KJ-1A-27665-EN-C (print), KJ-1A-27665-EN-E (ePub), Luxembourg (Luxembourg), 2017.

[7] I. Sartori, A. Napolitano, A.J. Marszal, S. Pless, P. Torcellini, and K. Voss. Criteria for definition of net zero energy buildings. In *International Conference on Solar Heating, Cooling and Buildings (EuroSun 2010)*. EuroSun 2010, 2010.

[8] A. Kamenders, R. Stivriņš, and G. Žogla. Minimum energy performance standards (meps) in the residential sector. *The European Economic and Social Committee (EESC)*, 2022.

[9] V. Földváry, G. Bekö, S. Langer, K. Arrhenius, and D. Petráš. Effect of energy renovation on indoor air quality in multifamily residential buildings in slovakia. *Building and Environment*, 122:363–372, 2017.

[10] International Energy Agency. Energy efficiency in buildings – buildings 2020, 2020. Accessed: 2025-11-19.

[11] M. Manic, D. Wijayasekara, K. Amarasinghe, and J.J. Rodriguez-Andina. Building energy management systems: The age of intelligent and adaptive buildings. *IEEE Industrial Electronics Magazine*, 10(1):25–39, 2016.

[12] A. Tejani, H. Gajjar, V. Toshniwal, and R. Kandelwal. The impact of low-gwp refrigerants on environmental sustainability: An examination of recent advances in refrigeration systems. *ESP Journal of Engineering & Technology Advancements*, 2(2):62–77, 2022.

[13] M. Jamil and S. Mittal. Building energy management system: A review. In *2017 14th IEEE India Council International Conference (INDICON)*, pages 1–6. IEEE, 2017.

[14] EN 14825:2022 air conditioners, liquid chilling packages and heat pumps with electrically driven compressors for space heating and cooling – testing and rating at part load conditions and calculation of seasonal performance, 2022. Standard.

[15] M. Mannan and S.G. Al-Ghamdi. Indoor air quality in buildings: A comprehensive review on the factors influencing air pollution in residential and commercial structure. *International Journal of Environmental Research and Public Health*, 18(6), 2021.

[16] R. Sedoni, M. Romani, and P.E. Santangelo. A hybrid model for the assessment of indoor environmental quality in buildings: An insight into mold growth. *Energy Reports*, 13:4114–4125, 2025.

[17] A. Tejani and R. Khandelwal. Enhancing indoor air quality through innovative ventilation designs: A study of contemporary hvac solutions. *ESP International Journal of Advancements in Science & Technology*, 1(2):35–48, 2023.

[18] G. Murano, F. Caffari, and N. Calabrese. Energy potential of existing reversible air-to-air heat pumps for residential heating. *Sustainability (2071-1050)*, 16(14), 2024.

[19] O. Eguiarte, A. Garrido-Marijuán, P. de Agustín-Camacho, L. del Portillo, and A. Romero-Amorrortu. Energy, environmental and economic analysis of air-to-air heat pumps as an alternative to heating electrification in europe. *Energies*, 13(15):3939, 2020.

[20] W. Li, J. Wang, W. Shi, and J. Lu. High-efficiency cooling solution for exhaust air heat pump: Modeling and experimental validation. *Energy*, 254:124396, 2022.

[21] D. Siegele, F. Ochs, and W. Feist. Novel speed-controlled exhaust-air to supply-air heat pump combined with a ventilation system. *Applied Thermal Engineering*, 162:114230, 2019.

[22] S. Xu, J. Niu, G. Ma, and J. Wu. Research on working characteristics of composite two-stage ventilation heat recovery system with heat pipe and heat pump. *Energy*, 304:132130, September 2024.

[23] X. Jia, G. Ma, F. Zhou, S. Liu, G. Wu, and Q. Sui. The applicability and energy consumption of a parallel-loop exhaust air heat pump for environment control in ultra-low energy building. *Applied Thermal Engineering*, 210:118292, 2022.

[24] C. Liang, X. Li, X. Meng, W. Shi, J. Gu, B. Wang, and Y. Lv. Experimental investigation of heating performance of air source heat pump with stable heating capacity during defrosting. *Applied Thermal Engineering*, 235:121433, 2023.

[25] X. Cao, C. Yang, Z. Sun, Y.M. Lu, M.M. Chang, L.L. Shao, and C.L. Zhang. A novel packaged outdoor air dehumidifier with exhaust air heat pump – Experiment and simulation. *Applied Thermal Engineering*, 181:115986, November 2020.

[26] C.H. Liang, L.Z. Zhang, and L.X. Pei. Performance analysis of a direct expansion air dehumidification system combined with membrane-based total heat recovery. *Energy*, 35(9):3891–3901, 2010.

[27] B. Guo, X. Huang, Q. Li, Y. Fan, Y. Yang, Y. Wang, and J. He. A complete ASHP-based HVAC hybrid model for building energy retrofits via two-stage event-triggered model predictive control. *Journal of Building Engineering*, 100:111624, April 2025.

[28] L. Tang, H. Xie, Y. Wang, and Z. Xu. Deeply flexible commercial building HVAC system control: A physics-aware deep learning-embedded MPC approach. *Applied Energy*, 388:125631, June 2025.

[29] P. Li, D. Vrabie, D. Li, S.C. Bengea, S. Mijanovic, and Z.D. O'Neill. Simulation and experimental demonstration of model predictive control in a building HVAC system. *Science and Technology for the Built Environment*, 21(6):721–732, August 2015.

[30] Q. Si, J. Wei, Y. Li, and H. Cai. Optimization for the Model Predictive Control of Building HVAC System and Experimental Verification. *Buildings*, 12(10):1602, October 2022.

[31] G. Dermentzis, F. Ochs, D. Siegele, and W. Feist. A façade integrated micro-heat pump–energy performance simulations. *IBPSA, Bausim*, 2014.

[32] M. Anderson, M. Buehner, P. Young, D. Hittle, C. Anderson, J. Tu, and D. Hodgson. An experimental system for advanced heating, ventilating and air conditioning (hvac) control. *Energy and Buildings*, 39(2):136–147, February 2007.

[33] M. Dongellini, C. Naldi, and G.L. Morini. Influence of sizing strategy and control rules on the energy saving potential of heat pump hybrid systems in a residential building. *Energy Conversion and Management*, 235:114022, 2021.

[34] P. Sakulpipatsin, J. Cauberg, H. van der Kooi, and L. Itard. Application of the exergy concept to ventilation using heat recovery from exhaust air. In *Proceedings of Clima*, 2007.

[35] X. Sun, J. Wu, and R. Wang. Exergy analysis and comparison of multi-functional heat pump and conventional heat pump systems. *Energy Conversion and Management*, 73:51–56, September 2013.

[36] A.C. Ispir, G.O. Rodriguez, W. De Vries, and M. Speetjens. Digital twin development of a full-scale industrial heat pump. *Applied Thermal Engineering*, 269:125921, June 2025.

[37] A. Shirani, A. Merzkirch, J. Roesler, S. Leyer, F. Scholzen, and S. Maas. Experimental and analytical evaluation of exhaust air heat pumps in ventilation-based heating systems. *Journal of Building Engineering*, 44:102638, December 2021.

[38] A.K. Albdoor, Z. Ma, P. Cooper, F. Al-Ghazzawi, J. Liu, C. Richardson, and P. Wagner. Air-to-air enthalpy exchangers: Membrane modification using metal-organic frameworks, characterisation and performance assessment. *Journal of Cleaner Production*, 293:126157, April 2021. Publisher: Elsevier BV.

[39] A.K. Albdoor, Z. Ma, and P. Cooper. Moisture diffusion measurement and evaluation for porous membranes used in enthalpy exchangers. *Energy Procedia*, 160:499–506, February 2019. Publisher: Elsevier BV.

[40] E.J. Lee, J.P. Lee, and N.H. Kim. Moisture transfer characteristics of a licl-impregnated paper membrane used for an enthalpy exchanger. *Journal of Mechanical Science and Technology*, 27(5):1527–1537, 2013.

[41] G. Baldinelli, A. Rotili, R. Narducci, M.L. Di Vona, and A. Marrocchi. Experimental analysis of an innovative organic membrane for air to air enthalpy exchangers. *International Communications in Heat and Mass Transfer*, 108:104332, November 2019. Publisher: Elsevier BV.

[42] I.R. Abadi, B. Aminian, R. Huizing, S. Rogak, and S. Green. Orientation dependent permeability in asymmetric composite membranes. *Journal of Membrane Science*, 652:120474, 2022.

[43] A.Y.T. Al-Zubaydi and G. Hong. Experimental investigation of counter flow heat exchangers for energy recovery ventilation in cooling mode. *International Journal of Refrigeration*, 93:132–143, 2018.

[44] M. Nasif, R. Al-Waked, G. Morrison, and M. Behnia. Membrane heat exchanger in hvac energy recovery systems, systems energy analysis. *Energy and Buildings*, 42(10):1833–1840, 2010.

[45] H.J. Cho, S.Y. Cheon, and J.W. Jeong. Experimental analysis on energy recovery ventilator with latent heat exchanger using hollow fiber membrane. *Energy Conversion and Management*, 278:116706, 2023.

[46] R. Al-Waked, M.S. Nasif, G. Morrison, and M. Behnia. CFD simulation of air to air enthalpy heat exchanger. *Energy Conversion and Management*, 74:377–385, October 2013.

[47] R. AL-Waked, M.S. Nasif, G. Morrison, and M. Behnia. CFD simulation of air to air enthalpy heat exchanger: Variable membrane moisture resistance. *Applied Thermal Engineering*, 84:301–309, June 2015.

[48] A. Engarnevis, R. Huizing, S. Green, and S. Rogak. Heat and mass transfer modeling in enthalpy exchangers using asymmetric composite membranes. *Journal of Membrane Science*, 556:248–262, June 2018.

[49] L.Z. Zhang. Heat and mass transfer in a cross-flow membrane-based enthalpy exchanger under naturally formed boundary conditions. *International Journal of Heat and Mass Transfer*, 50(1-2):151–162, January 2007.

[50] M. Pourhoseinian, N. Asasian-Kolur, and S. Sharifian. CFD investigation of heat and moisture recovery from air with membrane heat exchanger. *Applied Thermal Engineering*, 191:116911, June 2021.

[51] R. Sebai, R. Chouikh, and A. Guizani. Cross-flow membrane-based enthalpy exchanger balanced and unbalanced flow. *Energy Conversion and Management*, 87:19–28, November 2014.

[52] I.S. Kang, T.K. Ahn, and J.C. Park. A performance evaluation of plate type enthalpy exchanger through cfd analysis of elements. *Korean Journal of Air-Conditioning and Refrigeration Engineering*, 29(1):1–6, 2017.

[53] D. Siegele and F. Ochs. Effectiveness of a membrane enthalpy heat exchanger. *Applied Thermal Engineering*, 160:114005, 2019.

[54] X.D. He, S. Liu, and H.H. Asada. Modeling of vapor compression cycles for multivariable feedback control of hvac systems. *Journal of Dynamic Systems, Measurement, and Control*, 119(2):183–191, 06 1997.

[55] M. Gräber, N.C. Strupp, and W. Tegethoff. Moving boundary heat exchanger model and validation procedure. In *EUROSIM Congress on Modelling and Simulation*, 2010.

[56] D. Kim, D. Ziviani, J.E. Braun, and E.A. Groll. A moving boundary modeling approach for heat exchangers with binary mixtures. *Energy Procedia*, 129:466–473, 2017.

[57] P. Mithraratne, N. Wijeysundera, and T. Bong. Dynamic simulation of a thermostatically controlled counter-flow evaporator. *International Journal of Refrigeration*, 23(3):174–189, 2000.

[58] W.D. Gruhle and R. Isermann. Modeling and control of a refrigerant evaporator. *Journal of Dynamic Systems, Measurement, and Control*, 1985.

[59] M. Giovannini and M. Lorenzini. Switching criteria analysis for a condenser moving boundary model. In *Journal of Physics: Conference Series*, volume 2685, page 012040. IOP Publishing, 2024.

[60] B.P. Rasmussen and B. Shenoy. Dynamic modeling for vapor compression systems—part ii: Simulation tutorial. *HVAC&R Research*, 18(5):956–973, 2012.

[61] R. Sedoni, P.E. Santangelo, D. Angeli, M. Romani, and L. Fioravanti. An analytical model of evaporator performance under frosting conditions for lumped-parameter simulations of heat pumps. In *Journal of Physics: Conference Series*, volume 2940, page 012015. IOP Publishing, 2025.

[62] H. Qiao, V. Aute, and R. Radermacher. Dynamic modeling and characteristic analysis of a two-stage vapor injection heat pump system under frosting conditions. *International Journal of Refrigeration*, 84:181–197, 2017.

[63] A. Desideri, B. Dechesne, J. Wronski, M. Van den Broek, S. Gusev, V. Lemort, and S. Quoilin. Comparison of moving boundary and finite-volume heat exchanger models in the modelica language. *Energies*, 9(5):339, 2016.

[64] Center for Environmental Energy Engineering. CoilDesigner®. Software, 2025. Available at: https://optimizedthermalsystems.com/coildesigner/.

[65] P.A. Domanski, D.A. Yashar, and J. Wojtusiak. *EVAP-COND; Simulation Models for Finned-Tube Heat Exchangers with Circuitry Optimization, Version 5.0*. National Institute of Standards and Technology, Gaithersburg, MD, 2021.

[66] Y. Hayashi, A. Aoki, S. Adachi, and K. Hori. Study of frost properties correlating with frost formation types. *ASME Journal of Heat and Mass Transfer*, 1977.

[67] Y. Hayashi, K. Aoki, and H. Yuhara. Study of frost formation based on a theoretical model of the frost layer. *Heat Transfer Research*, 6(3):79–94,, 1977.

[68] Y. Hayashi, K. Aoki, and H. Yuhara. Study of frost formation in forced convection. *Transactions of the Japan Society of Mechanical Engineers*, 42(355):885–892, 1976.

[69] C.T. Sanders. *The influence of frost formation and defrosting on the performance of air coolers*. PhD thesis, Technical University of Delft, Netherlands, 1974.

[70] J.D. Yonko. An investigation of the thermal conductivity of frost while forming on a flat horizontal plate. Master's thesis, The Ohio State University, 1965.

[71] P.T. Brian, R.C. Reid, and Y.T. Shah. Frost deposition on cold surfaces. *Industrial & Engineering Chemistry Fundamentals*, 9(3):375–380, 1970.

[72] D. O'Neal and D. Tree. A review of frost formation in simple geometries. *ASHRAE Transactions*, 91:267–281, 06 1985.

[73] M.A. Dietenberger. A frost formation model and its validation under various experimental conditions. Technical report, NASA, 1982.

[74] M. Kandula. Effective thermal conductivity of frost consideringmass diffusion and eddy convection. *Special Topics & Reviews in Porous Media: An International Journal*, 1(4), 2010.

[75] Y.X. Tao, R. Besant, and K. Rezkallah. A mathematical model for predicting the densification and growth of frost on a flat plate. *International Journal of Heat and Mass Transfer*, 36(2):353–363, 1993.

[76] R. Le Gall, J. Grillot, and C. Jallut. Modelling of frost growth and densification. *International Journal of Heat and Mass Transfer*, 40(13):3177–3187, 1997.

[77] S. Padhmanabhan. *Study of frost growth on heat exchangers used as outdoor coils in air source heat pump systems*. PhD thesis, Oklahoma State University, 2011.

[78] H. Qiao, V. Aute, and R. Radermacher. Dynamic modeling and characteristic analysis of a two-stage vapor injection heat pump system under frosting conditions. *International Journal of Refrigeration*, 84:181–197, 2017.

[79] X. Bai, S. Liu, S. Deng, L. Zhang, and M. Wei. A modelling study on the frosting characteristics of a novel dual-fan outdoor coil in an air source heat pump unit. *Applied Thermal Engineering*, 222:119933, 2023.

[80] J. Cui, W. Li, Y. Liu, and Y. Zhao. A new model for predicting performance of fin-and-tube heat exchanger under frost condition. *International Journal of Heat and Fluid Flow*, 32(1):249–260, 2011.

[81] E. Afrasiabian, O. Iliev, S. Lazzari, and C. Isetti. Numerical simulation of frost formation on a plate-fin evaporator. In *Proceedings of the 3rd World Congress on Momentum, Heat and Mass Transfer (MHMT'18) Budapest, Hungary, ICMFHT*, volume 125, pages 1395–1411, 2018.

[82] Directive 2009/125/ec of the european parliament and of the council of 21 october 2009 establishing a framework for the setting of ecodesign requirements for energy-related products. Official Journal of the European Union L 285, 2009.

[83] Regulation (eu) 2017/1369 of the european parliament and of the council of 4 july 2017 setting a framework for energy labelling and repealing directive 2010/30/eu. Official Journal of the European Union L 198, July 2017.

[84] European Committee for Standardization (CEN). EN 13141-7:2021 ventilation for buildings — performance testing of components/products for residential ventilation — part 7: Performance testing of ducted mechanical supply and exhaust ventilation units (including heat recovery), 2021. European Standard.

[85] European Committee for Standardization (CEN). EN 13141-8:2014 ventilation for buildings — performance testing of components/products for residential ventilation — part 8: Performance testing of non-ducted mechanical supply and exhaust ventilation units (including heat recovery), 2014. European Standard.

[86] European Committee for Standardization (CEN). EN 16573:2017 ventilation for buildings — performance testing of components/products for residential buildings — multifunctional balanced ventilation units for single family dwellings, including heat pumps, 2017. European Standard.

[87] European Commission. Commission regulation (eu) no 1253/2014 of 7 july 2014 implementing directive 2009/125/ec of the european parliament and of the council with regard to ecodesign requirements for ventilation units. Official Journal of the European Union, OJ L 337, 25.11.2014, pp. 8–26, 2014. Text with EEA relevance.

[88] European Commission. Commission regulation (eu) no 813/2013 of 2 august 2013 implementing directive 2009/125/ec of the european parliament and of the council with regard to ecodesign requirements for space heaters and combination heaters. Official Journal of the European Union, OJ L 239, 6.9.2013, pp. 136–161, 2013. Text with EEA relevance.

[89] D. Hunt, N. Mac Suibhne, L. Dimache, D. McHugh, and J. Lohan. Advances in multifunctional balanced ventilation technology for dwellings and arising challenge to quantify energy efficiency and renewable generation contributions using international test standards. *Renewable and Sustainable Energy Reviews*, 134:110327, 2020.

[90] C. Wemhoener, T. Afjei, and R. Dott. Iea hpp annex 28–standardised testing and seasonal performance calculation for multifunctional heat pump systems. *Applied Thermal Engineering*, 28(16):2062–2069, 2008.

[91] Performance rating of air-to-air exchangers for energy recovery ventilation equipment (ahri standard 1060-2023 (i-p)), 2023. Approved 8 November 2023.

[92] S. Documentation. Simulation and model-based design, 2024.

[93] Y. Men, X. Liu, and T. Zhang. Experimental and numerical analysis on heat and moisture recovery performance of enthalpy wheel with condensation. *Energy Conversion and Management*, 246:114683, 2021.

[94] M.J. Moran, H.N. Shapiro, D.D. Boettner, and M.B. Bailey. *Fundamentals of engineering thermodynamics*. John Wiley & Sons, 2010.

[95] R.K. Shah and D.P. Sekulic. *Fundamentals of heat exchanger design*. John Wiley & Sons, 2003.

[96] J. Min and J. Duan. Comparison of various methods for evaluating the membrane-type total heat exchanger performance. *International Journal of Heat and Mass Transfer*, 100:758–766, 2016.

[97] A. Engarnevis, R. Huizing, S. Green, and S. Rogak. Heat and mass transfer modeling in enthalpy exchangers using asymmetric composite membranes. *Journal of Membrane Science*, 556:248–262, June 2018.

[98] Y. Muzychka and M. Yovanovich. Laminar forced convection heat transfer in the combined entry region of non-circular ducts. *ASME Journal of Heat and Mass Transfer*, 126(1):54–61, 2004.

[99] L.Z. Zhang, C.H. Liang, and L.X. Pei. Conjugate heat and mass transfer in membrane-formed channels in all entry regions. *International Journal of Heat and Mass Transfer*, 53(5-6):815–824, 2010.

[100] J. Min, T. Hu, and X. Liu. Evaluation of moisture diffusivities in various membranes. *Journal of Membrane Science*, 357(1-2):185–191, 2010.

[101] K. Križo, A. Kapjor, and M. Holubčík. Polymer membranes for enthalpy exchangers. *Energies*, 15(16):6021, 2022.

[102] L.Z. Zhang, C.H. Liang, and L.X. Pei. Heat and moisture transfer in application scale parallel-plates enthalpy exchangers with novel membrane materials. *Journal of Membrane Science*, 325(2):672–682, 2008.

[103] J. Min and M. Su. Performance analysis of a membrane-based energy recovery ventilator: Effects of membrane spacing and thickness on the ventilator performance. *Applied Thermal Engineering*, 30(8-9):991–997, 2010.

[104] C. Co. *Flow of fluids through valves, fittings, and pipe*. Number 410. Crane Company, 1988.

[105] V. Gnielinski. On heat transfer in tubes. *International Journal of Heat and Mass Transfer*, 63:134–140, 2013.

[106] A. Cavallini and R. Zecchin. A dimensionless correlation for heat transfer in forced convection condensation. In *International Heat Transfer Conference Digital Library*. Begel House Inc., 1974.

[107] M.M. Shah. A new correlation for heat transfer during boiling flow through pipes. *ASHRAE Transactions*, 82(2):66–86, 1976.

[108] R. Sánta. The analysis of two-phase condensation heat transfer models based on the comparison of the boundary condition. *Acta Polytechnica Hungarica*, 9(6):167–180, 2012.

[109] A. Filip, F. Băltăreţu, and R.M. Damian. Comparison of two-phase pressure drop models for condensing flows in horizontal tubes. *Mathematical Modeling in Civil Engineering*, 10(4):19–27, 2014.

[110] S.E. Haaland. Simple and explicit formulas for the friction factor in turbulent pipe flow. *Journal of Fluids Engineering*, 105(1):89–90, 03 1983.

[111] W. Lockhart. Proposed correlation of data for isothermal two-phase, two-component flow in pipes. *Chemical engineering progress*, 45(1):39–48, 1949.

[112] W. Kays and A. London. *Compact Heat Exchangers*. Krieger Publishing Company, 1998.

[113] C.C. Wang, K.Y. Chi, and C.J. Chang. Heat transfer and friction characteristics of plain fin-and-tube heat exchangers, part ii: Correlation. *International Journal of Heat and Mass Transfer*, 43(15):2693–2700, 2000.

[114] C.C. Wang, C.J. Lee, C.T. Chang, and S.P. Lin. Heat transfer and friction correlation for compact louvered fin-and-tube heat exchangers. *International journal of heat and mass transfer*, 42(11):1945–1956, 1999.

[115] C.C. Wang, K.Y. Chi, and C.J. Chang. Heat transfer and friction characteristics of plain fin-and-tube heat exchangers, part ii: Correlation. *International Journal of Heat and Mass Transfer*, 43(15):2693–2700, 2000.

[116] H. Nemati and S. Samivand. Simple correlation to evaluate efficiency of annular elliptical fin circumscribing circular tube. *Arabian Journal for Science and Engineering*, 39(12):9181–9186, 2014.

[117] F. Suárez, S.D. Keegan, N.J. Mariani, and G.F. Barreto. A novel one-dimensional model to predict fin efficiency of continuous fin-tube heat exchangers. *Applied Thermal Engineering*, 149:1192–1202, 2019.

[118] K. Górnicki, R. Winiczenko, A. Kaleta, and A. Choińska. Evaluation of models for the dew point temperature determination. *Technical Sciences*, 20(3):241–257, 2017.

[119] K. Wark. *Thermodynamics*. McGraw-Hill Science, Engineering & Mathematics, 1988.

[120] M. Fossa and G. Tanda. Modelling of frost growth in simple geometries and passages. In *Modelling and Simulation: 16 th IASTED International Conference Proceedings*, 2005.

[121] H. Chen, L. Thomas, and R.W. Besant. Fan supplied heat exchanger fin performance under frosting conditions. *International Journal of Refrigeration*, 26(1):140–149, 2003.

[122] P. Tu, H. Inaba, A. Horibe, Z. Li, and N. Haruki. Fin efficiency of an annular fin composed of a substrate metallic fin and a coating layer. *ASME Journal of Heat and Mass Transfer*, 128, 08 2006.

[123] D. Siegele. *Optimization and Appliance of small Air Exhaust Heat Pumps with Focus on Alpine Regions*. Dissertation, University of Innsbruck, Innsbruck, Austria, 2019.

[124] K. Nawaz, A.F. Elatar, and B.A. Fricke. A critical literature review of defrost technologies for heat pumps and refrigeration systems. Technical report, Oak Ridge National Laboratory (ORNL), Oak Ridge, TN (United States), 08 2018.